Multicopter flow fields and their influence on a spray released from multicopters.

Illia Chyrva

A thesis submitted for the degree of

Doctor of Philosophy

in

Mechanical Engineering

Department of Mechanical Engineering

University of Canterbury

New Zealand

November 2021

Acknowledgement

I would like to express my gratitude to Professor Mark Jermy for providing endless guidance and support in this research project. His professionalism and expert supervision have always encouraged me to not slip into complacency but reach a new height.

I would like to thank an associate supervisor, Dr Tara Strand, for expert guidance. This project would be impossible without a strong connection with the industry. Special thanks to Dr Brian Richardson for providing his experimental result in spraying from multicopters.

I would like to express an appreciation to Dr Christina Dunker for her expert guidance in PIV experimentation. A quick start would be impossible without such advice. My sincere gratitude to Dr Natalia Kabaliuk for health and safety laboratory guidance and critical review of the papers. My acknowledgement to Professor Mathieu Sellier for providing his expertise in modelling.

My acknowledgement to workshop technicians of UC mechanical engineering department, Bill Mohs, Julian Phillips, Julian Murphy, Dave Read, who provided me support in various tools available in mechanical engineering workshops.

Abstract

Multicopters are remote-controlled vertical take-off and landing unpiloted aerial vehicles (UAVs). When used for releasing particulates (crop seeding, targeted fertiliser, and aerial spraying), they are a convenient tool for farms situated in rocky or mountainous terrain that does not allow for the use of helicopters or aeroplanes. Their small size and high manoeuvrability are also attractive for spraying near sensitive areas (e.g., riverbeds, lakes, native forest, residential areas).

Understanding the behaviour of spray is crucial for targeted spray dispersal and for the protection of sensitive areas. This research studies multicopter wake and its influence on the performance of spraying liquid.

The primary experimental technique used for the study of multicopter wake was stereo particle image velocimetry (SPIV), supplemented by constant temperature anemometry (CTA) with a three-axial probe.

The study analysed the isolated rotor wakes of the APC 1047 (127 mm radius, 119.3 mm pitch), APC 1045 (127 mm radius, 114.3 mm pitch), APC 1040 (127 mm radius, 101.6 mm pitch) and DJI E7000 (420 mm radius, 230 mm pitch). The isolated wake vector field, normalized by rotor tip velocity, was found to remain similar for each rotor with changing rotational speed.

Multicopters can be divided into two-rotor sections, allowing a simplified experimental setup using two rotors instead of four or more. APC 1045 counter-rotating coplanar rotor pairs were used for the analysis of multicopter rotors in hover, at rotor arc spacings of 02R, 0.36R and 0.55R (R=rotor radius). SPIV experimental analysis shows the rotor wakes tilting towards each other. The tilt angle decreases with increased tip spacing. Two counter rotating coplanar DJI

E7000 rotors with 0.2R rotor tip spacing also demonstrated tilted wakes. The tilt may be explained by interaction between wakes creating a low-pressure zone between them.

A region of upwash was detected with APC 1045 rotors at rotor arc distances of 0.2R, 0.36R and 0.55R. The upwash region was observed at every rotational position and phase difference for DJI E7000 rotors at an arc distance of 0.2R. Upward velocity magnitude is dependent on the angular position of the rotor, peaking when one of the rotor tips is at its closest approach to the neighbouring rotor's arc. It is weakly dependent on rotational speed over the range of 1740-2150 rpm. Upwash generation may be explained by interaction between the tip vortices and wakes of the two rotors.

APC 1045 counter-rotating rotor pairs were analysed in the presence of lateral velocity. In streamwise configuration, the wake of the windward rotor tilts 20-25º more than that of the leeward rotor at lateral velocities of 6 m/s, 10 m/s and 14 m/s. The shading of the leeward wake by the windward wake is the cause of the difference in tilt angles.

In the presence of lateral velocity with a streamwise rotor configuration, the roll-up vortex is attached to the windward side of the windward rotor disk and extends in the direction of the airflow relative to the multicopter. With a spanwise rotor configuration, the roll-up vortex is attached to the windward side of both rotors and extends in the direction of the airflow near the free side of the rotor disk. However, in the presence of another counter-rotating rotor, the upwash region does not have a downstream lateral component at lateral velocities between 2-6 m/s.

Based on SPIV analysis data used to track spray deposition near the rotors, it is recommended to avoid placing the spray nozzle immediately under the arc swept by the rotor tip (0.8R-1R), especially in the zone between rotors. This draws some spray upwards, decreasing spraying

efficiency and potentially entering the multicopter's electrical components. The recommended nozzle position is the zone of strongest downwash (0.5-0.7R).

A fast-computing model for spray pattern prediction was developed in OpenFoam, using rotor disk simplification as a boundary condition inside the domain. The velocity field boundary condition was obtained from SPIV data. The rotor boundary condition used the turbulence kinetic energy data obtained via CTA. The atmospheric wind model was incorporated into the model and can be used on-demand. The effect of plant canopy was introduced with a porous medium model.

Two DJI E7000 coplanar counter-rotating rotors were modelled in hovering flight. The modelled velocity field below the rotors was within one standard deviation of SPIV experimental results. The modelled velocity field between rotors was not within one standard deviation. The upward velocity region was not reproduced in the model.

Two APC 1045 rotors were modelled at 2 m/s, 6 m/s, 10 m/s lateral velocity in streamwise and spanwise configurations. In streamwise configuration, the leeward rotor is shaded by the windward rotor, therefore the inclination angle of the leeward rotor is smaller than that of the windward rotor. The roll-up vortices are observed in the model. The location of the roll-up vortices is similar in the model and experiment in both spanwise and streamwise configurations.

A DJI Agras MG-1 multicopter was modelled to allow comparison of swath patterns in the model and experimental results. Two roll-up vortices are present in the multicopter and extend in a streamwise direction. The model output was used for spray pattern prediction by applying Lagrangian particle tracking. An evaporation model was implemented in a particle tracking algorithm.

The spray footprints of two nozzle positions were modelled in hovering flight and compared to experimental results, revealing that the model can be used for spray footprint evaluation. Differences between the model and the experiment may be explained by absence of tip vortices in the model.

The swath pattern in the wake of a DJI Agras MG-1 multicopter in three different flights (true airspeed 3.627 m/s, ground speed 2.85 m/s, and crosswind speed 0.736 m/s; true airspeed 3.234 m/s, ground speed 2.9 m/s, and crosswind speed 2.164 m/s; true air speed 4.88 m/s, ground speed 4.88 m/s, and crosswind speed 0.04 m/s), is comparable in the model and experiment. The effective swath width (30% line separation) is within one standard deviation of the model.

In all flight trials, the modelled swath was closest to the experimentally obtained swath when the surface roughness of the ground was equal to 0.5 m (bushes) and the rotational speed of all rotors was equal to 2475 rpm with 0.75R (0.2m) tall plant canopy (grass) introduced to the model.

The model can be used to evaluate the swath pattern left on the ground by the multicopter. It showed acceptable validity for hovering flight and flight velocities of up to 2.8-5 m/s when flight parameters can be approximately estimated. The computational time of the model is 12 minutes.

UNIVERSITY OF CANTERBURY
Te Whare Wānanga o Waitaha
CHRISTCHURCH NEW ZEALAND

Deputy Vice-Chancellor's Office
Postgraduate Research Office

Co-Authorship Form

This form is to accompany the submission of any thesis that contains research reported in co-authored work that has been published, accepted for publication, or submitted for publication. A copy of this form should be included for each co-authored work that is included in the thesis. Completed forms should be included at the front (after the thesis abstract) of each copy of the thesis submitted for examination and library deposit.

Please indicate the chapter/section/pages of this thesis that are extracted from co-authored work and provide details of the publication or submission from the extract comes:

CHYRVA, I, DUNKER, C, KABALIUK, N, JERMY, MC. *Rotor-rotor interaction of remotely piloted multicopter and their influence on an on-board spraying system.* Fluids in New Zealand (FINZ), Feb 2019, Dunedin, New Zealand

Please detail the nature and extent (%) of contribution by the candidate:

The contribution of the candidate to the publication amounts to ~85% based on the overall time and effort dedicated to the final outcome. The candidate developed, implemented and led all experimental work in consultation with the supervisors.

Certification by Co-authors:

If there is more than one co-author then a single co-author can sign on behalf of all

The undersigned certifies that:

- The above statement correctly reflects the nature and extent of the Doctoral candidate's contribution to this co-authored work
- In cases where the candidate was the lead author of the co-authored work he or she wrote the text

Name: *Prof. Mark Jermy* Signature: *Mark Jermy* Date: *01.11.2021*

UNIVERSITY OF CANTERBURY
Te Whare Wānanga o Waitaha
CHRISTCHURCH NEW ZEALAND

Deputy Vice-Chancellor's Office
Postgraduate Research Office

Co-Authorship Form

This form is to accompany the submission of any thesis that contains research reported in co-authored work that has been published, accepted for publication, or submitted for publication. A copy of this form should be included for each co-authored work that is included in the thesis. Completed forms should be included at the front (after the thesis abstract) of each copy of the thesis submitted for examination and library deposit.

Please indicate the chapter/section/pages of this thesis that are extracted from co-authored work and provide details of the publication or submission from the extract comes:

CHYRVA, I, STRAND T, C, KABALIUK, N, JERMY, MC. *Experimental investigation of upward velocity region between adjacent counter-rotating rotors using SPIV technique.* Fluids in New Zealand (FINZ), Feb 2021, Christchurch, New Zealand

Please detail the nature and extent (%) of contribution by the candidate:

The contribution of the candidate to the publication amounts to ~85% based on the overall time and effort dedicated to the final outcome. The candidate developed, implemented and led all experimental work in consultation with the supervisors.

Certification by Co-authors:

If there is more than one co-author then a single co-author can sign on behalf of all

The undersigned certifies that:

- The above statement correctly reflects the nature and extent of the Doctoral candidate's contribution to this co-authored work
- In cases where the candidate was the lead author of the co-authored work he or she wrote the text

Name: *Prof. Mark Jermy* Signature: *Mark Jermy* Date: *01.11.2021*

UNIVERSITY OF CANTERBURY
Te Whare Wānanga o Waitaha
CHRISTCHURCH NEW ZEALAND

Deputy Vice-Chancellor's Office
Postgraduate Research Office

Co-Authorship Form

This form is to accompany the submission of any thesis that contains research reported in co-authored work that has been published, accepted for publication, or submitted for publication. A copy of this form should be included for each co-authored work that is included in the thesis. Completed forms should be included at the front (after the thesis abstract) of each copy of the thesis submitted for examination and library deposit.

Please indicate the chapter/section/pages of this thesis that are extracted from co-authored work and provide details of the publication or submission from the extract comes:

CHYRVA, I, STRAND T, DUNKER C, KABALIUK, N, GEOGHEGAN, P, JERMY, MC. *Experimental investigation of upward velocity region between adjacent counter-rotating rotors using SPIV technique.* 22nd Australasian Fluid Mechanics Conference, Brisbane, Australia

Please detail the nature and extent (%) of contribution by the candidate:

The contribution of the candidate to the publication amounts to ~85% based on the overall time and effort dedicated to the final outcome. The candidate developed, implemented and led all experimental work in consultation with the supervisors.

Certification by Co-authors:

If there is more than one co-author then a single co-author can sign on behalf of all

The undersigned certifies that:

- The above statement correctly reflects the nature and extent of the Doctoral candidate's contribution to this co-authored work
- In cases where the candidate was the lead author of the co-authored work he or she wrote the text

Name: *Prof. Mark Jermy* Signature: *Mark Jermy* Date: *01.11.2021*

UNIVERSITY OF CANTERBURY
Te Whare Wānanga o Waitaha
CHRISTCHURCH NEW ZEALAND

Deputy Vice-Chancellor's Office
Postgraduate Research Office

Co-Authorship Form

This form is to accompany the submission of any thesis that contains research reported in co-authored work that has been published, accepted for publication, or submitted for publication. A copy of this form should be included for each co-authored work that is included in the thesis. Completed forms should be included at the front (after the thesis abstract) of each copy of the thesis submitted for examination and library deposit.

Please indicate the chapter/section/pages of this thesis that are extracted from co-authored work and provide details of the publication or submission from the extract comes:

CHYRVA, I, STRAND T, DUNKER C, KABALIUK, N, JERMY, MC. *Experimental investigation of the upward velocity region between adjacent counter-rotating rotors (article ready for submission)*

Please detail the nature and extent (%) of contribution by the candidate:

The contribution of the candidate to the publication amounts to ~85% based on the overall time and effort dedicated to the final outcome. The candidate developed, implemented and led all experimental work in consultation with the supervisors.

Certification by Co-authors:

If there is more than one co-author then a single co-author can sign on behalf of all

The undersigned certifies that:

- The above statement correctly reflects the nature and extent of the Doctoral candidate's contribution to this co-authored work
- In cases where the candidate was the lead author of the co-authored work he or she wrote the text

Name: *Prof. Mark Jermy* Signature: *Mark Jermy* Date: *01.11.2021*

Table of Contents

List of Figures

List of Tables

Abbreviations

AgDisp	Agricultural dispersion
CAD	Computer aided design
CCD	Charge-coupled device
CFD	Computational fluid dynamics
CHARM	Comprehensive Hierarchical Aeromechanics Rotorcraft Model
CTA	Constant temperature anemometry
DEHS	Di-ethyl-hexyl sebacate
ESC	Electronic speed controller
LDV	Laser Doppler velocimetry
Nd:Yag	Neodymium-doped yttrium aluminium garnet
PIV	Particle Image velocimetry
RANS	Reynolds Averaged Navier Stokes
PWM	Pulse width modulation
S.D.	Standard deviation
SNR	Signal to noise ratio
SPIV	Stereo particle image velocimetry
SST	Shear Stress transport
TKE	Turbulence kinetic energy
UAV	Unpiloted aerial vehicles
WMO	World meteorological organisation

1. Literature review

Unpiloted aerial vehicles (UAVs) are aerial vehicles without an onboard crew. They can be controlled by a pilot from the ground or can perform autonomous flight using prepared programs or artificial intelligence. A UAV that uses more than one rotor to generate lift is called a multicopter.

Although the era of unmanned flight vehicles began a century ago, they were rarely used for agricultural spraying until recently. The primary agricultural application of UAVs today is field surveillance (Rahman et al., 2021), but the practical possibilities of multicopter UAVs are much greater. UAVs could be used for crop seeding, targeted fertiliser, and aerial spraying (Rahman et al., 2021). The main advantage of UAVs is their relatively small size compared to piloted helicopters, allowing for precise targeting. This is particularly attractive for spraying herbicides and pesticides near sensitive areas such as water reservoirs and residential areas. Added benefits include low initial capital cost, low financial risk, and high safety. UAVs are a convenient tool for small farms situated in rocky or mountainous areas. Usually, the terrain complexity of terraced hillside farms does not allow for the use of helicopters or aeroplanes. Many multirotor aircraft have the advantages of good manoeuvrability, ability to hover, and vertical take-off and landing, making them suitable for complex and diverse terrains such as terraced hills and slopes (Rahman et al., 2021).

Sprayed liquid released from the craft tends to follow the path formed by massless particles (streamline) (Bilanin et al., 1989). The presence of rotors alters the streamlines, influencing the path of the spray. Understanding the behaviour of spray is crucial for optimal spray dispersal on crops, while understanding the maximum possible drift of spray after release from the craft is important to protect sensitive areas (e.g., riverbeds, lakes, native bushes).

This chapter describes the multicopters currently used for spray dispersion and the methods used to evaluate spray deposition. The prediction of spray deposition is divided into two parts: predicting the wake generated by the multicopter and predicting spray behaviour under the influence of multicopter wakes.

The velocity field is divided into two parts: near-field wake and far-field velocity field. The near field is the space around and up to 4 rotor radiuses away from the multicopter. Flow within the near field is mainly generated and altered by components of the multicopter (rotor, body, spraying system). The far-field described the space further than 4 rotor radiuses from the multicopter. Flow in the far-field is mainly affected by flight parameters (flight velocity, flight height), atmospheric wind and plant canopy.

Spray deposition can be evaluated numerically or experimentally. Both methods are demonstrated in this chapter, which examines how spray deposition on plants depends on both multicopter flight parameters (height, speed) and plant parameters (phenotype, wettability, roughness).

1.1 Agricultural spraying multicopters

This section describes commonly used spraying UAVs. Multicopters are categorised by the following parameters (Vu et al., 2019):

1. Number of rotors (quadcopter, octocopter, hexacopter etc…)
2. Rotor layout (+, X, mixed (mix of + and X layouts))
3. Propulsion system (coaxial rotor system, single rotor system, ducted rotor system)

The DJI Agras MG-1 (https://www.dji.com/nz/e7000/info#specs, accessed 01.09.2020) is the legacy version of DJI Agras spraying multicopters with a mixed rotor layout (Figure 1.1).

Figure 1.1 DJI Agras MG-1 multicopter (https://www.dji.com/nz/mg-1/info#specs, accessed 01.09.2020)

The DJI Agras MG-1 consists of 8 rotors with a single rotor propulsion system. Each rotor measures 266.5x178 mm (radius x pitch). The manufacturer publishes performance data for individual rotors (https://www.dji.com/nz/e2000/info#specs, accessed 01.09.2020) for DJI Agras Mg-1 multicopters (Figure 1.2)

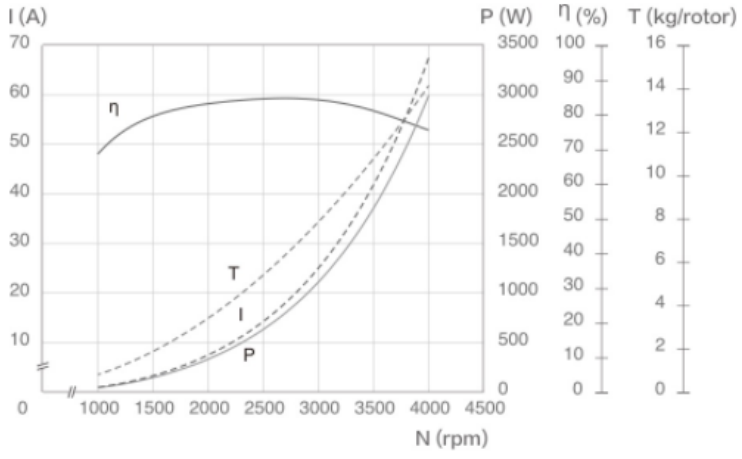

I – Current, P – Input Power, η – Electrical Efficiency, T – Thrust, N – Rotational Speed
The data above was measured with an input voltage of 44.4 V, at a temperature of 25°C and sea level. The rotational speed was adjusted by the throttle.

Figure 1.2 Performance curves of the DJI E2000 propulsion system (https://www.dji.com/nz/e2000/info#specs accessed 31.10.2021).

The spraying system of the DJI Agras Mg-1 consists of four XR11001 nozzles, each with a flow rate of 0.43 L/min. The maximum capacity of the tank is 10 litres. Richardson et al. (2019) and Martin et al. (2019) used this drone for experimental spray pattern evaluation.

The newer version of this multicopter, with increased spray liquid capacity, is the DJI Agras T20 (Figure 1.3).

Figure 1.3 DJI Agras T20 Multicopter (https://www.dji.com/nz/t20 accessed 01.09.2020)

It has a mixed layout with six 420x230 mm (radius x pitch) rotors. The parameters of the propulsion system are shown in Figure 1.4 (https://www.dji.com/nz/e7000/info#specs 01.09.2020):

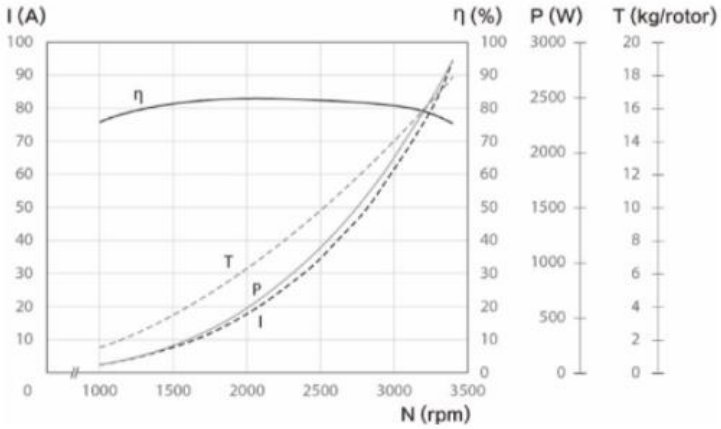

I – Current, P – Input Power, η – Electrical Efficiency, T – Thrust, N – Rotational Speed
The data above was measured with an input voltage of 44.4 V, at a temperature of 25°C and sea level. The rotational speed was adjusted by the throttle.

Figure 1.4 Performance curves of DJI E7000 propulsion system (https://www.dji.com/nz/e7000/info#specs accessed 31.10.2021)

The spray system consists of eight SX11001VS nozzles, each with a flow rate of 3.6 L/min. The maximum capacity of the tank is 20 litres.

An example of a multicopter with an X configuration coaxial thrust system is the Aeronavics Icon (Figure 1.5). This UAV has 8 PJP-T-L rotors mounted coaxially, two per propulsion unit. The PJP-T-L rotors measure 190.5x127 mm (radius x pitch) with a maximum thrust of 28.49N per rotor (https://www.xoarintl.com/multicopter-propellers/precision-pair/PJP-T-L-Precision-Pair-Multicopter-Carbon-Fiber-Propeller-Low-Kv-Motor/, accessed 01.09.2020).

Figure 1.5 Aeronavics Icon coaxial multicopter (Teske et al., 2018).

Teske et al. (2018) used the Aeronavics Icon for their experimental evaluation of spray patterns.

Other multicopters are also available for spraying applications. Most have a mixed layout with a single rotor propulsion system, as summarised by Rahman et al. (2021).

1.2 Near-field rotor wake

The rotor is the element of a multicopter that creates lift by spinning around its axis. Rotors consist of a hub with attached blade or blades. The blades spin around a vertical axis, describing a horizontal disk known as the rotor disk (Johnson et al., 2013). Rotors are usually characterised by two parameters: rotor radius and rotor pitch. Pitch is expressed as a ratio of forwards distance per revolution (in the absence of slip). The typical cross-section of each blade is an aerofoil shape. The common rotor has the following geometric characteristics (Figure 1.6):

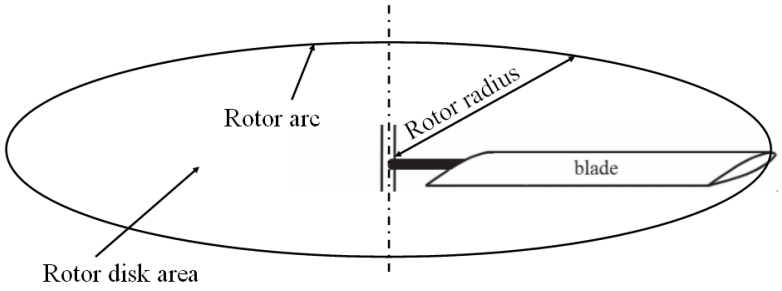

Figure 1.6 Rotor geometrical characteristics (adapted from Johnson et al., 2013)

1.2.1 Near-field wake models

1.2.1.1 Analytical models for near-field rotor wake analysis

This section discusses the most important analytical models for the evaluation of wake. The isolated rotor wake can be described by finding three components of velocity (downwash, radial and swirl) at every point on the rotor disk.

There are many methods of isolated wake evaluation, including momentum theory, blade element theory, and vortex theory. The basic method is momentum theory (Figure 1.7), which applies the conservation laws of fluid mechanics to the rotor and its wake.

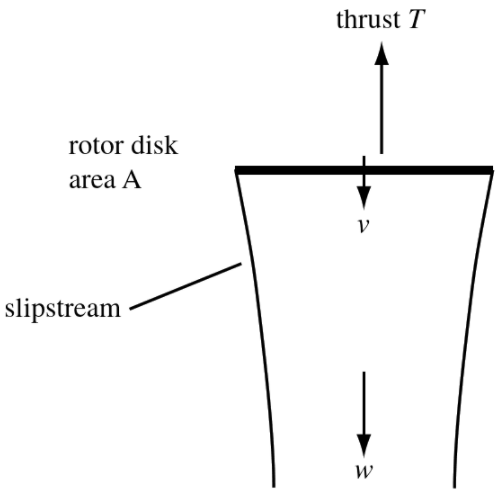

Figure 1.7 Description of rotor wake based on the momentum theory (Johnson, 2013).

Based on momentum theory, rotor thrust at the rotor disk is equal to (Equation 1.1):

$$T = \dot{m}v = 2\rho A v^2 \quad \text{(Equation 1.1)}$$

Where $\dot{m}$ is mass flow rate,

v is induced velocity,

ρ is air density,

and A is rotor disk area.

Therefore, in momentum theory the induced flow through the rotor disk is (Equation 1.2):

$$v = \sqrt{\frac{T}{2\rho A}} \quad \text{(Equation 1.2)}$$

The swirl and radial velocity components are neglected in momentum theory. The downwash is uniform over the rotor disk.

Blade element theory is a mathematical model that divides the blade into finite two-dimensional aerofoils and computes the force on each cross-section. Then the force is integrated along the rotor blade, giving an estimation of force and torque for the entire rotor (Johnson et al., 2013). The induced velocity of the rotor in hover flight can be predicted as follows (Equation 1.3):

$$v = \frac{\sigma a \omega R}{16}\left[\sqrt{1 + \frac{32}{\sigma a}\theta r} - 1\right] \quad \text{(Equation 1.3)}$$

Where σ is blade solidity,

ω is rotor rotational speed,

R is rotor radius,

θ is angle of attack at any position of rotor blade r,

and a is airfoil lift curve slope at any position of rotor blade r

Swirl, tip vortex velocity and root losses are neglected. The most precise fundamental wake analysis was performed by Gray et al. (1956). Their work led to the conclusion that single-bladed wake geometry consists of a vortex sheet (shed from the trailing edge) and a tip vortex. The vortex sheet is attached to the blade. The tip vortex is emitted by the blade tip and propagates downstream with the vortex sheet (Figure 1.8). The tip vortex is created by the pressure difference on the top and bottom surfaces of the blade. The air, which tends to move from the zone of high pressure to the zone of low pressure, escapes through the tip of the rotor.

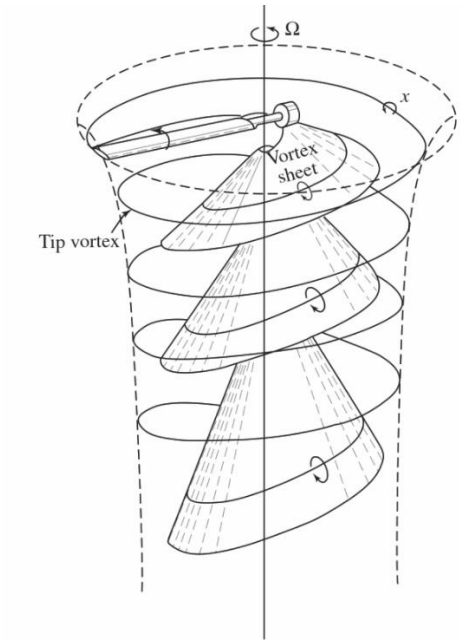

Figure 1.8 Vortex sheet generated by a single bladed rotor (Grey et al., 1956; Johnson, 2013)

Based on the results presented by Gray et al., Landgrebe (1971) developed a prescribed vortex model. In terms of dimensionless azimuth angle φ the wake can be described as follows (Equation 1.4, Equation 1.5):

$$z = K_1\phi \qquad \phi < \phi_1$$
$$z = K_1\phi_1 + K_2(\phi - \phi_1) \qquad \phi > \phi_1 \quad \text{(Equation 1.4)}$$

$$r = K_4 + e^{-K_3\phi}(1 - K_4) \quad \text{(Equation 1.5)}$$

Where *z* is the vertical coordinate from the rotor disk

$\phi_1 = \frac{2\pi}{N}$ is the age of encounter with the following wake.

Langrabe (1971) specified the coefficients (Table 1.1)

Table 1.1 The coefficients for the prescribed vortex model (Langrabe, 1971)

	K_1	K_2
Tip vortex	$0.25(C_T/\sigma + 0.001\theta_{tw})$	$(1 + 0.01\theta_{tw})\sqrt{C_T}$
Outside sheet edge	$1.55\sqrt{C_T}$	$1.90\sqrt{C_T}$
Inside sheet edge	0	$-\left(0.0025\theta_{tw}^2 + 0.099\theta\right)\sqrt{C_T}$

and the spanwise coefficients (Equation 1.6, Equation 1.7):

$$K_3 = 0.145 + 27C_T \quad \text{(Equation 1.6)}$$

$$K_4 = 0.78 \quad \text{(Equation 1.7)}$$

The prescribed model fully describes the wake geometry. These models can be used for wake evaluation. However, the precision of wake description is much lower for multicopters than for helicopters (Shukla et al., 2018). All the methods mentioned above were developed for helicopter rotors. The primary assumption is that the Reynolds number is very high, and therefore the flow is inviscid and irrotational everywhere except the high-velocity region under

the rotor. Outside the very high-velocity region under the helicopter rotor, flow can be calculated using the potential flow method. For multicopter rotors with lower Reynolds number, the effects of viscosity are comparable (by order of magnitude) to the effects of inertia. Therefore, viscosity cannot be neglected when evaluating multicopter wakes (Shukla et al., 2018).

1.2.1.2 Numerical models for the near rotor wake analysis

The most common numerical method of wake computation is computational fluid dynamics (CFD) analysis. There are several articles reporting CFD analysis of multicopter wake (Stajuda et al., 2016; Yeong et al., 2016; Alexandrov et al., 2013). Weerasinghe et al. (2017) and Fengbo et al. (2017) performed an analysis of a quadcopter in forward flight and in hovering mode. The turbulence model was k-epsilon, which required approximately 3 million cells to analyse the full quadcopter for convergence.

A possible simplification of CFD computation is the virtual blade model. In this model, the rotor is replaced by an equivalent rotor disk of the same diameter (Stajuda et al., 2018; Bianchini et al., 2017). The hub can either be modelled as a wall or not be modelled at all. In the virtual blade model, the thickness of the disk is only one cell. The source term in the virtual disk cells can be either momentum of velocity, velocity, or pressure. The velocity or pressure required for the source can be obtained from precise CFD analysis of the rotor or experiment.

The time-marching free-wake model to study multirotor systems (Lee et al., 2009) was implemented with a wake instability effect. The wake instability effect was incorporated in the model with the vortex core diffusion effect modelled using empirical relaxation (Leishman et al., 2002). Lee et al. (2009) showed that time-marching free-wake models can be used for multicopter systems.

Teske et al. (2018) utilised CHARM, a self-contained rotor/wake/body computational analysis that models rotorcraft blade aerodynamics and dynamics in hover and forward flight (http://www.continuum-dynamics.com/pr-charm.html, accessed 28.01.2019). Free vortex wake methods arise from a discontinuous description of the rotor vorticity field. Under the action of the local velocity field, the wake elements are allowed to change to force-free locations. The free wake model was incorporated with AGDISP software for spray pattern prediction. Teske et al. (2018) showed that this approach can be used for some types of multicopters.

1.2.2 Near-field rotor wake features observed in experimental and computational analysis

1.2.2.1 Coplanar counter-rotating rotors

Several authors (Aleksandrov et al., 2013; Shukla et al., 2017; Hvang et al., 2015) observed thrust degradation in coplanar counter-rotating rotors. Equation 1.2 shows that the rotor downwash is the function of rotor thrust. Aleksandrov et al., (2013) measured the thrust of APC (Landing Products Inc. Woodland, CA. USA) 10x4.5 (127 mm radius, 114.3 mm pitch) counter-rotating, coplanar rotors as a function of in-plane separation. They found a maximum 10% thrust decrease due to blade-blade proximity, starting from a distance of 4.6 rotor radii between shafts at rotational speeds of between 3000 and 6000 rpm. The thrust coefficient of DJI 240mm-radius rotors was found to decrease at a separation distance of three rotor radiuses (Zhou et al., 2017). The thrust of each rotor was reduced by 1.7% relative to a single isolated rotor. Additionally, the measured thrust fluctuations of rotors at a separation distance of 2.1 rotor radiuses were 3.5 times stronger than those of a single rotor due to blade-blade interactions. The authors concluded that a tip-distance-dependent downwash interaction region between rotors reduces their total thrust.

Zhou et al. (2017) showed a region of separation from the rotating system between two rotors in his PIV analysis (Figure 1.9).

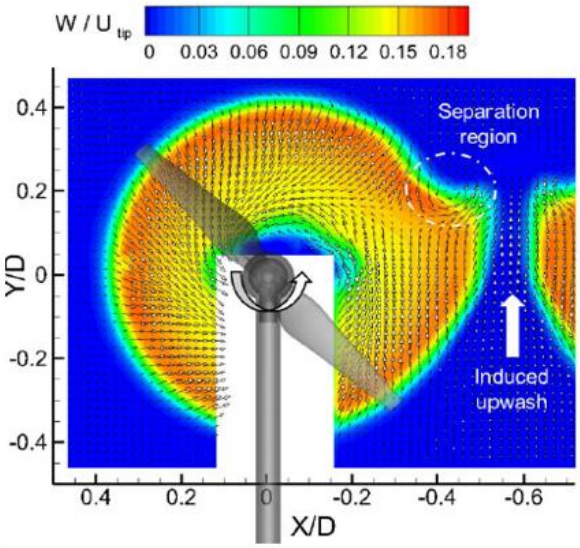

Figure 1.9 Separation region near the rotor interaction (Zhou et al., 2017)

The separation region generated due to the proximity of the rotor was reported at distances of up to two rotor radiuses. For a full multicopter with 4 or more rotors, the separation region may be a larger elongated velocity region along the body of the multicopter. Fengbo et al. (2017) performed a CFD analysis and obtained the velocity magnitude distribution for the six-rotor multicopter (Figure 1.10).

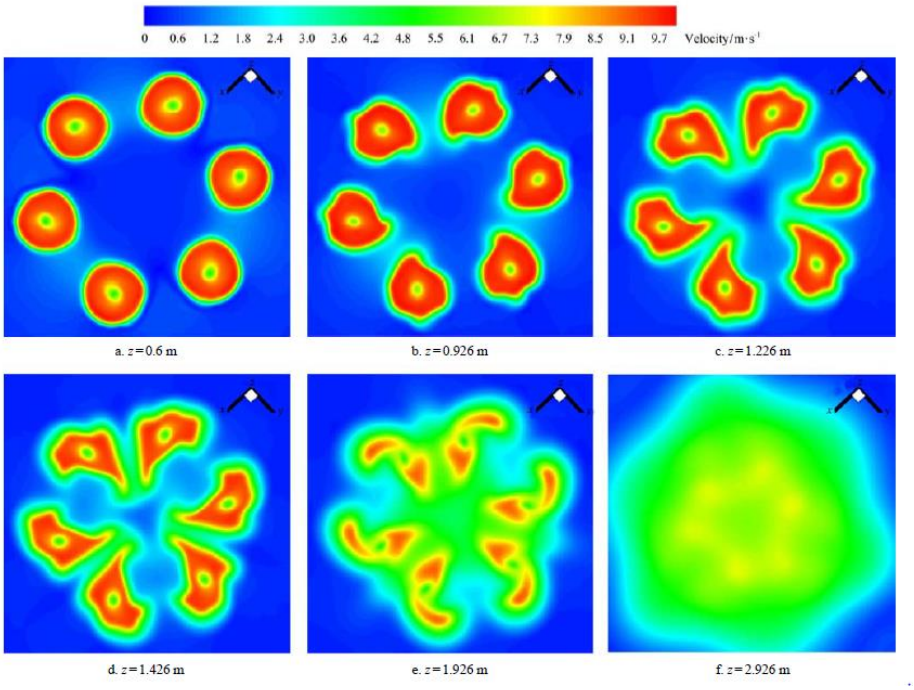

Figure 1.10 Separation region near rotor interaction. Top view (Fengbo et al., 2017)

In their research, Fengbo et al. (2017) compared their numerical prediction of downwash speed to a flight measurement with an error of around 10%.

Another noticeable effect is a region of upward velocity between co-planar counter-rotating rotors. Mehrabi et al. (2020) found that tufts attached to the ground under two coplanar rotors were lifted upward in the zone between rotors. They used two 660 mm coplanar non-overlapping rotors with a distance of one rotor radius between rotor tips. Particle image velocimetry confirmed upwash in the region between rotors (Zhou et al., 2017; Shukla et al., 2013). Shukla et al. (2017) state that upwash velocity magnitude depends on the strength of the rotor tip vortices.

The time-marching free-wake model to study multirotor systems (Lee et al., 2009) found that when interference effects are included in the model, a region of upwash between tandem rotors is observed, i.e., air travelling vertically, counter to the main downwards flow from the rotors.

The wake instability effect was introduced to the model with the vortex core diffusion effect modelled using empirical relaxation (Leishman et al., 2002). The authors supposed that induced velocity generated by one rotor wake causes an upward velocity on the other rotor near the wake edge. The free wake model can also predict thrust variation. Thrust variation and upward velocity are both caused by rotor-to-rotor interactions.

1.2.2.2 Flight in lateral velocity conditions

Multicopters are used for mass spraying as well as targeted spraying. Mass spraying requires forward movement of multicopter, meaning the effects of lateral velocity on the wake must be observed.

In their computational study of rotor-to-rotor interaction, Misiorowski et al. (2019) described several effects of the presence of lateral velocity: roll-up vortices, tip vortices and root vortices. The authors suggested that roll-up vortices are present next to the tip of the rotor and are stronger on the advanced part of the rotor (Figure 1.11).

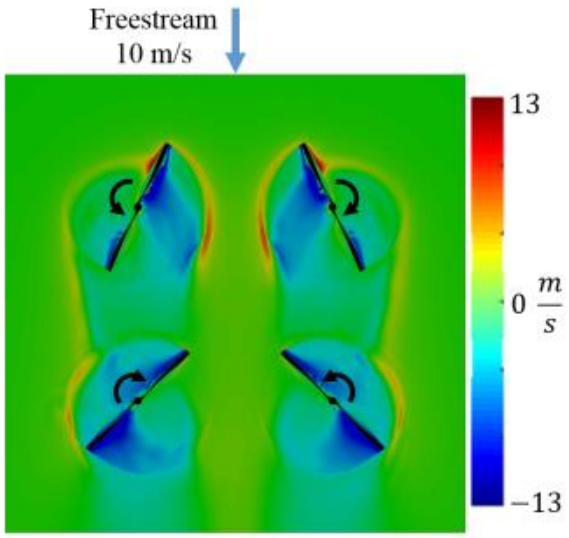

Figure 1.11 Induced velocity in the rotor plane for the cross configuration in forward flight (Misiorowski et al., 2019)

Moreover, Wang et al., (2015) showed that actuator disk models can predict the side roll-up vortices (Figure 1.12). The intensities of these vortices are equal on both sides of the rotor.

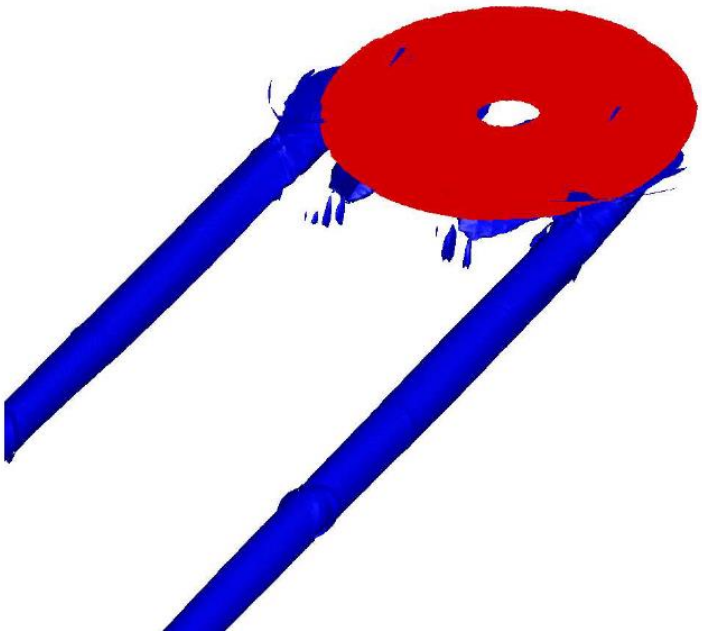

Figure 1.12 Isosurface plot of wake vorticity of CFD actuator disk model (Wang et al., 2015)

Another effect, observed by Yoon et al. (2017), is a difference in the geometric angle of tilt of the windward rotor wake compared to that of the leeward rotor wake (Figure 1.13).

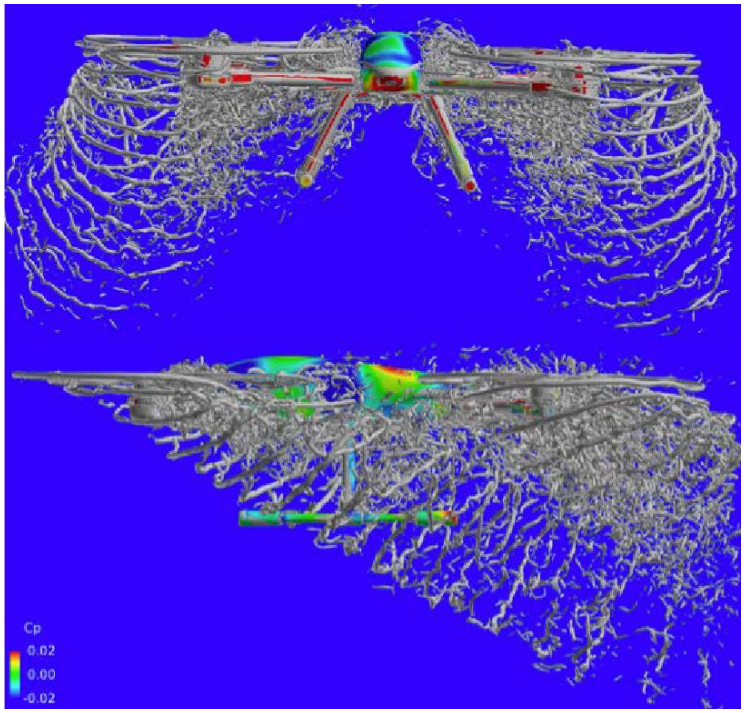

Figure 1.13 Iso-surfaces of Q-criterion and surface pressure in forward flight (Yoon et al., 2017)

1.3 Far-field wake interaction features

The far-field is the region further than 4 rotor radiuses from the multicopter. Far-field velocity is a mix of velocity fields generated by the multicopter and the atmosphere. Moreover, the wake from the multicopter interacts with terrain (ground, crop, canopy).

1.3.1 Ground effect and its influence on the downwash

The interaction between the ground and rotors appears both in flight with lateral flight velocity and in hovering flight. The effect of the interaction of a rotor wake with the ground is called ground effect. In ground effect, the wake of the multicopter bounces off the solid surface, generating additional lift on the rotors. Ground effect is accompanied by lateral velocity generated in all directions around the multicopter. This effect is known for helicopters.

According to foundational research by Cheesman et al. (1959), ground effect in helicopters can be neglected if distance to the ground is more than 1.5 rotor radiuses. Several scholars (Griffins et al., 2005; Sharf et al., 2014) have stated that ground effect is stronger in multirotor systems and can be observed up to 4 rotor radiuses from the ground. Sanchez-Cuevas (2017) characterised ground effect for multicopters (Figure 1.14) and found that in close proximity flight only the front multicopter rotor might experience the ground effect because of the pitch of the multicopter required for the forward flight.

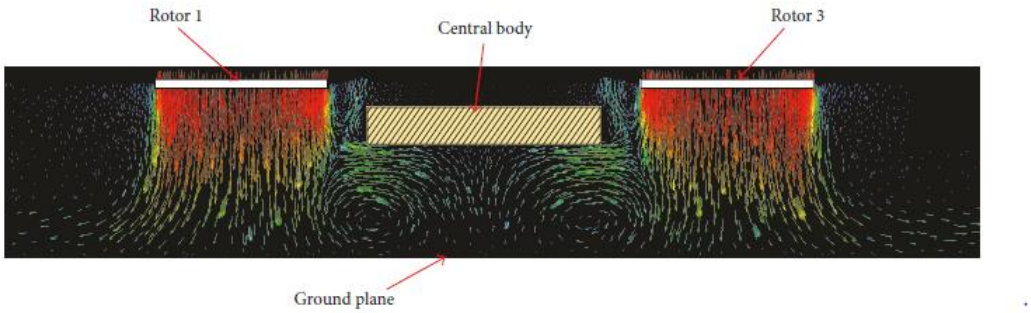

Figure 1.14 Ground effect and body interaction (Sanchez-Cuevas et al., (2017))

1.3.2 Interaction of wake and plant canopy

Plant canopies affect multicopter wake by blocking the horizontal and vertical displacement of air masses through the canopy. It is generally assumed that wake penetration through the canopy has an inverse relationship with canopy density (Hong et al., 2021). Chen et al. (2013) reported that wake penetration through the canopy depends on the growth stage of the plant. In relation to spraying, an increase in canopy density decreases the drift of the spray. However, very dense canopies with stiff foliage (e.g., orange, grapefruit) deflect the airflow (Hong et al., 2021). This would mean increased drift and poor delivery of spray to the centre of the plant.

Guo et al. (2021) studied the wind-induced response of rice plants, finding that the plant response depends on flight height and speed. The obtained images of the spraying multicopter show the response area of the rice plant (Figure 1.15)

Figure 1.15 Rice plant response to the wake of a flying multicopter: (left) height 1.2 m, flight speed 1.4 m/s; (centre) height 2.4 m, flight speed 2.4 m/s; (right) height 5.1m, flight speed 3.4 m/s (Guo et al., 2021)

Guo et al. (2021) found that, at a height of 1.2 m and flight speed of 1.4 m/s, the area of induced plant response is 1-10 m^2. The area of induced plant response increases to more than 10 m^2 when height is 2.4 m, and flight speed is 2.4 m/s. No induced areas were reported when height was 5.1 m, and flight speed was 3.4 m/s; however, roll-up vortices generated by the flying multicopter were clearly observable.

Shi et al. (2021) modelled the influence of the wake on tomato plants when spraying in a greenhouse. Their experimental research validated the CFD modelling of a multicopter with four 115 mm-radius rotors. The height of the plant was 1 metre above the ground. The tomato plant was modelled using a porous medium based on the Darcy–Forchheimer law. They found that increasing the flight height increased the penetration of the wake through the tomato plant and proved that porous medium models can be used to study the influence of wake interaction with plant canopy.

1.4 Spraying operations

1.4.1 Computational analysis of spray deposition

The industry standard for spray pattern evaluation is AgDisp software (Continuum Dynamics Inc., Ewing, NJ, USA). AgDisp utilizes the Lagrangian approach to track the group of similarly sized droplets that descend in the wake of the craft (Teske et al., 2002, 2018; Bilanin et al., 1989). Teske et al., (2018) found that spray deposition can be evaluated using AgDisp for particle tracking and CHARM for wake modelling (free wake computational model, Continuum Dynamics Inc., Ewing, NJ, USA).

Wen et al. (2019) utilised the Lattice-Bolzman CFD analysis to compute droplet behaviour in a multicopter flow field. They used four 383 mm-radius rotors in flight with lateral velocity. The analysis was conducted with four "extra fine" nozzles attached to the boom under the multicopter. They found that rotor wake affects the droplets in such a way that the droplets form a horseshoe pattern on the ground. Their computational analysis was validated in wind tunnel experiments (Figure 1.16).

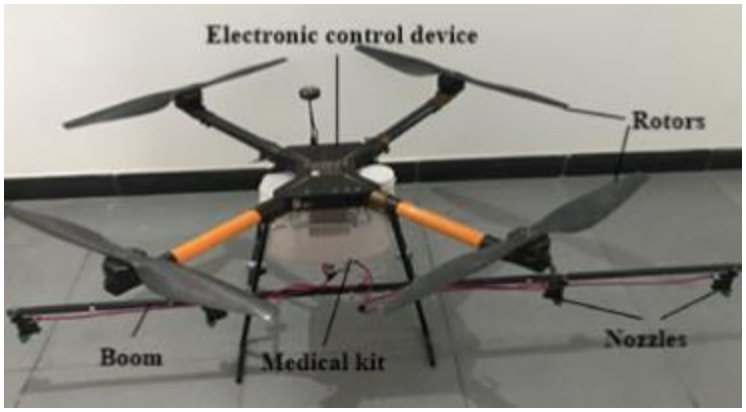

Figure 1.16 Multicopter with four 383 mm-radius rotors and four attached spraying nozzles (Wen et al., 2019)

Sarghini et al. (2017) analysed the downwash coaxial and normal layout of quadcopters using Lagrangian particle tracking inside a velocity field generated using Navier-Stokes equations (Ansys Fluent). They found that the layout with a single rotor has a bigger influence on droplets and a wider spray deposition than the coaxial layout. Additionally, they stated that the deposition of droplets depends on the position of the nozzle.

1.4.2 Experimental analysis of spray deposition

1.4.2.1 Methods of evaluation of spraying efficiency

Richardson et al. (2019) tested spray deposition on the ground using string tensioned across the spray area. The string was wound onto a spool and stored in a dark place. In the laboratory, the fluorescence was quantified by pulling the string through a fluorimeter. The deposition was calculated by reference to the concentration of tracer in the appropriate tank samples.

Another method used by Richardson et al. (2019) was to spray the fluorescent tracer on steel plates. The spray was allowed to dry and was stored in the dark. Fluorescence on plates was determined by washing the plates using the known amount of water. Fluorescence was measured at 514 nm following excitation at 425 nm using standard fluorometric techniques (Narin et al., 2015).

Another method of capturing flow deposition is spraying on water-sensitive paper (Guo et al., 2019).

1.4.2.2 Spray deposition in multicopter wake

Richardson et al. (2019) evaluated the swath pattern while spraying from a DJI Agras MG-1 multicopter. They highlighted the sensitivity of the spray pattern to the nozzle position in relation to the flight direction and flight height. Martin et al. (2019) confirmed these results,

adding that the spray pattern for the V6A (H2S UAV, Casselberry, Florida, USA) multicopter with a different nozzle layout is less sensitive to multicopter height above the canopy.

Wen et al. (2021) found that the spray forms a double-peak pattern. The pattern depends on spray height and multicopter speed (Figure 1.17). In their experimental procedure, the multicopter was fixed to a stationary rig. Lateral velocity was generated using a wind tunnel. The spray pattern was evaluated using a string with fluorescence.

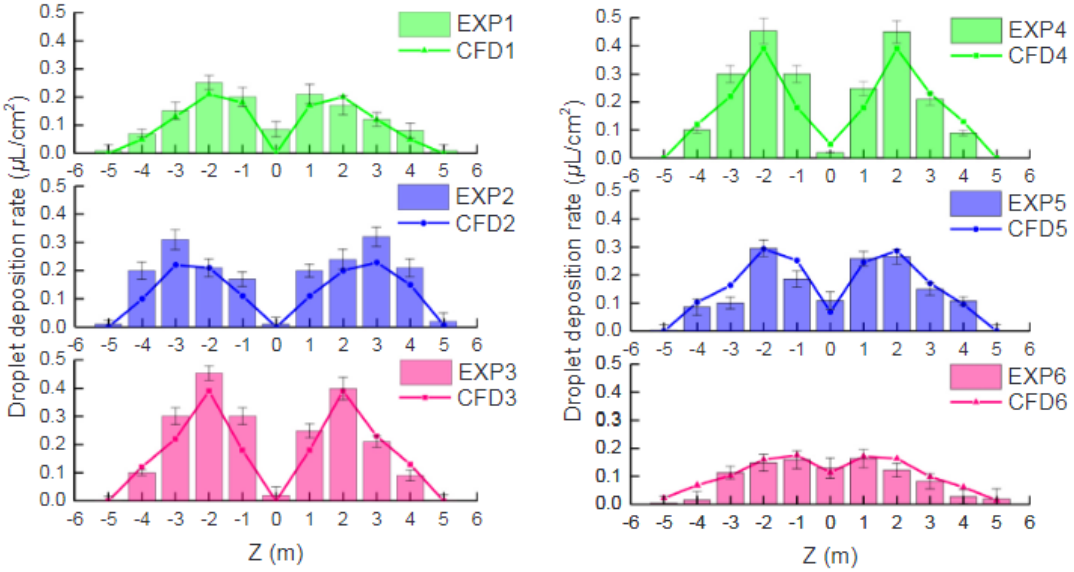

Figure 1.17 Droplet pattern on the ground with EXP1(CFD1): flight height 2 m, flight speed 2 m/s; EXP2(CFD2): flight height 2 m, flight speed 4 m/s; EXP3(CFD3): flight height 2 m, flight speed 6 m/s; EXP4(CFD4): flight height 2 m, flight speed 6 m/s; EXP5(CFD5): flight height 1.5 m, flight speed 6 m/s ; EXP6(CFD6): flight height 1 m, flight speed 6m/s (Wen et al., 2019)

1.4.3 Influence of the plant canopy on the spray deposition

For successful spraying, it is important to know what fraction of the canopy's surface is covered by liquid sprayed from the quadcopter. The early models incorporated in AgDisp used probabilistic penetration through the canopy. The canopy was treated as homogeneous in the lateral direction. It was assumed that if the droplet was intercepted by the canopy, it was

retained by the canopy. Schou et al. (2011), by conducting an experimental spray of the plant canopy, suggested that this assumption overestimates the spray deposition on the plant because droplets might bounce off the canopy. A recent study found that droplet deposition is influenced by the size and velocity of droplets, spray formulations, and leaf surface features (Dorr et al., 2014).

Massinon et al., (2017) evaluated the capture efficiency of different plant species such as avocado, barnyard grass, cabbage, and bean. They categorized the plant properties by wettability and surface roughness (Table 1.2).

Table 1.2 Spray capture efficiency parameters of different plant species Massinon et al., (2017)

Species	Static contact angle (o)	Wettability	Leaf surface roughness	Leaf surface polarity
Bean	60	easy	smooth	polar
Avocado	76	moderate	very smooth	non-polar
Cabbage	The droplet is completely repulsed	very difficult	rough	very non-polar
Barnyard grass	The droplet is completely repulsed	very difficult	very rough	relatively neutral

They used a single flat fan XR11003VP nozzle (Spraying Systems Co., Wheaton, IL, USA) with a volume mean diameter of 202 microns. A high-speed camera was used to capture the bouncing and secondary breakup of droplets deposited on the leaves. It was observed that on

easy-to-wet plants, bouncing does not occur, and the predominant effect is adhesion. On difficult-to-wet plants there is a high probability of bouncing, which dominates over adhesion. The polarity of the plant also has a big impact on the adhesion properties of the plant. The bounce is more likely to appear on very non-polar plants (e.g., cabbage) than on relatively neutral plants (e.g., barnyard grass).

For spraying from a multicopter, Guo et al. (2021) divided crops by phenotype. They describe crop phenotype by three parameters: crop height, crop density and crop bending resistance. Each parameter was given a score. The combined score is shown in (Table 1.3):

Table 1.3 Rice phenotype depending on height, density and bending resistance (Guo et al., 2021)

Crop phenotype	Height (m)	Score	Density (plants per m^2)	Score	Bending resistance (N)	Score	Comprehensive score
A	1.18-1.20	3	18.0	3	5.43044	2	8
B	1.12-1.15	2	17.5	2	5.54802	3	7
C	1.00-1.10	1	15.1	1	4.82752	1	3

They found that crop phenotype is the second-most important factor in spray deposition after flight parameters (speed, height). The droplet deposition volume gradually decreased with decreasing crop phenotype score. The growth status of phenotype A was the highest, meaning the canopy had a better ability to intercept spray droplets. Guo et al. (2021) used a quadcopter UAV with four 325 mm-radius rotors. Four Teejet nozzles were mounted on the boom under the multicopter. Droplet deposition was measured by measuring deposition on a water-sensitive plate.

1.5 Conclusion

This chapter has described multicopters used for spray dispersion and the methods used to evaluate spray deposition. Spray deposition prediction was split into two parts: prediction of multicopter wakes and prediction of spray behaviour under the presence of multicopter wakes.

The velocity field was separated into two sections: near field wake analysis and far-field velocity field analysis. Near-field refers to the region around the multicopter that is within four rotor radiuses of the multicopter. The flow existing inside the four rotor radiuses of a multicopter is mostly generated and changed by the multicopter's components (rotor, body, spraying system). The rotor wake is affected by the adjacent counter-rotating rotor. Interaction effects can be observed with two coplanar counter-rotating rotors, with a strong upward velocity region. Roll-up vortex generation was observed in flight with lateral velocity. Roll-up vortices can be predicted using rotor disk simplification in CFD.

Flow in far-field volume is affected by multicopter flight parameters, ground effect, atmospheric wind, and plant canopy. Ground effect is stronger for flying multicopters than for single-rotor crafts. Wake is affected by plant canopy and depends on plant phenotype.

Spray deposition can be evaluated either numerically or experimentally. This chapter has shown how spray deposition on plants depends on multicopter flight parameters (height, speed) and plant parameters (phenotype, wettability, roughness).

1.6 Research objectives

The objective of the research is a study of the performance of spraying liquid under the influence of downwash from a multicopter. The research developed recommendations for agricultural institutes, farms, and other users of multicopters for the correct application of the machines and recommendations for the design of multicopter spraying systems. Furthermore, the model of spray deposition for different types of multicopters was developed. The goals of the research are the following:

1. Understand the distribution of spray under the flying multicopter.
2. Develop a model that can predict the disposition of spray.
3. Develop recommendations for users of spraying multicopters.
4. Develop recommendations for designers of multicopter spraying systems.

2. Principles of measurement techniques

2.1 Particle image velocimetry

Particle image velocimetry (PIV) is an optical technique used for instantaneous velocity field measurements. Compared to constant temperature anemometry (CTA) or laser Doppler velocimetry (LDV), it has the advantage of being a non-intrusive method (Chatellier and Fitzpatrick, 2005). The measured velocity field dimension is not limited to a single point (unlike LDV and CTA) and can be expanded by using a more powerful laser or other particles. The disadvantage of PIV is its relatively low measurement frequency compared to CTA or LDV (15Hz vs 1000kHz for CTA). It is computationally expensive compared to CTA.

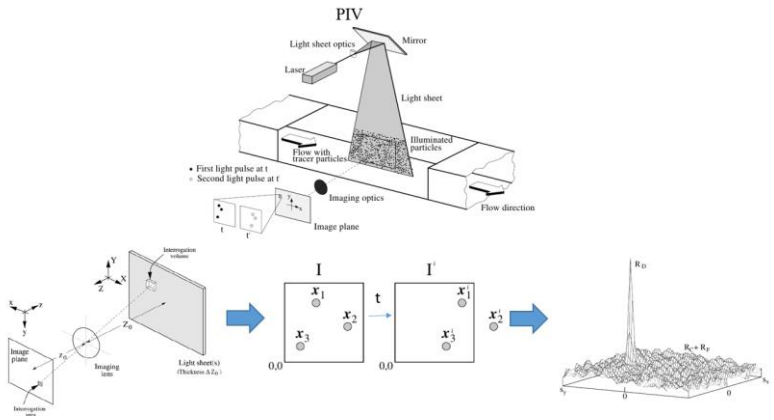

Figure 2.1 Principle of stereo particle image velocimetry (adapted from Raffel et al., 2007).

A basic PIV system can be used to measure two-dimensional flow within the laser light sheet location. The laser sheet is developed by a sequence of lenses and a laser beam that passes through these lenses (Figure 2.1).

The camera is focused on the laser light sheet. It captures images with a known time delay between frames. For processing, the images are divided into interrogation windows. The system can be modified by adding another camera to capture the third component of velocity (stereo particle image velocimetry, or SPIV). A traverse system can be introduced for capturing several planes (scanning particle image velocimetry).

2.1.1 Laser and optics

Most of the experiments were performed with A Quantel EverGreen EVG000 70 Nd:YAG (neodymium-doped yttrium aluminium garnet;Nd:$Y_3Al_5O_{12}$) (70-200 mJ @ 532 nm, 15Hz) laser (Table 2.1).

Table 2.1 Quantel EverGreen EVG000 70 Nd:YAG characteristics [https://www.quantel-laser.com/en/products/item/evergreen-70-200-mj-.html accessed 1.12.2020].

Laser model	EVG00070
Wavelength (nm)	532
Pulse repetition rate (Hz)	15
Energy (mJ)	70
Pulse-to-pulse energy stability (%RMS)	<2.5
Energy drift over 8 hours (%)	10
Pulse width (ns)	≤12

Near field nominal beam diameter (mm)	5
Polarization	linearly polarized, vertical
Spectral purity (%)	>98
Near field beam profile	flat-top, uniform
Manual variable energy attenuator included (15 dB attenuation)	Yes

The laser beam was converted into a sheet with a Dantec guiding arm and Dantec light-sheet optics [https://www.dantecdynamics.com/components/light-guiding-arms/, accessed 02.04.2021]. Using the guiding arm, the laser beam is enclosed within the tube, allowing free movement around the base of the arm within a 1.5 m radius. The arm's base has a mirror that can be adjusted in a vertical and horizontal direction to move the laser beam laterally. The arm's free end has lenses that convert the laser beam into the laser sheet.

2.1.2 Camera

The current setup uses two TSI Model l630091 Power View™ 4MP– HS CCD cameras (Table 2.2). The 4MP sensor can capture a pair of images within a time delay. The maximum capture frequency of pairs of images is 17Hz.

Table 2.2 TSI Model l630091 Power View™ 4MP– HS characteristics [https://tsi.com/product-components/powerview-cameras-630090/ accessed 01.12.2020].

Specifications on the 630091 PowerView 4MP-HS Camera	
Imaging device	Progressive Scan Interline CCD w/microlens
Light sensitive pixels	4.19 million pixels, 2048×2048
Pixel size	7.4×7.4 μm
Active area	15.2mm × 15.2 mm
Dynamic range	12 bits (deliver up to 4096 grey levels)
Minimum frame straddling time for PIV capture	195 ns
Frame rate	32 frames/second
CCD quantum efficiency	52% at 500 nm
Operating temperature	-40 to 85°C
Camera lens mount	F-mount for Nikon lens
Operation modes	Free run, Triggered and Frame Straddling
Power	12 volt (at 1 amp)

The camera has Scheimpflug angle adjustment that can be changed by tilting the camera's enclosure. This changes the angle of the sensor plane relative to the lens to optimise the image's focus (Raffel et al., 2007). Additionally, the mounting support has a rotating platform, allowing the camera to be rotated around its vertical axis.

2.1.3 Synchronisation

The synchronisation of the camera and laser was controlled by Insight 4G software and performed by a LaserPulse 610036 synchroniser. The synchroniser was connected to a computer with an RS232 cable. BNC cables were connected to the laser (flash lamps and Q-switch). Another cable was connected to the camera to trigger the capture (Figure 2.2) (TSI PIV Camera PowerViewPlus 4MP-HA installation manual 6008043A 7/15/2014). The setup of the SPIV system remained the same for all experiments.

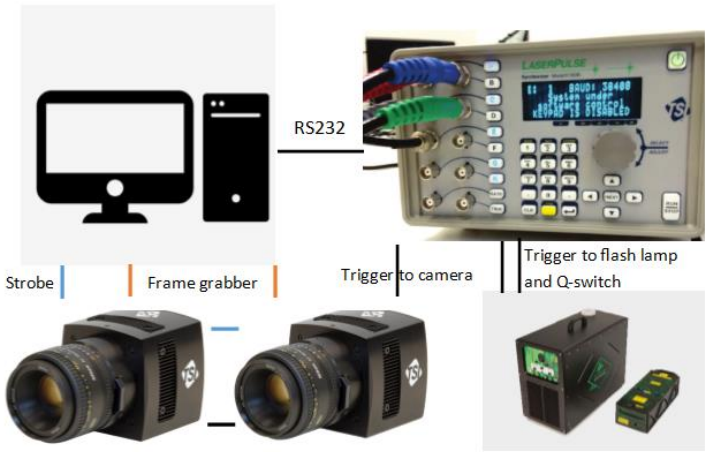

Figure 2.2 Key components and their connection in the SPIV system.

2.1.3.1 Timing diagram

The SPIV timing diagram is shown in Figure 2.3.

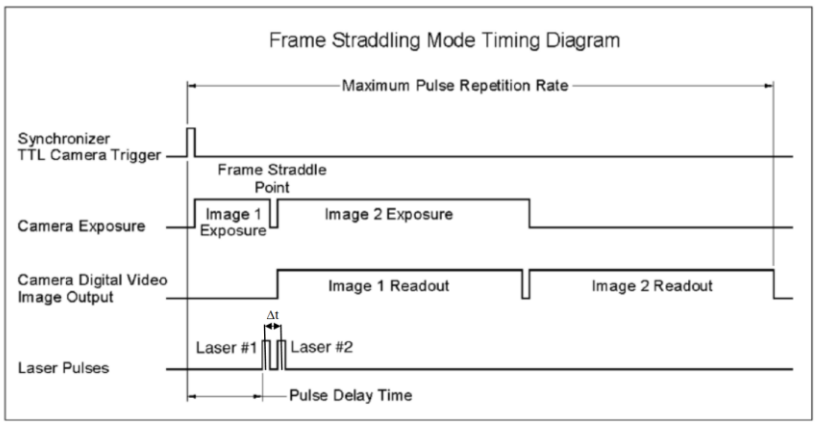

Figure 2.3 SPIV timing diagram in frame straddling mode (adapter from INSIGHT 4G™ user's guide (2015)).

The *Δt* is the time between two laser pulses. The displacement of particles is measured within the time delay. It is individual for every experiment and depends on the average displacement of the particle in the field of view. In the experiments described in this thesis, it ranged from 30 to 60 microseconds. The pulse delay time was chosen to have the laser pulse in image 1 and image 2. After setting the timing diagram images can be captured and processed.

2.1.4 Particle seeding

The tests were conducted in an open environment, meaning that the seeding particles must not be harmful to the surroundings or operators. It is impossible to use solid particles, such as alumina or silver-coated glass particles (Raffel et al., 2007, Adrian et al., 1991); thus, liquid particles must be generated. The general recommendations for the size and concentration of moving particles are that (Scharnowski et al., 2020):

- The Stokes number for the moving particle is less than one.

- The seeding particle must occupy more than one pixel on the camera's picture (ideally 2-4 pixels, rectangular shape).
- The distribution of particles should be homogeneous in the field of view.

Several particle generators were trialled: ultrasonic nebulisers, a smoke machine with smoke oil, a Laskin nozzle with DEHS (di-ethyl-hexyl sebacate), a Laskin nozzle with water-glycerin mixture, a smoke machine with water-glycerin mixture, and a spray nozzle (Table 2.3).

The Laskin nozzle with the water-glycerin mixture was chosen for the experiments. It is simple in manufacturing and operation. In the latest tests, the Laskin nozzle was substituted with the modified smoke machine that allowed a number of particles per interrogation window closer to the ideal of 15.

Table 2.3 Advantages and disadvantages of different spraying techniques.

Method of particle generation	Advantages	Disadvantage
Nebulisers	Fast and easy set-up Low initial cost Near zero outlet velocity	A small density of particles Low droplet life span
Agricultural spray	Fast and easy set-up	High outlet velocity 100 microns in average droplet size (high Stokes number)

Method of particle generation	Advantages	Disadvantage
Laskin nozzle with DEHS	Small initial cost of design Long particle life span Scalable Small particle size	Requires engineering and manufacturing Scalable up to 6 nozzles DEHS is hard to remove from surfaces
Laskin nozzle with glycerin-water mixture	Small initial cost of design Long particle life span Scalable Small particle size Simple cleaning	Produces low density of particles compared to the smoke machine
Smoke Machine with smoke oil	Fast and easy set-up	Expensive device High density of generated smoke Very small particle size (impossible to capture at the desired magnification) Fire alarms are sensitive to the smoke generated

Method of particle generation	Advantages	Disadvantage
Smoke machine with a glycerin-water mixture	Fast and easy set-up Low initial cost Small particle size Produces smoke with a density between a that of a smoke machine with smoke oil and a Laskin nozzle Remote control	Fire alarms are sensitive to the smoke generated Requires modification to allow precise temperature control

2.1.4.1 Laskin nozzle

A Laskin nozzle particle generator consists of pipes with blocked ends dipped into a mixture of water and glycerin (Raffel et al., 2007). There are four holes on the side of the pipe. The impactor plate is placed above the holes. There are holes in the impactor plate. Several nozzles are placed inside pressurised containers. The nozzles are connected to the air supply (Figure 2.4). According to Raffel et al. (2007), the maximum pressure should not exceed 1 bar. However, Kähler et al. (2004) stated that a Laskin nozzle could be used with higher pressure if the pressurised container is able to withstand it. If the pressure is higher than 2 bars, the impactor plate does not influence the number and size of particles (Kähler et al., 2004).

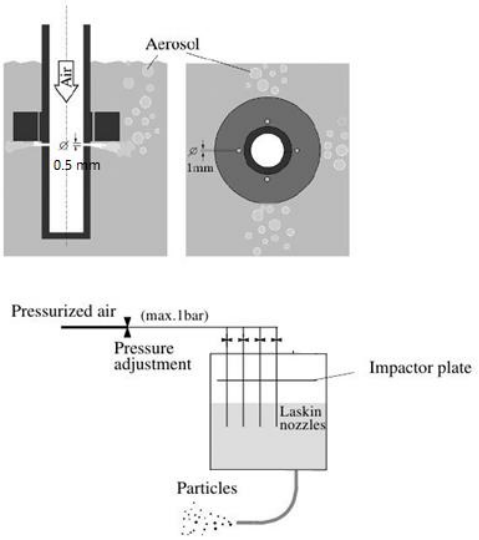

Figure 2.4 Laskin nozzle schematics [Raffer et al. p24, fig. 2.10. (2007)].

The designed Laskin nozzle consists of four 10mm-diameter copper pipes with four 0.5mm holes on the pipes' sides. The impactor plate has a 25mm diameter and four 1mm holes (Figure 2.5). The impactor plate was placed above the 0.5mm holes in the copper pipe.

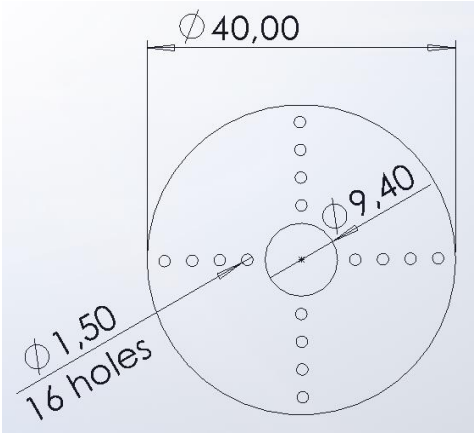

Figure 2.5 Impactor plate drawing designed for use in a Laskin nozzle.

The pressurised container consists of two chambers divided by a wall, with a 50mm gap between the dividing wall and lid. One of the chambers has the working liquid inside; another

chamber has a particle outlet. The dividing wall is required to keep the working liquid inside the first chamber. The particles generated in the first chamber travel to the outlet through the gap between the wall and the lid and then to the outlet (Figure 2.6).

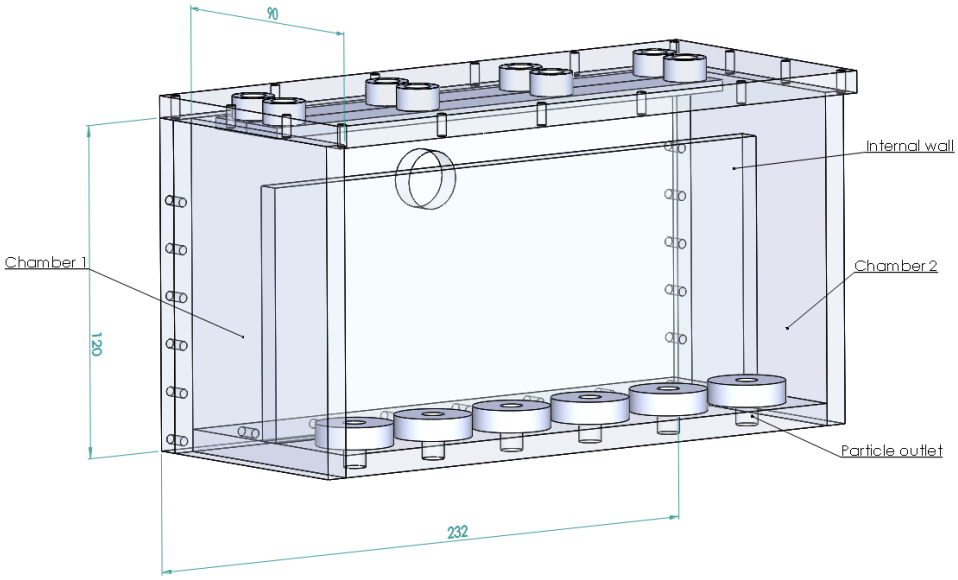

Figure 2.6 Laskin nozzle tank 3d model.

The Laskin nozzle was manufactured from an 8 mm thick acrylic sheet (Figure 2.7). The working liquid was 10% glycerin, 90% water. The aim was to use as little glycerin as possible to give sufficient lifetime to the particles yet limit the deposition of glycerin on nearby surfaces. The mixture proportion was found experimentally.

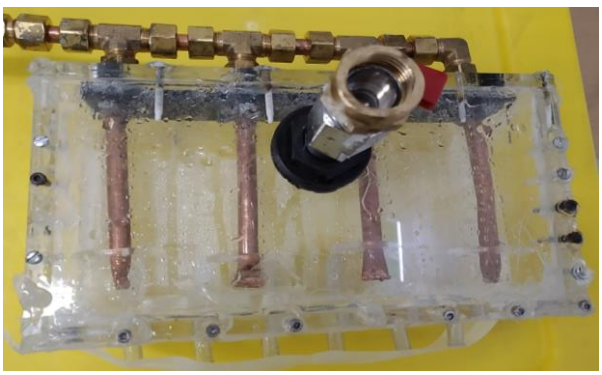

Figure 2.7 The Laskin nozzles and chamber.

2.1.4.2 Smoke Machine

The DF-1500A (1500 Watt) (Figure 2.8) smoke machine was used to improve the experimentation by increasing the concentration of particles. Initially, the run time of the single burst of smoke was not long enough for a single experiment. The smoke machine was upgraded with an Arduino microcontroller and K-type thermocouple that allowed control of the nozzle's temperature. The temperature was set to 260 C^{o} ± 10 ^{o}C. The evaporating liquid was 25% glycerin, 75% water mixture. The proportion was found experimentally. The aim was to have smoke that remained in the air throughout the experiment yet limit the deposition of glycerin on nearby surfaces.

Additionally, a pipe with a blocked end and 10mm holes were fitted to the smoke machine so the smoke could be delivered and evenly distributed along the measurement region.

Figure 2.8 DF-1500A smoke machine with remote control and modified temperature switch.

2.1.4.3 Particle size measurement

A TSI Aerotrak 9310 [https://tsi.com/products/cleanroom-particle-counters/portable-particle-counters/aerotrak-portable-particle-counter-9310/ accessed 29.09.2021] optical particle

counter was used to measure the particle size distribution of both seeding devices. The machine's output is the number of predefined particles per 28.3 litres of air passed through the sizer. The particles' measured size was divided into bins of 0.3-0.5, 0.5-1, 1-3, 3-5, 5-10, and 10-25 micron diameter. Each measurement accumulated data for 1 minute. The inlet for the sizer was placed one meter away downstream.

The background particle distribution was recorded in the laboratory. Then three independent tests for each particle generator were performed. The background distribution was subtracted from each measurement. The percentage of total particles in each size bin was calculated for each test. Then these percentages were averaged over three tests. The results are presented in Table 2.4.

Table 2.4 Size particle range by bins for smoke machine and Laskin nozzle.

Particle size range(microns)	Laskin #1	Laskin #2	Laskin #3	Smoke #1	Smoke #2	Smoke #3	Smoke #4	Mean Laskin	Mean smoke
0.3 -0.5	62.65	47.92	48.02	34.75	44.82	74.82	54.87	55.29	44.81
0.5-1	0.00	0.00	0.00	0.00	4.04	0.00	0.00	0.00	1.35
1-3	33.26	41.88	45.57	44.43	42.58	21.56	40.81	37.57	42.60
3-5	3.68	8.96	5.81	15.91	8.12	3.26	4.28	6.32	9.43
5-10	0.41	1.24	0.60	4.92	0.45	0.35	0.05	0.83	1.81
10-25	0.00	0.00	0.00	0.00	0.00	0.00	0.00	0.00	0.00
	100.00	100.00	100.00	100.00	100.00	100.00	100.00		

The diagram below represents the averaged percentage of the total number of particles per bin by number for each of the two generator types (Figure 2.9).

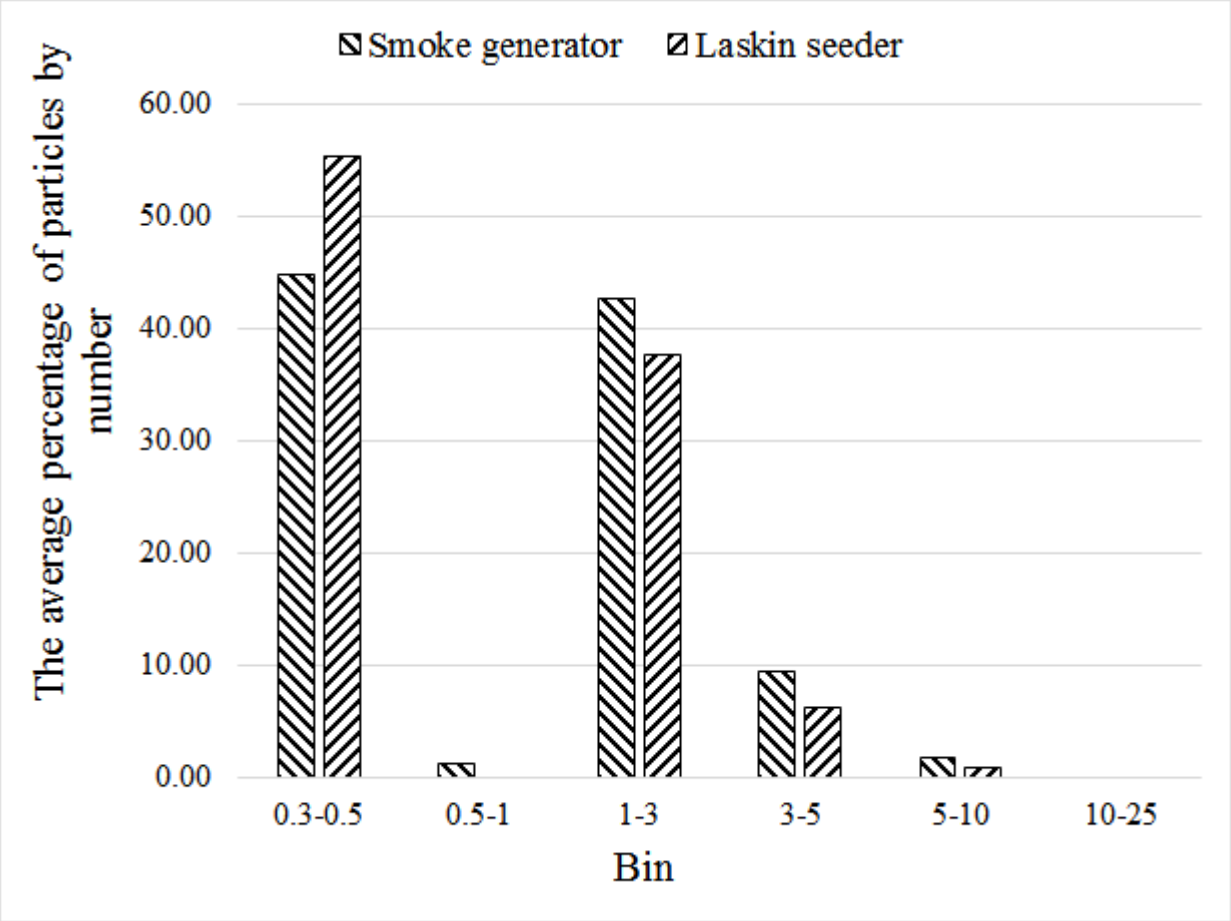

Figure 2.9 The average percentage of particles by number in the measured bin for smoke generator, and Laskin seeder.

The vast majority of particles are either in the 0.3-0.5 micron bin or the 1-3 micron bin. The 0.3-0.5 micron particles may be the dust lifted from nearby surfaces. The smaller particles are not visible in the light sheet but contribute to the background noise. The 3-5 micron bin contained 5-10% of the particles by number.

The average intensity on the PIV image is proportional to the square of the diameter of the particle (Raffel et al., 2007, Hulst et al., 1957). It is assumed that distribution of particles is

uniform within the bin. The diagram below represents the percentage of the total surface area of particles per bin for each of the two generator types (Figure 2.10).

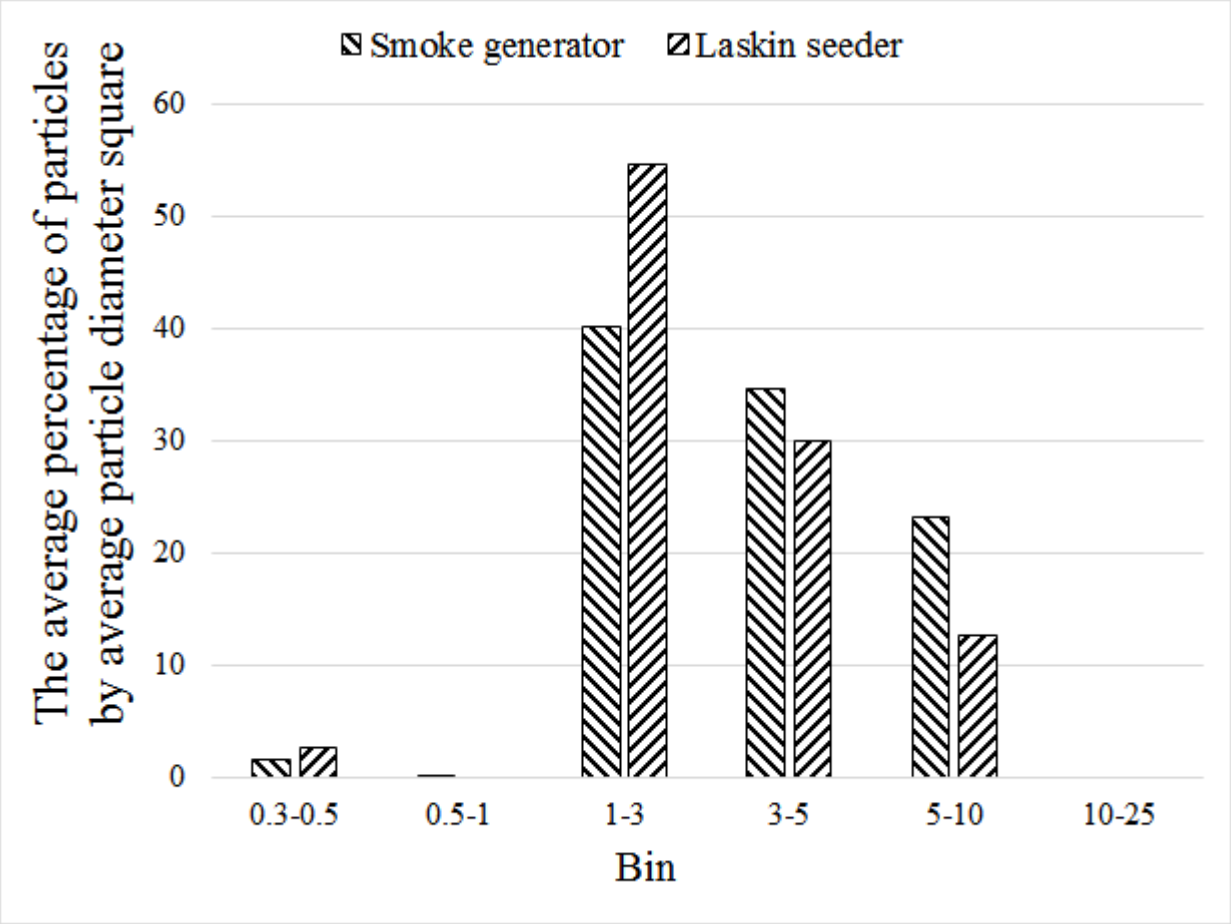

Figure 2.10 The average percentage of particles by particle diameter square in the measured bin smoke generator and Laskin seeder.

The vast majority of the surface area of particles are either in the 1-3 micron bin or the 3-5 micron bin. The smaller particles are not visible in the light sheet but contribute to the background noise.

The Stokes number is a measure of particle motion fidelity (Raffel et al., 2007, Marshall et al., 2014) that shows how well the tracer particles follow the streamlines.

$$S = \frac{\tau \cdot U}{l_o} \qquad \text{(Equation 2.2)}$$

Where τ is relaxation time, seconds,

l_o is the characteristic dimension of the obstacle, m,

U is airflow velocity, m/s.

$$\tau = \frac{\rho_p \cdot d_p^2}{18\mu} \qquad \text{(Equation 2.3)}$$

Where ρ is the density of the particle, kg/m^3,

d_p diameter of particle, meters,

μ kinematic viscosity of air m^2/s.

In SPIV experiments, the Stokes number should not exceed 1 (Raffel et al., 2007). Assuming that the particle is of the maximum size of 3 microns (Figure 2.11 left) or 5 microns (Figure 2.11 right), the PIV experiments can be trusted if the experimental conditions are outside the hatched area above the red line.

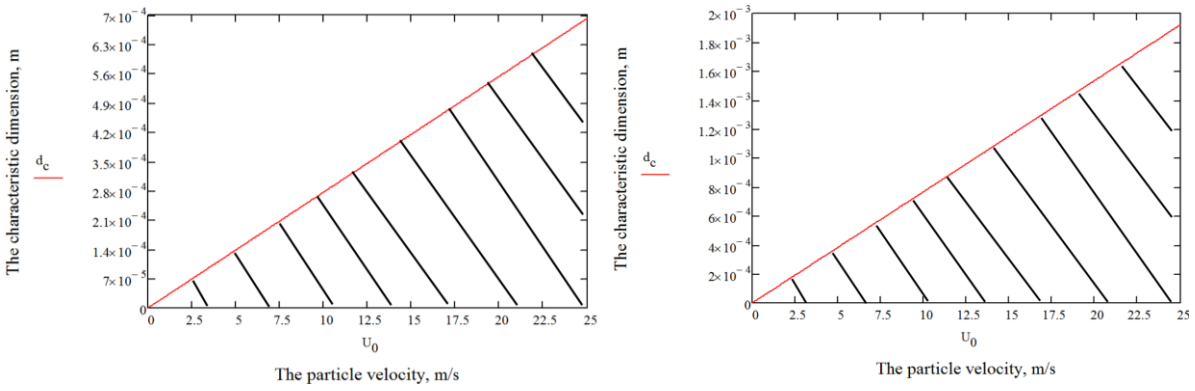

Figure 2.11 Minimum allowable characteristic dimension of the obstacle depending on the velocity of a moving particle (left: 3-micron particle; right: 5-micron particle).

The maximum Stokes number is expected in the tip vortex due to the high velocity and small radius of curvature of the pathline. The typical diameter of the visible border of the tip vortex is 5244 microns=5.2443•10^{-3} m (Figure 2.12). This point was chosen because the largest

velocity in the rotor wake is expected to lie in the vortex core. The measured velocity is 18 m/s. The point with coordinates ($5.2443 \cdot 10^{-3}$, 18) lies above the red line for 5-micron particles; thus, experimental results can be trusted at this point. In this case, the Stokes number is equal to 0.176.

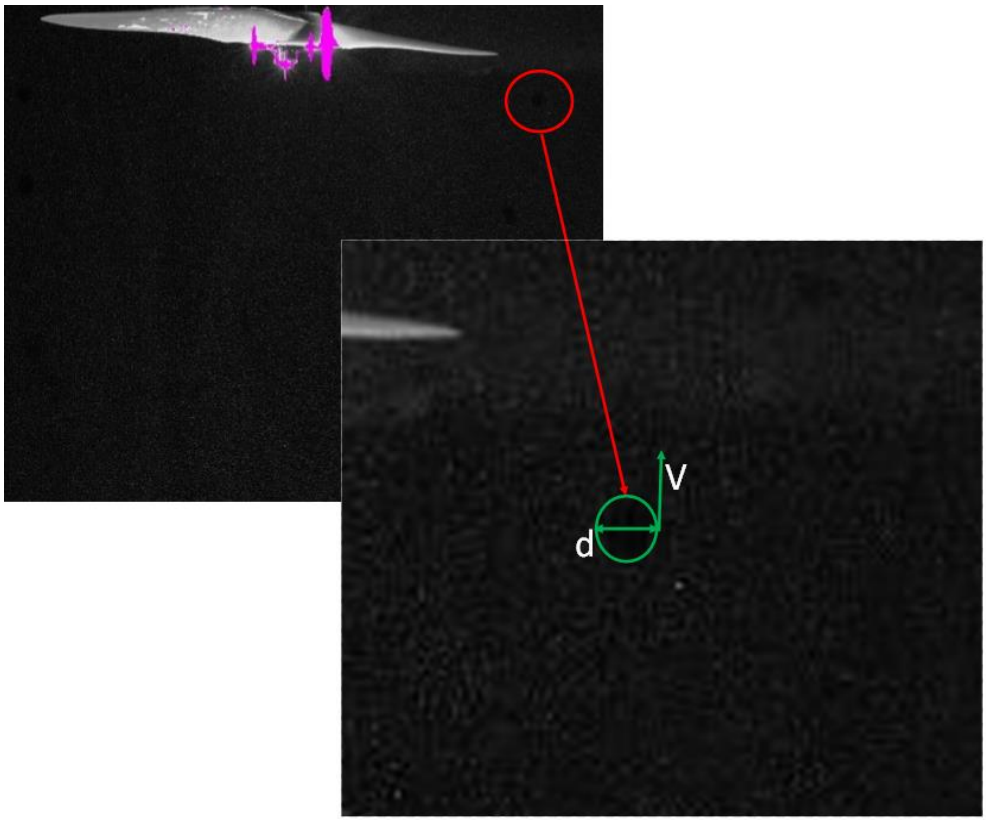

Figure 2.12 The visible tip vortex, the green circle is the visible border of the vortex core (5244 microns).

2.1.5 PIV measurement process

Insight 4G commercial software (TSI) was used to capture and process the data. Tecplot 2013 and Tecplot 2016 were used for post-processing of the obtained data. TSI Insight 4G (Version 11.03227) is the software used for capture and processing of PIV images.

2.1.5.1 Perspective calibration

In all experiments, the two cameras were always on the same side of the laser light sheet (Figure 2.13).

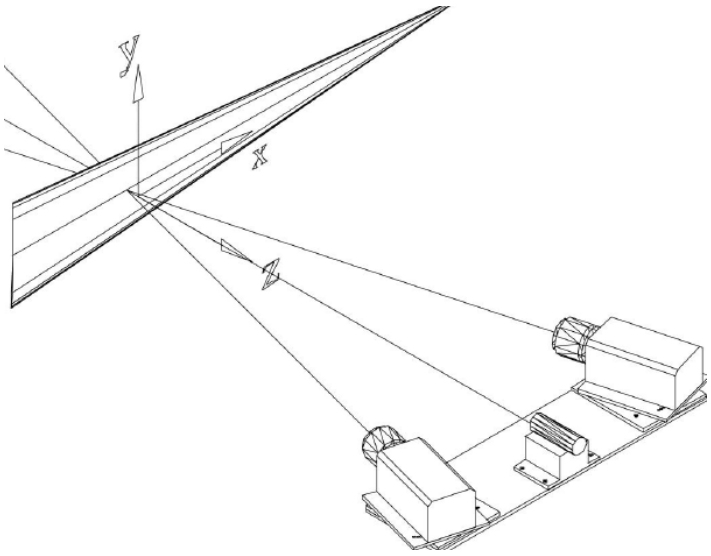

Figure 2.13 Example of the camera's position relative to the lightsheet (INSIGHT 4G™ user's guide (2015)).

The advantage of this configuration is the simple setup of both cameras on the same table (aluminium beam). In SPIV, the camera and laser need to be aligned and calibrated to know the actual position of instruments around each other. In the calibration process, the perspective calibration image needs to be taken using the four-plane target (Model 640054) with a predefined dot grid (Figure 2.14). The advantage of a four-plane target is that it can be used without traverse (INSIGHT 4G™ user's guide, 2015).

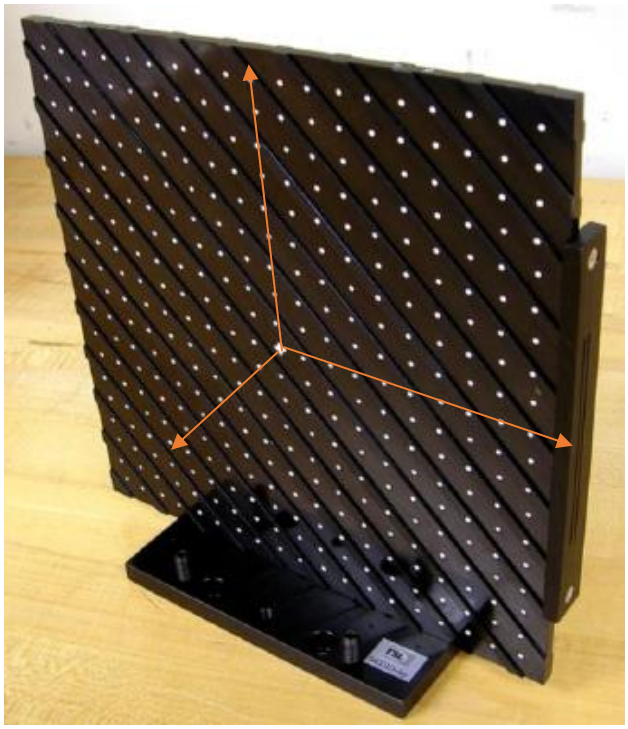

Figure 2.14 Four plane target with predefined dot grid used for SPIV calibration.

Each side of the target has two planes with 1 mm spacing between them (Z direction). Each plane has white dots 15 mm away from each other (X and Y directions). The fiducial mark (white cross) is in the centre of the target. To capture the perspective calibration image, two cameras were set as in Figure 2.13, overlapping the capturing zone and with the target's fiducial mark in the centre of the field of view.

The laser light sheet was aligned with the side of the target that faces the camera. The camera was focused on the same plane, and the Scheimpflug angle was adjusted so that the whole image is in focus. After aligning, the perspective calibration image was taken and analysed. The cross-correlation technique was used to detect the calibration markers location (Prasad, 2000). In experiments, the obtained pixel size ranged from 140 to 180 microns per pixel, depending on the experiment.

The volumetric coordinate field (x,y,z) (Equation 2.4) can be translated into two-dimensional coordinates on the image plane for each camera:

$$(\hat{x}, \hat{y}) = F(x, y, z) \quad \text{(Equation 2.4)}$$

where F(x,y,z) (Equation 2.5) is the third-order polynomial function

$$F(x, y, z) = a_0 + a_1 x + a_2 y + a_3 z + a_4 x^2 + a_5 xy + a_6 y^2 + a_7 x^2 + a_8 yz + a_9 z^2$$
$$a_{10} x^3 + a_{11} x^2 y + a_{12} xy^2 + a_{13} y^3 + a_{14} x^2 z + a_{15} xyz + a_{16} y^2 + a_{17} xz^2 + a_{18} yx^2$$

(Equation 2.5)

The image space mapping coefficients (a_i) were found by least-squares fitting.

2.1.5.2 Stereo Automapping

Stereo automapping optimises perspective calibration by removing misalignment between the calibration target and laser light sheet. For stereo automapping, the particles must be introduced to the field of view and must be illuminated by the laser. At least one hundred image pairs must be taken for stereo automapping. An example of the automapping field can be seen in Figure 2.15. The aim is to minimise the disparity vectors (green vectors) and have as few bad vectors as possible (red vectors). Vector validation was performed by a local median test with a 5x5 pixel kernel.

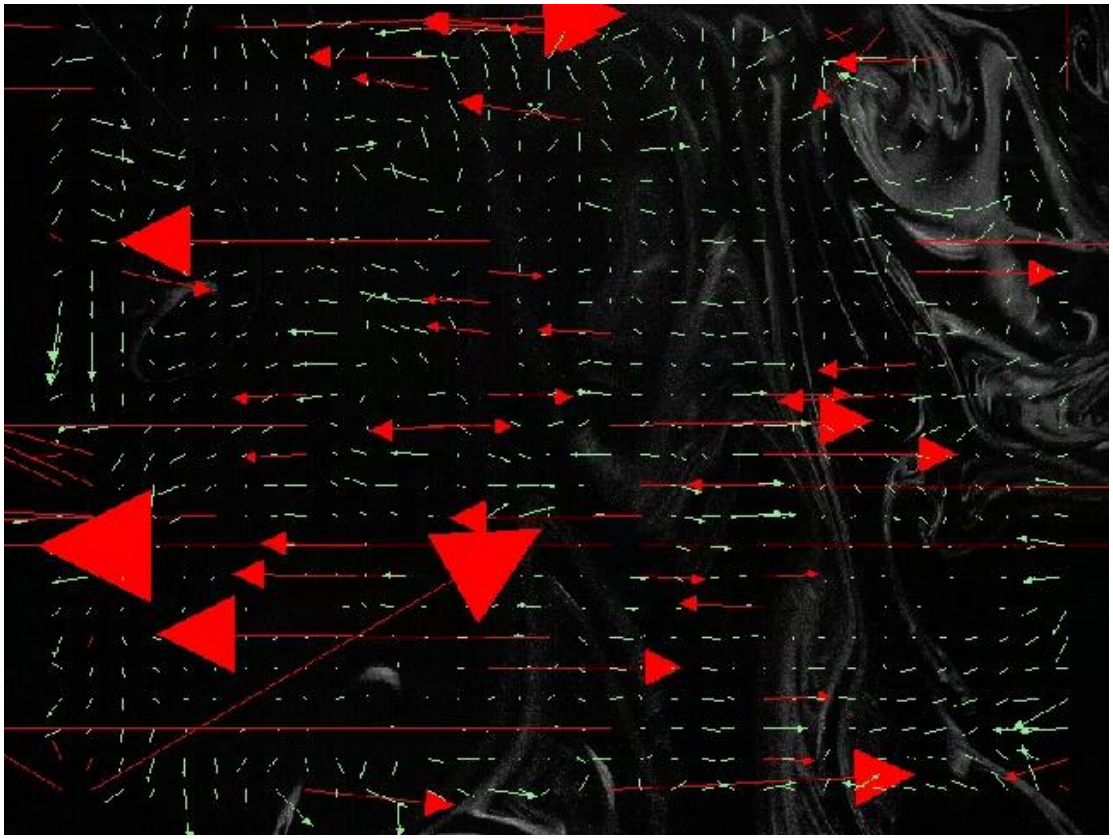

Figure 2.15 Stereo automapping disparity correction vector field.

The process is iterative and requires 4-5 iterations. The numerical criteria for a successful stereo automapping process are disparity root mean square (RMS) and the fraction of correct vectors. In all the experiments, the number of correct vectors was more than 750 out of 910, and RMS was less than 1 pixel. In this example, the calibration window can be seen in Figure 2.16

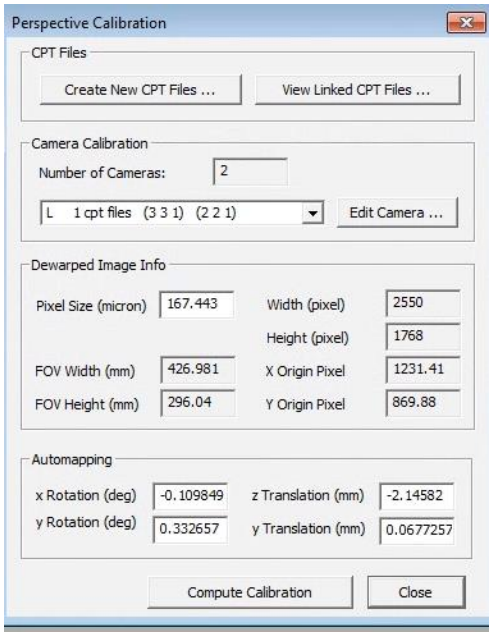

Figure 2.16 The stereo automapping window of 4G image acquisition software.

In the bottom of Figure 2.16, the result of automapping shows the misalignment between the target and laser light sheet.

2.1.5.3 Image processing

Image processing consists of pre-processing (alternation of image), processing (calculating displacement) and post-processing (comparing the obtained result, filling the holes, vector validation).

In some experiments, the pre-processing stage involved background subtraction of the mean intensity image. It allowed the removal of features that appear on every frame, such as

reflecting beams, fixtures, rotors etc. Examples of raw and subtracted images are given in Figure 2.17.

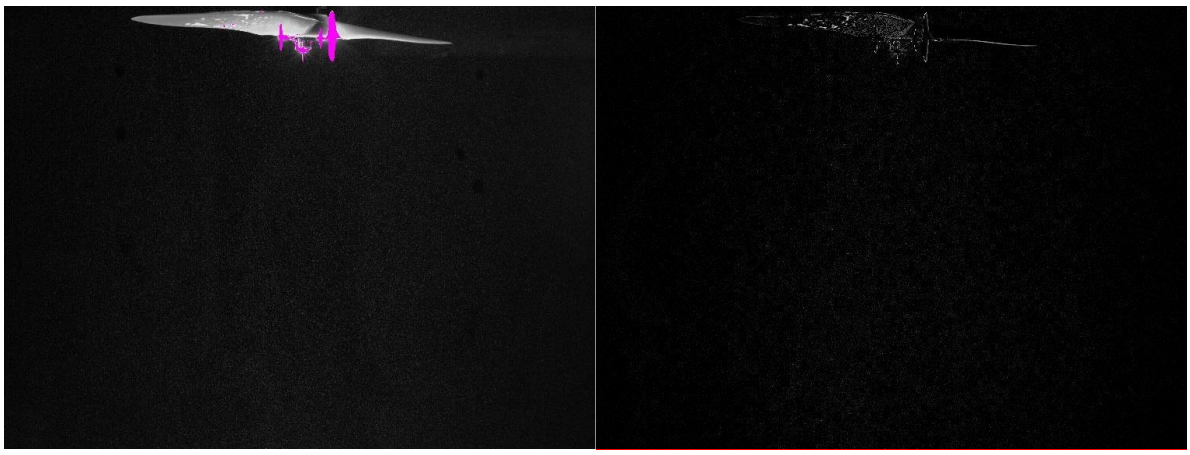

Figure 2.17 Raw image (left) and background-subtracted image (right).

The rotor shown in Figure 2.17 was in the field of view in every frame, but background subtraction removed it from the field of view. However, as can be seen, some of the particles were lost due to subtraction.

The processing tab has the following view (Figure 2.18)

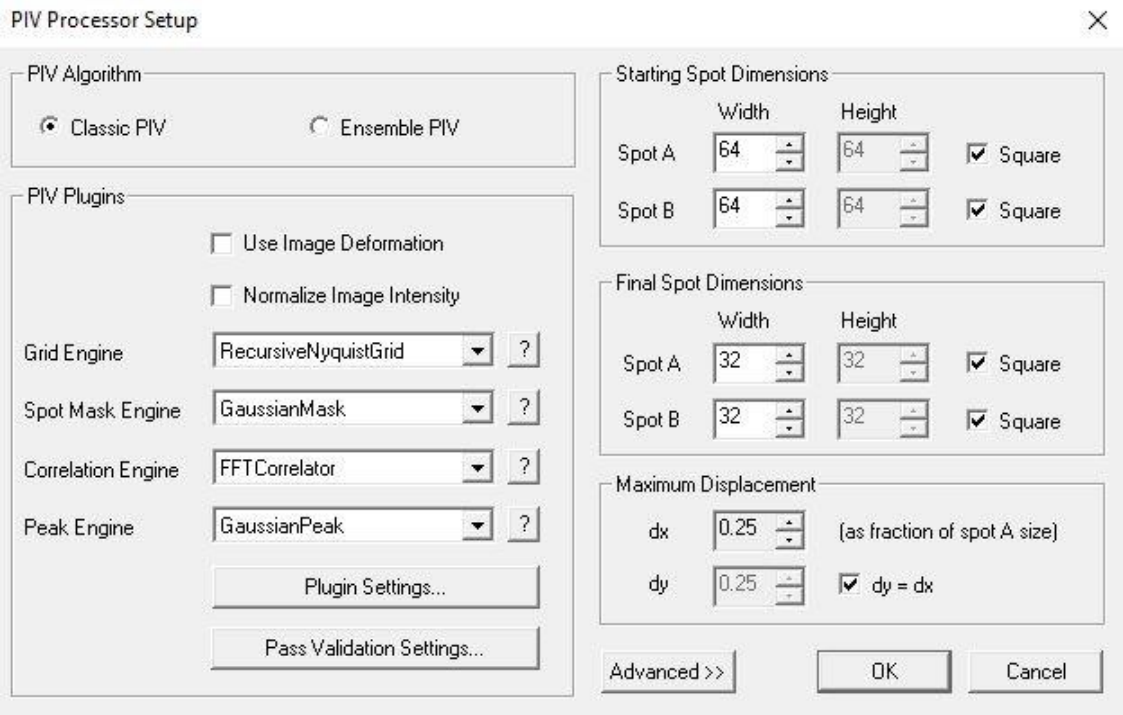

Figure 2.18 processing tab of INSIGHT 4G image acquisition software.

The settings in Figure 2.18 returned the highest number of correct vectors and were used in all experiments.

After vector processing, local vector validation and vector conditioning by the neighbourhood vector were performed. Vectors that failed the local validation were replaced by valid secondary peaks or local medians. Approximated vectors obtained in post-processing (yellow arrows) were displayed in the obtained vector velocity field (Figure 2.19).

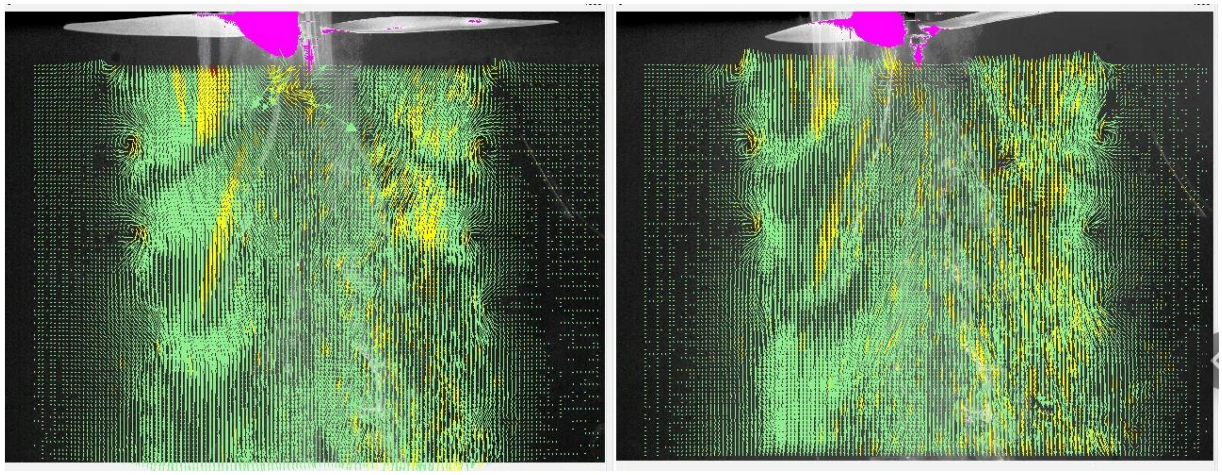

Figure 2.19 Vector field obtained after processing the raw image. "Good vectors" are shown in green, "approximated" vectors in yellow.

The chosen criteria for successful processing (and for a successful experiment overall) is the number of correct vectors. This must be close to 100% in the field of interest and more than 50% through the image.

2.1.6 Traverse system

In most of the experiments, the velocity was measured in parallel planes at a distance ranging from 5-80mm. This was achieved by traversing the rotor system. Two traverse systems were used in all experiments: one-dimensional and two-dimensional. Both traverse systems were calibrated prior to the experiment. The expected calibration error is 0.005mm.

A one-dimensional ball-screw traverse system was used where a load of more than 50N was expected (Figure 2.20 left). The maximum distance travelled was 1500mm with 0.1mm increments. A two-dimensional traverse has a smaller capacity but can travel up to 1500mm in both horizontal and vertical directions. The increment of the two-dimensional traverse was 1 mm in the vertical and horizontal directions (Figure 2.20 right).

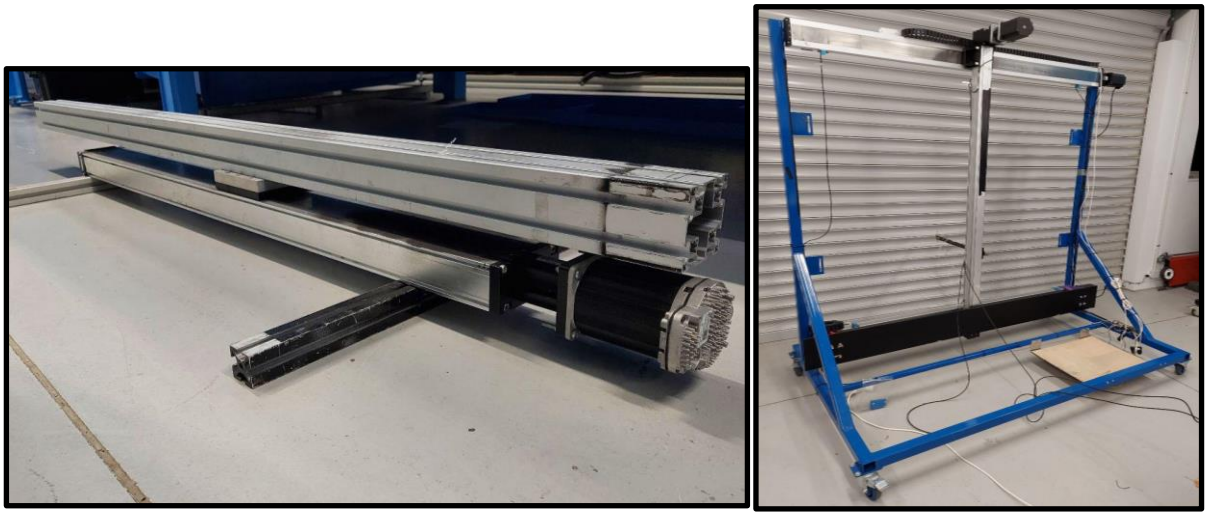

Figure 2.20 Traverse used in experiments; left: one-dimensional traverse, right: two-dimensional traverse.

2.1.7 Interpolation between parallel planes

The inverse distance weighted interpolation was used to fill the data point between parallel plane zones of PIV data (Tecplot 2013 User's Manual. (2013)).

A variable's value in the destination zone at a data point is computed of the PIV zone's function. The PIV zones are located in the parallel planes within known distinct between the planes. The values from the PIV zone are averaged to the data points between known zones using inverse-distance interpolation. A function of the distance between each source data point and the destination data point is used to weight the average (Tecplot 2013 User's Manual. (2013)).

$$\phi_d = \frac{\sum \omega_s \phi_s}{\sum \omega_s} \qquad \text{(Equation 2.6)}$$

where ϕ_d is the values of the zone between PIV data planes (the destination point),

and ϕ_s is the values of the zone of PIV data the source point (source),

and ω_s is the weighting function defined as:

$$\omega_s = D^{-e} \qquad \text{(Equation 2.7)}$$

D is the distance between the PIV data planes.

2.1.8 Uncertainty and Standard deviation of SPIV measurement

The uncertainty of SPIV remains incompletely determined (Correspondence with TSI engineers, May 2020). No function to estimate the uncertainty of SPIV data has yet been built into the 4G software. However, it does have functions to estimate the uncertainty separately for each camera. This function is accessible through Classic PIV processing routine in INSIGHT 4G™ (the analysis in which each pair of images is analysed separately) (INSIGHT 4G™ user's guide, 2015) and available for individual planar images from each camera. The uncertainty in velocity values was determined using the peak signal-to-noise ratio method, which assumes that error in pixel displacement follows a Gaussian distribution (Charonko et al., 2017; Bhattacharya et al., 2017). This uncertainty was expressed as velocity magnitude. From this, uncertainty as a percentage of the local velocity magnitude was calculated.

The standard deviation was accessed through Classic PIV in 4G TSI. In Classic PIV, the velocity in each image pair is computed separately. The average velocity and standard deviation were calculated from a sequence of images obtained in a single experiment.

2.2 Constant temperature anemometry

SPIV can cover most of the experimental needs; however, the maximum capture rate of 15 Hz does not provide adequate time resolution to show the effect of blade passing, or to measure turbulence kinetic energy. Additionally, it cannot measure within 10 mm of the rotor due to the

rotor's high reflectivity. Constant temperature anemometry (CTA) was used to measure the velocity at a higher time resolution and closer to the rotor.

CTA uses convection from heated wires (hot-wire probes) to measure velocity (Bruun, 1996; Cordani, 2018). The disadvantage of CTA is that it is limited to the measurement of a single point. Additionally, the physical presence of the probe alters the flow.

A Dantec multichannel CTA Model 54N81 with three-dimensional 55P91 probe and MiniCTA 4.10.00 software were used in the experiments. The probe was calibrated using a standard two-points velocity calibration method with the Dantec hot wire calibration device [https://www.dantecdynamics.com/components/cta-calibration-systems/, accessed 04.12.2020]. The frequency of sampling was set to 1 kHz. The coordinate probe system is shown in Figure 2.21

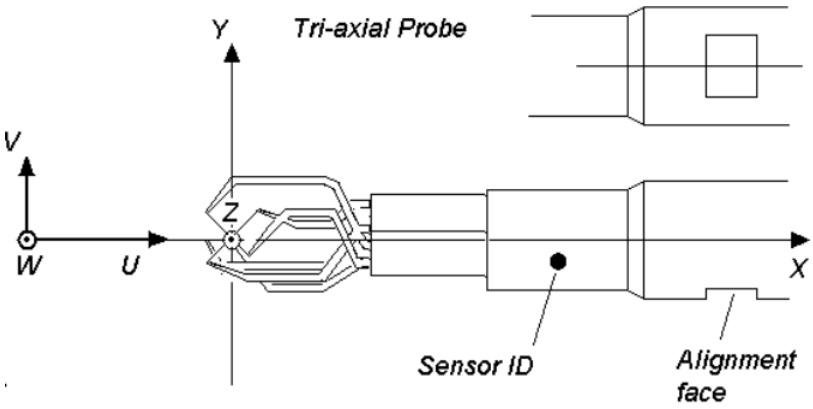

Figure 2.21 Dantec 55P91 probe image with coordinate system and alignment face [adapted from MiniCTA software v4.10, installation, and user's guide, 2010].

According to the MiniCTA software v4.10, installation, and user's guide (2010), the main direction of the main flow direction should lie within a 35-degree cone in the direction of the positive X-axis; thus, the probe was always oriented parallel to the rotors' downwash. As in the PIV experiments, the probe in the CTA experiments was traversed using two perpendicular

traverses with an increment of 5 mm. The data was reduced by averaging the velocity over the number of measurements at each position of the traverse (Equation 2.8).

$$U_{mean} = \frac{1}{n\sum U_i} \quad \text{(Equation 2.8)}$$

In addition to mean velocity in U, V and W directions, the standard deviation (Equation 2.9) was calculated:

$$U_{std} = \left(\frac{1}{N-1}\sum_1^N (U_i - U_{mean})^2\right)^{0.5} \quad \text{(Equation 2.9)}$$

The turbulence kinetic energy (Equation 2.10) is equal to the sum of squares of standard deviations of each velocity component:

$$k = 0.5U_{std}^2 \quad \text{(Equation 2.10)}$$

2.2.1 Velocity sampling uncertainty in CTA measurements

The sources of uncertainty in constant temperature anemometry are divided between anemometry uncertainties, calibration/conversion uncertainties, data acquisition-related uncertainties, and uncertainties relating to experimental conditions.

The major source of error in CTA measurement is calibration error. The anemometer was calibrated using the Dantec hot wire calibration device. The uncertainty due to errors (Equation 2.11) in calibration can be expressed as:

$$U(U_{cal}) = \frac{1}{100} STDV(U_{cal}(\%)) \quad \text{(Equation 2.11)}$$

$$STDV(U_{cal}) = \pm a(\%) + b_{cal}(m/s) \quad \text{(Equation 2.12)}$$

Using the dedicated calibrator, a(%) is equal to 1%, b_{cal}(m/s) can be neglected when velocity is above 5 m/s (Equation 2.12) (Jørgensen, 2002).

The conversion uncertainty is stochastic with a normal distribution function (Equation 2.13) (Jørgensen, 2002):

$$U(_{lin}) = \frac{1}{100} STDV(\Delta U_{lin}(\%)) \quad \text{(Equation 2.13)}$$

Where *STDV(*$\Delta U_{lin}(\%)$) is the SD% of curve fitting error. The curve fitting error was calculated in the MiniCTA software after performing the two-step calibration.

The data acquisition uncertainty is related to A/D board resolution uncertainty. The uncertainty is a stochastic function with square distribution (Equation 2.14):

$$U(Ures) = \frac{1}{\sqrt{3}} \cdot \frac{1}{U} \cdot \frac{E_{AD}}{2^n} \cdot \frac{\partial U}{\partial E} \quad \text{(Equation 2.14)}$$

Where: E_{AD} is A/D board input range

n is resolution in bits

$\frac{\partial U}{\partial E}$ is sensitivity factor of the calibration curve.

The uncertainties related to experimental conditions consist of probe positioning variation, ambient pressure variations, and temperature variations. Probe positioning variation can be expressed as the function of positioned angle θ (Equation 2.15), (Jørgensen, 2002):

$$U(U_{pas}) = \frac{1}{\sqrt{3}}(1 - \cos\theta) \quad \text{(Equation 2.15)}$$

Temperature variation can be experienced if the temperature during calibration is different from the temperature during the experiment (Equation 2.16) (Jørgensen, 2002). If not corrected, the relative standard uncertainty is:

$$U(U_{temp}) = \frac{1}{\sqrt{3}} \cdot \frac{1}{U} \cdot \frac{1}{T_w - T_0} \left(\frac{A}{B} U^{-0.5} + 1\right)^{0.5} \quad \text{(Equation 2.16)}$$

Changes in temperature will also change the density of the air, contributing to uncertainty.

As with temperature, changes in ambient pressure will also change the density of the air. The standard uncertainty will have the following form (E. Jørgensen, 2002):

$$U(U_{\rho,P}) = \frac{1}{\sqrt{3}} \cdot \left(\frac{P_0}{P_0 + \Delta P} \right) \qquad \text{(Equation 2.17)}$$

Using a Dantec CTA calibrating device, the total standard uncertainty should not exceed 1% (Jørgensen, 2002, Chapter 13).

3. Measurement of an isolated near rotor wake

This chapter investigates the velocity field of different rotors that are differ in size, are not geometrically similar, and differ in aerodynamic performance. This chapter presents the differences and similarities between the wakes of isolated rotors and explores the assumptions used for rotor wake comparison.

The radius of typical crop-spraying multicopter rotors starts from 260 mm. Two of the most popular crops spraying multicopters are the DJI Agras T20 and DJI Agras MG-1. The DJI E7000 propulsion system was chosen for wake mapping in hover because the DJI Agras T20 and DJI Agras T10 multicopter, used for spray application, (https://www.dji.com/nz/t20/specs, accessed 25.03.2021) utilises such rotors. The DJI E2000 (used in DJI Agras MG-1 multicopter https://www.dji.com/nz/mg-1, accessed 25.03.2021) and DJI E7000 are scaled versions of each other. It is assumed that DJI E7000 and DJI E2000 rotor sets have a similar wake structure.

The evaluation of multicopter wake requires testing in a wind tunnel to understand wake features in a flight with lateral velocity. The University of Canterbury open-circuit wind tunnel measures 1500x1500 mm, with its ceiling 2-metres above the laboratory floor. Testing a DJI E2000 (266.5 mm radius (7.5 rotor radiuses from the ground)) or DJI E7000 (420 mm radius (4.76 rotor radiuses from the ground)) rotor in such constrained conditions would mean testing it in ground effect. From the literature (Chapter 1), it is known that ground effect can affect the wake of a multicopter operating near the ground (Tanabe et al., 2021). To reduce the influence of ground effect while using the wind tunnel, it was decided to use a 127 mm radius rotor that can fit into the wind tunnel in a 2-, 4- or 8-rotor layout.

For the test in hovering, DJI E7000 rotors were mounted with a horizontal rotational axis to avoid a ground influence. For the test in the wind tunnel, rotors from APC (Landing Products Inc., Woodland, CA, USA) were chosen. Among the 127 mm multicopter rotors available on the market, only APC publishes rotor performance data and offers a wide variety of sizes and pitches. The 127 mm-radius rotors fitted to the wind tunnel has a 15.74 radius distance from the ground. This is enough to be out of ground effect. Of the 127 mm rotors in the APC family, the APC 1047 (127 mm radius, 119.3 mm pitch) and APC 1045 (127 mm radius, 114.3 mm pitch) are available both clockwise (CW) and counterclockwise (CCW) forms. The APC 1040 (127 mm radius, 101.6 mm pitch) is not available as a counter-rotating pair.

3.1 Rotor thrust and power characteristics

If two rotors have the same thrust coefficient (Equation 3.1), power coefficient (Equation 3.2) and tip Mach number (Equation 3.3), the performance will be similar, although details of the wake may be different. It is assumed that the effects of the interaction observed on APC rotors can be extended to the larger DJI rotors because rotors are similar.

Thrust coefficient is given by Equation 3.1 (Johnson, 2013, Chapter 1):

$$C_t = \frac{T}{\rho n^2 D^4} \qquad \text{(Equation 3.1)}$$

where T is thrust

ρ is the density of the air,

n is the rotational speed of the rotor,

and D is the diameter of the rotor.

Power coefficient is given by Equation 3.2 (Johnson (Chapter 1), 2013):

$$C_P = \frac{P}{\rho n^3 D^5} \quad \text{(Equation 3.2)}$$

where P is power.

Tip Mach number is given by Equation 3.3 (Johnson, 2013, Chapter 1):

$$M_{tip} = \frac{V_{tip}}{c} \quad \text{(Equation 3.3)}$$

where V_{tip} is the tangential velocity of the blade tip,

and c speed on sound in the air at selected altitude and temperature.

The following rotors were chosen for comparison: APC 1047, APC 1045, APC 1040, DJI E7000 and DJI E2000. The rotors' thrust, power and related rpm were collected from performance data for zero lateral velocity published on the manufacturers' websites (Table 3.1, Table 3.2, Table 3.3, Table 3.4, Table 3.5).

Table 3.1 DJI E7000 performance [https://www.dji.com/nz/e7000 accessed 25.03.2021].

Rotational Speed, Hz	Power (Watt)	Cp	Thrust (N)	Ct	V tip (m/s)	Mach
16.71	88.71	0.0371	14.85	0.0872	44.10	0.13
25.07	233.87	0.0290	34.46	0.0899	66.15	0.19
29.24	402.00	0.0314	47.82	0.0917	77.18	0.23
33.42	596.77	0.0312	60.96	0.0895	88.20	0.26

Rotational Speed, Hz	Power (Watt)	Cp	Thrust (N)	Ct	V tip (m/s)	Mach
41.78	1104.83	0.0296	95.95	0.0901	110.25	0.32
50.13	1919.35	0.0297	137.29	0.0896	132.30	0.39

Table 3.2 DJI E2000 performance [https://www.dji.com/nz/e2000 accessed 25.03.2021].

Rotational Speed, Hz	Power (Watt)	Cp	Thrust (N)	Ct	V tip (m/s)	Mach
16.71	88.71	0.0358	14.85	0.0847	44.42	0.13
25.07	233.87	0.0280	34.46	0.0874	66.62	0.19
29.24	402.00	0.0303	47.82	0.0891	77.73	0.23
33.42	596.77	0.0301	60.96	0.0870	88.83	0.26
41.78	1104.83	0.0285	95.95	0.0876	111.04	0.32
50.13	1919.35	0.0287	137.29	0.0871	133.25	0.39

Table 3.3 APC 1047 performance [https://www.apcprop.com/files/PER3_10x47SF.dat accessed 25.03.2021].

Rotational Speed, Hz	Power (Watt)	Cp	Thrust (N)	Ct	V tip (m/s)	Mach
33.42	2.98	0.0617	0.80	0.1398	26.67	0.08
50.13	10.44	0.0640	1.81	0.1409	40.01	0.12
66.85	24.61	0.0636	3.21	0.1408	53.34	0.16
83.56	46.98	0.0622	5.02	0.1409	66.68	0.19
100.27	80.54	0.0617	7.22	0.1409	80.01	0.23
116.98	132.73	0.0640	9.84	0.1410	93.35	0.27
133.69	205.81	0.0665	12.91	0.1417	106.68	0.31
150.40	305.74	0.0694	16.50	0.1431	120.02	0.35
167.11	439.22	0.0727	20.63	0.1449	133.35	0.39

Table 3.4 APC1045 performance [https://www.apcprop.com/files/PER3_10x45MR.dat accessed 25.03.2021]

Rotational Speed, Hz	Power (Watts)	Cp	Thrust (N)	Ct	V tip (m/s)	Mach
33.42	2.24	0.0463	0.62	0.1093	26.67	0.08
50.13	7.46	0.0457	1.43	0.1118	40.01	0.12
66.85	17.15	0.0443	2.54	0.1117	53.34	0.16
83.56	32.81	0.0434	3.99	0.1120	66.68	0.19
100.27	55.93	0.0428	5.75	0.1121	80.01	0.23
116.98	87.99	0.0424	7.84	0.1123	93.35	0.27
133.69	129.01	0.0417	10.27	0.1127	106.68	0.31
150.40	197.61	0.0448	13.12	0.1137	120.02	0.35

Table 3.5 APC 1040 performance [https://www.apcprop.com/files/PER3_10x4.dat accessed 25.03.2021].

Rotational Speed, Hz	Power (Watt)	Cp	Thrust (N)	Ct	V tip (m/s)	Mach
33.42	1.49	0.0308	0.55	0.0968	26.67	0.08
50.13	5.97	0.0366	1.24	0.0968	40.01	0.12
83.56	26.85	0.0355	3.46	0.0972	66.68	0.19
100.27	45.49	0.0348	5.00	0.0975	80.01	0.23
116.98	71.59	0.0345	6.83	0.0979	93.35	0.27
133.69	108.13	0.0349	8.95	0.0983	106.68	0.31
150.40	161.82	0.0367	11.42	0.0990	120.02	0.35
167.11	231.91	0.0384	14.23	0.0999	133.35	0.39

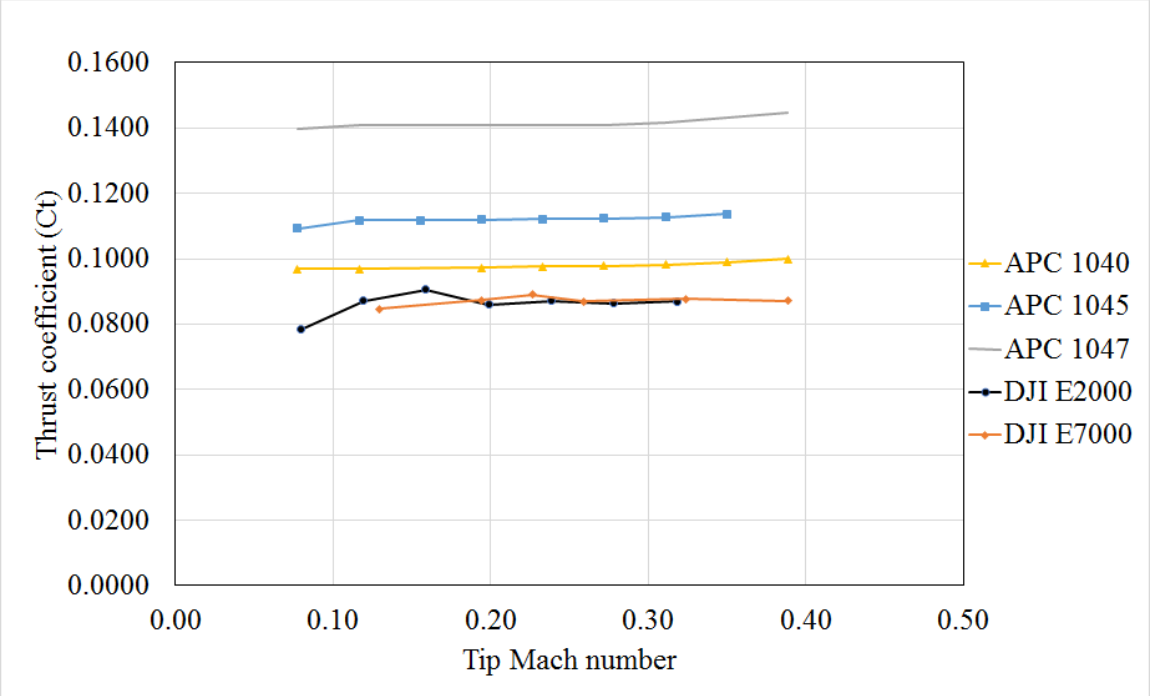

Figure 3.1 Thrust coefficient as function of tip Mach number for APC 1045 (blue), DJI E7000 (orange), APC 1047 (grey), APC 1040 (yellow), DJI E2000 (black).

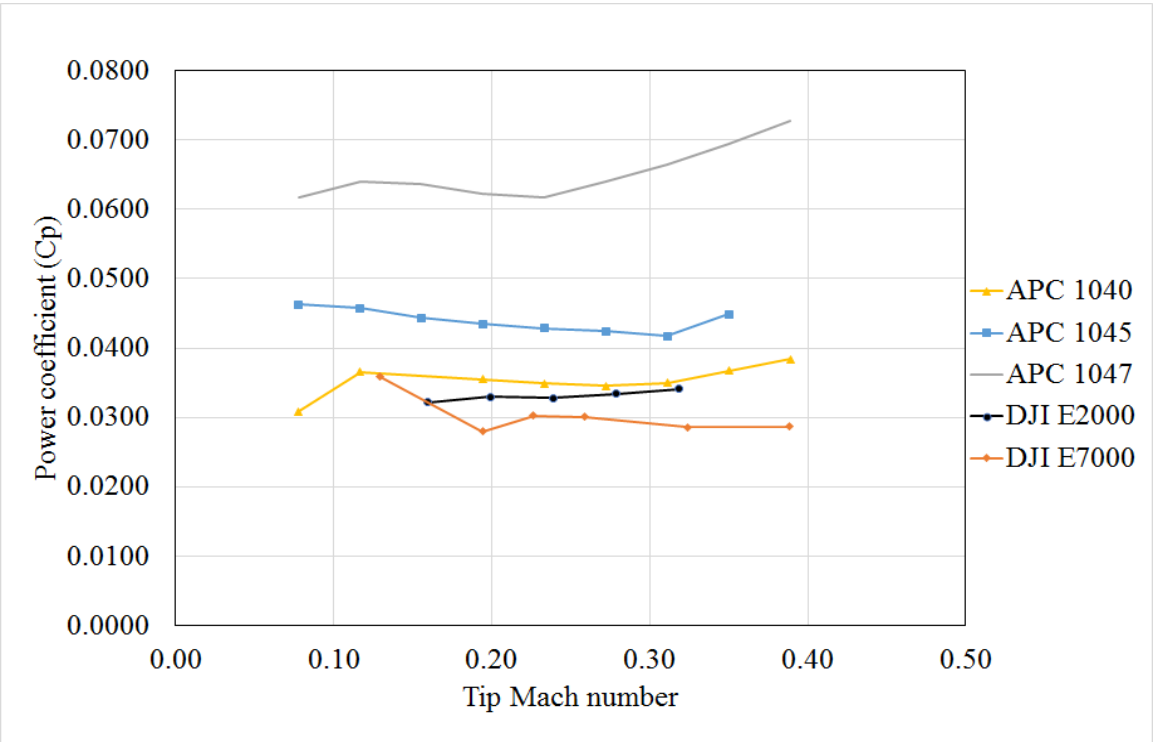

Figure 3.2 Power coefficient as function of tip Mach number for APC 1045 (blue), DJI E7000 (orange), APC 1047 (grey), APC 1040 (yellow), DJI E2000 (black).

The rotor most aerodynamically similar to the DJI E7000 and DJI E2000 rotors is the APC 1040 (Figure 3.1, Figure 3.2). However, it is not available in counterclockwise versions; thus, it cannot be used in a multicopter. The APC1040 rotor was evaluated singly. For analysis of the wake with the available facilities, the most suitable rotor is the APC 1045. However, APC 1047 and APC 1040 rotors were tested alone for the modelling of the wake of a multicopter. The DJI E2000 was not tested further because their wakes are expected to have a similar structure to the DJI E7000 rotor. The DJI E2000 and DJI E7000 have similar thrust coefficients.

3.2 Experimental evaluation of velocity flow field of single isolated rotor

Two experimental methods were used to evaluate the downwash of the isolated rotor: constant temperature anemometry (CTA) and particle image velocimetry (PIV or SPIV) (see Chapter 2).

All motors were controlled with a pulse width modulated (PWM) signal from a radio control handset (RadioLink AT9S, Shenzhen, China). The rotational speed was measured by an optical interrupter. The interrupter was bolted to the mounting beam. A ring with a tongue was mounted on the motor's shaft. When the tongue passed between the transmitter and receiver of the interrupter, it interrupted the signal. The signal was read at 38.5 kHz frequency and the rotational speed recalculated to revolutions per second and revolutions per minute. The readings were verified with a digital tachometer. The measurement error was less than 1%.

3.2.1 Propulsion system used in experiments

3.2.1.1 APC family rotors

The APC family rotors were mounted on Sunnysky X2212 motors driven by Hobbyking 40 A electronic speed controllers (ESCs). In isolated rotor tests, the rotor was mounted beneath the rectangular mounting beam (20x20 mm) in such a way that the beam least obstructs the flow.

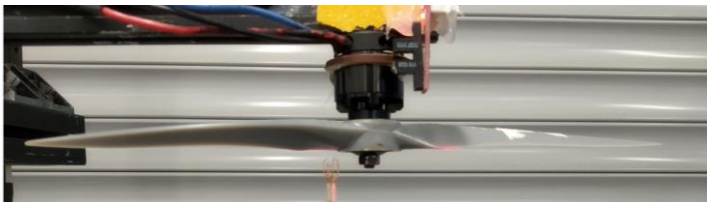

Figure 3.3 The mounting of Sunnysky X2212 rotor with APC 1040 rotor on the aluminium beam.

The power supply was a CHUX S-2000-50V AC-DC (Chance Electric LLC, Foshan, China) converter with adjustable voltage and current. The voltage was set to 14.4V.

3.2.1.2 DJI family rotors

The DJI E7000 system is a self-contained system that comes with a carbon-fibre tubular beam. A connector was designed to clamp the carbon fibre tube and bolt it to a T-slot aluminium beam (Figure 3.4). Because the rotor on the DJI E7000 can be mounted only one way, the downwash on the rotor was always directed towards the carbon fibre tube, obstructing the flow. This is typical for commercial multicopters.

Figure 3.4 The mounting of the DJI E7000 system (left) to the aluminium slotted beam; the connector to attach the carbon fibre tube to the slotted beam (right).

The rotor was powered by a CHUX S-2000-50V AC-DC converter set to 44.4V. The current was limited to 80 A. This was sufficient to spin the rotor at 2600 RPM. The controlling and rotational speed measurement systems were the same as for the APC system.

3.2.2 CTA measurement

For the CTA measurements, a 55P91 three-directional hot-wire probe was used with the CTA system described in Chapter 2. The advantage of this probe is the possibility of capturing the U, V, and W components of velocity simultaneously. The alignment face (Chapter 2, Figure 2.21, notch on the probe) of the probe was directed towards the rotor blade tip. The following coordinate system was used in CTA measurements. The CTA was sampling for 1024 milliseconds at a rate of 1 kHz. CTA measurements are averaged from 1024 successive measurements. During one CTA data acquisition at 5400 RPM, the rotor made 94.151 revolutions.

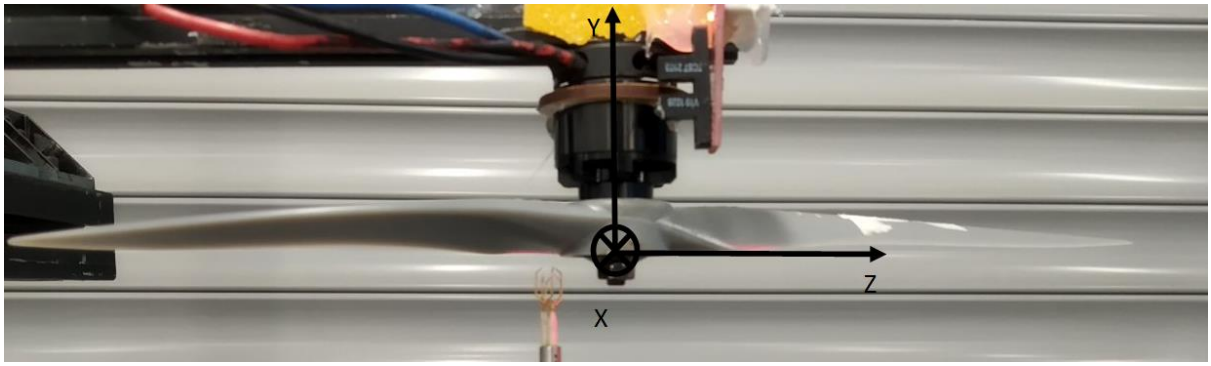

Figure 3.5 The CTA 55P91 probe and APC 1040 rotor with coordinate system used in CTA experiments.

The whole rotor system was traversed with 5 mm increments in the sideways direction along the rotor blade (Z-axis) on a two-dimensional traverse (Chapter 2, Figure 2.20).

For the APC rotors, the wake was measured at a vertical distance of 2 mm from the rotor disk along the radius of the rotor. The rotational speed was 5400 rpm (1 measurement per 33.1° of rotor rotation). Additional data was collected at -55mm (-0.43R) vertical distance (Y) from the rotor origin. The nearest solid surface was 2 meters (-15.74R) away from the rotor in a vertical (Y) direction. The measurements started from 0.11R as the motor shaft was in the way of the probe.

The DJI rotor was installed horizontally pointing towards the wall located -12 meters away from the rotor (-28.6R), due to the limitation of the height of the laboratory. The rotational speed of the rotor was 1740 rpm (10.8° per one CTA measurement). The measurement started from 0.18R because of the placement of the carbon fibre mounting tube.

The wake of the rotor was described by three velocity components: downwash, swirl, and radial component. The downwash velocity component is negative along the entire radius of the rotor. For the first 0.75-0.8R from hub to tip, it increases in magnitude, then decays in the final 0.15-0.2R near the tip. The radial velocity is always directed towards the tip. The magnitude of radial

velocity increases towards the tip and peaks at 0.75-0.8R. The source of the radial velocity component is the flow between the upper and lower surface of the rotor disk resulting from the pressure difference. The swirl velocity peaks at 0.2-0.3R and then decays towards the tip. The swirl velocity is due to rotor induced torque (Johnson, 2013, Chapter 3). The measured velocity was normalised by the rotor tip velocity, which is equal to 71.8 m/s at 5400 rpm for APC rotors and 76.52 m/s at 1740 rpm for the DJI rotor. The error bars shown in Figure 3.6 through Figure 3.8 represent the standard deviation (1 S.D. of the mean). The high level of fluctuation in velocity near the rotor is due to the different blade positions at every moment of capture above the CTA probe.

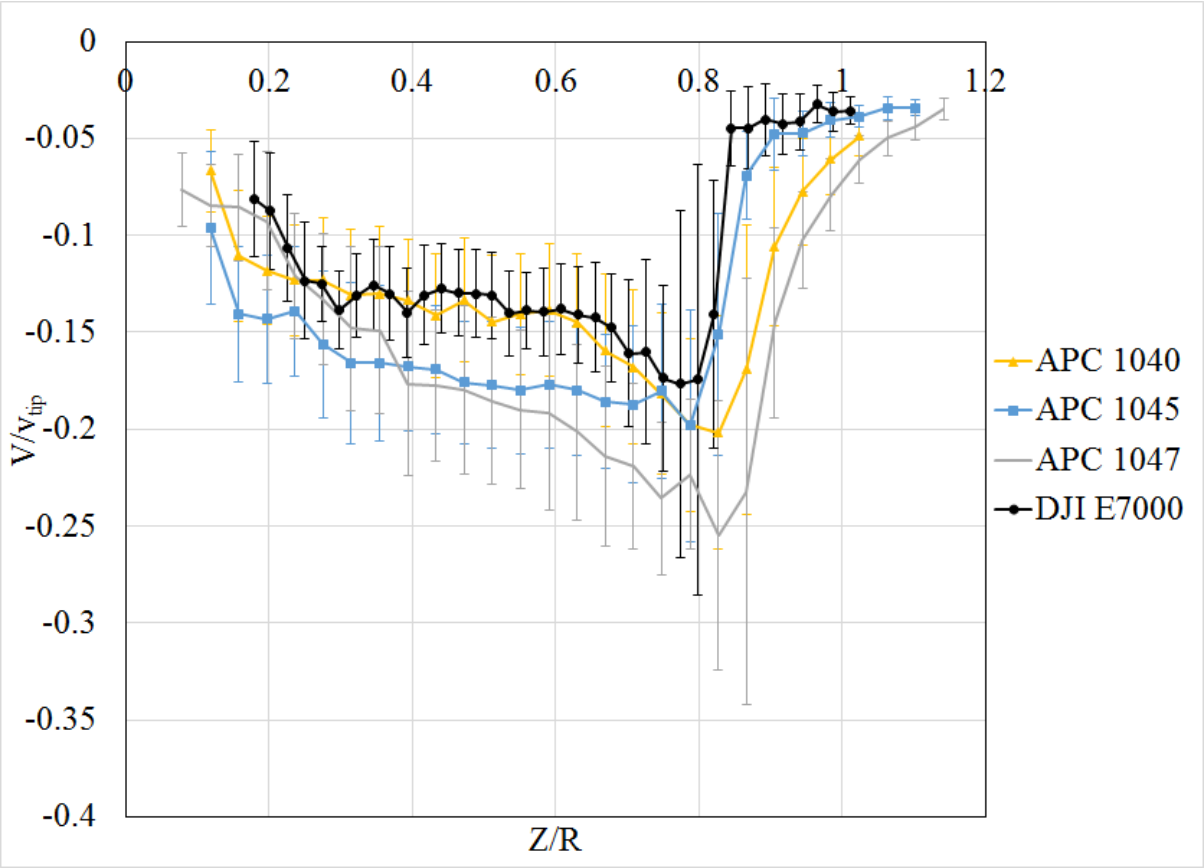

Figure 3.6 Downwash velocity components (m/s) as a function of radial coordinate (X/R) of the APC 1047 (orange), APC 1040 (grey), APC 1045 (yellow) and DJI E7000 (blue) measured by CTA.

The peak downwash for the APC 1047 rotor is at 0.82R and equal to -0.25 of tip velocity on average. The standard deviation peaks at 0.86R where the downwash fluctuation peaks at -0.34. The peak downwash speed for the APC 1040 rotor is at 0.83R and equal to -0.2 on average. The peak downwash speed for the APC 1045 rotor is at 0.79 rotor radius and equal to -0.2 on average. The peak downwash speed for the DJI E7000 rotor is at 0.8R and equal to 0.17 on average.

Comparison of the flow of different rotors showed that the APC 1040 and DJI E7000 have similar downwash structures from hub to 0.8R. After 0.8R, the downwash structure varies with rotor type. From 0.8R to 1R the DJI E7000 is reasonably similar to the APC1045. The APC 1047 rotors' downwash is stronger than the other rotors because it has a higher pitch.

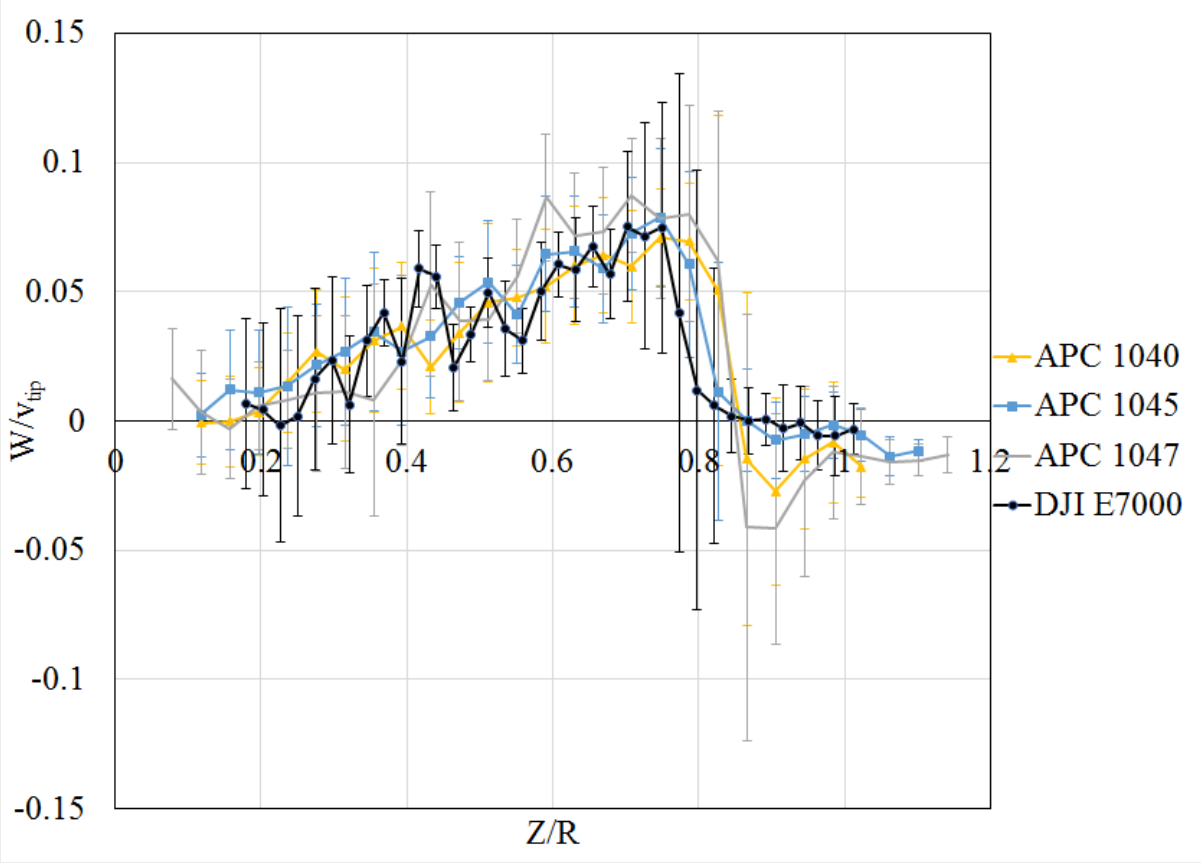

Figure 3.7 The normalised radial velocity components as a function of radial coordinate (X/R) of the APC 1047 (orange), APC 1040 (grey), APC 1045 (yellow) and DJI E7000 (blue) measured by CTA.

The radial velocity component of the APC 1047 peaks at 0.75R equal to 0.08. The peak radial velocity component of the APC 1045 rotor is 0.07 at 0.75R. The peak radial velocity component of the APC 1040 rotor is 0.065 at 0.8R. The peak radial velocity component of the DJI E7000 rotor is 0.07 at 0.75R.

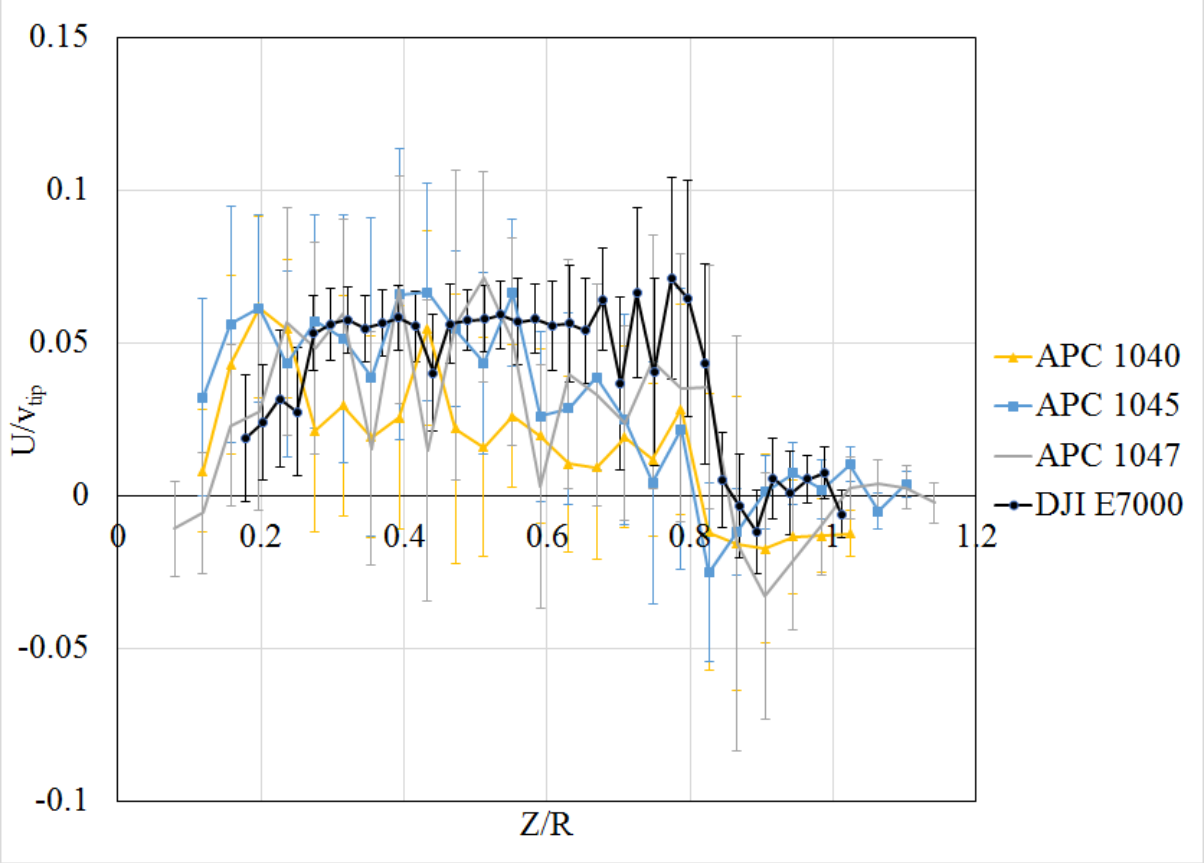

Figure 3.8 The normalised swirl velocity components (m/s) as a function of radial coordinate (X/R) of the APC 1047 (orange), APC 1040 (grey), APC 1045 (yellow) and DJI E7000 (blue) measured by CTA.

The swirl velocity remains relatively constant with position but has high temporal fluctuations in velocity from the hub to 0.7R -0.8R for all rotors.

The method of calculation of turbulence kinetic energy (TKE) was described in Chapter 2. Figure 3.9 shows the turbulence kinetic energy for all rotors tested. The TKE was normalised

by the square of rotor tip velocity v_{tip}^2. The rotor tip velocity (v_{tip}) was equal to 71.8 m/s at 5400 rpm for APC rotors and 76.52 m/s at 1740 rpm for the DJI rotor.

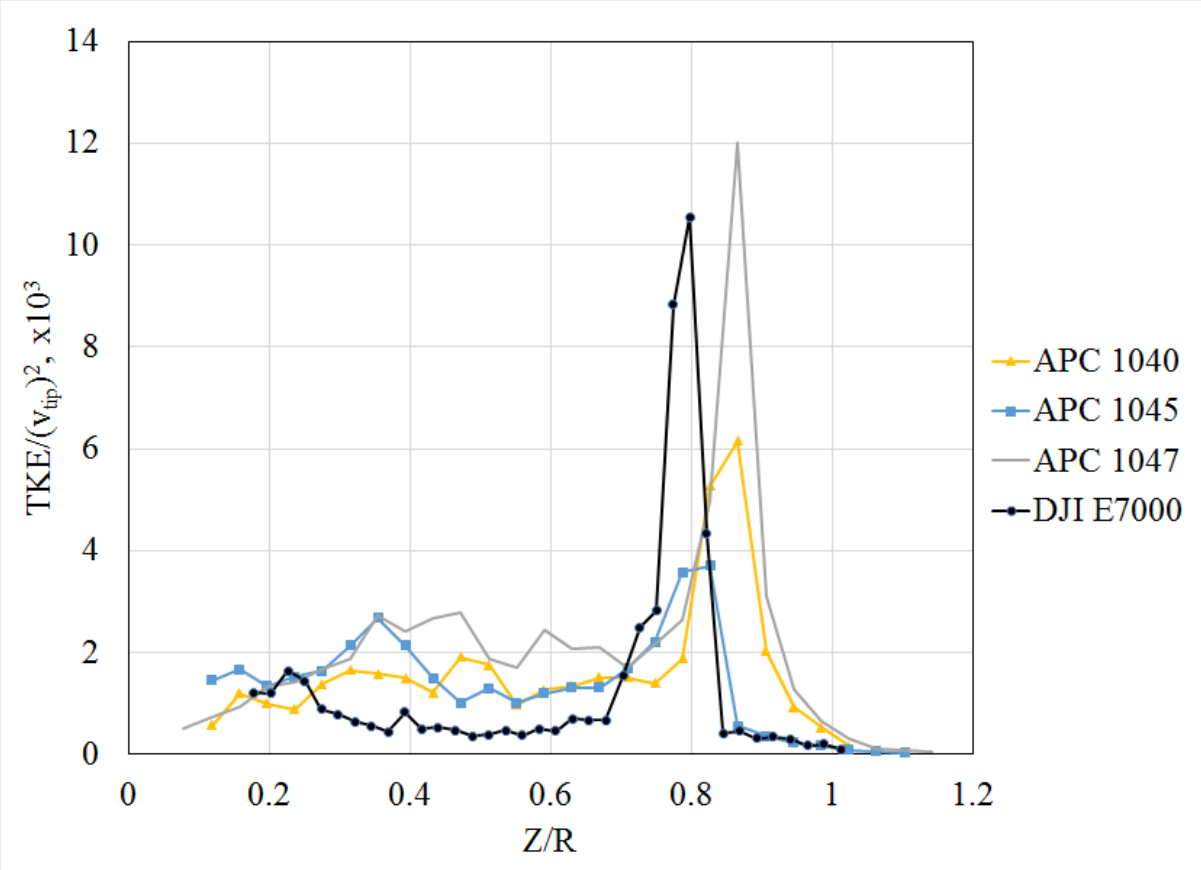

Figure 3.9 The normalised turbulence kinetic energy (TKE) as a function of radial coordinate (X/R) of the APC 1047 (orange), APC 1040 (grey), APC 1045 (yellow) and DJI E7000 (blue) measured by CTA.

The peak in TKE is explained by the generation of the tip vortex. As has been mentioned, the tip vortex has a helical structure and is attached to the tip of the rotor. In the CTA measurements, the vortex appears in the point of measurement two times per revolution of the rotor. The TKE can be used as a source in the model that predicts the wake in the far-field.

3.2.3 PIV measurement

A PIV system was set up, so the laser illuminates the plane that passes through the center of the rotor along the downwash. The pixel size for this experiment was 138.1 microns, field of view 351x244 mm. The tracing particles were generated by the smoke machine. The coordinate system was set to be the same as in CTA experiments with origin in the rotor's hub and Y negative downwash (V).

The rotors used in the experiment are the APC 1040, APC 1045, APC 1047 and DJI E7000. The field of view was large enough to capture the flow field of the 127 mm radius APC rotors, but not to capture the flow field of the DJI rotor; thus, only half of that rotor's downwash was captured.

3.2.3.1 Rotor velocity field

A detailed representation of the rotor wake features is presented using the example of an APC 1045 rotor with 5400 rpm rotational speed. The rotor wake is shown in Figure 3.10 by velocity components and wake vorticity.

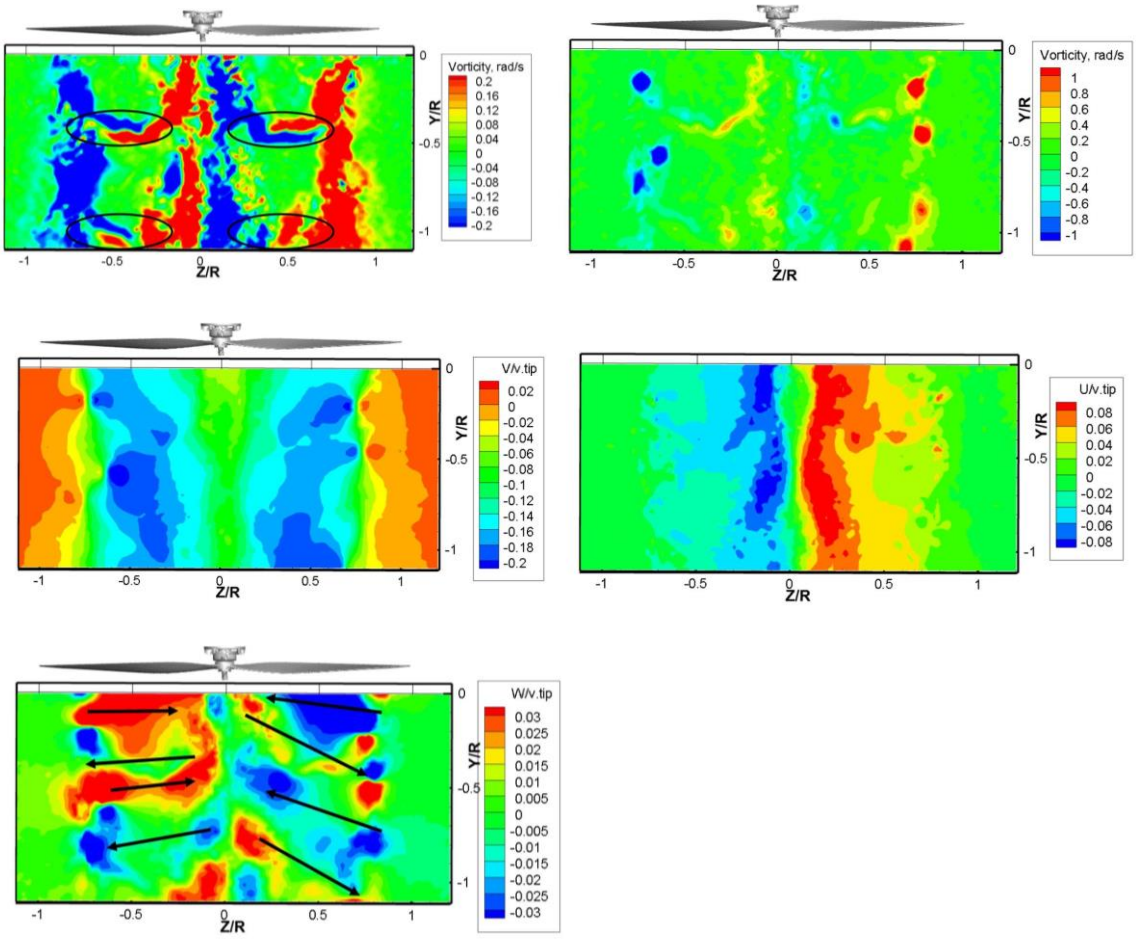

Figure 3.10 APC 1045 rotor wake at 5400 rpm rotational speed. Top left: vorticity, rad/s, band -0.2 rad/s to 0.2 rad/s; Top right: vorticity, rad/s, band -1 rad/s to 1 rad/s. Central left: normalised downwash component (V); central right: normalised swirl velocity component (W). Bottom: normalised radial velocity component (U).

In Figure 3.10 (top left), the ellipses highlight the vortex sheet generated by rotor blades. Vortex sheet phenomena were described in Chapter 1. The vortices attached to the outer part of the vortex sheet were located by plotting the vorticity field with a larger band (-1 rad/s to 1 rad/s) (Figure 3.10 top right).

The swirl components of the wake velocity field (U/v_{tip}, Figure 3.10 (central right)), generated by the induced torque of the rotor, follow the direction of rotation of the rotor. Figure 3.10 bottom shows the radial velocity component. The arrows in Figure 3.10 bottom show the

predominant direction of the radial velocity component. The source of the radial velocity component is the tip vortex. In the top part of the tip vortex, the radial velocity vector points towards the rotor shaft. The radial velocity vector points away from the rotor shaft on the bottom part of the tip vortex. Therefore, the radial velocity component is periodic along the vertical axis (Y/R).

3.2.3.2 Comparison of velocity field in different rotational speeds

The velocity flow field was measured at a range of different rotational speeds (Table 3.6)

Table 3.6 Rotational speeds and tip velocity for the DJI E7000 (R=420 mm) and APC (R=127 mm) family rotors.

Rotational speed, RPM	v_{tip}, m/s DJI E 7000 (R=420 mm)
1500	65.97
1600	70.38
1700	74.79
1740	76.52
1800	79.168
1900	83.567
2000	87.966
2100	92.365
2200	96.764
2300	101.163
2400	105.562
2500	109.961

Rotational speed, RPM	v_{tip}, m/s APC family rotors (R=127 mm)
4000	53.198
5000	66.502
5400	71.8
6000	79.796
6500	86.451

The figures below show velocity magnitude normalised by corresponding tip velocity (Figure 3.11 Figure 3.14).

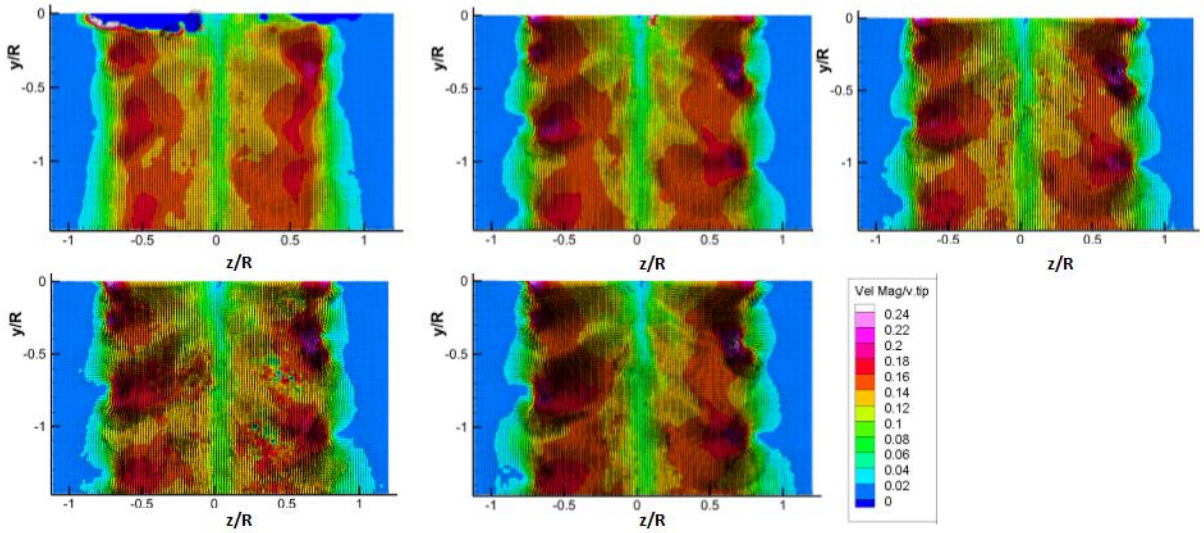

Figure 3.11 The velocity magnitude normalised by rotor tip velocity of the APC 1040 rotor, at rotational speeds of 4000 (top left), 5000 (top middle), 5400 (top right), 6000 (bottom left), and 6500 rpm (bottom right).

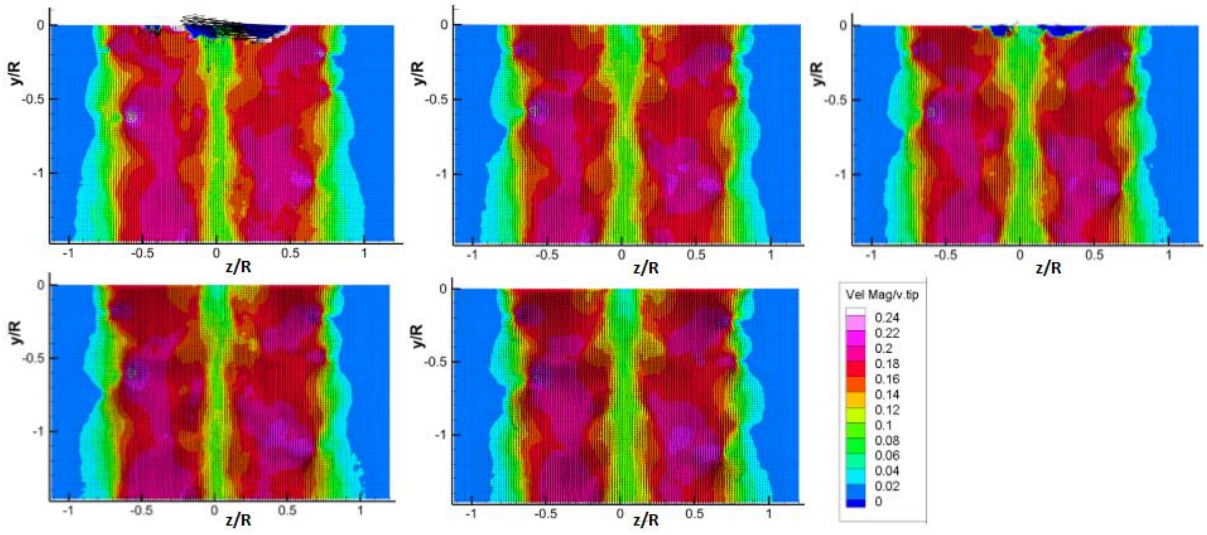

Figure 3.12 The contour plot with vectors of velocity magnitude normalised by tip velocity of APC 1045 rotor, at rotational speeds of 4000 (top left), 5000 (top middle), 5400 (top right), 6000 (bottom left), and 6500 rpm (bottom right).

The downwash of the APC 1047 is the strongest because of the greater pitch (i.e., greater thrust coefficient). The downwash of APC 1047 has a wide low-velocity region under the hub. It is supposed that the greater normalised velocity of the rotor generates eddies under the motor hub. These approximate coordinates are y/R=-0.5; x/R=-0.2 and y/R=-11; x/R=-0.15 (Figure 3.13).

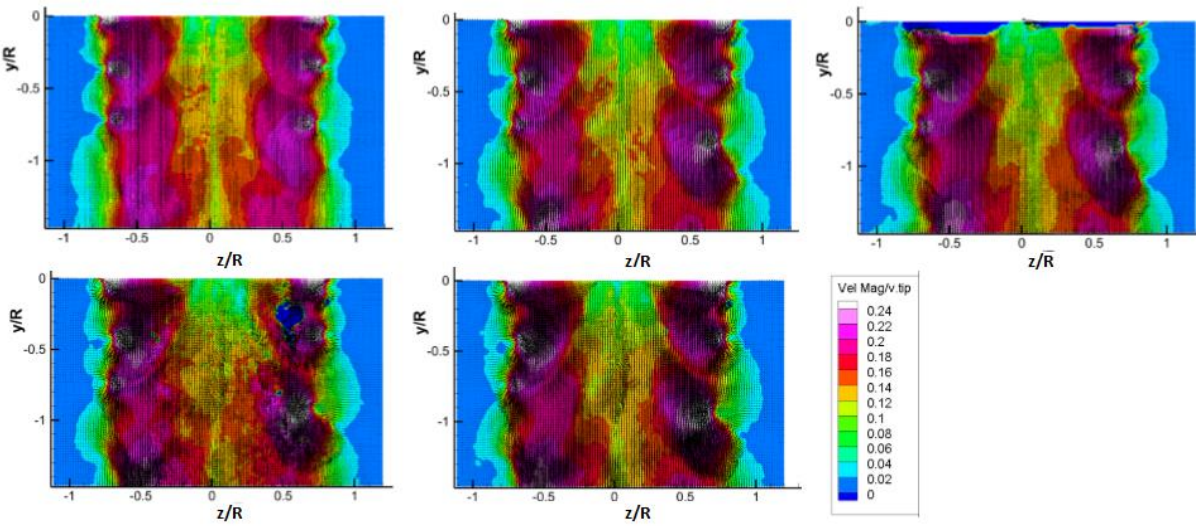

Figure 3.13 The velocity magnitude normalised by rotor tip velocity of the APC 1047 rotor, at rotational speeds of 4000 (top left), 5000 (top middle), 5400 (top right), 6000 (bottom left), and 6500 rpm (bottom right).

The DJI rotor downwash data starts from 0.1R and ends at 0.9R because of the field of view limitation (Figure 3.14). The normalised velocity fields for the DJI E7000 rotor are similar across the range of measured rotational speeds.

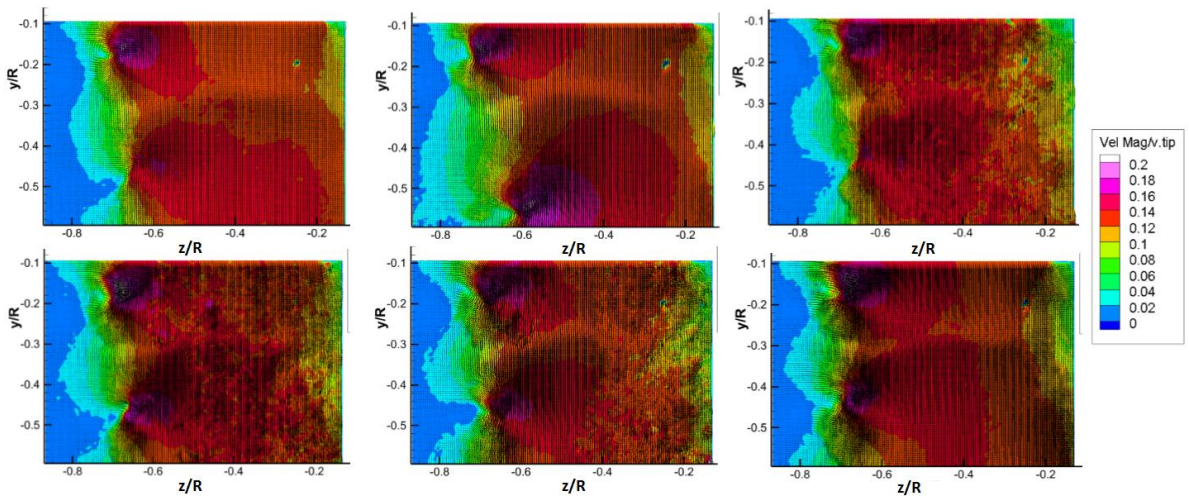

Figure 3.14 The velocity magnitude normalised by rotor tip velocity of the DJI E7000 rotor, at rotational speeds of 1500 (top left), 1740 (top middle), 1900 (top right), 2100 (bottom left), 2300 (bottom middle), and 2500 rpm (bottom right).

The high-velocity bands (0.12-0.2) occupy similar ranges on normalised coordinates. In the APC rotors, the normalised wake velocity increases with increasing speed, but the spatial extent of the band of high speed (0.12-0.2) remains similar for all three rotors tested.

The wakes of APC and DJI rotors are similar. The high-velocity bands occupy the space between z/R =-0.2-0.7. The wakes have the typical vortex sheet structure with oscillating velocity towards -y/R. There is the low-velocity region under the motor and at the tip. The variation of the width of the high-velocity region is a result of the helical vortices emitted from the tips of blades, observed in every rotor tested.

3.2.4 Comparison of CTA and PIV data

According to vortex theory, the wake for a single-bladed rotor can be represented as following (Figure 3.15):

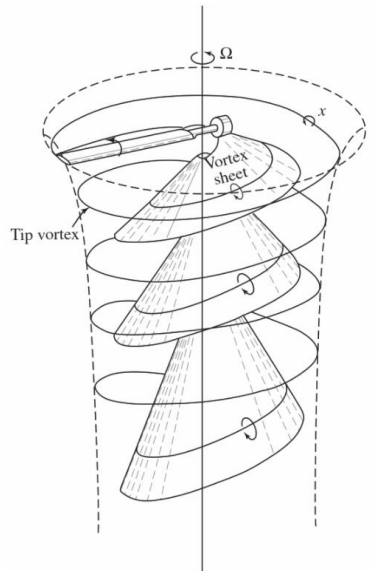

Figure 3.15 The wake structure of the single-bladed rotor according to the vortex theory (adapted from Johnson, 2013, Chapter 4).

During one CTA data acquisition at 5400 rpm, the rotor made 94.151 revolutions. CTA measurements are averaged from 1024 data points. In contrast, the PIV data is phase-locked to when the rotor blade was immediately above the laser sheet. Therefore, the flow fields cannot be compared directly. To compare CTA and PIV measurements, the data between two tip vortex rings in the PIV experiment was extracted and averaged over the y/R coordinate (Figure 3.16).

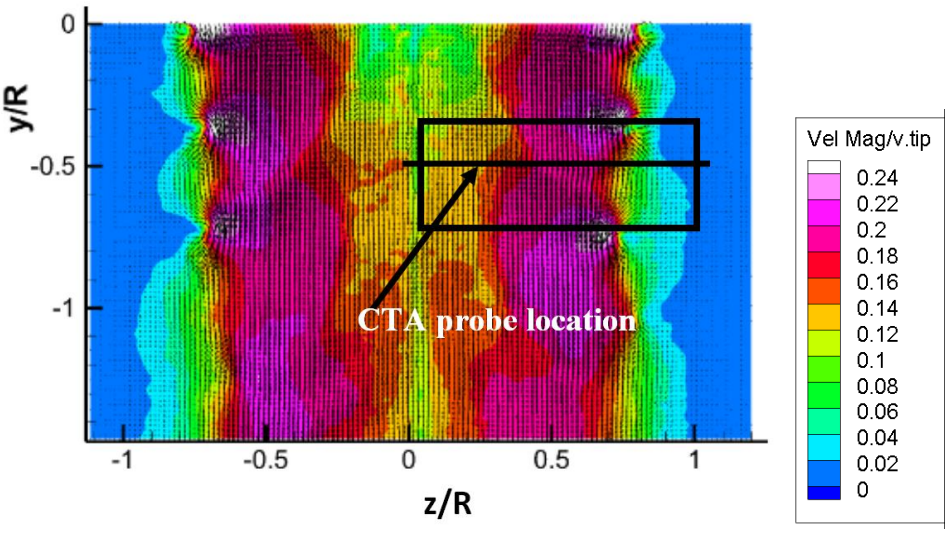

Figure 3.16 The APC 1045 rotor's wake at 4000 rpm. The black box is the range of data extracted for comparison with CTA.

By averaging the data over y/R coordinate, two assumptions have been made:

1) Velocity is not affected by the viscous effects (i.e. it does not decay) within the distance between complete turns of the helical tip vortex.

2) The vertical distance between vortex rings (helical distance) is uniform

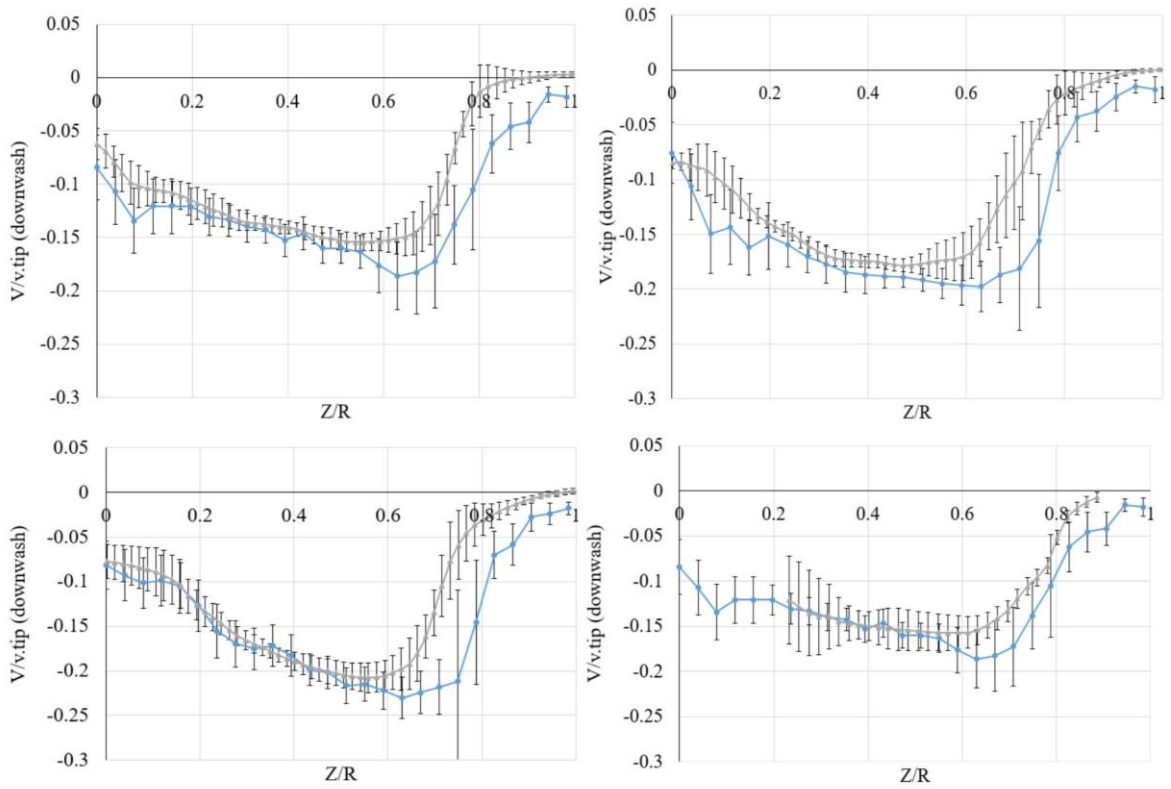

Figure 3.17 CTA (blue) and PIV (grey) comparison of the downwash velocity component for the APC 1047 rotor (top left), the APC 1045 rotor (top right), the APC 1040 rotor (bottom left), and the DJI E7000 rotor (bottom right).

The measured downwash (V/v_{tip}) is within one standard deviation from 0 to peak downwash for all rotors except the APC 1045. The observed difference in the downwash peak (0.6-0.8R depending on the rotor to rotor tip (1R)) is due to the periodical tip vortex in the CTA data.

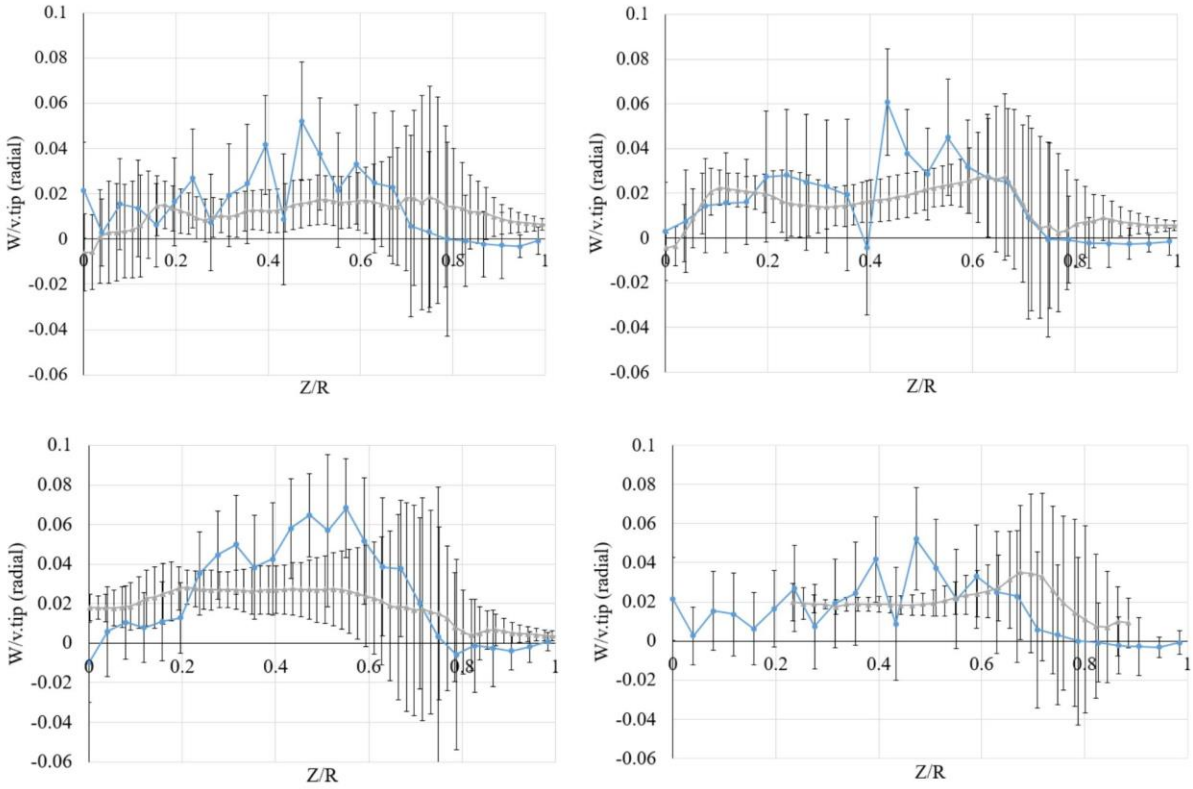

Figure 3.18 CTA (blue) and PIV (grey) comparison of the radial velocity component for the APC 1047 rotor (top left), the APC 1045 rotor (top right), the APC 1040 rotor (bottom left), and the DJI E7000 rotor (bottom right).

The radial components of velocity are within the standard deviation. Similarly to downwash, the difference in radial components is observed at 0.7R to 1R.

The swirl components are similar for PIV and CTA measurements, which means that the swirl remains steady over one revolution of the rotor temporally. The difference between datasets of downwash is greatest where the assumption of no viscous effects is least valid.

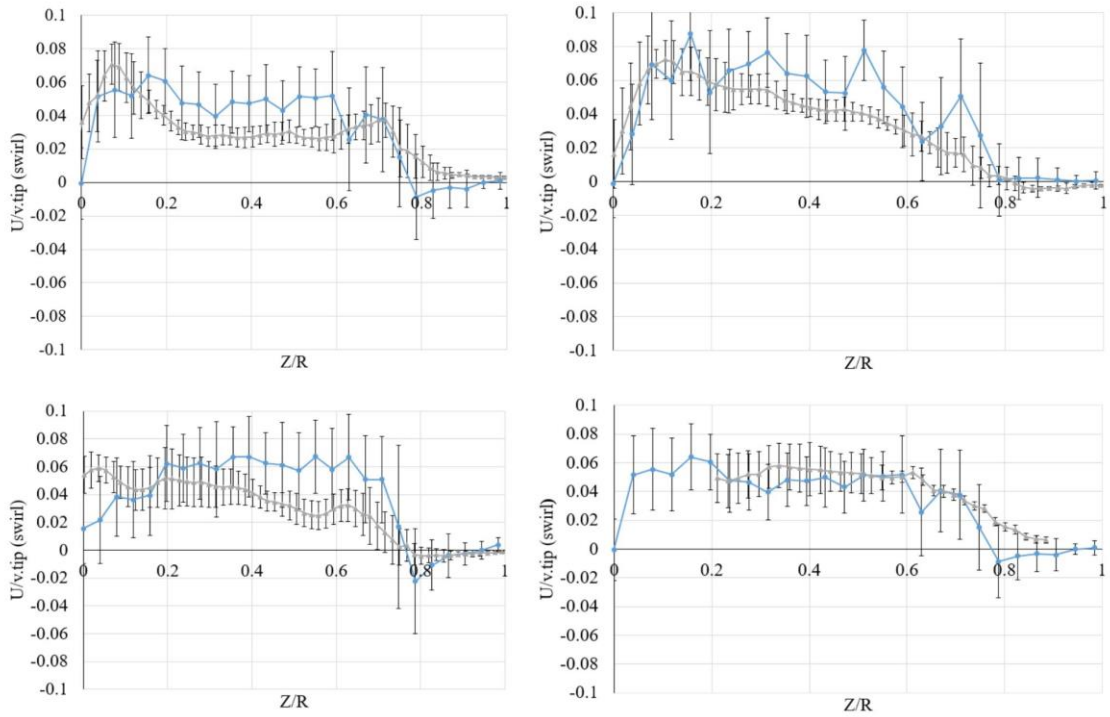

Figure 3.19 CTA (blue) and PIV (grey) comparison of the swirl velocity component for the APC 1047 rotor (top left), the APC 1045 rotor (top right), the APC 1040 rotor (bottom left), and the DJI E7000 rotor (bottom right).

All components of velocities in CTA and PIV experimental measurements are mostly agreed within one standard deviation at Z/E=0...0.7R. From 0.7R to 1R, all velocity components do not agree within one standard deviation because of a rotor tip vortex influence. Large values of standard deviation after 0.7R reflect the influence of the tip vortex that makes periodic appearances.

3.3 Conclusion of the Chapter

This chapter presents the differences and similarities between the wakes of isolated rotors and explores the assumptions used for rotor wake comparison.

The most aerodynamically similar to the DJI E7000 and DJI E2000 rotors is the APC 1040. It is not available in counterclockwise versions; thus, it cannot be used in a multicopter. For analysis of the wake of a multicopter with the available facilities, the most suitable rotor is the APC 1045. APC 1047 and APC 1040 rotors were tested alone for the modelling of the wake of a multicopter.

APC 1040, APC 1045, APC 1047 and DJI E7000 isolated rotor wakes were analysed using constant temperature anemometry (CTA) and particle image velocimetry (PIV). The wake vector field, normalised by rotor tip velocity, remains the same with changing rotational speed. The data obtained in PIV and CTA are mostly agreed within one standard deviation at Z/E=0...0.7R. The difference between datasets at Z/E=0...1R is observed because the assumption of no viscous effects is least valid at this portion of the rotor.

The data obtained in CTA and PIV experiments can be used for fast multicopter wake analysis (Chapter 6).

4. Measurement of near multicopter wake

A typical multicopter has several rotors. The wakes of rotors interact (Chapter 1), generating upward velocity regions.

This chapter investigates whether the velocity field for the complete multicopter can be treated as an addition of the velocity fields of each pair of counter-rotating rotors. It simplifies the experimental setup.

Counter-rotating pairs of DJI E7000 (420 mm radius; 230 mm pitch) and APC 1045 (127 mm radius; 119 mm pitch) non-overlapping rotors were tested in hover. The APC 1045 rotors were tested at rotor arc distances of 0.2R, 0.36R and 0.55R (R= rotor radius). For the DJI E7000, the wake was obtained for 0.2R rotor arc spacing.

Spraying is usually performed with lateral velocity (either wind or forward velocity). The multicopter was represented by a pair of rotors, spinning in opposite directions, and sharing the same rotor plane. The APC 1045 rotors were arranged either: a) one downstream of the other ("arranged streamwise") or b) side by side ("arranged spanwise"). The horizontal distance between the rotor axes was varied. Lateral velocities (wind tunnel jet speeds) tested were 2 m/s, 6 m/s, 10 m/s and 14 m/s.

The velocity flow field experimentally obtained in this chapter was used in Chapter 5 to evaluate droplet behaviour near multicopter and in Chapter 6 to compare with the fast computational model of multicopter flow fields.

4.1 Experimental evaluation of near field flowfield of multiple adjacent rotors in hovering flight

4.1.1 Experimental setup

Two or more adjacent co-planar rotors were used in these experiments. The in-plane distance between the rotor arcs is defined by the blue arrow in Figure 4.1.

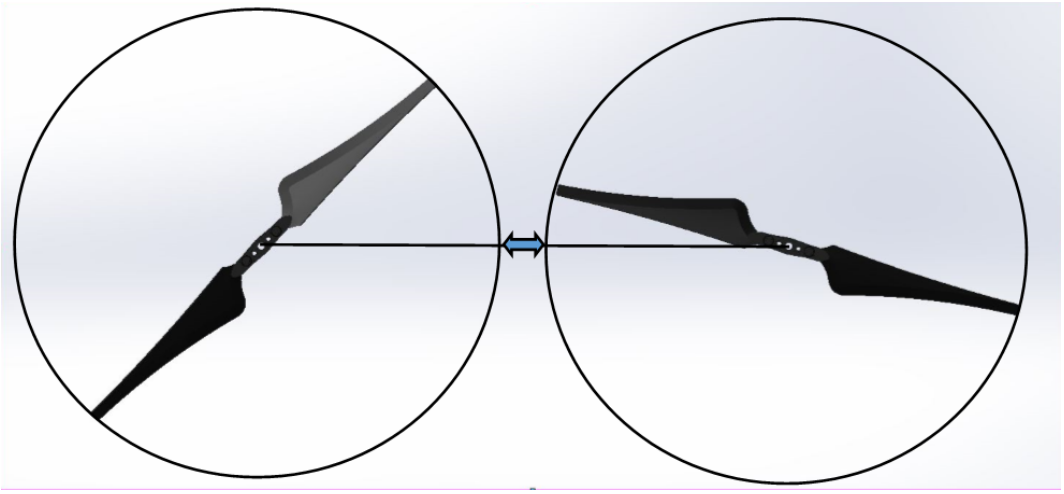

Figure 4.1 The in-plane distance between the rotor tip arcs

All motors were controlled with a pulse width modulated (PWM) signal from a radio control handset (RadioLink AT9S, Shenzhen, China). The rotational speed was measured by an optical interrupter. The interrupter was bolted to the mounting beam. A ring with a tongue was mounted on the motor's shaft. When the tongue passed between the transmitter and receiver of the interrupter, it interrupted the signal. The signal was read at 38.5 kHz and was recalculated to revolutions per second and revolutions per minute. The readings were verified with a digital tachometer. The measurement error was less than 1%. An additional optical sensor, mounted

on every motor, was used to trigger the laser when both rotors coincided at a predefined rotational angle.

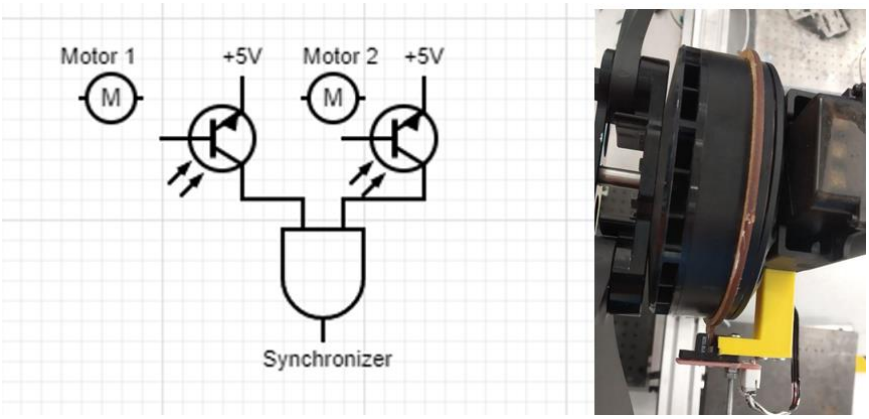

Figure 4.2 General schematic and physical interrupter of two-rotor experimental setup.

4.1.1.1 Two and four-rotor experimental setup

The modern multicopter has four or more rotors that interact with each other (Chapter 1). For the analysis of interaction effects, the PIV was used. PIV allows instantaneous velocity fields to be obtained. To generate a quality experimental output 50 image pairs were captured. All rotors should be in the same position in every frame. However, the synchronisation of four rotors for PIV testing is time consuming and, therefore, practically impossible for a large variety of testing conditions. Thus, the interaction of two rotors was observed. Yoon et al. (2017) modelled the flow around a hovering multicopter with CFD. They showed that the velocity field for the complete multicopter is an addition of the velocity fields of each pair of counter-rotating rotors. To prove such a concept the vector field of two coplanar counter-rotating rotors was compared to the downwash of four coplanar rotors in PIV experiments.

The multicopter used in the test consisted of 8 APC 1045 rotors driven by Sunnysky X2212 motors. The shortest distance between adjacent rotor shafts is 280mm (2.2R). The distance between rotor arcs is 26mm (0.2R). The controlling signal was fed to all of the ESCs

simultaneously. The multicopter was mounted on the two-dimensional traverse. In four-rotor tests, rotors 1, 2, 3 and 4 rotated at 5400 RPM. In two-rotor tests, rotors 1 and 2 rotated at 5400 RPM.

In two-rotor tests, rotors 1 and 2 were phase-locked; the blades were in the closest approach to each other. When the test with four rotors was performed, all 4 rotors were phase locked. Rotor 1 and rotor 2 were in the closest approach to each other. Rotor three and rotor four were in the closest approach to rotor 1 and rotor 2 arcs respectively (Figure 4.3).

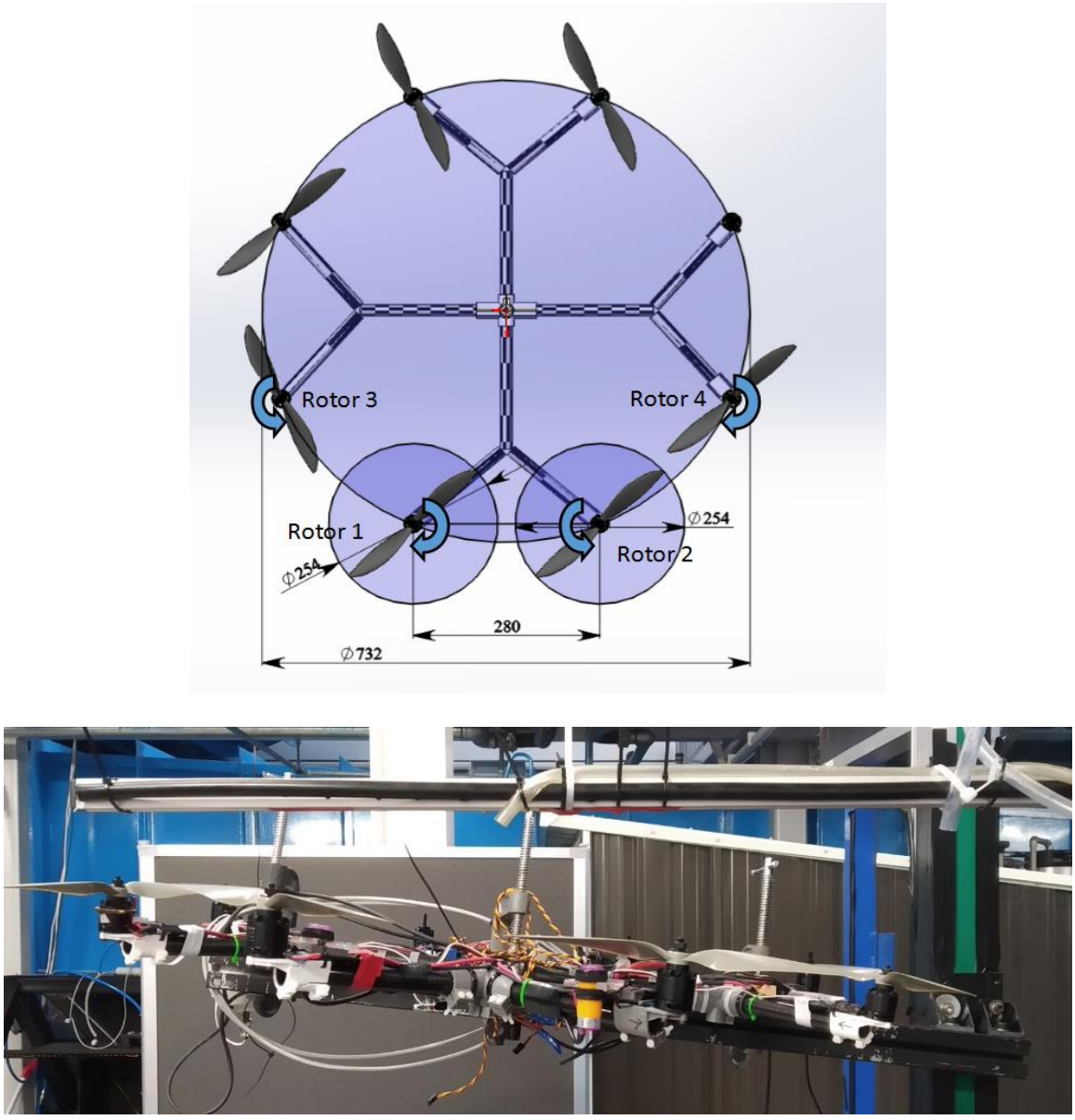

Figure 4.3 The multicopter: layout with dimensions (top), photograph (bottom).

The PIV system was set to record the velocity beneath two adjacent rotors (rotors 1 and 2). The field of view was 447x311 mm, pixel size 176 pixel/micron. Traversing the multicopter laterally (-Z/+Z) with an increment of 5mm, the maximum traverse distance was +-130mm (+-1.02R). The data between the captured planes were interpolated using inverse-distance weighted interpolation (Chapter 2, section 2.1.7).

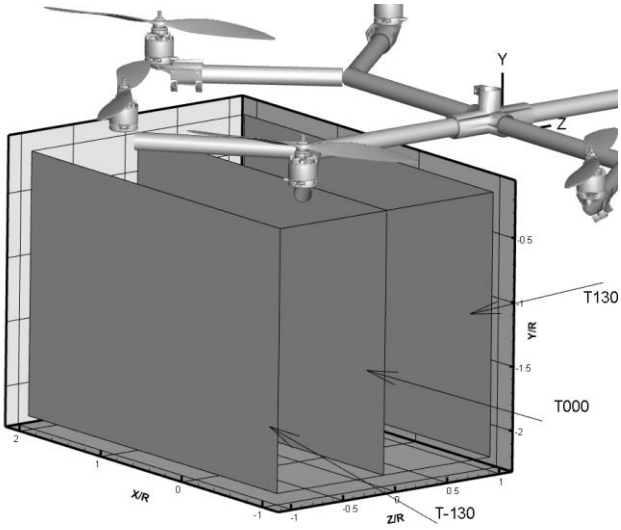

Figure 4.4 CAD model of the multicopter with the domain of the PIV data shown. T000 is a vertical Y/R-X/R plane with Z/R=0; T130 is a vertical Y/R-X/R plane with Z/R=1.023; T-130 is a vertical Y/R-X/R plane with Z/R=-1.023

4.1.1.2 Two APC 1045 adjacent rotor experimental setup

The counter-rotating APC 1045 rotors were mounted on Sunnysky X2212 motors with maximum thrust equal to 1.15 kg [http://en.rcsunnysky.com/x-fixedwingseries/1101.html, accessed 13.01.2020] and driven by Hobbyking 40A ESCs. The motors were mounted on a slotted tube attached to the vertical column (Figure 4.5). The slotted tube allows for ease of changing the spacing between the tips of the rotors. The rotor axis was vertical and thrust direction vertically upwards, i.e., the usual direction when flying.

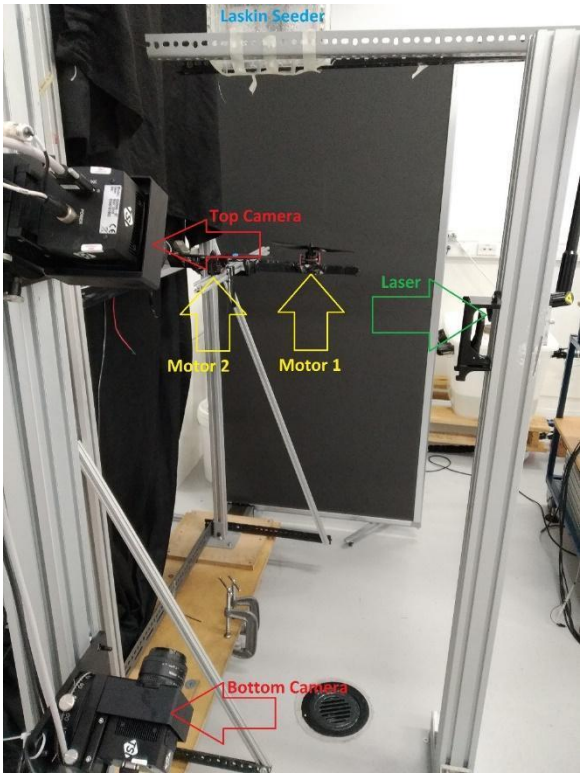

Figure 4.5 APC 1045 setup. Red arrows: camera system, green arrow: laser lenses, yellow arrow: motors.

The results presented in this paper are at 5400 RPM. The tips were in the closest position to each other in experiments. The distance between the tips was equal to 26mm (0.2R), 45 mm (0.36R) and 70 mm (0.55R).

4.1.1.3 Two DJI E7000 adjacent rotor experimental setup

The DJI rotor setup was mounted with the rotor axes horizontal because it was impossible to operate them out of ground effect within the laboratory. In configuration 1 (Figure 4.6), rotors were mounted one above the other and placed 11 meters (26R) away from the wall in the downwash direction. The nearest wall was in the upwash direction, 2.5 meters (5.6R) away.

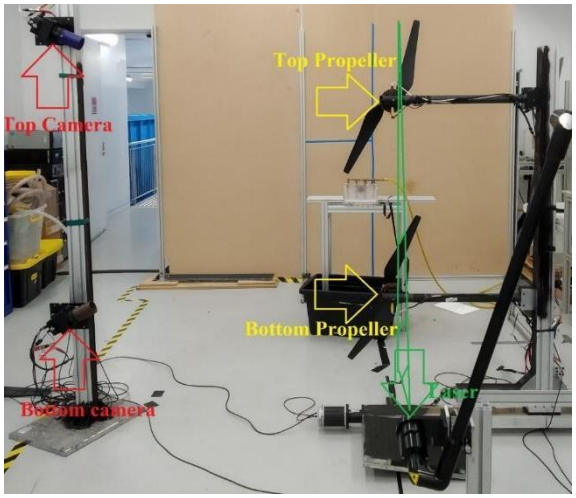

Figure 4.6 DJI E7000 laboratory setup, configuration 1.

The entire region in which upwash existed was captured in configuration 1 at the rotational positions where the rotor tips were in the closest approach to each other. The rotor system was traversed in the +-Z direction with an increment of 5mm. The velocity fields were interpolated between the imaged planes using the inverse-distance weighted interpolation method (Section 2.1.7).

In configuration 2, the rotors were mounted side by side (Figure 4.7) and were placed 12 m (28.6R) away from the nearest wall in the downwash direction.

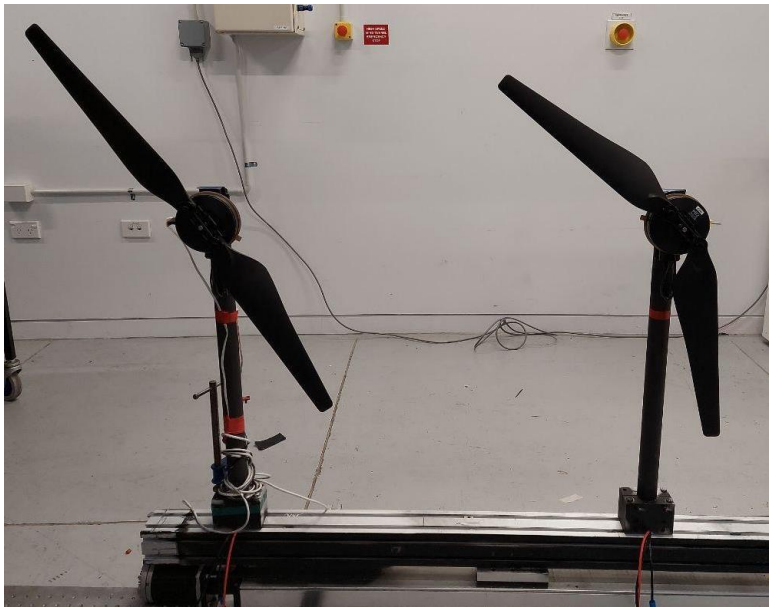

Figure 4.7 DJI E7000 laboratory setup, configuration 2.

The DJI E7000 rotors were tested at 1740 rpm, as used during hover of the DJI AGRAS T16 multicopter without payload. Additional data were obtained at 2150 RPM. The tip spacing was 86mm (0.2R).

Several rotor angular positions in relation to each other were tested in configuration 2. There were characterized by the α and β angles (Figure 4.8, Table 4.1). The rotor system was mounted on the traverse, and additional data with Z=+-80mm (Z/R=+- 0.19) were collected.

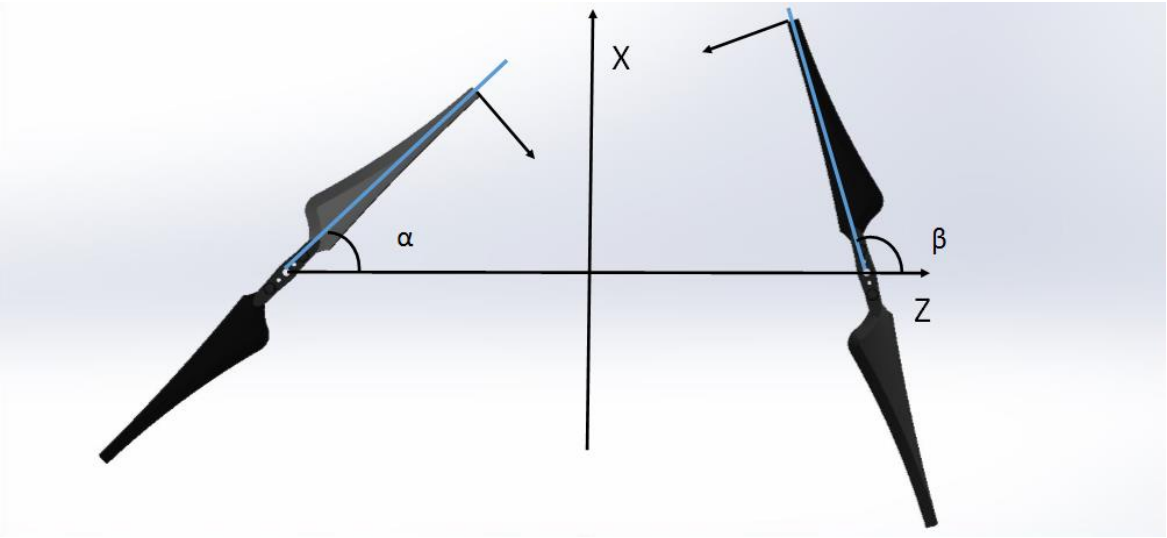

Figure 4.8 Definition of α and β angles.

Table 4.1 α and β angles phase angles captured in experiments.

α (deg)	0											
β (deg)	0	15	30	45	60	75	90	105	120	135	150	165
α (deg)	45											
β (deg)	0	15	30	45	60	75	90	105	120	135	150	165
α (deg)	90											
β (deg)	0	15	30	45	60	75	90	105	120	135	150	165
α (deg)	135											
β (deg)	0	15	30	45	60	75	90	105	120	135	150	165

4.1.2 Results

4.1.2.1 Validity of the usage of two rotors

The result presented in Figure 4.9 (Top left and top right) is the iso-surface of velocity magnitude normalised by tip velocity for the tested rotational speed (5400 rpm, 71.4 m/s). Figure 4.9 (Bottom left and bottom right) shows the Z/R-X/R plane when Y/R=-1.2.

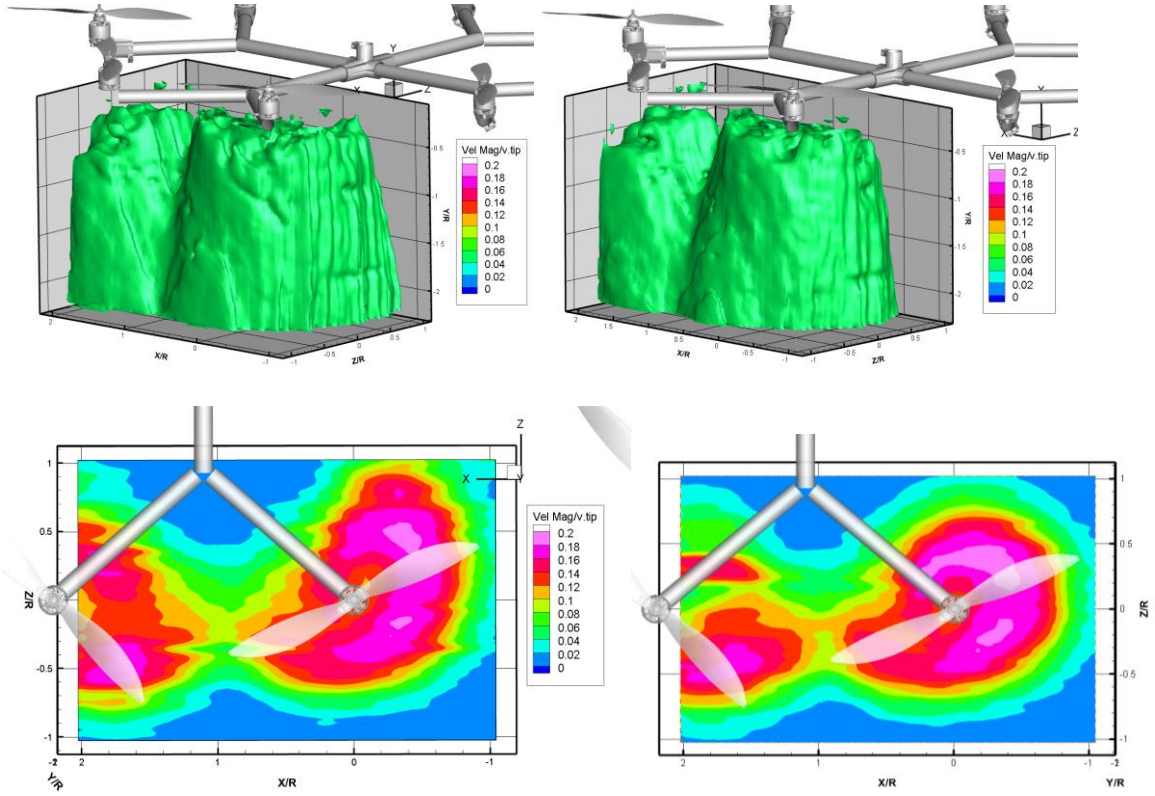

Figure 4.9 The isosurface of velocity magnitude normalised by tip velocity (vel mag/v.tip=0.06) of multicopter wake: with four rotors rotating (top left), and with two rotors rotating (top right). The slice X/R-Z/R plane with Y/R=-1.2 contoured by velocity magnitude normalised by rotor tip velocity: with four rotors rotating (bottom left), and with two rotors rotating (bottom right).

The qualitative comparison between four-rotor and two-rotor tests found that there are no significant differences in captured velocity magnitude and spatial extent of the wake velocity, except in the region where the downwash of rotors 3 and 4 influenced the downwash from rotors 1 and rotor 2. The downwash from rotors 1 and 2 merged with the downwash from rotors 3 and 4. This effect is observed in Figure 4.9 (bottom left and right), where the downwash from rotors 1 and 2 elongated towards rotors 3 and 4 (+Z/R).

Quantitative analysis was performed by using the magnitude similarity index (Hu et al., 2015)

$$MSI = 1 - \frac{\sqrt{(U_2-U_4)^2+(V_2-V_4)^2+(W_2-W_4)^2}}{V_{2.mag}+V_{4.mag}} \qquad \text{(Equation 4.1)}$$

where U_2, V_2, W_2 is velocity vector component in 2-rotor experiment,

U_4, V_4, W_4 is velocity vector component in 4 rotor experiment,

$V_{2.mag}$ is velocity magnitude in a two-rotor experiment,

$V_{4.mag}$ is the velocity magnitude in four rotor experiments.

MSI takes a value between 0 and 1 where 1 corresponds to a best fit. Figure 4.10 presents the MSI calculated in Equation 4 on planes Z/R-Y/R when X/R=-0.67 and when X/R=1.5.

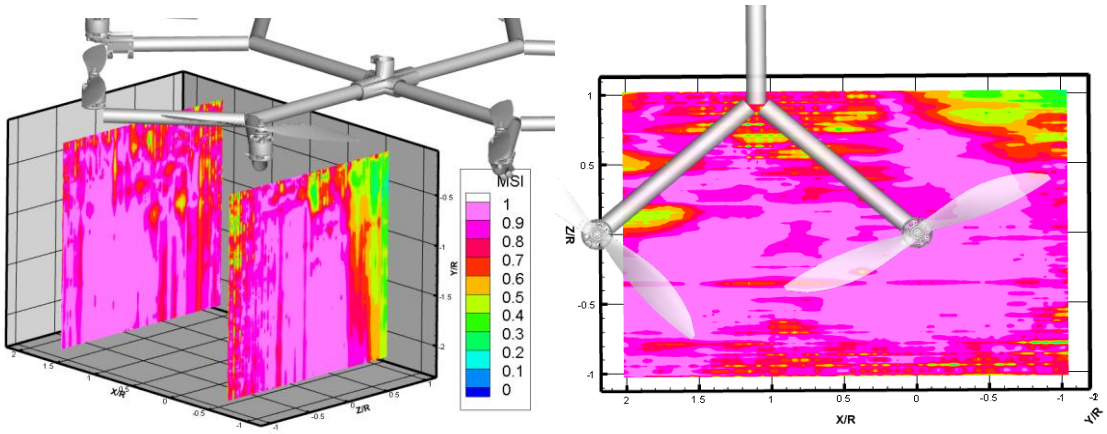

Figure 4.10 The CAD model of multicopter with MSI contour plot: left) Vertical (Z/R-Y/R) planes at X/R=-0.67 and X/R=1.5; right) Horizontal (X/R-Z/R) slice plane at Y/R=-1.2.

The MSI is less than 0.4 in the zone of 3rd and 4th rotor influence. The MSI under the rotor 1 and 2 is larger than 0.9. Zones under the rotor with a ratio less than 0.4 is the noise that is coming from irregular flow created by mounting tubes.

In a hovering flight, the velocity field of two rotors is a valid representation of a multicopter. A study of interaction effects between rotors can be performed using two rotors. The 3rd and

4th rotors don't alter the flow between the 1st and 2nd rotors. This simplification is valid for PIV analysis with phase-locked rotors.

In a flight with lateral velocity, two-rotor simplification is also valid. However, due to additional effects of interaction between lateral velocity and rotor wake, several rotor positions relative to the lateral velocity direction must be analysed.

4.1.2.2 APC 1045

As described in the literature review, the rotor wake consists of downwash, tangential (swirl) velocity and radial velocity. Two adjacent rotors have similar flow structures. However, the direction of streamlines of the wake of two adjacent rotors are tilted towards each other. In Figure 4.11 the tip separation is 0.2R (left), 0.45R (centre) and 0.55R (right). The plane Y/R-Z/R passes through the shafts of two rotors (X/R=0). The streamlines are coloured by velocity magnitude normalised by tip speed.

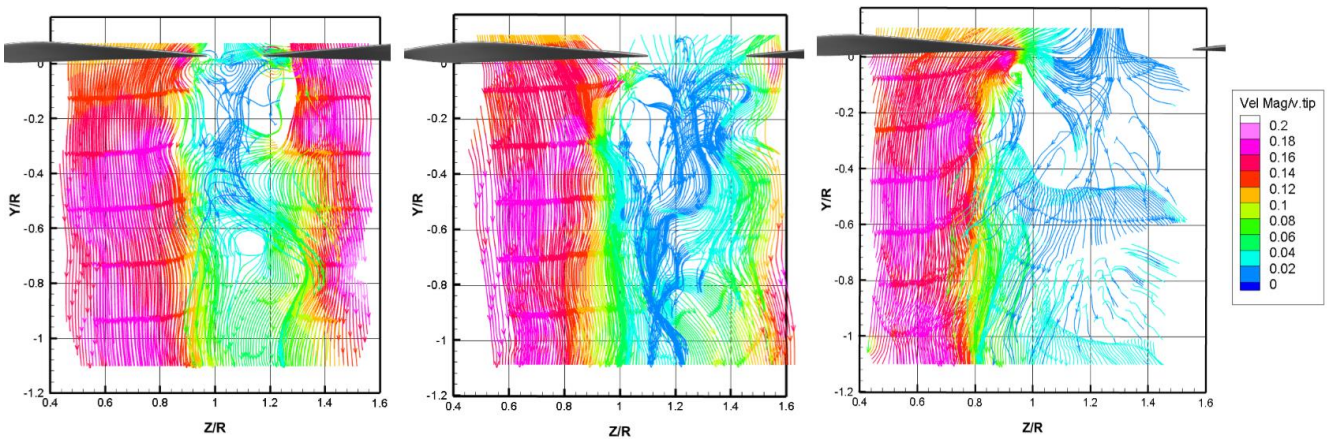

Figure 4.11 Streamlines of APC1045 rotor wake coloured by velocity magnitude normalised by rotor tip velocity on the Y/R-Z/R plane passing through the shafts of two rotors (X/R=0) when the shortest distance between rotor arcs normalised by rotor radius is: 0.2R (left); 0.45R (middle); 0.55R (right).

The tilt angle of the streamlines to the Y/R axis decreases with increasing tip separation. It is equal to 4° approximately when the tip separation is 0.2R and 1.5° when tip separation is 0.45R.

When the distance between rotor tips is 0.55R, the tilt of the downwash is not observed and wake from a rotor under the influence of an adjacent rotor is similar to the wake from an isolated rotor. However, outside the wake, there is a difference between the flow field of an isolated rotor and of two adjacent rotors at 0.55R separation. The streamlines outside the wake of an isolated rotor point towards the centre of the rotor. However, the streamlines between adjacent rotors point to the plane passing through the rotor shafts.

Tilted wakes will eventually merge. The criteria used here for the merging of two downwashes is an absence of the low-velocity region between rotors. Figure 4.12 represents the vertical plane Y/R-Z/R passing through the rotor shafts (X/R=0). Figure 4.12 is the composition of three vector fields that were stitched together by inverse-distance weighted interpolation (section 2.1.7). The streamlines are coloured by velocity magnitude normalised by tip speed. The increased extent of the velocity vector field was obtained by traversing the PIV setup vertically down in -Y/R direction.

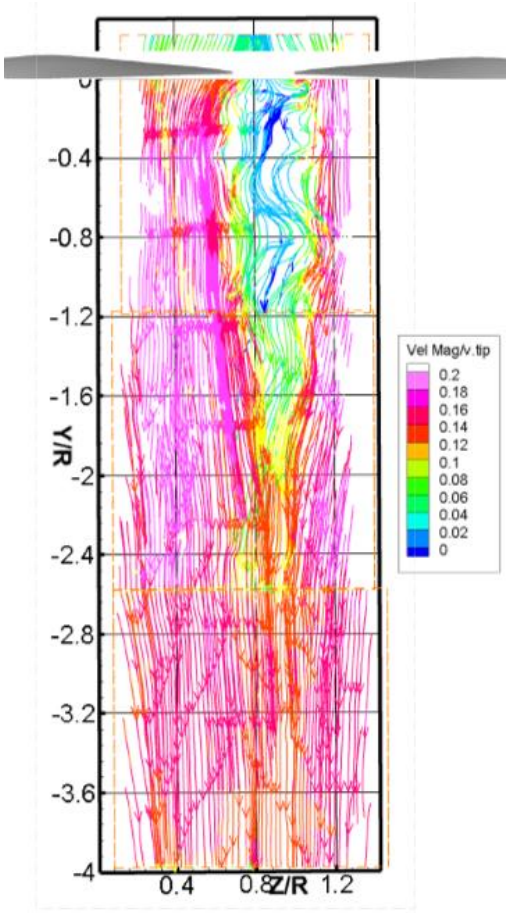

Figure 4.12 Streamlines of APC 1045 rotor wake coloured by velocity magnitude normalised by rotor tip velocity on the Y/R-Z/R plane passing through the shafts of two rotors (X/R=0), when the shortest distance between rotor arcs normalised by rotor radius is 0.2R.

Outside the wake and zone of interaction, the vortices are close enough that a region of upwash velocity is generated. This effect is important for spray application and hence is discussed further in section 4.1.2.4.

4.1.2.3 DJI E7000

The DJI E7000 system is significantly larger than the APC 1045; therefore, the relative dimensions of the captured data are smaller within the field of view of the camera. Figure 4.13 demonstrates the downwash of the DJI E7000 rotor affected by adjacent counter-rotating wake.

The streamlines on a plane (Y/R-Z/R) passing through the shafts of both rotors (X/R=0) are coloured by velocity magnitude normalised by rotor tip velocity.

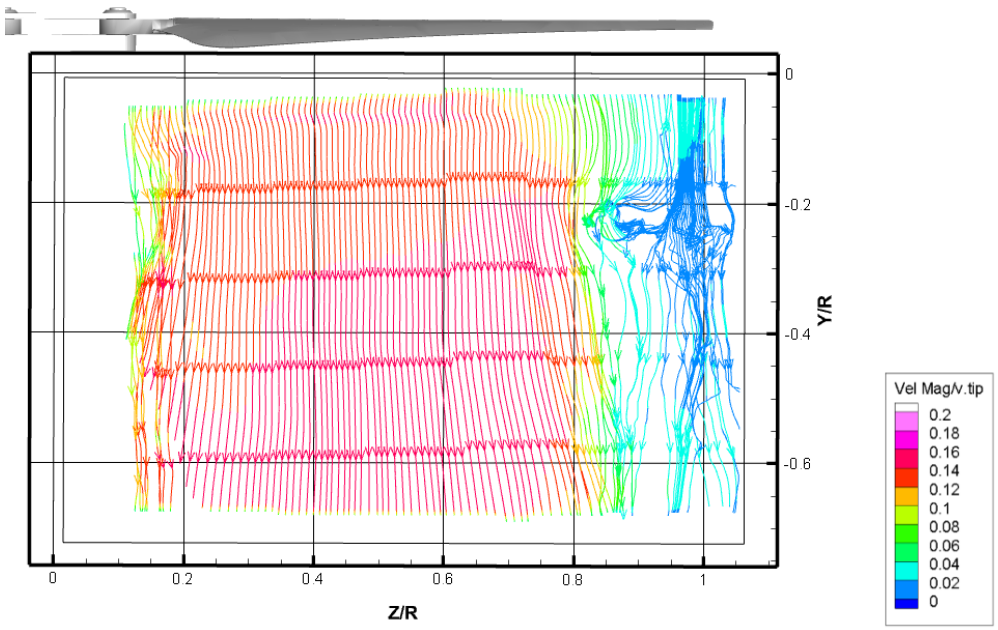

Figure 4.13 Streamlines of DJI E7000 rotor wake coloured by velocity magnitude normalised by rotor tip velocity on the Y/R-Z/R plane (X/R=0) when the shortest distance between rotor arcs normalised by rotor radius is 0.2R.

The high speed (red-purple) regions are the downwash of the two rotors. The downwash from one tilt towards the downwash of the other at an angle of approximately 4°. The merge region was not captured in these experiments due to the large distance to this point. The effect is similar to the effect observed in APC 1045 rotors.

4.1.2.4 The upward velocity region

During experimental analysis, it was noticed that two interacting wakes generate the region of upward velocity. For the upward velocity region observation, the coordinate system was changed. The new origin was placed between the rotors on the plane in which both rotors spin (Figure 4.14)

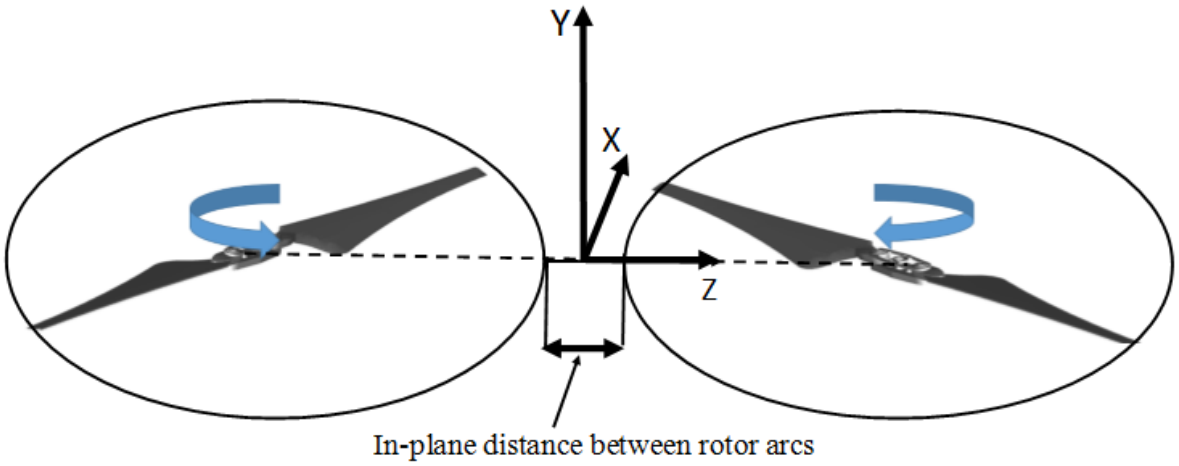

Figure 4.14 Coordinate system of two counter-rotating rotors for upward velocity region observation

It was supposed that the upward velocity was mainly generated by interacting tip vortices. The schematic of upward velocity region generation is presented in Figure 4.15.

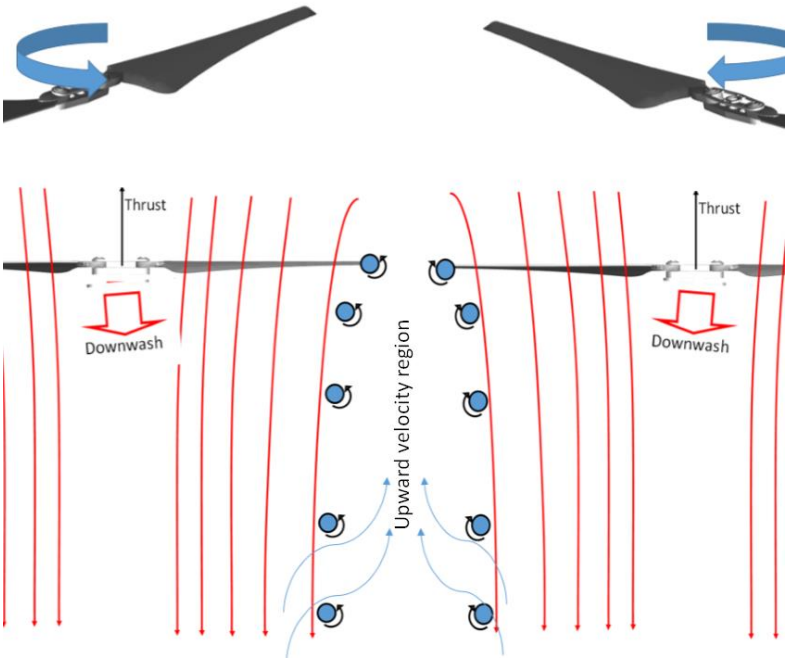

Figure 4.15 A schematic of upward velocity region generation

The velocity field of the APC 1045 and DJI E7000 rotors with a 0.2R rotor arc separation and both rotors at closest approach (α=β=0º) is shown in Figure 4.16. The iso-surface is the upward velocity equal to 0.02 (v=1.5 m/s). The colour contours show the velocity magnitude.

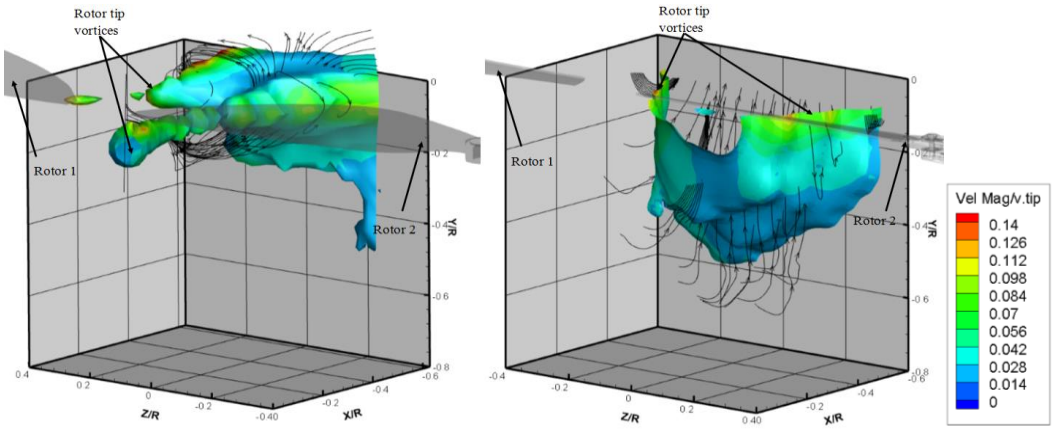

Figure 4.16 Upwash velocity (V, m/s) isosurface +1.5 m/s (left: DJI E7000 rotors; right: APC 1045 rotors).

Both rotors generate upward velocity between the rotor arcs. The difference between DJI and APC velocity fields may be explained by the different geometry of the rotors (e.g pitch, rotor blade twist, blade tips). The maximum upward velocity magnitude is greater for the DJI E7000 rotor (absolute value and normalised by tip speed). In both DJI E7000 and APC 1045 rotors, the maximum upward velocity magnitude is observed near the rotor tip vortices.

4.1.2.5 The spatial extent of the upward velocity region

4.1.2.5.1 APC 1045

In Figure 4.17, the plane Y/R-Z/R is sliced at X/R=0.5. The contour colour scheme shows the normalised magnitude of the vertical (V), m/s component of velocity.

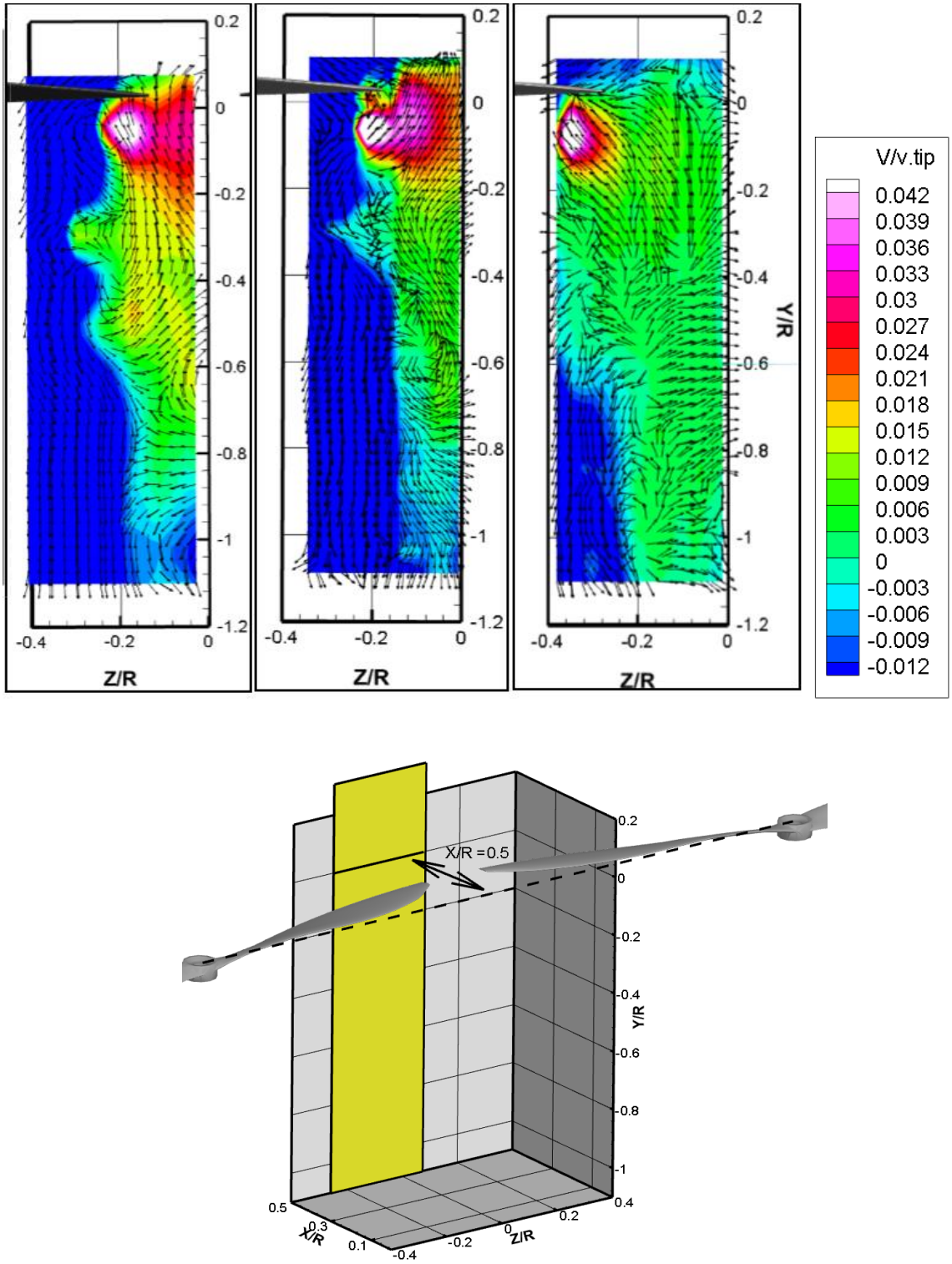

Figure 4.17 APC 1045 vertical velocity (V, m/s) contour plot in Z/R-Y/R plane when X/R=0.5 (left: 0.2R tip arc distance; central: 0.36R tip arc distance, right: 0.55R tip arc distance); bottom image: isometric view with CAD model of rotors and slicing plane

The upwash velocity is generated in the zone between the rotors. The vertical extent of the upward velocity region increases as the distance between the rotors increases: the extent of the upward velocity region in the Y/R (vertical) direction is equal to -0.7R, -0.8R and -1R at 0.2R, 0.36R and 0.55R tip arc distances, respectively. The region of upwash occupies the space between adjacent rotor wakes (blue contour in Figure 4.17).

4.1.2.5.2 DJI E 7000

Processing several parallel planes in configuration 1 (rotors mounted one above the other) of DJI E7000 rotors showed the symmetry of the upward velocity region around plane X/R-Y/R when Z/R=0. Figure 4.18 (top) is the plane Y/R-Z/R sliced at X/R=0.5. Figure 4.18 (bottom) is the plane X/R-Z/R sliced at Y/R=0.1. The colour contours show the magnitude of the vertical (V), m/s component of velocity. The rotors and slicing planes are shown on the right of Figure 4.18. The maximum upward velocity component V, m/s, is greater than 0.04 near the tip vortex.

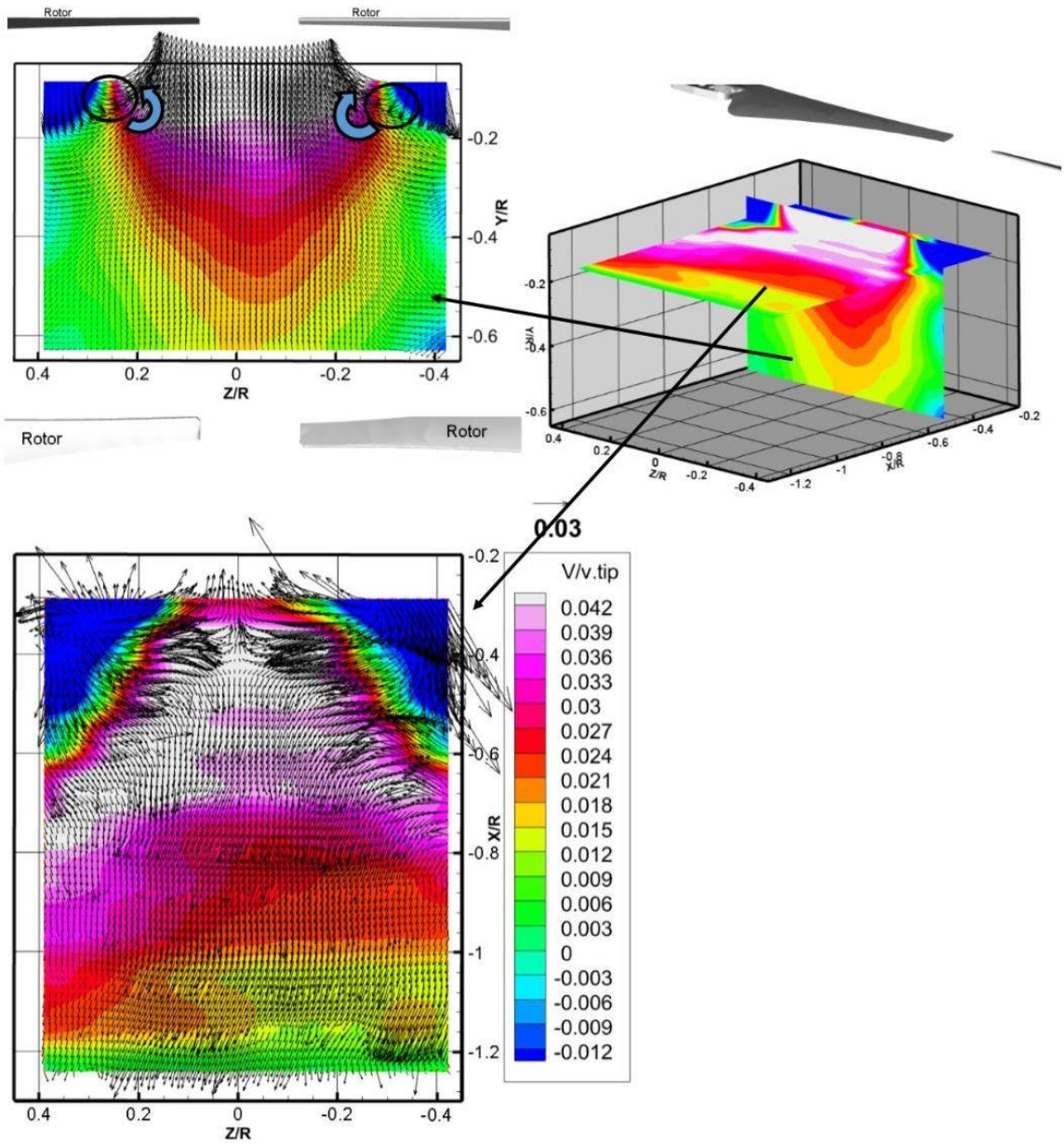

Figure 4.18 DJI E7000 rotors with 0.2R tip separation upwash velocity contour plot (V, m/s) at the top: Z/R-Y/R plane at X/R=0.5 with a highlighted position of vortex rings emitted from the tip of the rotor, bottom: X/R-Z/R plane at X/R=0.1; right image: isometric view with CAD model of rotors and slicing plane

The position and direction of rotation of tip vortices was marked in Figure 4.18. The vorticity vector field defined the position of vortices (Figure 4.19). They are situated at the peak of the vorticity field.

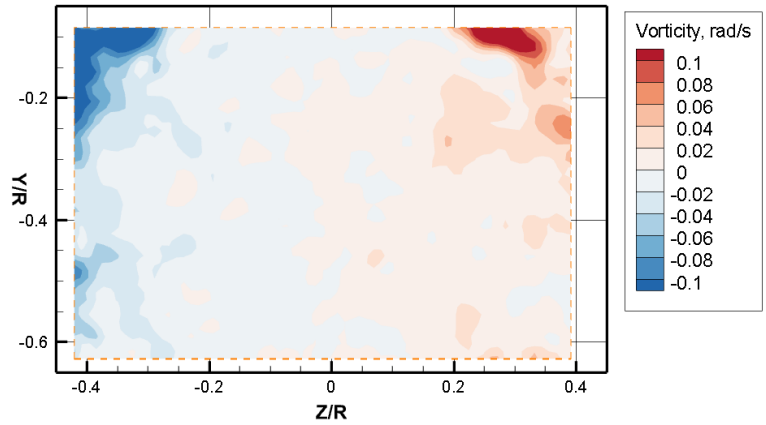

Figure 4.19 Contour plot of vorticity of Z/R-Y/R plane at X/R=0.5

The greatest upward velocity magnitude was observed under the rotor tip, where the vortex has had little time to expand or decay (recorded in configuration 2). For example, in Figure 4.20: the left rotor blade (α) has advanced 45º past the plane passing through both rotor axis 45˚ ago, but the right blade (β) has advanced 135º past the same plane 135˚ ago. The position of the rotors and data planes is shown in Figure 4.20. The position of the rotor on the CAD model represents the current position in the experiment. The maximum upward velocity equals 2.4 m/s under the left rotor and 1.8 m/s under the right rotor.

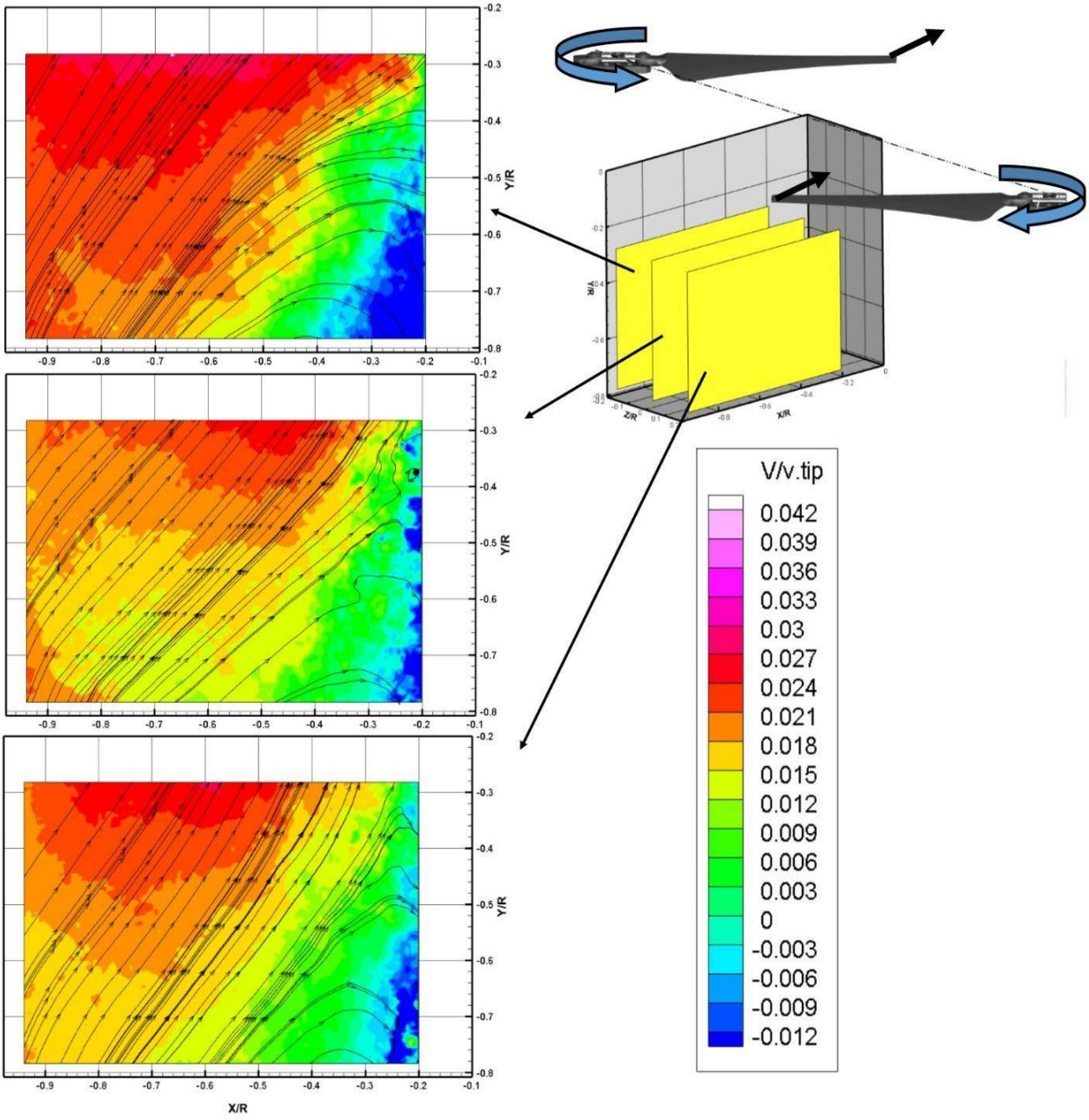

Figure 4.20 Upwash velocity contour plot (V, m/s) in X/R-Y/R plane when α=45˚, β=45˚. Left: Z/R=-0.19, centre: Z/R=0, right: Z/R=0.19. The yellow planes in the CAD model are the data planes.

4.1.2.5.3 The upward velocity region with different rotor angular positions

In Figure 4.21 (data collected in configuration 2), the V velocity ranges from -0.012 to 0.042.

The left rotor (on the image) rotates clockwise; the right rotor rotates anticlockwise.

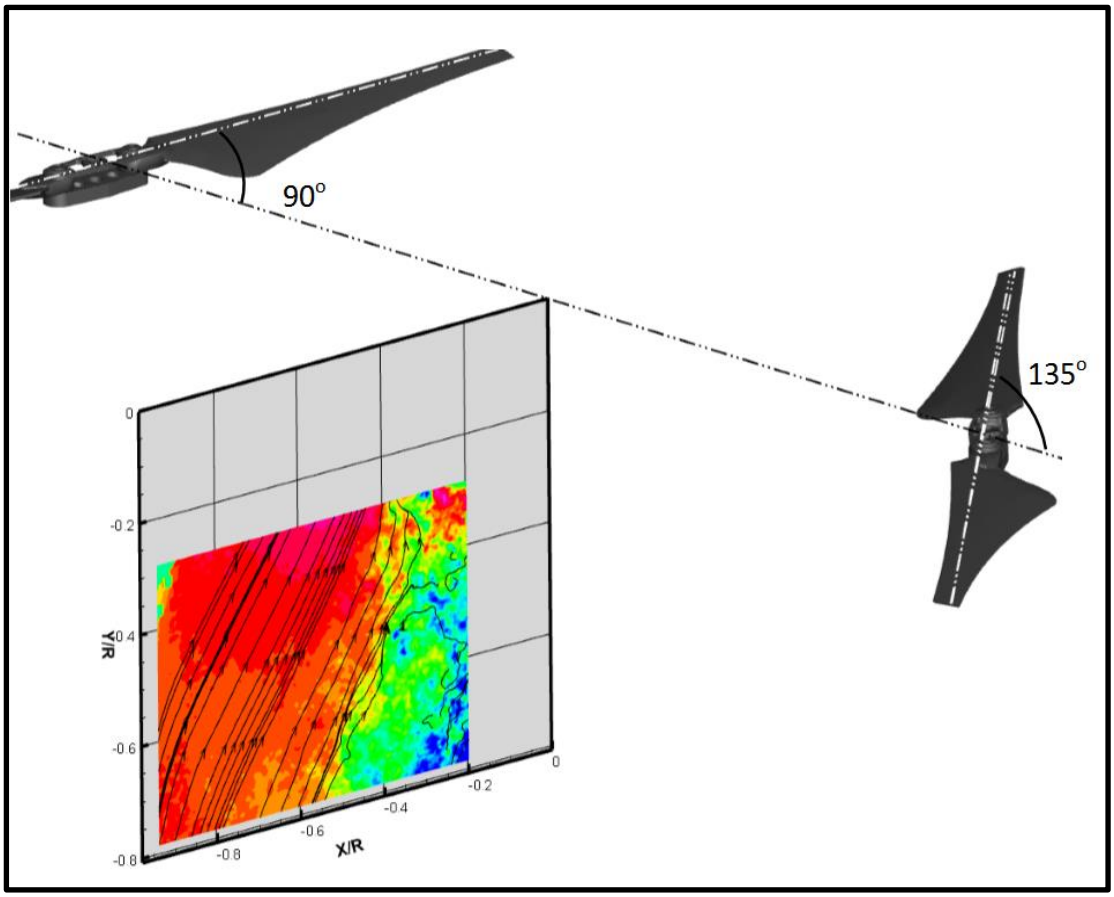
90°
135°
0
-0.2
-0.4
-0.6
-0.8
Y/R
X/R

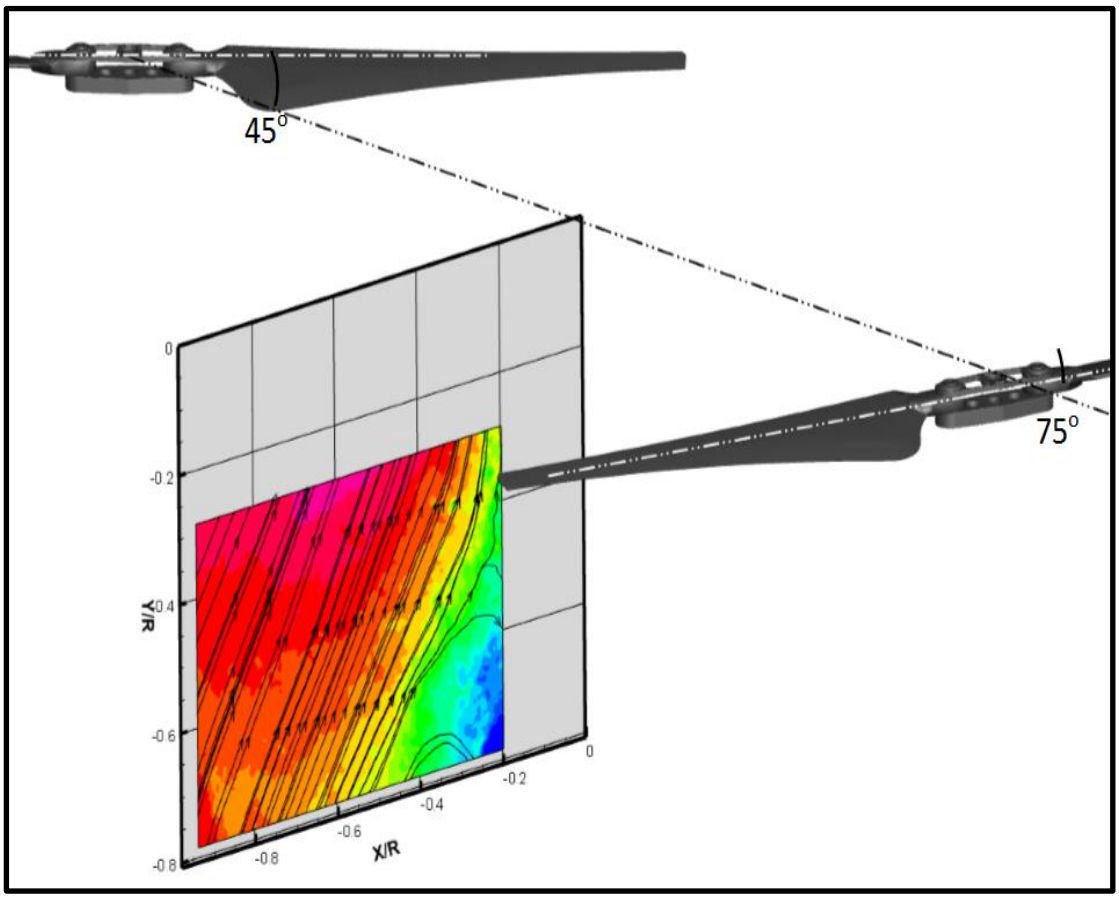
45°
75°
0
-0.2
-0.4
-0.6
-0.8
Y/R
X/R

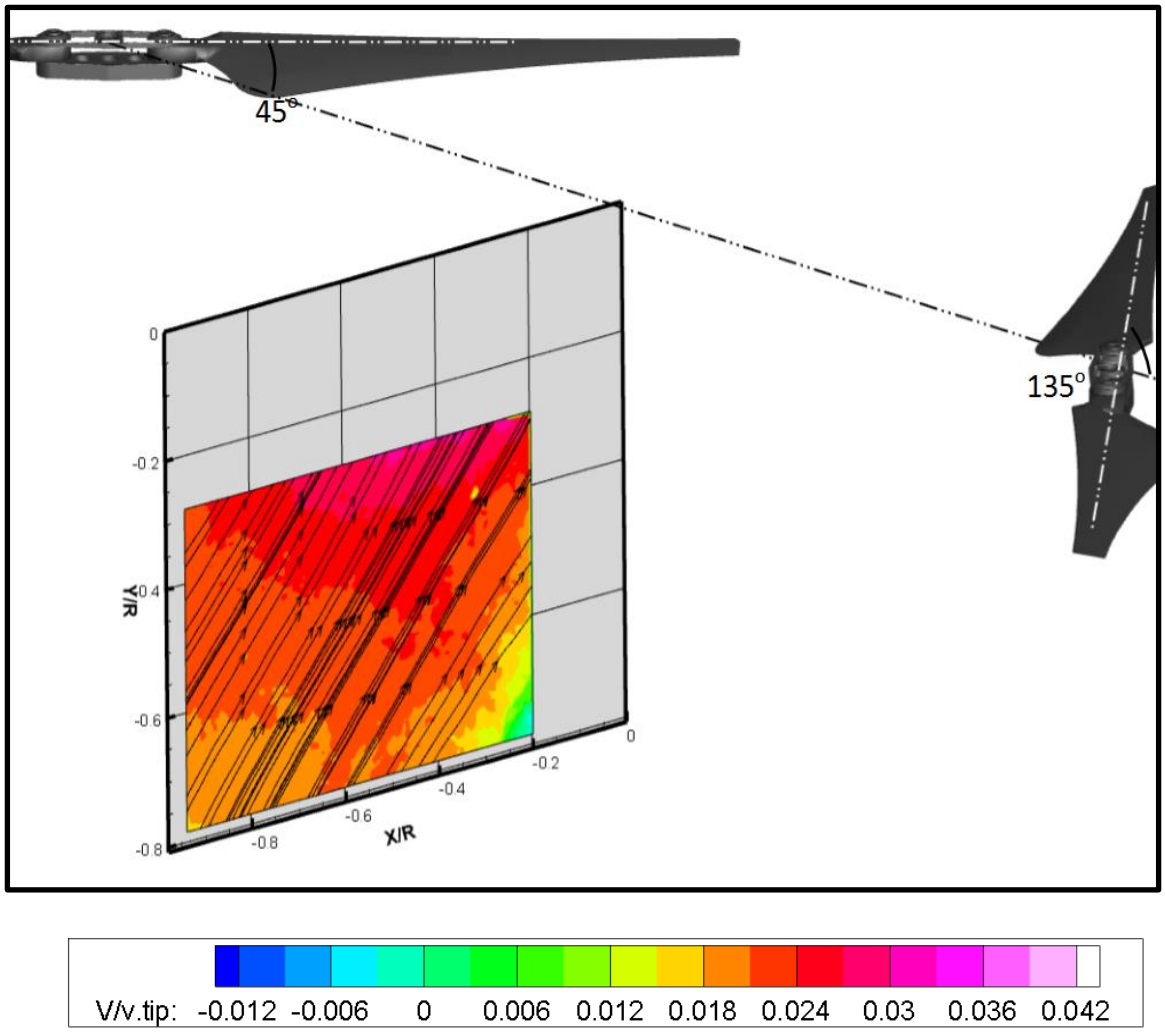

Figure 4.21 The upwash velocity contour plot (V, m/s) in X/R-Y/R plane when Z/R=0. Top: α=90˚, β=135˚; center: α=0˚, β=0˚; bottom: α=135˚, β=45˚. The CAD model shows the position on the rotor in the experiment and can be used for geometrical reference.

An upwash region between rotors was detected at every angular position of the rotor. The upward velocity (V) magnitude depends on the angular position of the rotor. To understand the relationship between upwards velocity and angular position, the *maximum* upward velocity was measured in each experiment. The data is grouped by phase lag. The phase lag was determined as the smallest positive angle between blades of counter-rotating blades (α+β if α+β<90˚ or 180˚-(α+β) if α+β>90˚). The mean and standard deviation of maximum velocity are depicted in Figure 4.22 (error bars are one standard deviation of mean).

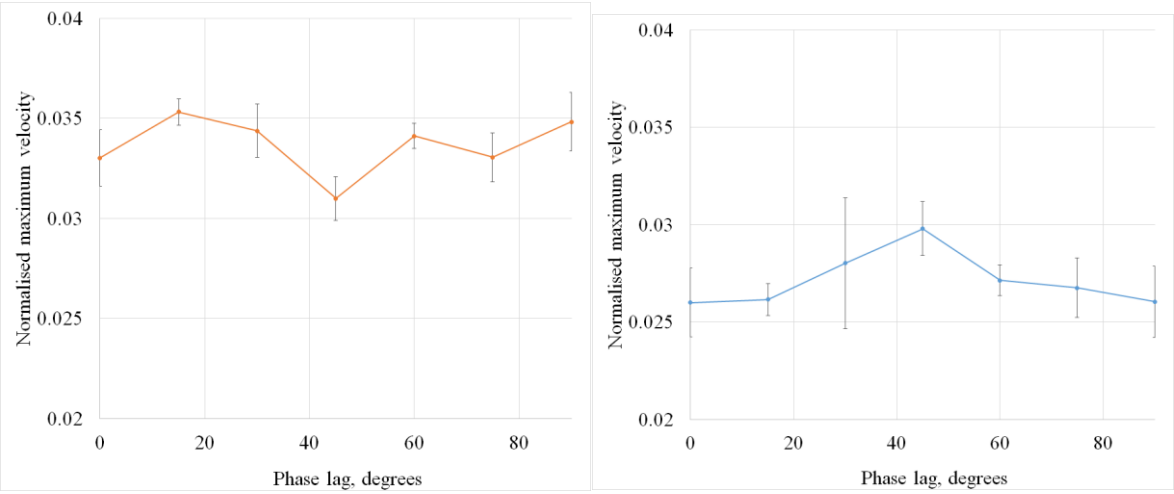

Figure 4.22 Normalised maximum velocity in the field of view depending on phase difference in degrees, when either: (left plot): one rotor is in closest approach to the neighbouring rotor's arc (α or β=0˚), or (right plot): neither rotor is in closest approach to the neighbouring rotor's arc (α and β ≠0˚)

The greatest upward velocity magnitude was observed when one of the rotors was at the closest approach to the neighbouring rotor's arc (α or β=0˚). In all other cases (α or β≠0˚), the maximum upward velocity was observed when the phase difference between the rotors was 45˚.

4.1.2.5.4 The upward velocity region at different rotational speeds

In Figure 4.23, the upward velocity region, V, m/s, at plane X/R-Y/R sliced at Z/R=0 is shown in two different rotor positions for two different rotational speeds (standard operational rotational speed range): 2150 rpm (M=0.278, M is Mach number, Chapter 3, Equation 3.3) and 1740 rpm (M=0.225). These positions were chosen as they represent the extreme cases of upward velocity.

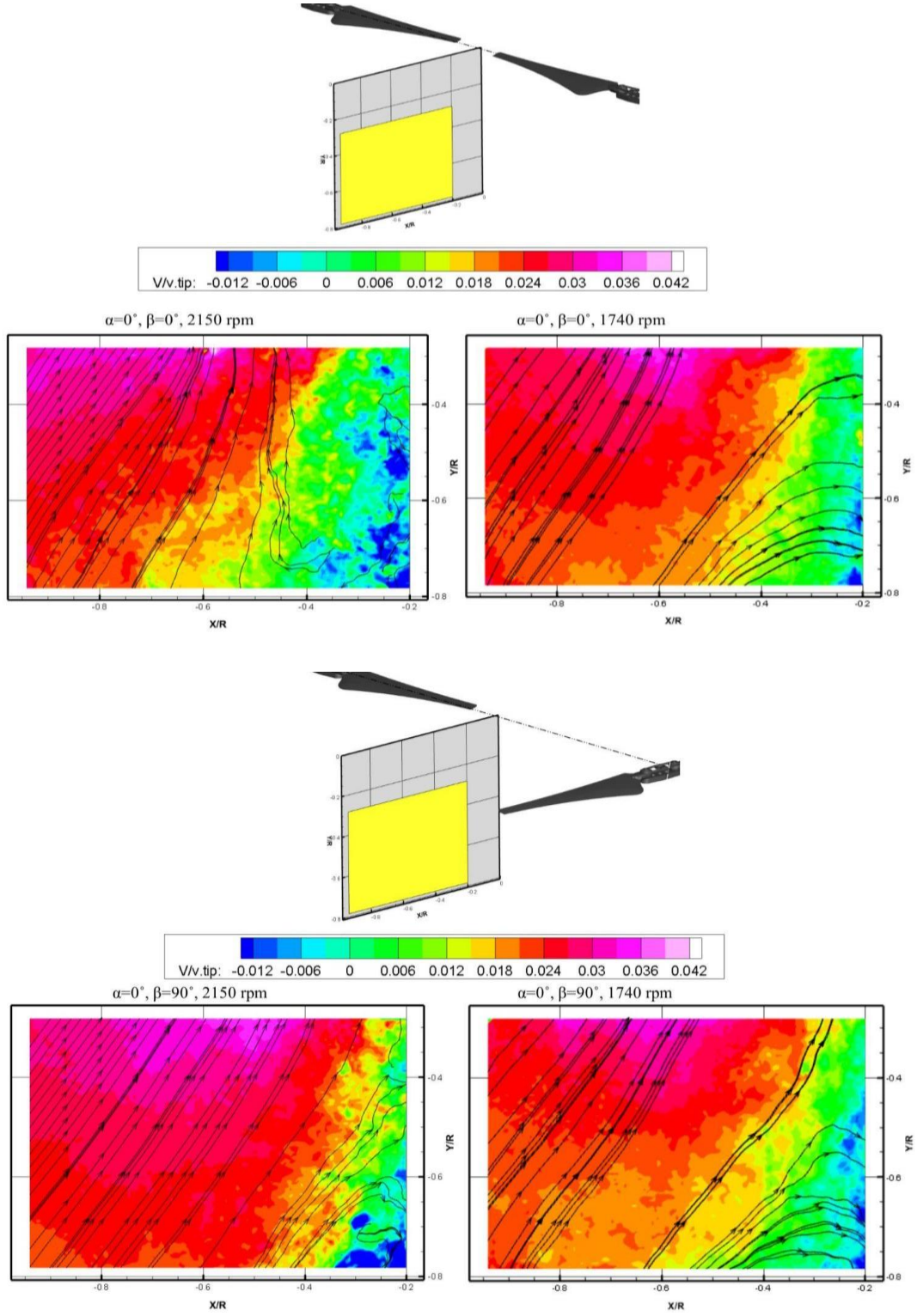

Figure 4.23 Upwash velocity (V, m/s) at X/R-Y/R plane when Z/R=0. Top left: α=0°, β=0°, 2150 rpm (M=0.278), top right: α=0°, β=0, 1740 rpm (M=0.225), bottom left: α=0°, β=90°, 2150 rpm (M=0.278), bottom right: α=0° β=90° 1740 rpm (M=0.225). The CAD model shows the position of rotors in the experiment.

From the experimental data above, the velocity magnitude has no relationship or a weak relationship with rotational speed (from 1740 rpm (M=0.225) to 2150 rpm (M=0.278), which is the standard operational rotational speed range.

4.1.3 Uncertainty in PIV measurement

The uncertainty in velocity values was determined using the peak to noise ratio method, which assumes that error in pixel displacement follows a Gaussian distribution (INSIGHT 4G™ user's guide (2015)). Uncertainty is evaluated for a single position of the traverse for each experiment. This uncertainty was expressed as velocity magnitude and recalculated to the percentage of velocity magnitude obtained from an experiment. There is little dependence on wake velocity. Figure 4.24 represents the experiment with 0.55R tip spacing. The position of the traverse is 0.23R away from the rotor hub (30mm) in Z/R direction. The Δt was equal to 40 microseconds.

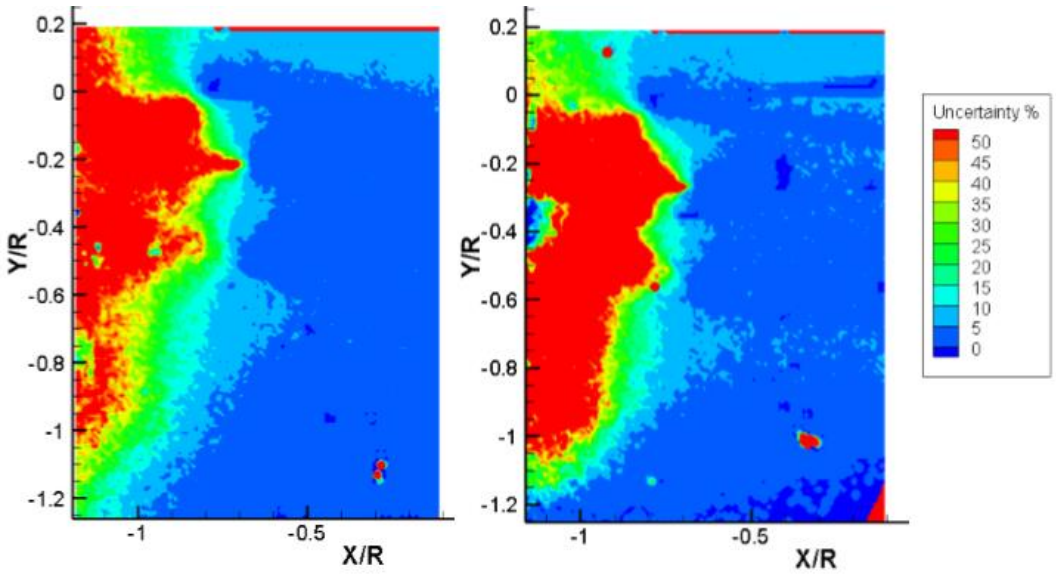

Figure 4.24 Uncertainty of velocity magnitude measurement for left and right camera X/R-Y/R at Z/R=0.23R, APC 1045, 0.55R spacing. Colour bars run from 0 to 50%.

The ratio of standard uncertainty to mean was < 8% in the rotor wake but exceeded 50% outside the wake due to very small mean velocities. The PIV experiment was tuned to evaluate the main downwash velocity (10-20 m/s), thus there is close to zero pixel displacement of the particles when velocity is close to 0 m/s.

Figure 4.25 represents the uncertainty for experiments in the zone of upward velocity of DJI E7000 rotors. As described above, the main focus of these experiments was the wake of the rotor. This meant the PIV system was tuned (by choice of Δt) for a high-velocity region, resulting in a high level of relative uncertainty between rotors in the zone of upward velocity. The Δt was equal to 50 microseconds.

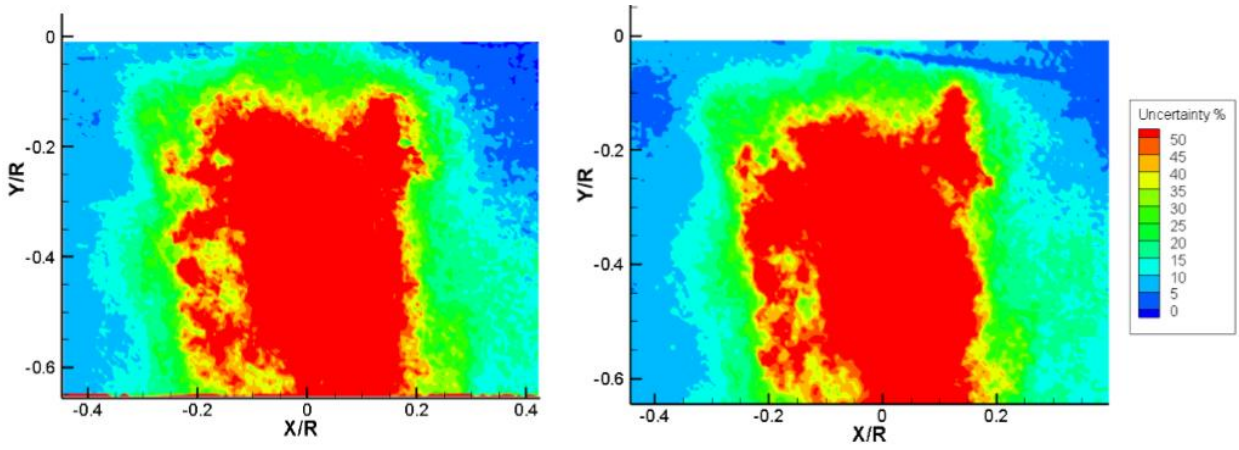

Figure 4.25 Uncertainty of velocity magnitude measurement for left and right camera X/R-Y/R at Z/R=0.5R, DJI E7000, 0.2R spacing. Colour bars run from 0 to 50%.

Unlike in the previous figure, the PIV was specifically tuned to capture the low upward velocity when acquiring the data shown in Figure 4.26. Thus, there is less than 20% uncertainty in 1-3.5 m/s velocity upward region and >50% in 0-1 m/s region (red contour). The Δt was equal to 90 microseconds.

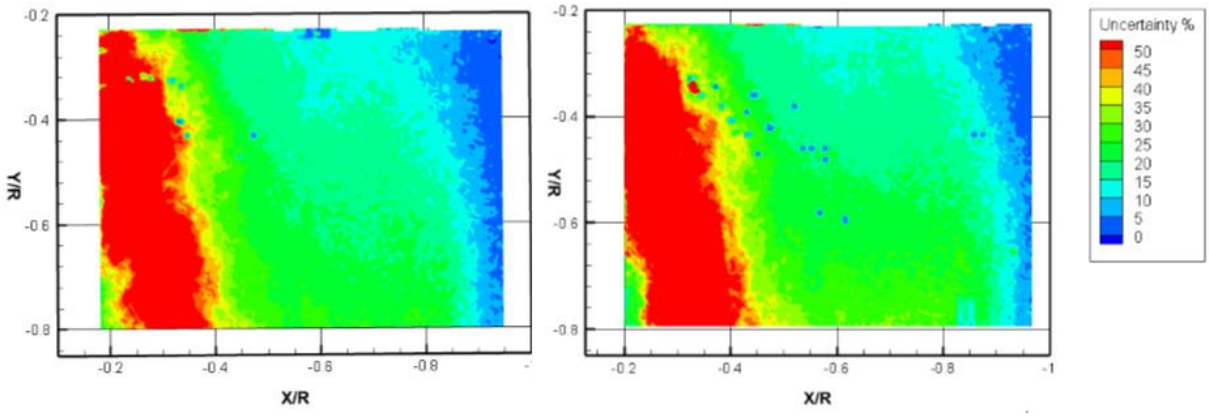

Figure 4.26 Uncertainty of velocity magnitude measurement for left and right camera X/R-Y/R at Z/R=0R (upward velocity region), DJI E7000, 0.2R spacing α=0˚, β=0˚. Colour bars run from 0 to 50%.

The level of uncertainties is acceptable in the region of interest. The effects, observed in the analysis, won't change within the uncertainty band for every condition tested.

4.2 Experimental evaluation of near field flowfield of two adjacent rotors flight with lateral velocity

4.2.1 Experimental setup

Spraying is usually performed with lateral velocity (either wind or forward velocity). Therefore, the lateral velocity should be added to the experimentation using a wind tunnel.

The multicopter was represented by a pair of rotors, spinning in opposite directions, sharing the same rotor plane. The APC 1045 rotors were arranged either: a) one downstream of the other ("arranged streamwise") or b) side by side ("arranged spanwise"). The horizontal distance between the rotor axes was varied. The University of Canterbury open-jet wind tunnel was

used to provide the lateral velocity that a multicopter experiences when flying horizontally. The tunnel jet is 1500 x 1500 mm in cross-section (Figure 4.27).

Figure 4.27 Wind tunnel setup. Two rotors (red arrows) in streamwise configuration. Labelled items are: rotors (red arrows), SPIV cameras and laser lens head (green arrows) and wind tunnel (blue arrow, pointing opposite to the direction of flow).

Flight speeds (wind tunnel jet speeds) tested were 2 m/s, 6 m/s, 10 m/s and 14 m/s. For efficient operation and control, multicopter spraying usually uses a flight speed ranging from 2-3.7 m/s (Lan et al., 2018).

PIV was used to obtain the velocity flow fields. The field of view was 428 x 296 mm (3.37Rx2.33R) with a pixel size of 167 microns.

The rotors were mounted on a ball-screw traverse and were traversed through the light sheet in a horizontal direction normal to the wind tunnel flow in 5mm increments (some data was acquired at 10mm increments). For each experiment, 62 to 75 planes were acquired. 3D fields were reconstructed in Tecplot Focus 2013 R1 using weighted inverse-distance interpolation to interpolate between planes.

4.2.2 Results

4.2.2.1 Rotors arranged streamwise

Reconstructed vector fields in the vertical plane passing through the rotor shafts (X/R- Y/R) at Z/R=0 show that the leeward downwash is shadowed by windward downwash and is tilted by 20 ^{o} to 25^{o} less than the downwash of the windward rotor. This is true for all flight speeds tested (Figure 4.28). At 14 m/s lateral velocity, the windward downwash is tilted by more than 45^{o} to the vertical, and the air in the bottom half of the figure is undisturbed by the rotors.

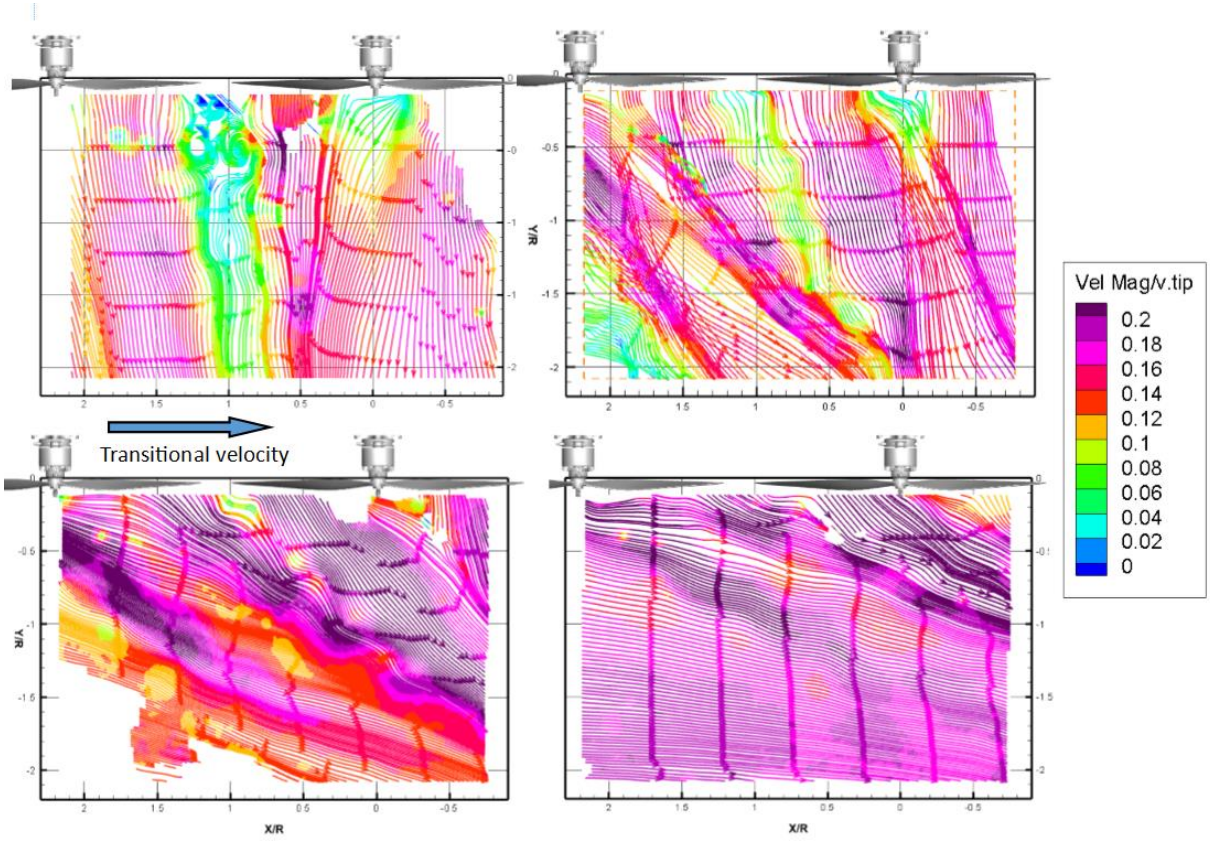

Figure 4.28 Velocity magnitude and streamlines on vertical planes through the axes of the rotors showing the tilt of the downwash of the front and rear rotors at flight speeds of 2 m/s (top left), 6 m/s (top right), 10 m/s (bottom left), and 14 m/s (bottom right). Rotor positions shown with CAD inserts above each plot.

When the lateral velocity is equal to 2 m/s, 6 m/s or 10 m/s the zone between rotors remains a slow speed zone as it is shadowed by the windward rotor. At 14 m/s lateral velocity, the slow speed zone between rotors wasn't observed.

Changes to the flow field as the distance between the rotor tip arcs is changed from 0.2R to 2.0R are shown in Figure 4.29. The plot plane is the vertical (X/R-Y/R) plane passing through Z/R=0 (the same plane as in Figure 4.28). The colour contour represents the velocity magnitude normalised by rotor tip velocity. The streamlines show the direction of the flow.

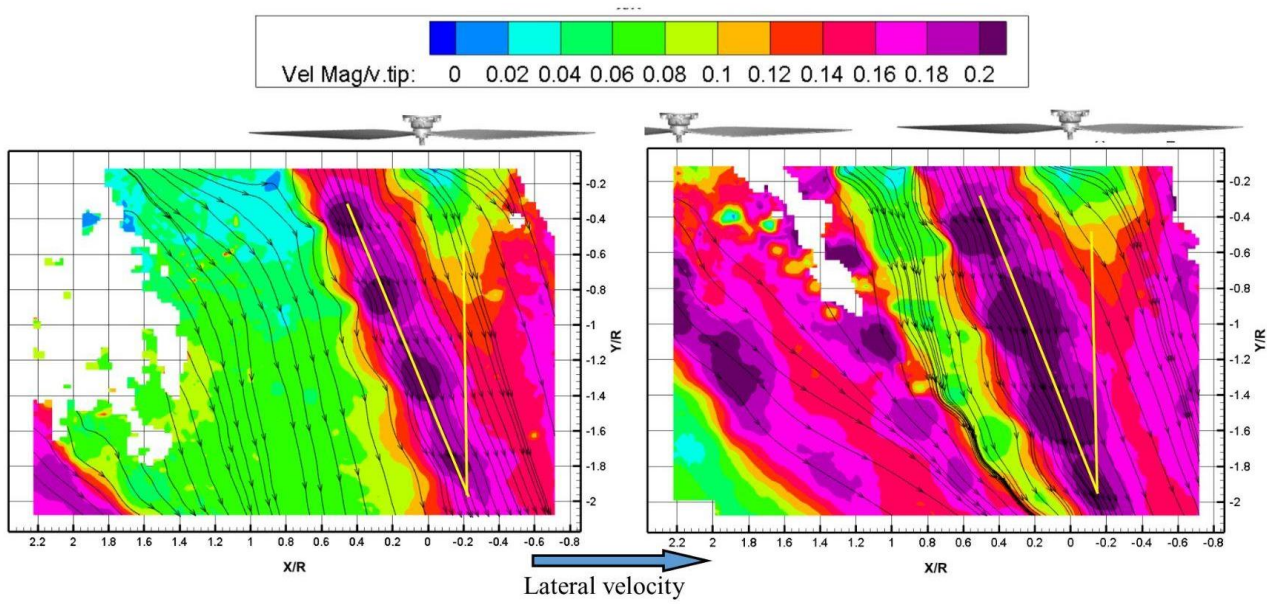

Figure 4.29 Velocity magnitude normalised by rotor tip velocity and streamlines on vertical planes through the axes of the rotors for different distances between rotor axes at a flight speed of 6 m/s; (left) distance equal to 2R between rotor tip arcs; (right) distance equal to 0.2R between rotor tip arcs. The yellow line indicates the angle of the rear rotor tilt relative to the vertical axis.

From Figure 4.29 the tilt of the rear rotor had no relationship or a weak relationship with rotor tip separation distance.

Horizontal planes X/R-Z/R through the SPIV data at Y/R=0.04 (left) and Y/R=1 (right) shows the downwash of the two rotors arranged streamwise in 6m/s lateral flow. The contour plot shows velocity magnitude normalised by tip velocity (Figure 4.30).

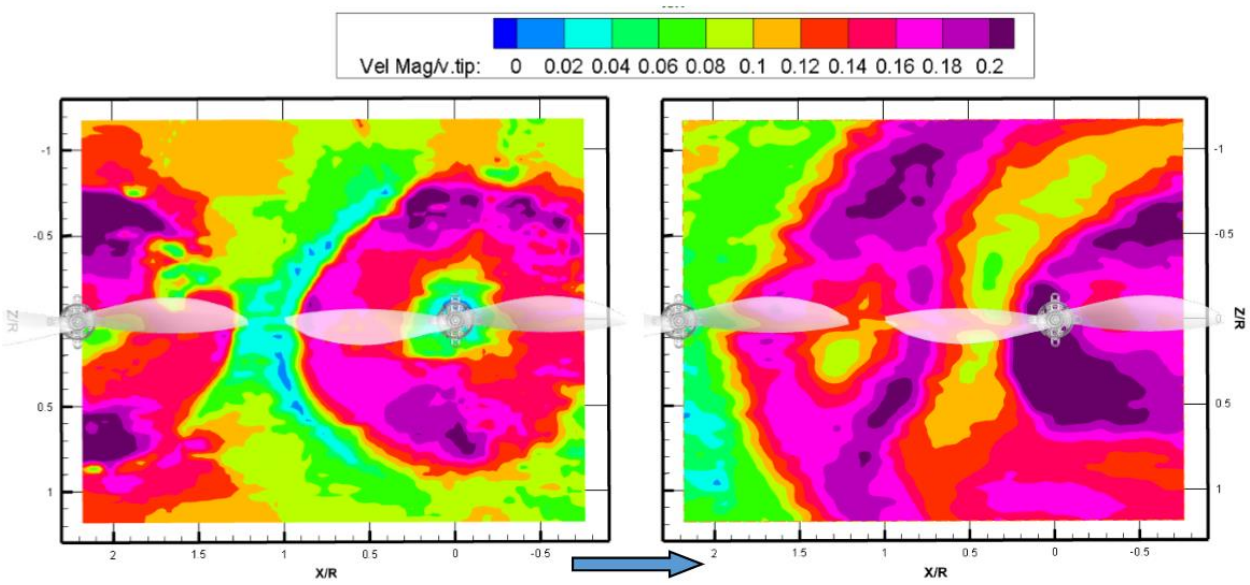

Figure 4.30 Velocity magnitude normalised by rotor tip velocity on horizontal planes below the rotor at flight speed of 6 m/s: (left) 0.04R below the rotor plane; (right) 1R below the rotor plane; distance equal to 0.2R between rotor tip arcs.

The lateral airflow deforms the downwash of the windward rotor into a horseshoe shape, whereas the downwash of the lee rotor remains circular. This is seen at lateral velocities from 6 m/s, up to the maximum tested velocity of 14 m/s.

There is a region of upward moving air created by the rotor tip, called the roll-up vortex. The effect is studied for helicopters and is present where the lateral velocity interacts with the tip vortex (Widnall et al., 1980; Joulain et al., 2017, Birch et al., 2003) (Figure 4.31). The pressure difference on the upper and lower rotor disk surface generates the vortex that is carried away by the lateral velocity.

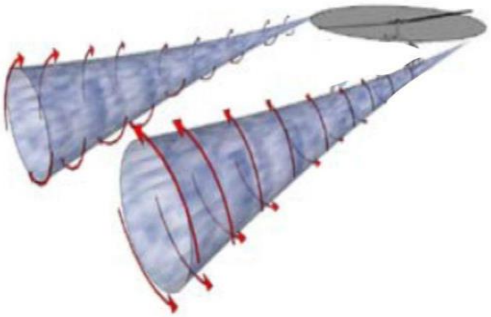

Figure 4.31 The roll-up vortex generated by tips of isolated rotor flying in lateral velocity conditions (Adapted from www.skybrary.aero, accessed 20.09.2021).

The rollup vortex appears at the side of the rotor disc; whereas the upwash region, described in section 4.1.2.4, is caused by the interaction of the tip vortices; and forms between rotor arcs (mostly with zero lateral velocity) (Figure 4.32).

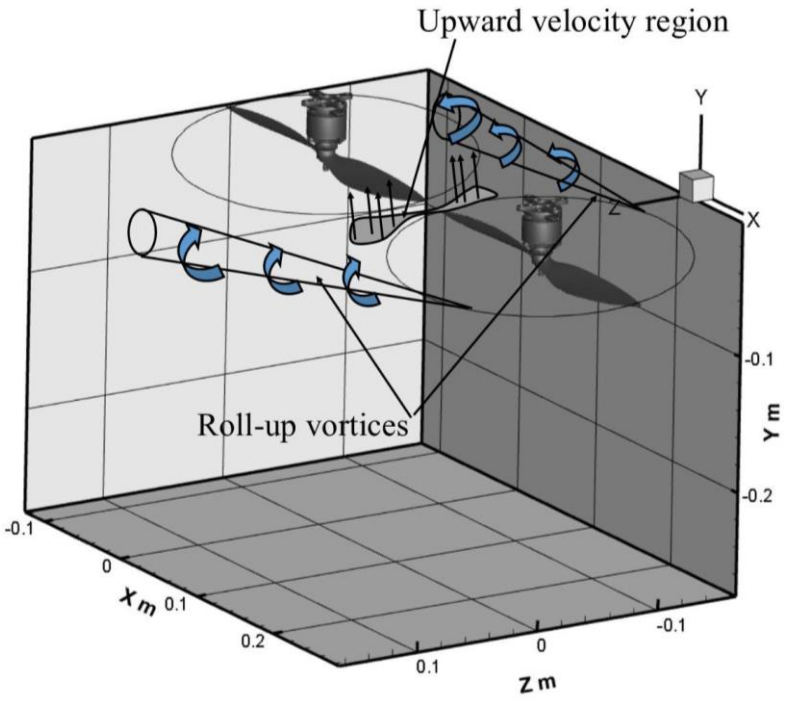

Figure 4.32 A schematic of roll-up vortex and upward velocity region positions.

At a flight speed of 6 m/s, this upward-moving region extends 1.2R below the rotor plane (Figure 4.33).

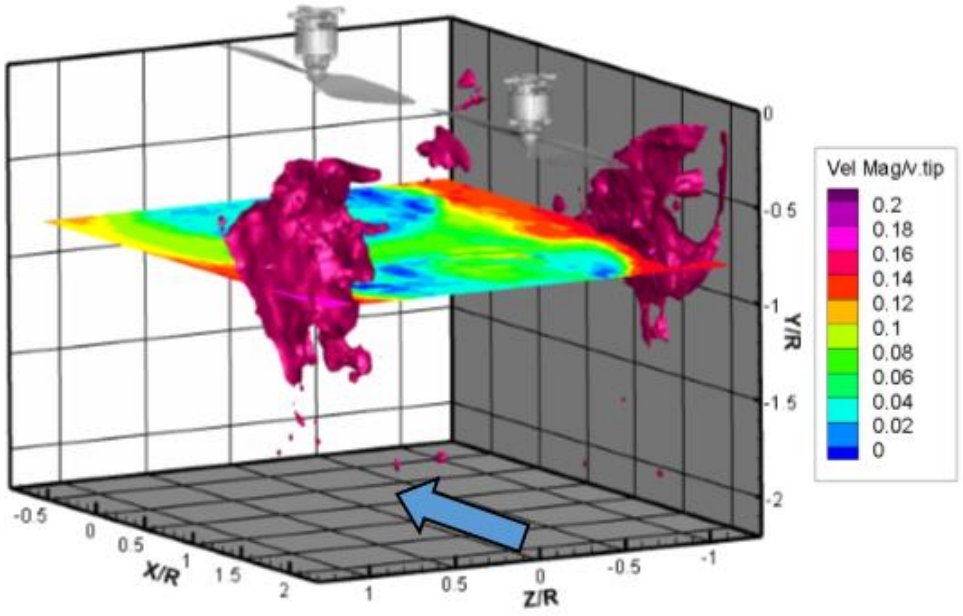

Figure 4.33 Isosurface of vertically upward air velocity V/v.tip=+0.024 at a flight speed of 6 m/s.

Previously, the leeward rotor has been observed to be shadowed by the windward rotor. The rollup vortex exists when two components are present in the flow: lateral velocity and tip vortex. The leeward rotor does not experience the lateral velocity, so there is no observation of the vortex of interaction on the leeward rotor.

The rollup vortex is also seen at 10 m/s lateral flow. It is shown by the iso-surface of $V/v_{tip}=+0.024$ (Figure 4.34).

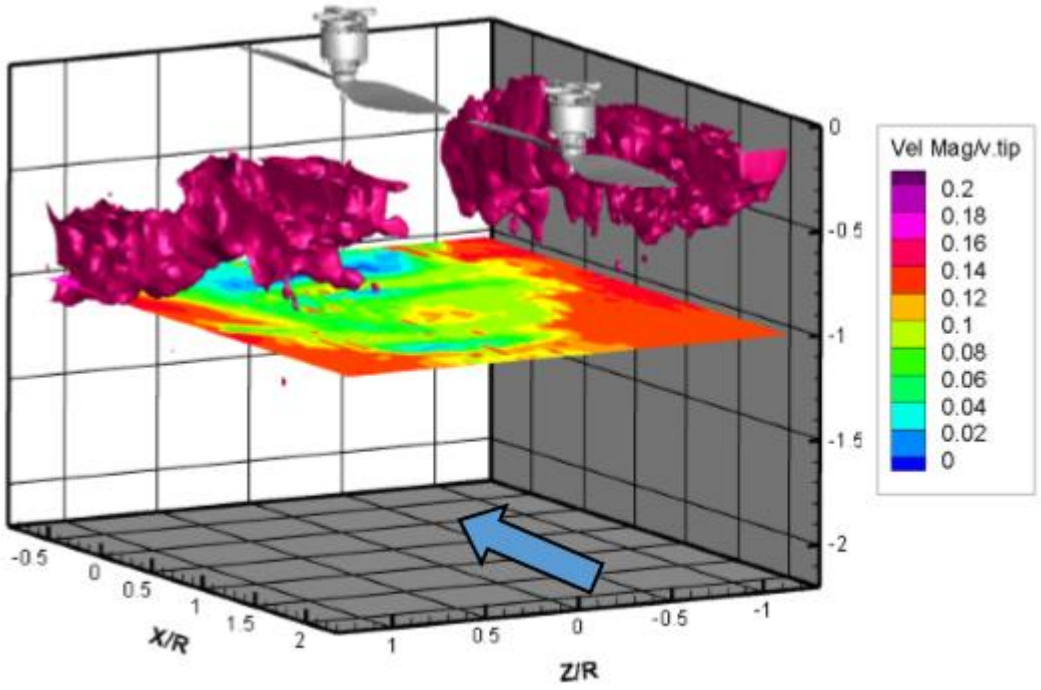

Figure 4.34 Iso-surface of vertically upward air velocity V/v.tip=+0.024 at a flight speed of 10 m/s.

As the flight speed increases, this region of upward velocity becomes smaller in the downwash direction (vertically down, -Y) and expands to the downwind sides (-X/R) In Figure 4.33 the downward spatial extent of the upward velocity region is -1.25R; whereas, in Figure 4.34 the downward spatial extent of the upward velocity region is -0.7R.

4.2.2.2 Rotors arranged spanwise

The zone of upward velocity, created by the tip vortex, exists at a flight speed of 2 m/s, but grows in volume as the flight speed increases (Figure 4.35) It is demonstrated by the Iso-surface of vertically upward air velocity $V/v_{tip}=+0.024$.

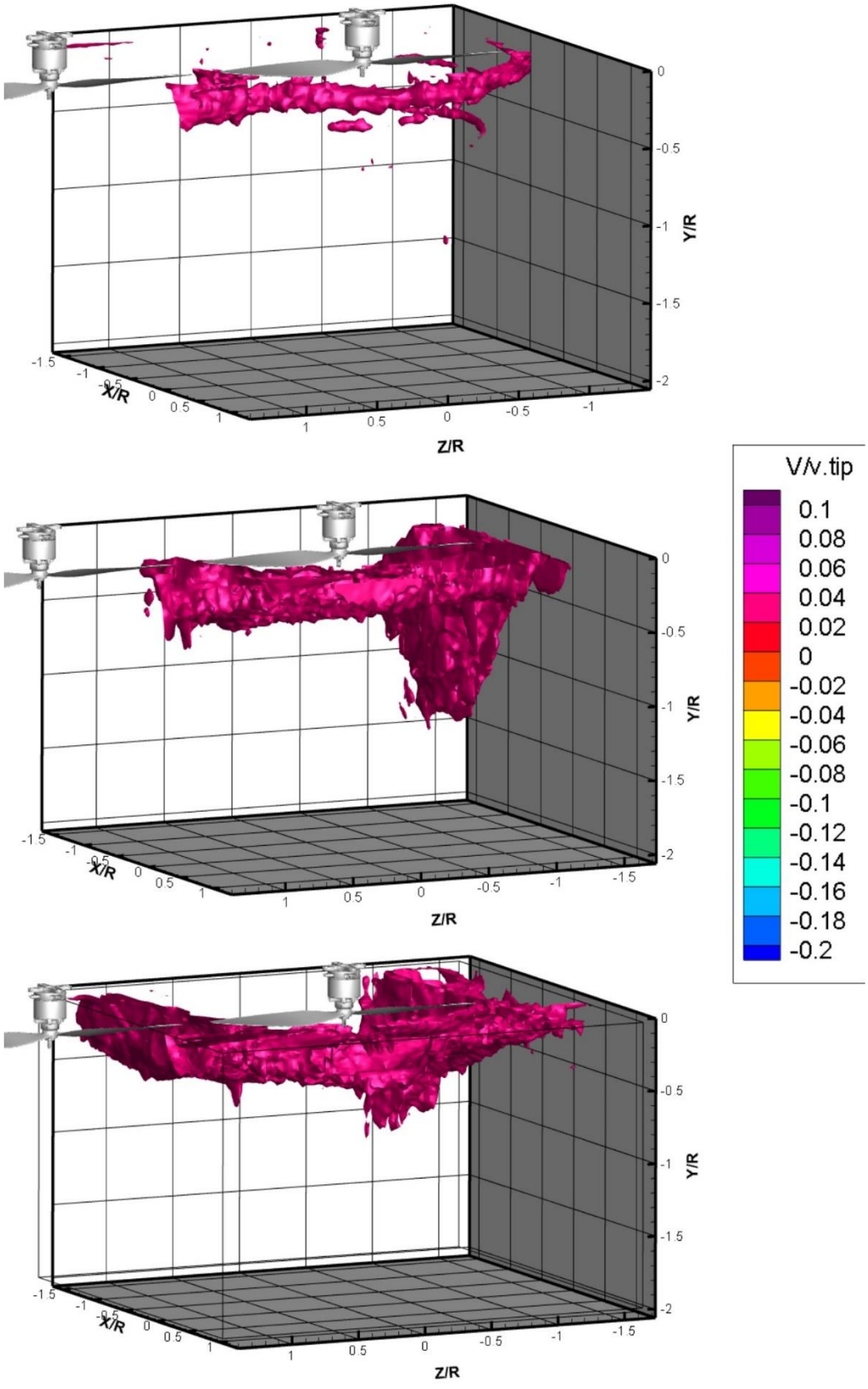

Figure 4.35 Iso-surface of vertically upward air velocity V/v.tip=+0.024; flight speed: top) 2m/s; middle) 6m/s; bottom)10m/s.

At flight speeds of 2 to 6 m/s, in the region of interaction between the two rotors, the tip upward velocity region does not extend downstream. However, on the side with no adjacent rotor, the tip upward velocity region extends downstream beyond the rotor. At a flight speed of 10 m/s the upward velocity region of the rollup vortex between rotors is similar to the upward velocity region with no adjacent rotor next to it.

4.2.3 Uncertainty in velocity measurement

4.2.3.1 Residual error

The residual error (INSIGHT 4G™ user's guide (2015)) between the left and right images doesn't exceed 2 pixels. Figure 4.36 shows iso-surfaces at 0.5, 1, 1.5 and 2 pixels. The residual error only exceeds 0.5 pixels in small regions of the vortex core. The core has a lower concentration of tracer particles, hence weaker correlation peaks. Residual error reduces as the lateral velocity increases.

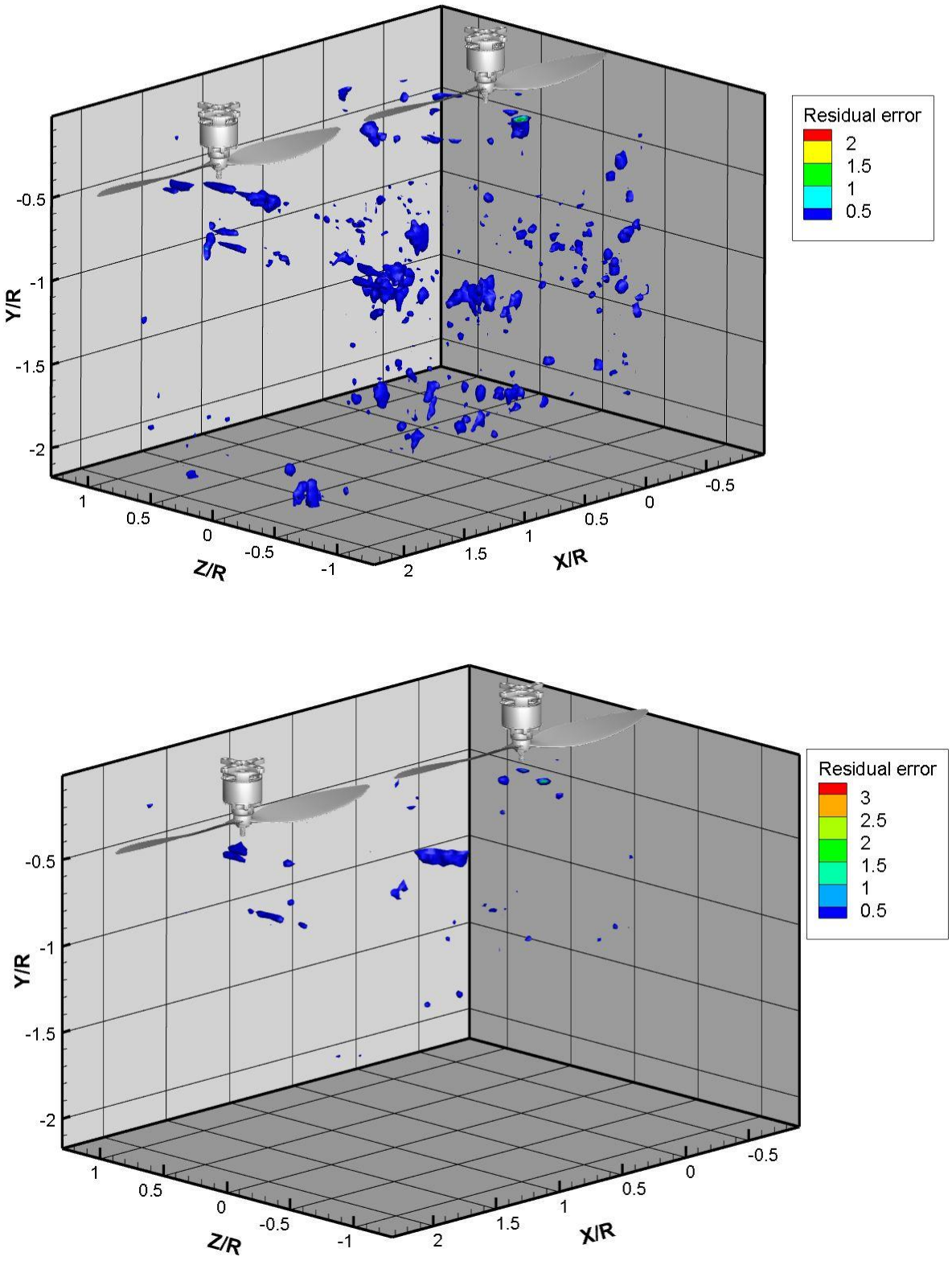

Figure 4.36 Residual error for rotors arranged streamwise at flight speeds of 2 m/s (top) and 10 m/s (bottom).

4.2.3.2 Velocity uncertainty in PIV measurement

The uncertainty in velocity values was determined using the peak to noise ratio method, which assumes that error in pixel displacement follows a Gaussian distribution (INSIGHT 4G™ user's guide (2015)). Uncertainty is evaluated for a single position of the traverse for each experiment (planes 30 mm away from the rotor shafts, i.e., z-coordinate 0.03m) and for lateral velocities of 2 m/s and 10 m/s. The ratio of standard uncertainty to velocity magnitude is presented from Figure 4.37 to Figure 4.40. For the rotors arranged streamwise, uncertainty for a lateral velocity of 2 m/s is shown in Figure 4.37 and for lateral velocity of 10 m/s in Figure 4.38. The field of view is the same as Figure 4.28 i.e., it includes two rotor downwashes. Regions with no data are shown in white. There is little dependence on lateral velocity. The ratio of standard uncertainty to mean velocity magnitude was < 8% in the wake, but exceeded 50% outside the jet due to very small mean velocities.

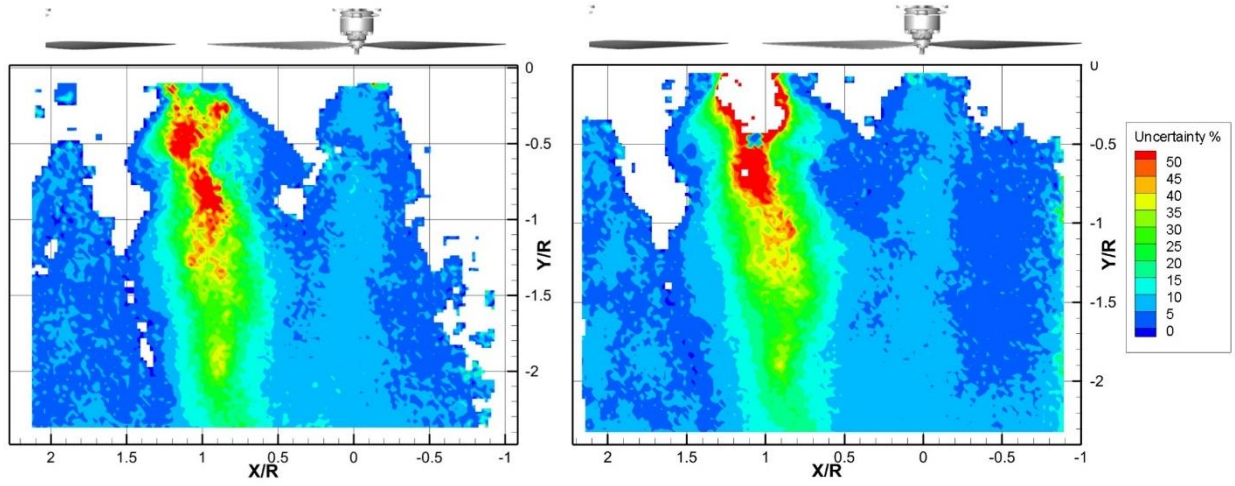

Figure 4.37 Uncertainty of velocity magnitude measurement for left and right camera, lateral velocity 2 m/s, streamwise configuration. Colour bars run from 0 to 50%.

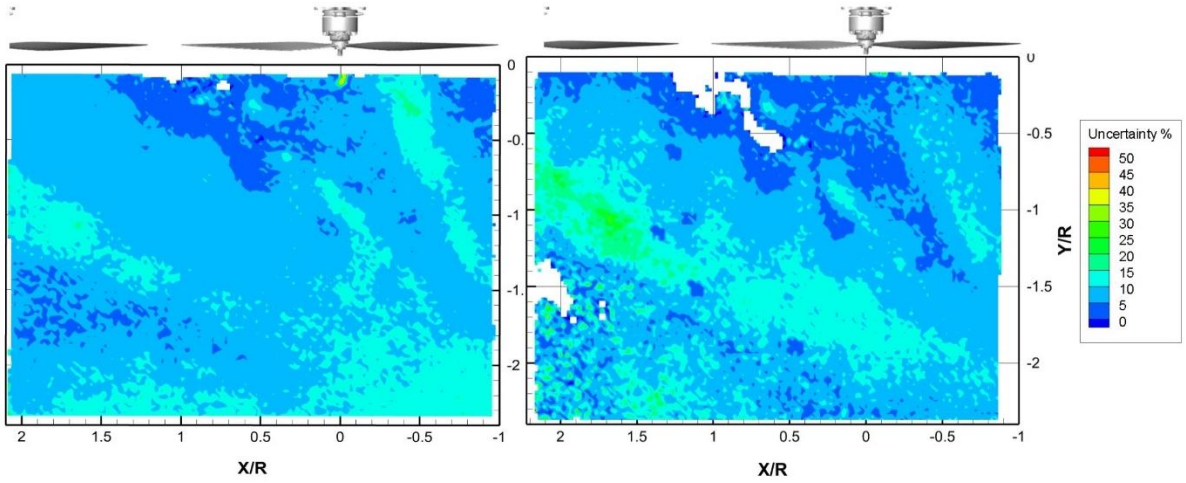

Figure 4.38 Uncertainty of velocity magnitude measurement for left and right camera, lateral velocity 10 m/s, streamwise configuration. Colour bars run from 0 to 50%.

For the rotors arranged spanwise, the ratio of standard uncertainty to velocity magnitude is shown for a lateral velocity of 2 m/s in Figure 4.39 and for 10 m/s in Figure 4.40. The values are similar to the streamwise configuration, with values < 8% within the downwash jet and values ~50% outside the jet where the displacement of the particles was small.

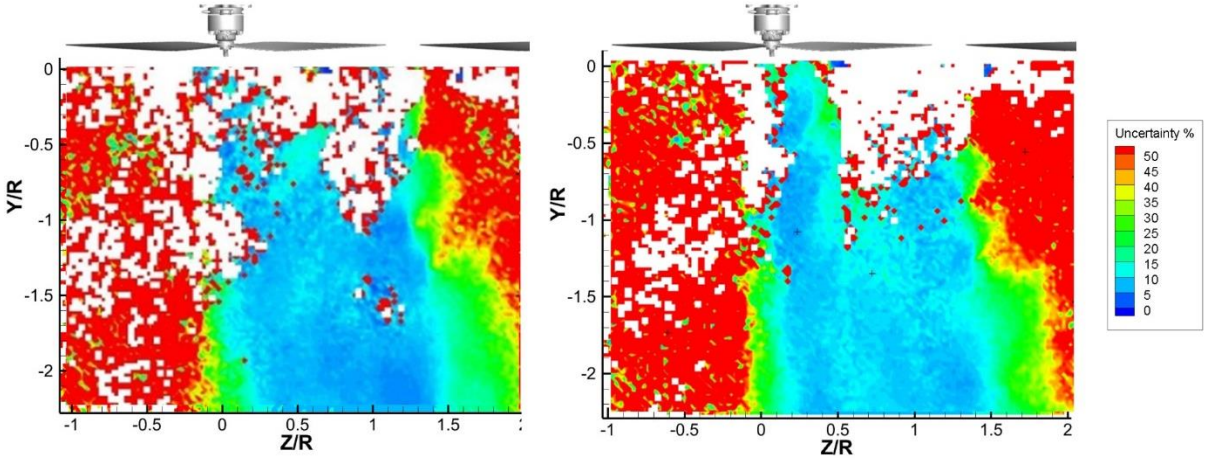

Figure 4.39 Uncertainty of velocity magnitude measurement for left and right camera, lateral velocity 2 m/s, spanwise configuration. Colour bars run from 0 to 50%.

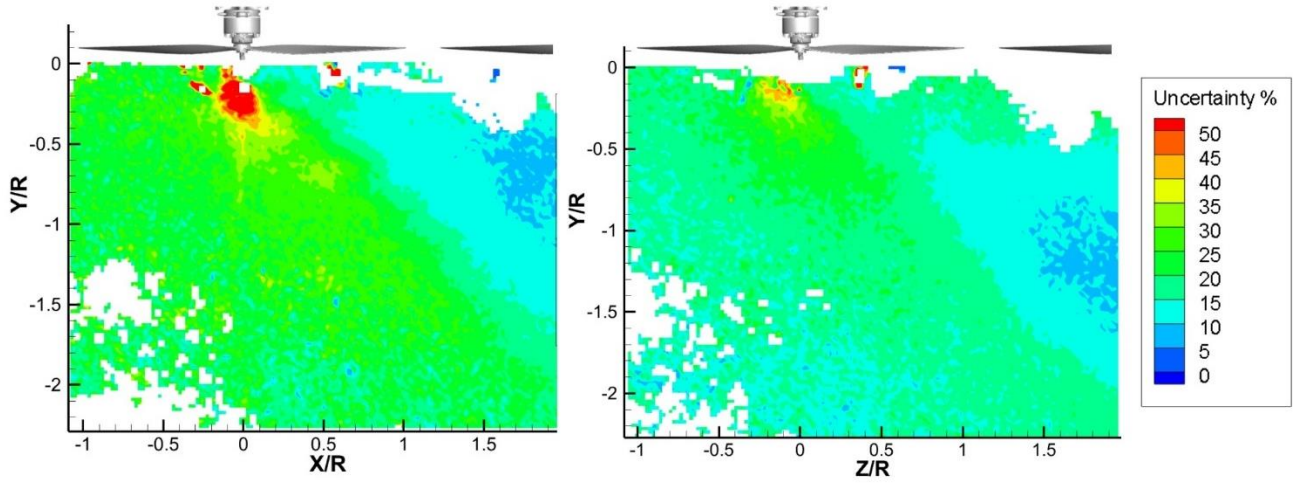

Figure 4.40 Uncertainty of velocity magnitude measurement for left and right camera, lateral velocity 10 m/s, spanwise configuration. Colour bars run from 0 to 50%.

The level of uncertainties is acceptable in the region of interest. The effects, observed in the analysis, won't change within the uncertainty band for every condition tested.

4.3 Discussion

4.3.1 Isolated rotor in hover

In hover, an isolated rotor (Chapter 3) generates a zone of low pressure inside the wake (compared to the ambient pressure). The wake and surrounding air pressure are symmetrical around vertical planes passing through the Z or X-axis. The streamlines outside the rotor wake point towards the wake. This was discovered in several experiments and is true for every rotor tested (Figure 4.41 APC 1045 rotor, light blue streamlines outside of rotor).

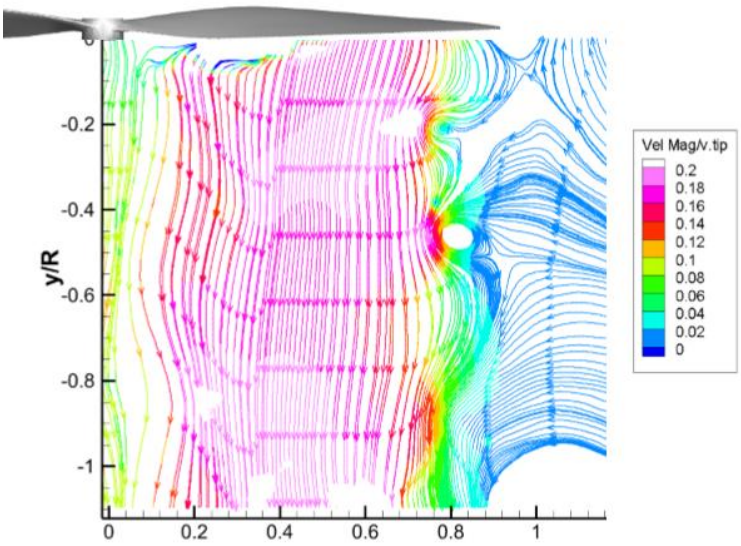

Figure 4.41 Streamlines of isolated APC 1045 rotor wake coloured by velocity magnitude normalised by rotor tip velocity on the Y/R-Z/R plane (X/R=0).

In an isolated rotor, the tip vortices are emitted from the tips of the rotor. They are the part of the wake and have a helical structure (Figure 4.42)

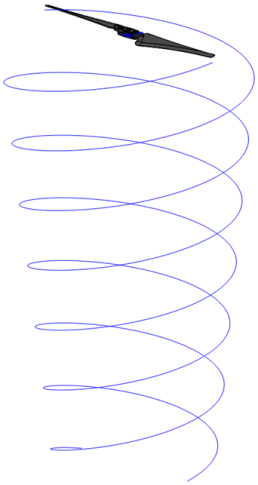

Figure 4.42 The CAD model of a single isolated rotor with helical tip vortices

4.3.2 *Two adjacent counter rotating rotors in hover*

In hovering flight, two-rotor wakes tilt towards each other. The pressure between the rotors is lower than the pressure outside of the rotor. To equalise the system, the two wakes tilt towards each other (Figure 4.43).

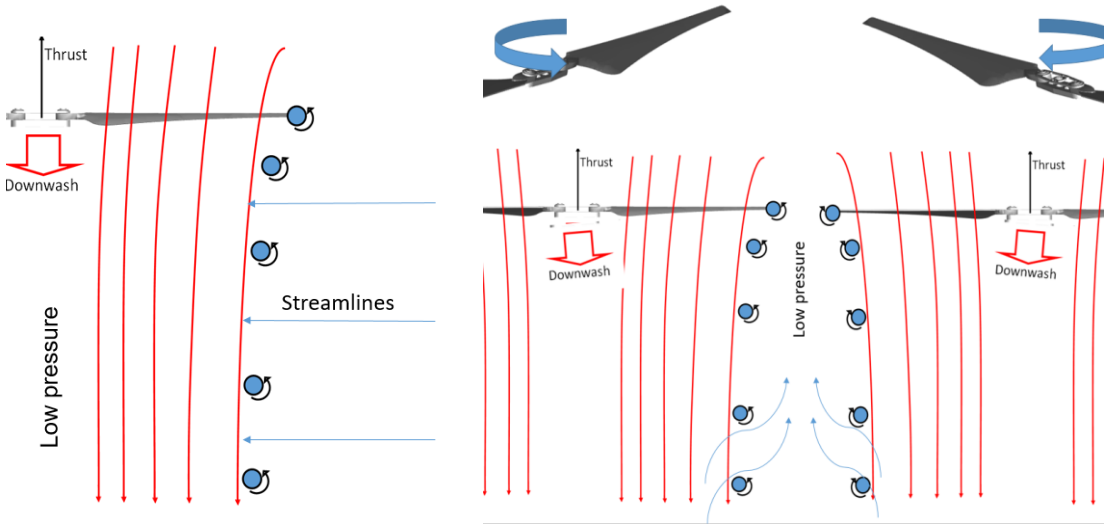

Figure 4.43 The schematic of upward velocity region generation due to the discharge region between two adjacent rotors: single rotor (left); two adjacent rotors (right).

4.3.3 *A region of upward velocity in hover*

The generation of the upwash velocity region is observed in coplanar rotors when the distance between rotor tips is smaller than 0.3R. This was demonstrated on the APC 1045 (254mm rotor with tapered tips) and the DJI E7000 (840mm rotor with rectangular tips). Shukla et al. (2019) used 272mm-diameter changeable pitch rotors with rectangular tip, reporting the upward velocity region generation. The study of 660mm coplanar rotor wake with the tapered tip in the ground demonstrated the generation of the upward velocity region (Mehrabi et al., 2020).

The upward velocity magnitude decreases with tip separation. It is explained by the increasing distance between tip vortex cores. Spatially, the upward velocity region size increases in the -Y/R direction with increasing separation of the tips (Figure 4.17).

The upwash velocity region is time-dependent with maximum velocity magnitude in the field of observation when α or β equal to 0˚. In such a position, the newly generated vortex is closest to another rotor arc. However, when α or β is not equal to 0˚ (none of the rotor tips is in its closest position to another rotor arc), the local maximum upward velocity magnitude is observed when the phase lag is 45˚ degrees. It is explained by the strongest vortex above the region of measurement at 45˚ phase lag.

From observations, the upward velocity magnitude does not depend on the rotational speed of the rotor (Figure 4.23). However, the vortex strength depends on rotational speed; thus, the upward velocity magnitude depends on rotational speed. To measure such dependence, measuring tools with higher than PIV resolution are required. This should be addressed in future work.

In the computational analysis, upwash velocity was observed using the free-wake model (Lee et al., 2009). For them, this effect was not observed when interactions were not included in the free-wake model. It is assumed and confirmed in current experimental observations that the main component causing the upward velocity is the rotors' interacting tip vortices. The strength of vortices is proportional to the time passed since it was generated by the tip (vortex age). The schematic of upward velocity region generation is presented in Figure 4.44.

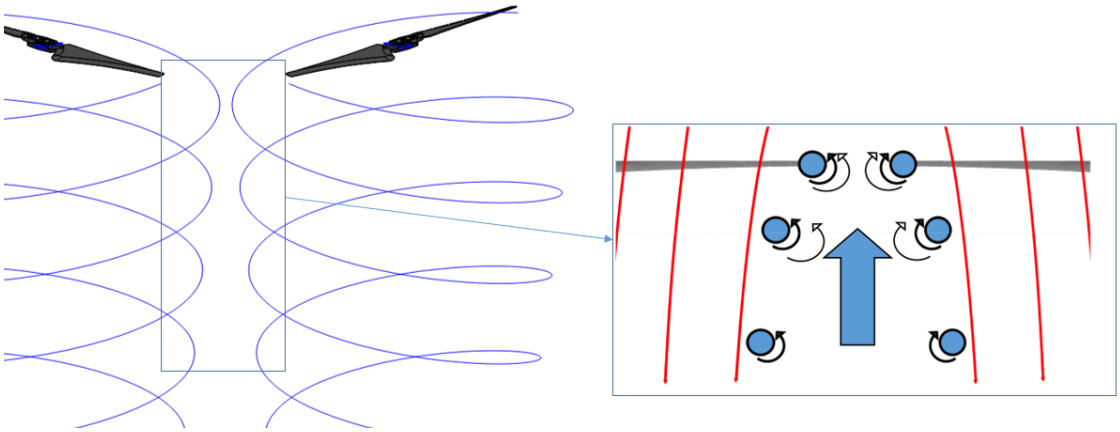

Figure 4.44 Schematic of upward velocity region generation due to the interaction of tip vortices between two adjacent rotors.

4.3.4 Flight in lateral velocity conditions

A flight with lateral velocity conditions is typical for spraying. In this chapter, streamwise and spanwise APC 1045 rotor configurations were observed for 2 m/s, 6 m/s, 10 m/s and 14 m/s.

The leeward rotor is shadowed by the windward rotor. This reduces the tilt angle of the leeward rotor wake compared to the windward rotor wake. This effect was observed in CFD analysis (Yoon et al., 2017) and confirmed by the experiments presented. The windward rotor changes the flow in front of the leeward rotor by changing the upstream velocity. Figure 4.30 confirms this, as the leeward rotor wake shape remains circular. The windward rotor wake deforms into a horseshoe shape. Another contributing factor to the different tilt angles of the rotor wakes is the zone of low pressure between rotors. Such an effect was observed in hovering flight. Although the region of upward velocity was not observed between rotors in streamwise configuration, the streamlines point towards the zone of interaction of two rotors. It confirms the existence of a discharge zone between rotors.

4.3.5 A roll-up vortices in a flight with lateral velocity conditions

Another effect that can affect the droplet distribution is the rollup vortices. This effect is well studied for helicopter rotors (Bauknecht et al., 2016). For multicopter wake, it has been evaluated in CFD analysis (Misiorowski et al., 2019). The cause of the rollup vortex is an interaction between lateral velocity and the tip vortices generated by the pressure difference between an upper and lower surface of the rotor disk. The rollup vortices generate the region of upward air movement behind the flying multicopter. In the streamwise configuration, the zones of upward velocity are attached to the windward part of the windward rotor tip. In the spanwise configuration, the zone of upward velocity is attached to the windward part of both rotors and extends from the free rotor tip to the direction of lateral velocity (Figure 4.35). The spatial extent of the upward velocity region increases with increasing lateral velocity. Between rotors the extent of the upward velocity region is not observed at 2 m/s and 6 m/s lateral velocities. However, the rollup vortex extends in the direction of lateral velocity when this velocity is greater than 10 m/s.

4.4 Conclusion of the chapter

In hovering flight, APC 1045 counter-rotating coplanar rotors were used. The closest distances between rotor arcs were 02R, 0.36R and 0.55R. PIV experimental analysis showed the tilt of the wakes towards each other. The tilt angle decreases with tip distance separation. Two counter-rotating coplanar DJI E7000 rotors with 0.2R rotor tip spacing demonstrated the same result. Two wakes are tilted towards each other. The source of the wake tilt is interaction between wakes, creating a low-pressure zone between them.

It is demonstrated that the region of upwash exists when the rotor tip spacing is 0.2R, 0.36R, and 0.55R in APC 1045 rotors. It is generated by tip vortices and observed outside of the rotor disk 0.6R-1R downstream, depending on tip spacing. The upwash region exists in DJI E7000 rotors when rotor tips are at 0.2R spacing in every position of the rotor relative to the counter-rotating rotor. The same effect was observed by other scholars, both in experiments and using a numerical approach. The observed maximum magnitude of upward velocity is equal to 3.2 m/s.

If the rotor tip is closest to the counter-rotating rotor arc, a 23% increase of upward velocity is observed. Otherwise, when rotors' phase lag is 45° the peak of upward velocity magnitude is observed. The upward velocity magnitude did not find any explicit dependency on rotational speed. It was observed that the upwash velocity magnitude does not depend on the rotational speed of the rotor. The precise measurement of upward velocity magnitude rpm dependency is addressed to future work.

In the presence of lateral velocity, the wakes of adjacent rotors in a multicopter configuration interact strongly. In the streamwise configuration, the wake of the lee rotor tilts 20-25^{o} degrees less than the windward one. This was observed at lateral velocities of 6 m/s, 10 m/s and 14 m/s. Increasing tip spacing to 2R at a lateral velocity of 6 m/s did not noticeably change the tilt angles of interacting wakes. The cause of different tilt angles between two wakes in the streamwise configuration is the shading of the leeward wake by the windward wake. Another contributing factor to the tilt of rotors is the zone of low pressure between rotors.

There are several zones of upward velocity in the wake in presence of the lateral velocity. In streamwise configuration this zone is attached to the windward side of the windward rotor disk. The upward velocity region extends downstream with lateral velocity. In spanwise configuration the zone of upward velocity is attached to the windward side of both rotors. It

extends downstream with lateral velocity near the free side of the rotor disk. However, in presence of another counter-rotating rotor, the zone of upward velocity does not have the downstream lateral component when lateral velocity is between 2-6 m/s. In the 10 m/s lateral velocity experiment, the upward velocity region in the zone of two-rotor interaction increases downstream in the direction of lateral velocity. This is observed near the tip of the rotor in streamwise and spanwise configurations of rotors.

Velocities observed using PIV and CTA near the rotor are used in the modelling of far-field multicopter wake. The velocities obtained in SPIV experiments are used for the computational analysis of droplet trajectories near the multicopter.

5. Influence of multicopter wake on spray trajectories

5.1 Introduction

In chapter 4 the near field wake structure was evaluated, showing that the wake depends on flight velocity, rotor rotational speed and multicopter geometry. This chapter analyses the influence of the wake on spray trajectories, using Lagrangian tracking of spray droplets through the air flow field measured with PIV and reported in the previous chapter.

5.2 Computational technique

5.2.1 Computational model

The air velocity flow field was obtained from the PIV measurement. The Lagrangian approach was used to evaluate droplet trajectories. Particle trajectories can be evaluated by applying Newton's Second Law to each individual particle:

$$m\vec{a} = \vec{F_g} + \vec{F_b} + \vec{F_d} \quad \text{(Equation 5.1)}$$

where $\vec{a}$ is droplet acceleration,

m is the mass of the droplet:

$$m = (\pi/6)d_0^3\rho \quad \text{(Equation 5.2)}$$

where $\rho = 1000\, kg/m^3$ is the density of droplet,

and d_0 is the droplet diameter.

$\vec{F}_g$ is gravity force:

$$\vec{F}_g = m\vec{g} \quad \text{(Equation 5.3)}$$

$\vec{F}_b$ is buoyancy force

$$\vec{F}_b = (\pi/6) d_0^3 \rho_{air} \vec{g} \quad \text{(Equation 5.4)}$$

$\vec{F}_d$ is particle drag force

$$\vec{F}_d = -(1/2) C_d A \rho_{air} \vec{V}_{rel} \left| \vec{V}_{rel} \right| \quad \text{(Equation 5.5)}$$

C_d is the drag coefficient that is the function of Reynolds (*Re*) number

$$(R_e = V_{rel} d_0 / v_{air}) \quad \text{(Equation 5.6)}$$

$$\vec{V}_{rel} = [\vec{u}_p - \vec{u}_f] \quad \text{(Equation 5.7)}$$

where V_{rel} is relative to the airdrop velocity

and u_p is a particle velocity

and u_f is air velocity

$$C_d = \begin{matrix} \frac{24}{Re}\left(1 + 0.15(Re)^{0.687}\right) & Re < 1000 \\ 0.44 & Re \geq 1000 \end{matrix} \quad \text{(Equation 5.8)}$$

Substituting all variables to the equation, the acceleration becomes

$$a_z = \frac{\frac{\pi}{2} r_p^2 \rho_f (u_{f_z} - u_{p_z}) || (u_f - u_p) || C_D}{m_p} - g_c \left(1 - \frac{\rho_f}{\rho_p}\right) \quad \text{(Equation 5.9)}$$

The model has been widely used in previous studies by several scholars (Guo et al., 2004, Kabaliuk et al., 2013, Clift et al., 2006).

The evaporation process occurs while the particle is travelling through the air. However, since the aim of this computation is to show the droplet behaviour near the multicopter, droplet travel duration is relatively short, so the evaporated mass can be neglected.

The velocity field near the multicopter is presented in Chapter 4. It was obtained using the inverse distance interpolation Tecplot Focus. The same software was used for particle tracking using the built-in Calculating Particle Paths and Streaklines function.

The integration time step was set so that particles travel less than one cell within the integration time step. The maximum number of steps should be large enough to enable particles to be tracked through the entire domain of the multicopter wake.

5.2.2 Nozzle parameters

Parameters of a typical spray that might be used in multicopter spraying were established. The droplet sizes produced by spray nozzles may be classified according to American Society of Agricultural and Biological Engineers [ASABE] Standard S572.1, 2009

Table 5.1 American Society of Agricultural and Biological Engineers [ASABE] Standard S572.1, 2009 droplet size classification

Size Classification	Volume Median Diameter (VMD) Range (Microns)
Extremely Fine	<60
Very Fine	61-105
Fine	106-235
Medium	236-340

Coarse	341-403
Very Coarse	404-502
Extremely Coarse	503-665
Ultra-Coarse	>665

For most nozzles, the log-normal distribution is a reasonable approximation to the true droplet size distribution. The geometric standard deviation (σ_g) describes the width of the distribution.

$$\log \sigma_g = \left[\frac{\sum n_i(\log D_i - \log D_g)^2}{N-1}\right]^{1/2} \quad \text{(Equation 5.10)}$$

Where *N* is the total number of particles,

D_{vmd} is the geometric volume mean diameter.

D_i is current particle diameter

n_i is number of particles with size D_i .

In a log-normal distribution size range expressed as:

$$10^{[\log D_{vmd} \pm 2 \log \sigma_g]} \quad \text{(Equation 5.11)}$$

95% of the particle diameters are within a size range.

The model used particles falling within the ASABE 572.1 “very fine” and “medium” classes (VMD 83 microns and 288 microns).

Pumps suitable for use in multicopters typically range from 3-9 bar output pressure; therefore, 6 bar was chosen as best representative. TXA800050 nozzle parameters were used as they produce a very fine droplet size range at 6 bars. The maximum flow rate for such nozzles is 0.2095 L/min (Teejet technologies, catalogue 51A-M). The cone angle is 80 degrees. The mass flow rate equation was used to calculate the outlet velocity of the spray.

$$u = \frac{\dot{m}}{C_d \rho A}$$ (Equation 5.12)

Where *Cd* is the discharge coefficient ranging from 0.91 to 0.94 (Post et al, 2017).

For very fine droplets, the calculated outlet velocity magnitude is 6 m/s. The outlet velocity was assumed to be the same for all droplets.

In the model, the nozzle was represented as 33 particles with different initial angles to the vertical (Figure 5.1) emitted from the same point. The cone angle, defining the limits of the spray, was equal to 80°, 56° and 28°. The angle between the X-axis and spray direction in the X-Z plane ranged from 0° to 360° with an increment of 30°. Outlet velocity was split into components according to the direction of spray.

Table 5.2 The spray outlet velocity component for $2\alpha_{cone}$=28°

β_{con}	0°	30°	60°	90°	120°	150°	180°	210°	240°	270°	300°	330°
U	1.452	1.257	0.726	0	-0.726	-1.257	-1.452	-1.257	-0.726	0	0.726	1.257
V	-5.822	-5.822	-5.822	-5.822	-5.822	-5.822	-5.822	-5.822	-5.822	-5.822	-5.822	-5.822
W	0	0.726	1.257	1.452	1.257	0.726	0	-0.726	-1.257	-1.452	-1.257	-0.726

Table 5.3 The spray outlet velocity component for $2\alpha_{cone}$=56°

β_{con}	0°	30°	60°	90°	120°	150°	180°	210°	240°	270°	300°	330°
U	2.817	2.439	1.408	0	-1.408	-2.439	-2.817	-2.439	-1.408	0	1.408	2.439
V	-5.298	-5.298	-5.298	-5.298	-5.298	-5.298	-5.298	-5.298	-5.298	-5.298	-5.298	-5.298
W	0	1.408	2.439	2.817	2.439	1.40 8	0	-1.408	-2.439	-2.817	-2.439	-1.408

Table 5.4 The spray outlet velocity component for $2\alpha_{cone}$=80°

β_{con}	0°	30°	60°	90°	120°	150°	180°	210°	240°	270°	300°	330°
U	3.857	3.34	1.928	0	-1.928	-3.34	-3.857	-3.34	-1.928	0	1.928	3.34
V	-4.596	-4.596	-4.596	-4.596	-4.596	-4.596	-4.596	-4.596	-4.596	-4.596	-4.596	-4.596
W	0	1.928	3.34	3.857	3.34	1.928	0	-1.928	-3.34	-3.857	-3.34	-1.928

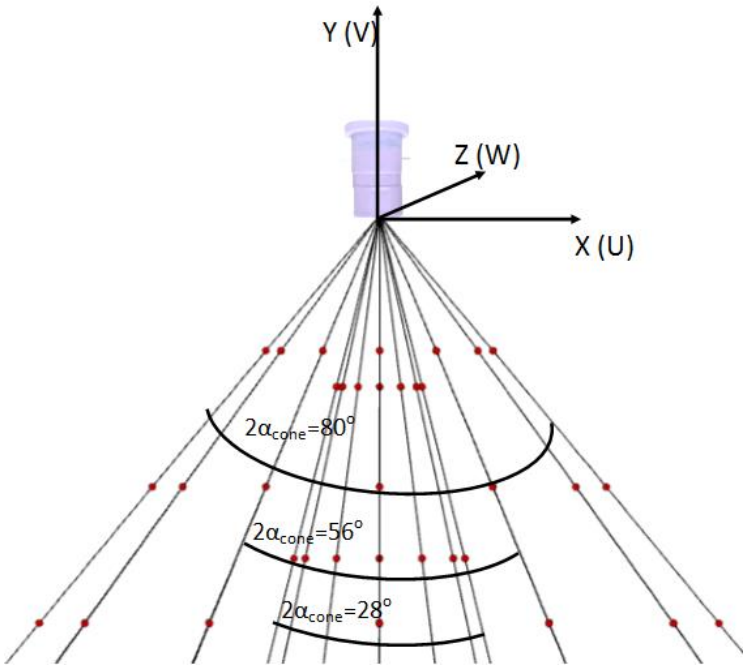

Figure 5.1 Example of particle trajectories with 80°, 56° and 28° cone angle

5.3 Spray trajectories in the flowfield

5.3.1 Computation of spray trajectories in hovering flight

5.3.1.1 APC 1045 rotors

Two virtual nozzles were inserted into the PIV data from the APC 1045 rotors (refer to Chapter 4 for the wake analysis). One of the nozzles is under the greatest downwash from the rotor (Figure 5.2, dark purple), while another is between rotors (Figure 5.2, light purple).

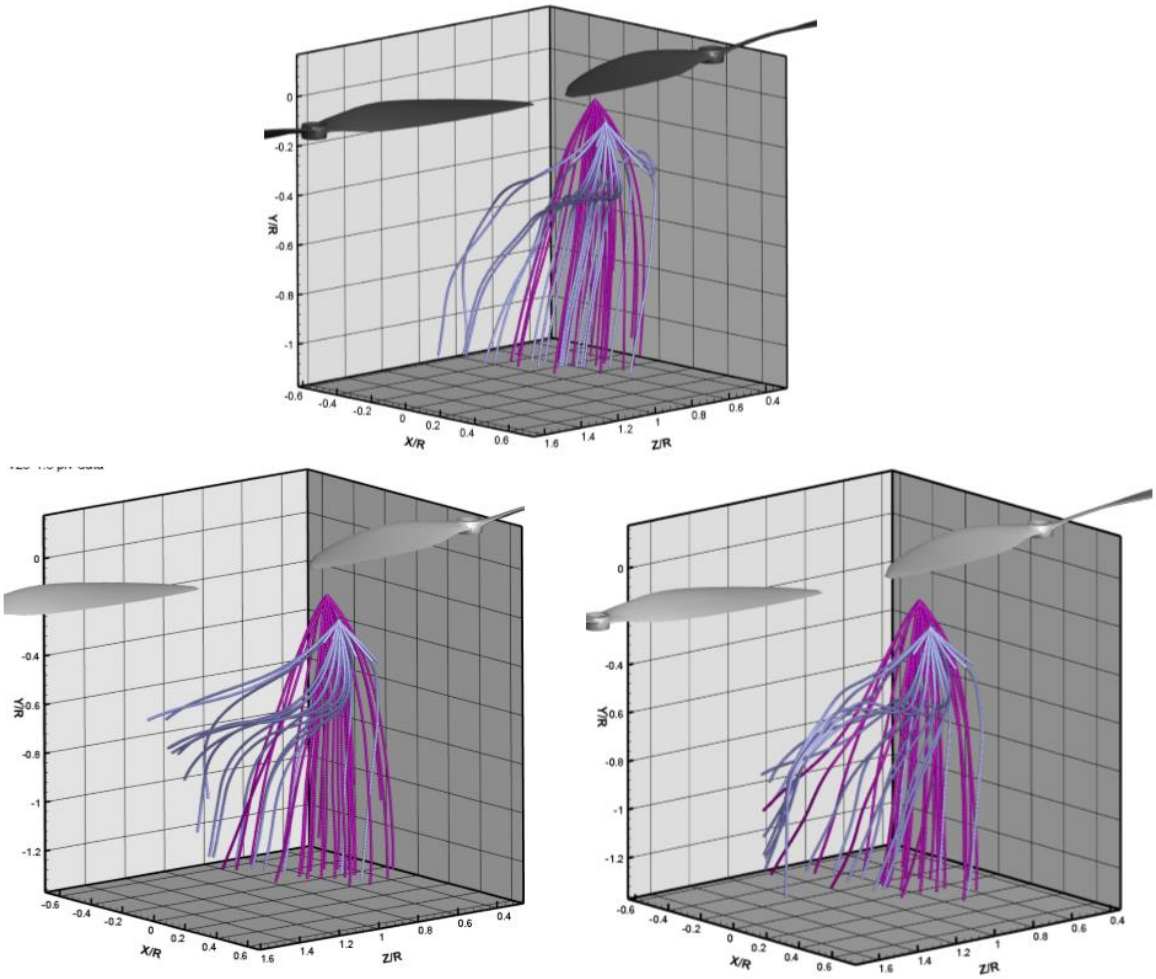

Figure 5.2 86-micron particles released under (dark purple) and between (light purple) APC 1045 rotors when relative distance between rotor arcs is: 0.2R (top); 0.45R (bottom left); 0.55R (bottom right).

The spray released under the greatest downwash travels downstream with the main downwash. It is slightly influenced by the swirling component of the wake. The spray released between rotors is in the upward velocity region. However, particles do not follow this upward motion as they have enough kinetic energy to leave the zone of upward velocity before equilibrating with the local air velocity. Instead, the spray travels laterally to the direction of rotation of rotors, influenced by the swirl component of the wake.

Medium droplets were released in the same location (Figure 5.3, red, between rotors) (Figure 5.3, orange, under the greatest downwash).

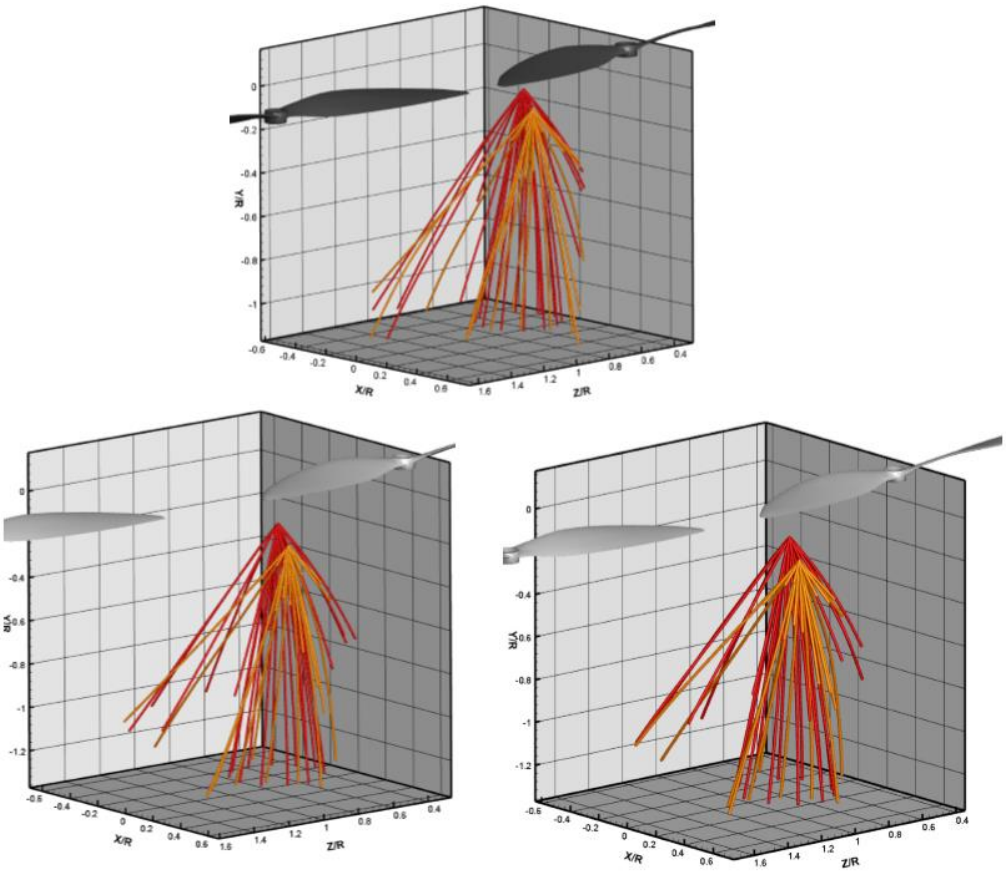

Figure 5.3 287-micron particles released under (red) and between (orange) APC 1045 rotors when relative distance between rotor arcs is: 0.2R (top); 0.45R (bottom left); 0.55R (bottom right).

The 287-micron particles take noticeably longer to equilibrate their velocity with the downwash than the 86-micron particles. Additionally, the medium droplets are less influenced by the velocity in the region of upward air motion.

5.3.1.2 DJI E7000 rotors

Virtual spray was released in the same relative position in the DJI E7000 PIV data as in the APC 1045 data. Two droplet size spectrums were used: very fine (purple, Figure 5.4 left) and medium (red, Figure 5.4 right).

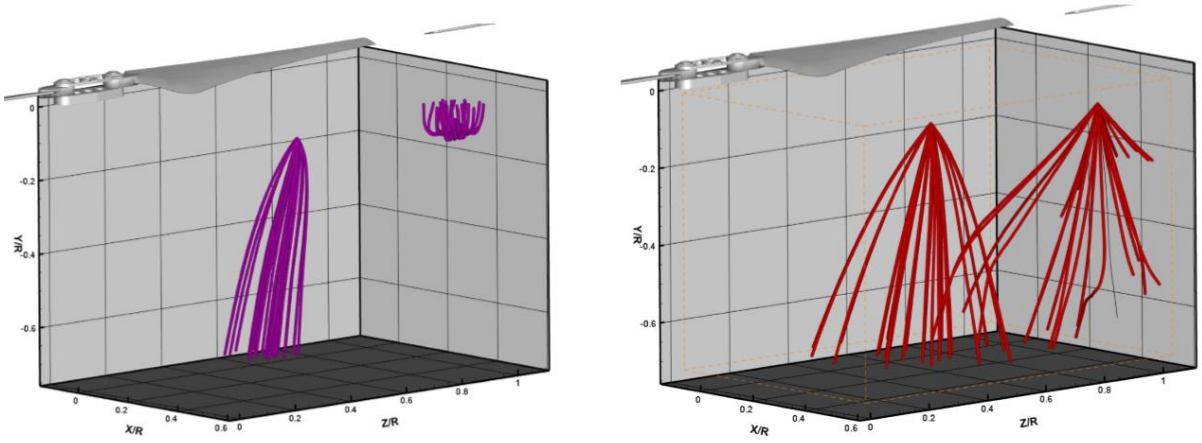

Figure 5.4 Particles released under and between DJI E7000 rotors when relative distance between rotor arcs is 0.2R. The particle size is: 87 microns (left); 287 microns (right).

Very fine droplets released under the greatest downwash travel downstream with it. Spray released in the zone of upward velocity travels vertically upwards. The medium droplet sizes take longer to equilibrate and are not significantly influenced by upward velocity.

5.3.2 Computation of spray trajectories for flight with lateral velocity

5.3.2.1 Rotors arranged streamwise

One nozzle was placed under each rotor, in the region where the downwash velocity was greatest. In Figure 5.5, purple lines show the path of 87-micron diameter droplets, while red

lines show 287-micron droplets. The 287-micron particles take noticeably longer to equilibrate their velocity with the downwash than the 87-micron particles.

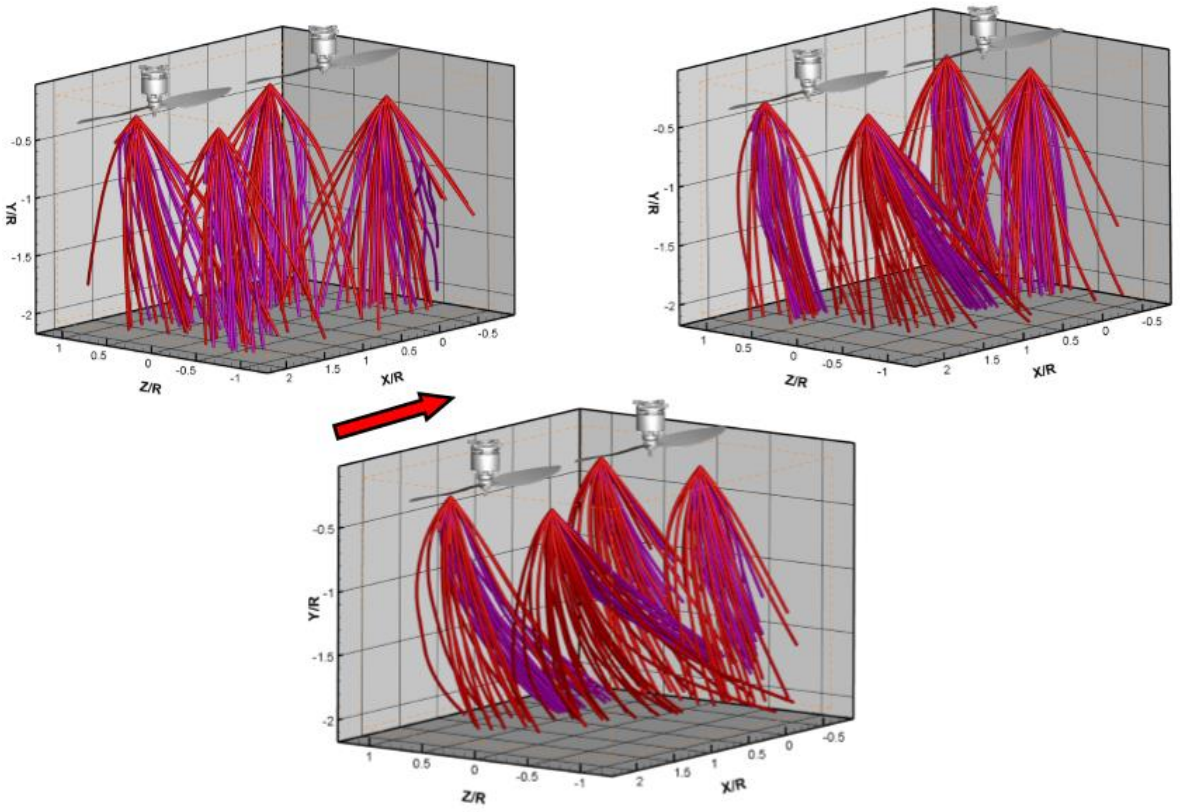

Figure 5.5 Modelling of spray in SPIV data; spray nozzles located under the strongest downwash at flight speeds of: 2m/s (top left); 6 m/s (top right); 10 m/s (bottom). Purple lines: trajectories of 87-micron diameter droplets, red lines: 287-micron droplets.

The smaller particles tend to follow the downwash, and there will be some separation of droplet sizes. It is expected this will be influenced by the ground effect if flying within a few rotor diameters of the ground or of plants. Additionally, spray from a nozzle placed under the front rotor tends to travel a greater distance downstream compared to spray from a nozzle placed under the rear propeller. This results from the difference in angles of tilt of the upwind and rear downwashes described above.

The region of upward air velocity mentioned above is of interest as some UAV spray systems have nozzles placed on a boom under the rotor tip. In Figure 5.6, nozzles are placed under the rotor tips, two nozzles per rotor. Spray droplets follow the lateral velocity to a much greater degree, travel further horizontally, and are more strongly influenced by the downwash swirl than when placed in the region of strongest downwash (Figure 5.6). For nozzles under the rotor tips, the dependence of spray direction on flight speed makes precise targeting of spray onto vegetation more difficult.

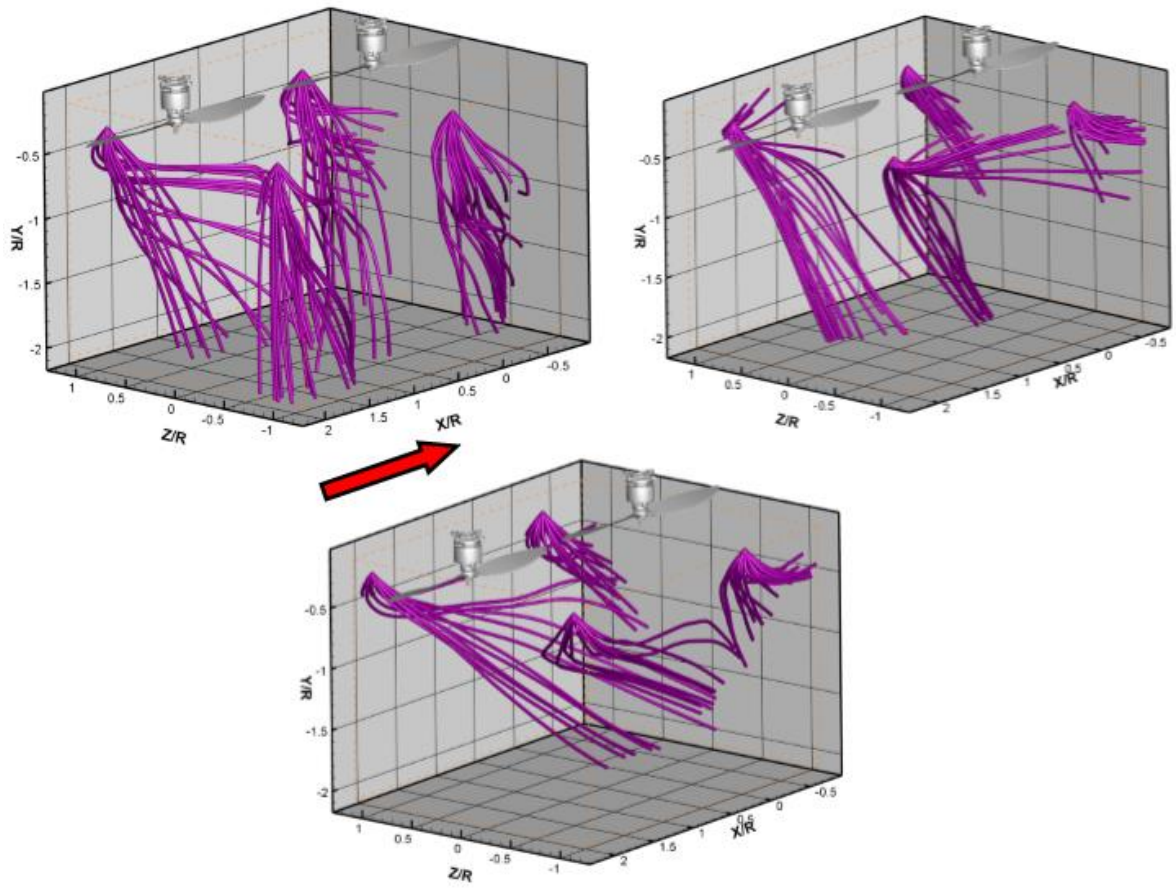

Figure 5.6 Modelling of spray in SPIV data; spray located under the tip of propeller at lateral velocities of 2m/s (top left); 6 m/s (top right); 10 m/s (bottom). Purple lines represent a spray size of 87 microns.

5.3.2.2 Rotors arranged spanwise

Three nozzle positions were tested: between the rotors, in the strongest downwash from the rotors (set to windward), and under the tip of the rotor on the side with no adjacent rotor (Figure 5.7). The 87- and 287-micron diameter droplets were tracked in the model.

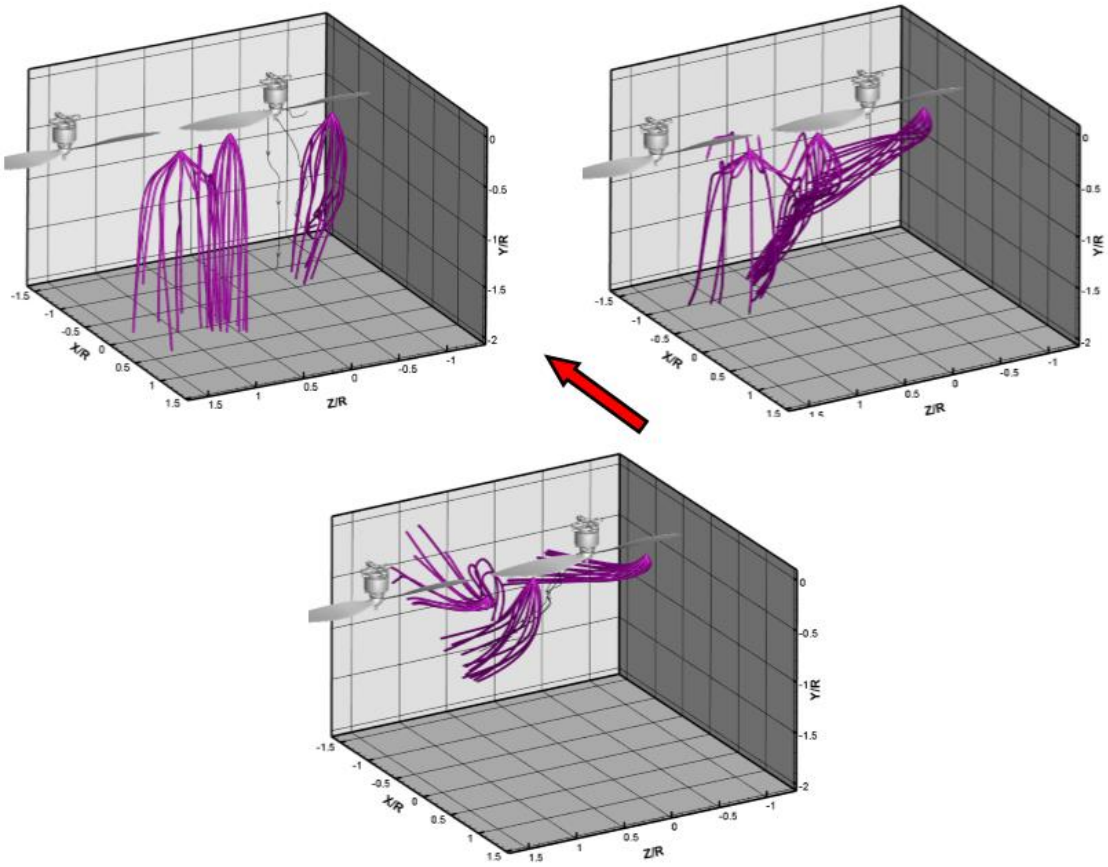

Figure 5.7 Spray modelling in SPIV data; spanwise arrangement of rotors at flight speeds of 6m/s, with droplet diameters of 87 microns (left) and 287 microns (right).

87-micron droplets are displaced further in the lateral wind direction. When the nozzle is placed between the rotors, (especially with 87-micron droplets) the trajectories follow a "step"-shaped path. The front (windward) part of the spray initially leaves the downwash, then is redirected by the lateral velocity (6 m/s) and turned back towards the downwash. The spray released under

the strongest downwash travels in the direction of the downwash, retaining its cone structure with a tilt in the downwind direction. Spray released under the rotor tip is caught in the upward velocity region, allowing the droplets to travel farther downstream and increasing the risk of spray missing the vegetation below or entering the multicopter's electronics.

5.4 Conclusions

For non-zero flight velocities, it is highly recommended to avoid placing the nozzle immediately under the arc swept by the rotor tip, especially in the zone between rotors, as this will result in some spray being drawn upwards, decreasing spraying efficiency and potentially entering the craft's electrical components.

By choosing the correct nozzle placement, smaller spray particles can be delivered to the target without drift caused by lateral velocity (wind, forward or side motion of the craft). The recommended position is the zone of strongest downwash. This location depends on the type of rotor but generally is between 0.5-0.7 times the rotor radius, measured from the axis of rotation.

An example of incorrect nozzle placement (Figure 5.8) is Shenzhen GC Electronic 10 (Shenzhen GC electronic LLC, Shenzhen, China) spraying multicopter and Hercules 10 (Dronevolt LLC, Villepinte, France) spraying multicopter.

Figure 5.8 Shenzhen GC Electronic 10 multicopter (left) [http://dronesonvideo.com/top-agriculture-crop-spraying-drones/ accessed 29.07.2021] and Hercules 10 multicopter (right) [https://www.dronevolt.com/en/expert-solutions/hercules-10-spray/, accessed 29.07.2021]

In both multicopters, the spray nozzles are located between rotors. In hover, it is assumed, the spray may be carried upwards, contaminating the parts of the multicopter. Moreover, the spray released from the outer nozzles on both multicopters may be carried away by rollup vortices.

6. Fast computational prediction of multicopter wakes.

Chapter 4 discussed the experimental evaluation of multicopter wake in different flight conditions. The experimental data on the wake velocity field is limited to 2-3 rotor radiuses around the multicopter. Extending the measured volume is time-consuming. The variety of flight conditions makes it impossible to test every flight condition within the constraints of the laboratory.

This chapter presents a fast computational analysis technique of multicopter wakes. The data obtained from the analysis was used in the prediction of spray patterns in the multicopter wake.

6.1 Model introduction

The aim was to compile a simplified model of near-field and far-field multicopter wake. The variables required for wake analysis were divided into flight-surroundings variables and multicopter variables:

Flight-surroundings variables:

1) Multicopter flight speed
2) Height of multicopter above ground
3) Local wind velocity and height of measured wind velocity
4) Terrain roughness
5) Obstacles on the ground, i.e., plant canopy, terraces, walls, etc.

Multicopter variables:

1) Rotor geometry and number
2) Rotor coordinates
3) Body (fuselage) geometry
4) Range of rotational speeds used on the multicopter
5) Multicopter weight

Due to the number of variables and the complexity of their inter-relationships, analytical models fail to predict the interaction between wakes (Shukla et al., 2018). Therefore, numerical modelling provides the best solution. Among several tools described in the literature review, computational fluid dynamics (CFD) is the most suitable. CFD allows the utilisation of experimentally obtained flow fields as boundary conditions and the extension of the flow field to the size required by the model using the Navier-Stokes equation. There are several general requirements for the modelling environment:

1. The software used to create and utilise the model is not dependent on any commercial product which requires a licence to minimise the purchasing and running cost of the model
2. The model is fast-computing and can be used by multicopter operators on a desktop office computer or a laptop as a set of libraries or compiled application to update predictions in the field, during spray operations
3. The model is flexible and can be altered when new multicopters or spraying methods are introduced

6.2 Governing equations

6.2.1 Navier-Stokes Equation

The Navier-Stokes equations describe the behaviour of fluid density, pressure, and velocity during flow. The equations are founded on the concepts of mass (Equation 6.1) and momentum (Equation 6.2) conservation.

The mass in the controlled domain can be neither created nor destroyed. Therefore, any change in density plus the mass flow difference between inlet and outlet of the domain equals zero:

$$\frac{\partial \rho}{\partial t} + \nabla\left(\rho \cdot \vec{U}\right) = 0 \qquad \text{(Equation 6.1)}$$

Where ρ is the density

U is the velocity vector,

and t is time.

If the fluid is Newtonian (the viscous stresses are proportional to the rate of deformation (Versteeg et al., 2011)), the x, y and z component of momentum equation equals to the sum of forces in the respective direction on the element of fluid (Versteeg et al., 2011) (Equation 6.2):

$$\rho\frac{Du}{Dt} = -\frac{\partial(p)}{\partial x} + \nabla(\mu\nabla u) + S_{Mx}$$

$$\rho\frac{Dv}{Dt} = -\frac{\partial(p)}{\partial y} + \nabla(\mu\nabla v) + S_{My}$$

$$\rho\frac{Dw}{Dt} = -\frac{\partial(p)}{\partial z} + \nabla(\mu\nabla w) + S_{Mz}$$

(Equation 6.2)

Where p represents pressure,

and S_{Mi} is a source of body forces (Gravitational, Coriolis, electromagnetic)

and μ is the dynamic viscosity (Versteeg et al., 2011).

D/Dt is the substantial derivative as follows (Equation 6.3):

$$\frac{D()}{Dt} = \frac{\partial()}{\partial t} + u \cdot \frac{\partial()}{\partial x} + v\frac{\partial()}{\partial y} + w \cdot \frac{\partial()}{\partial z} = \frac{\partial()}{\partial t} + U \cdot \nabla() \quad \text{(Equation 6.3)}$$

Given that the multicopter wake is transient and incompressible, the unknown variables are pressure and velocity. Equation 6.1 and Equation 6.2 cannot be solved analytically for multicopter wakes but a solution can be found numerically by applying continuity equations and boundary conditions (Andersson et al., 2020).

6.2.2 Discretization scheme and pressure-velocity coupling

Because the numerical solution of differential equations cannot create a continuous distribution of variables throughout the solution domain, the discretisation must be introduced. It is possible to represent the partial differential equations (PDE) algebraically in a stable and consistent manner using the following methods: the finite volume discretisation method, the finite difference method, and the finite element method. The finite volume discretisation method is the one most used in CFD because it converts the conservation laws into integral forms (Andersson, 2020).

Generally, the pressure and pressure gradient are not known beforehand. In the discretized equations for incompressible flow the density is constant (not linked to the pressure). Therefore, an introduced pressure-velocity coupling generates a new constraint to the solution. This constraint is: the resulting velocity should satisfy the continuity equation if correct pressure was applied to the momentum equations. The pressure-velocity linkage can be created by adopting one of an iterative solution strategy: the semi-implicit method for pressure linked equation (SIMPLE), the pressure implicit with split operator (PISO) method, and the PIMPLE (merged PISO-SIMPLE) method (Andersson et al., 2020, Versteeg et al., 2011). The SIMPLE

method was chosen as it suits steady-state incompressible turbulent flow and is reported to converge faster than other methods (Barton, 1998).

Solving the Navier-Stokes equation using the SIMPLE method involves substituting the momentum equation into the continuity equation. The momentum equation in the semi-discrete form is (Equation 6.4):

$$a_p\vec{U_p} = H\left(\vec{U}\right) - \nabla p \iff U = \frac{H\left(\vec{U}\right)}{a_p} - \frac{\nabla p}{a_p} \quad \text{(Equation 6.4)}$$

$$H\left(\vec{U}\right) = -\sum_n a_n U_n + \frac{\vec{U^o}}{\Delta t} \quad \text{(Equation 6.5)}$$

Where a_n is the matrix coefficients of neighbouring cells,

and U_n is the velocity of the cells,

$\frac{\vec{U^o}}{\Delta t}$ is contains all sources and unsteady term,

Then, the continuity equation is described as (Equation 6.6):

$$\nabla \cdot U = \sum_f \vec{S}\vec{U_f} = 0 \quad \text{(Equation 6.6)}$$

where $\vec{S}$ is the face area vector,

and $\vec{U_f}$ is the velocity on the face that is the product of the interpolation of momentum equation in the semi-discretized form (Equation 6.7):

$$\vec{U_f} = \left(\frac{H\left(\vec{U}\right)}{a_p}\right)_f - \frac{(\nabla p)_f}{(a_p)_f} \quad \text{(Equation 6.7)}$$

The pressure equation is obtained by substituting the velocity of the phase into the discretized continuity equation (Equation 6.8):

$$\nabla\left(\frac{1}{a_p}\nabla p\right) = \nabla\left(\frac{H\left(\vec{U}\right)}{a_p}\right) = \sum_f \vec{S}\left(\frac{H\left(\vec{U}\right)}{a_p}\right) \quad \text{(Equation 6.8)}$$

The SIMPLE algorithm is shown in Figure 6.1

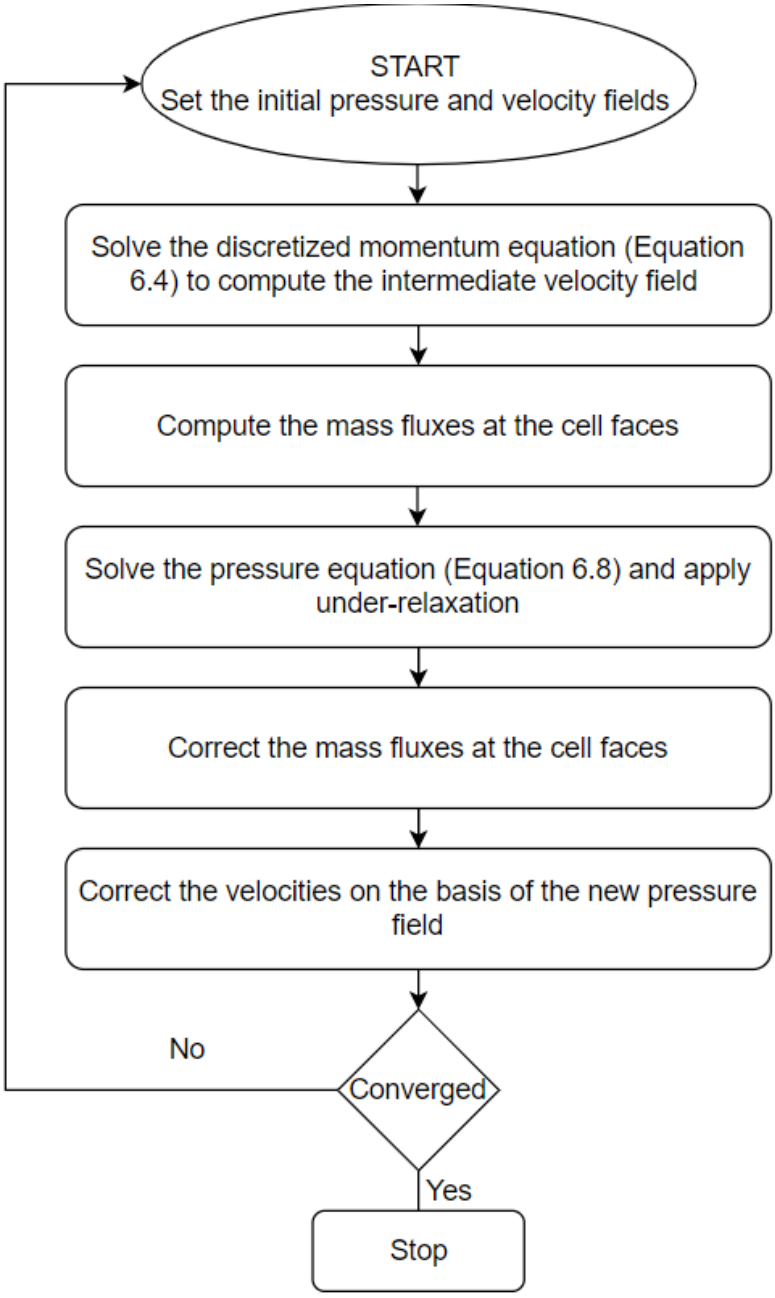

Figure 6.1 The SIMPLE algorithm (adapted from Versteeg et al., 2011)

6.2.3 Turbulence model

Turbulence is an irregularity in flow characterised by changes in pressure and velocity across a wide range of timescales. In computational fluid dynamics, several models for turbulent flow prediction are available. These include the Reynolds Average Navier-Stokes Simulation (RANS), large eddy simulation (LES), detached eddy simulation (DES), direct numerical simulation (DNS). LES, DES and DNS models are computationally expensive (Bogos, et al., 2015; Hart et al., 2016); therefore, RANS was implemented in this model.

The RANS family has several available turbulence sub-models (k-epsilon, k-omega, k-omegaSST, Spalart-Allmaras, etc.). The k-epsilon model works well in free stream conditions, whereas k-omega is good for near boundary turbulence prediction. k-omega shear stress transport (SST) combines the advantages of both models and switches from the k-epsilon model to the k-omega model in the free-stream conditions. It avoids the disadvantage of the k-omega baseline model of being too sensitive to the properties of free-stream turbulence.

The most precise RANS model for rotor wake analysis is the k-omega shear stress transport model (SST) (Muiruri et al., 2019, Menter, F. R, 1994, Meana-Fernández et al., 2019) because it combines the advantages of the k-epsilon model and the k-omega model. Therefore, it was chosen for the computational analysis.

k-omega SST is a two-equation turbulence model. k is turbulence kinetic energy (TKE) (Equation 6.9):

$$k = \frac{1}{2}\left(\overline{(u')^2} + \overline{(v')^2} + \overline{(w')^2}\right) \qquad \text{(Equation 6.9)}$$

Where u', v', w' are turbulent velocity components.

and ω(omega) is turbulence specific dissipation rate (Equation 6.10):

$$\omega = \frac{k^{0.5}}{C_{\mu}^{0.25} L} \quad \text{(Equation 6.10)}$$

where C_{μ}= 0.09 is a constant,

and L is a reference length scale.

The transport equation for turbulence kinetic energy is (Equation 6.11):

$$\frac{D}{Dt}(\rho k) = \nabla \cdot (\rho D_k \nabla_k) + \rho G - \frac{2}{3}\rho k(\nabla \cdot u) - \rho \beta^* w k + S_k \quad \text{(Equation 6.11)}$$

The transport equation for turbulence specific dissipation rate is (Equation 6.12):

$$\frac{D}{Dt}(\rho w) = \nabla \cdot (\rho D_w \nabla_w) + \frac{\rho \gamma G}{\nu} - \frac{2}{3}\rho \gamma w(\nabla \cdot u) - \rho \beta w^2 - \rho(F_1 - 1) C D_{kw} + S_w$$

(Equation 6.12)

Table 6.1 shows coefficients used in k-omega SST model.

Table 6.1 Coefficients used in k-omega SST turbulence model transport equations

α_{k1}	α_{k2}	$\alpha_{\omega 1}$	$\alpha_{\omega 2}$	β_1	β_2	γ_1	γ_2	β^*	a_1	b_1	c_1
0.85	1	0.5	0.856	0.075	0.0828	5/9	0.44	0.09	0.31	1	10

6.3 OpenFoam

There are many open-source CFD toolboxes available (Vogeltanz et al., 2015). However, the availability of wide support and wide use makes OpenFOAM a reliable toolbox.

OpenFoam (Open-Source Field Operation and Manipulation, https://www.openfoam.com/ accessed 19.08.2021) is the toolbox of utilities used for solving problems of continuum

mechanics. It is based on the C++ programming language and can be used in a Linux environment. OpenFoam includes utilities for pre-processing (e.g., blockMesh, snappyHexMesh, meshRefine), processing (e.g., simpleFoam, pimpleFoam, potentialFoam) and post-processing (e.g., paraFoam).

A typical OpenFoam project file set consists of folders: *0*, *constant* and *system*. Folder *0* contains the boundary conditions (e.g., velocity, pressure, TKE) (Figure 6.2). The *constant* folder contains files with constant parameters (e.g., generated mesh, turbulence properties). The *system* file contains files required for the OpenFoam system (e.g., *blockMesh*, *fvOptions*, *fvSolution*). For modelling, a folder named *boundary_backup* was generated. This folder contains the baseline boundary conditions that cannot be altered within the solver.

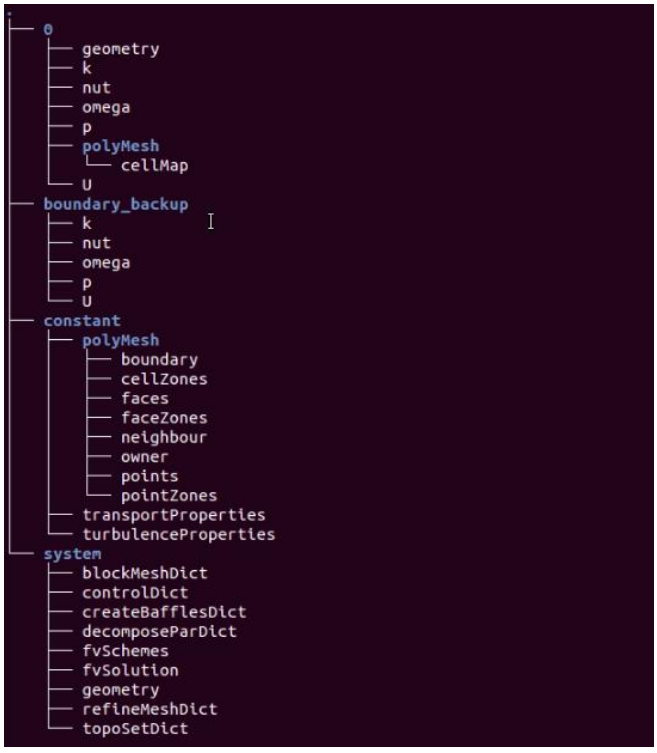

Figure 6.2 A typical OpenFoam model folder tree

6.3.1 Geometry and mesh generation

When modelling a multicopter, the Y-axis is in the direction of thrust, the X-axis is in the direction of flight, and the Z-axis completes the right-handed coordinate system. The origin of the domain depends on the problem. All geometrical and computational variables are described in the separate *"geometry"* file.

The rotors and the complete multicopter were described by rotor radius (*R, m*), a number of rotors (*nor*), multicopter radius (*Rm, m*), and tip spacing (*dr, m*) (Figure 6.3). Every rotor coordinate (*xrn, zrn*, where *n* is the rotor number) is computed based on these variables.

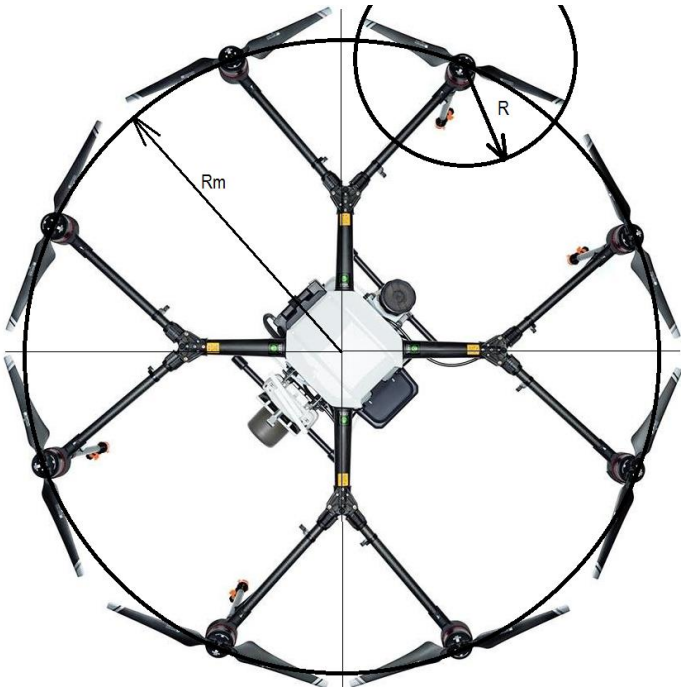

Figure 6.3 The multicopter parameters *Rm, R, nor=8* (octocopter) (Example DJI Agras MG-1).

The domain size and geometry are described as functions of rotor radius (*xmin, xmax, ymax, zmin, zmax*) or flight parameters (*ymin*) (Figure 6.4). The *ymin* variable equals the height above the ground. The size of the domain was found empirically for each computational case. The

size of the domain should be large enough to accommodate the majority of the spray parcels (Chapter 6).

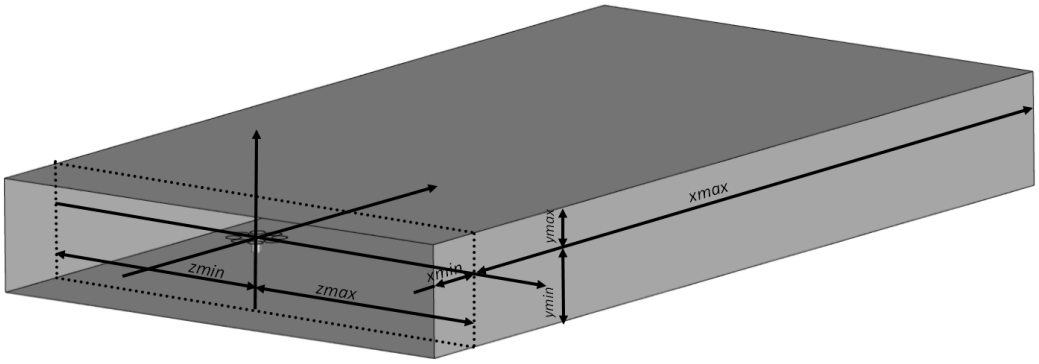

Figure 6.4 Domain size parameters

The *blockMesh* dictionary was used to mesh the model. In *blockMesh* the *vertices* represent the vertex of the block. Each block has 8 vertices. The vertex coordinates were read from a *geometry* file. The domain consists of a single block. The block has six sides. *fixedWalls* is the ground plane. *defaultWalls* is the top of the domain. *SideWall1* and *SideWall2* are the side walls (Figure 6.5).

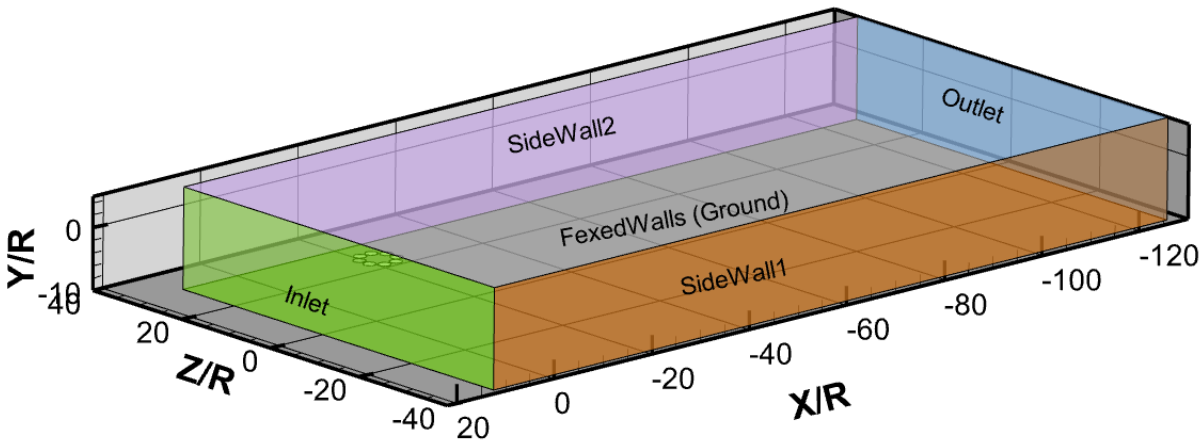

Figure 6.5 Boundary faces of the domain

OpenFoam reads the geometry file and generates a *DynamicCode* folder (can be found in the tree in Figure 6.2) with variables stored inside it. The number of divisions in each coordinate direction is specified in the geometry file. The number of cells is higher in the zone of rotors and then gradually decreases to the outlet and side walls of the domain. A portion of the domain, occupied by multicopter in X and Z directions, was selected in the *blockMesh* dictionary. In the selected portion, the ratio of the number of divisions in the selected direction (X or Z) to the total number of divisions in the selected direction was specified. For example, in Figure 6.6 the ratio of the number of divisions in the portion of multicopter was 0.4 in X direction and 0.6 in Z direction. The parallelepiped is the dominant element in the mesh.

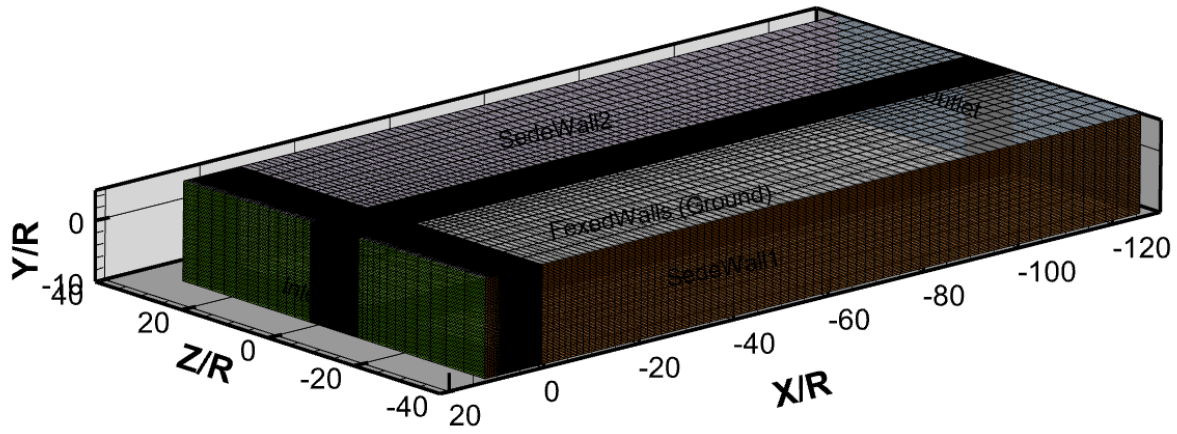

Figure 6.6 Example of generated mesh with multicopter.

6.3.1.1 Simplified multicopter rotor representation

In previous work it was discovered that the rotors should be immersed in the mesh to allow induced velocity flow on top of the rotor disk. The *topoSet* dictionary was used to specify the geometry of a rotor inside the domain. Each rotor coordinate (*xrn*, *zrn*) and radius were read from the *geometry* file to the *topoSet* dictionary. The *faceSet* type used the *CylinderToFace*

source to select the face cells inside the rotor disk. The *faceZoneSet* type splits the rotor cells and the domain (Figure 6.7)

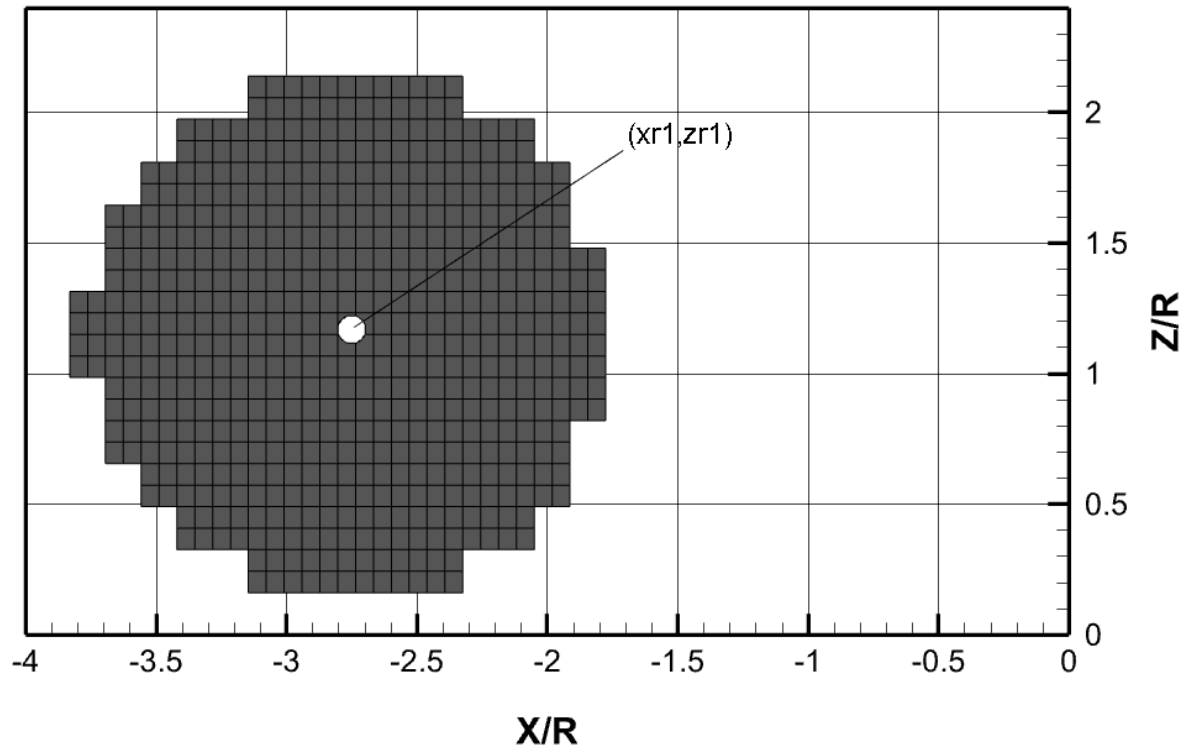

Figure 6.7 Example of generated rotor disk with mesh

To convert the internal faces into the boundary faces, the *createBaffles* dictionary was used. It overwrites the specified boundary faces (if any) and generates two sets of boundary conditions for a single *faceSet*. The boundaries are called *abc_master* and *abc_slave* (where *abc* is the name of corresponding *faceSet*). The generated boundaries, with information about face count and start face, can be found in *constant/polymesh/boundary.*

6.3.2 Boundary conditions

Boundary conditions are specific for each case scenario described in this chapter. In the model, boundary conditions can be separated into the following categories: rotor boundary conditions, atmospheric boundary conditions and lateral velocity boundary conditions.

6.3.2.1 Rotor boundary conditions

The wake velocity of the rotor can be specified as vector components (Equation 6.13) using *groovyBC* boundary conditions. *GroovyBC* is a mixed boundary condition that allows the variable to be specified using mathematical expressions instead of numerical discrete data.

$$vector(\frac{-Vsv(pos.z-b)}{\sqrt{(pos.x-a)^2+(pos.z-b)^2}}, -DW, \frac{Vsv(pos.x-a)}{\sqrt{(pos.x-a)^2+(pos.z-b)^2}}) \qquad \text{(Equation 6.13)}$$

Where *DW* and *Vsv* is an interpolation of normalised downwash and swirl velocity components as the function of normalised radius of the rotor *r/Rr*,

and *r* is the local coordinate of the specified rotor disk (Equation 6.14):

$$r = \sqrt{(pos.x - a)^2 + (pos.z - b)^2} \qquad \text{(Equation 6.14)}$$

where *pos.x* and *pos.z* are cell coordinates inside the rotor disk

and *a* and *b* are global *x* and *z* coordinates of the centre of the rotor.

In Chapter 3 it was found that the normalised wake velocity does not significantly change with rotational speed. Therefore, to specify velocity at the desired rotational speed, the velocity was multiplied by tip speed at a desired rotational speed.

The radial component (along the blade) was not introduced as a boundary condition. Chapter 3 showed that the main source of radial velocity, generated by a rotor, is the tip vortex. In the top part of the tip vortex, the radial velocity vector points towards the rotor shaft. On the bottom

part of the tip vortex, the radial velocity vector points away from the rotor shaft. Therefore, the radial velocity component is periodic along the vertical axis (Y/R) and would bring additional complexity to the model.

To mimic the tip vortex, a source of turbulent kinetic energy (TKE) was introduced into the model. Similarly to velocity, TKE was defined as a function of normalised rotor radius *r/Rr*. TKE was normalised by the square of tip velocity. The vortex represented by TKE does not have a helical structure and does not propagate with the wake.

6.3.2.2 Atmospheric boundary conditions

The atmospheric boundary conditions model in a neutral atmospheric boundary layer has been described and evaluated before (Hargreaves et al., 2007 and Yang et al., 2017). The velocity has a logarithmic distribution (Equation 6.15, Equation 6.16):

$$u = \frac{u^*}{\kappa} \ln\left(\frac{z-d+z_0}{z_0}\right) \quad \text{(Equation 6.15)}$$

$$u^* = \frac{u_{ref}\kappa}{\ln\left(\frac{z_{ref}+z_0}{z_0}\right)} \quad \text{(Equation 6.16)}$$

TKE (Yang, Yi, et al, 2009) also has a logarithmic distribution as a function of distance from the ground (Equation 6.17):

$$k = \frac{(u^*)^2}{\sqrt{C_\mu}} \sqrt{C_1 \ln\left(\frac{z-d+z_0}{z_0}\right) + C_2} \quad \text{(Equation 6.17)}$$

The specific dissipation rate profile is as follows (Equation 6.18):

$$\omega = \frac{u^*}{\kappa\sqrt{C_\mu}} \frac{1}{z-d+z_0} \quad \text{(Equation 6.18)}$$

The list of variables for Equation 6.15 through Equation 6.18 are presented in Table 6.2.

Table 6.2 The list of variables for Equations 5.15-5.18

k	Ground-normal turbulent kinetic energy (TKE) profile [m^2/s^2]
ω	Ground-normal specific dissipation rate profile [m^2/s^3]
u^*	Friction velocity [m/s]
κ	von Karman constant
C_μ	Empirical model constant
z	Ground-normal coordinate component [m]
d	Ground-normal placement height [m]
z_0	Aerodynamic roughness length [m]
u_{ref}	Reference mean streamwise wind speed at z_{ref} [m/s]
z_{ref}	Reference height being used in u^* estimations [m]
C_1	Curve-fitting coefficient profiles
C_2	Curve-fitting coefficient profiles

The roughness of the terrain is the normal vertical distance to the point above the surface of terrain where the wind speed equals zero. According to the World Meteorological Organisation (World meteorological organization, 2008), common terrains have the following typical roughness (Table 6.3):

Table 6.3 Roughness of terrain surface (World meteorological organization, 2008)

Terrain type	z_0, m
Open sea	0.0002
Mud flats, snow, no vegetation or obstacles	0.005
Open flat terrain; low grass, isolated obstacles	0.03
Low crops; occasional obstacles	0.10
High crops; scattered obstacles	0.25
Bushes; numerous obstacles	0.5
Regular large obstacle coverage (suburb, forest)	1.0
City	≥ 2

The roughness of terrain wasn't reported by Richardson et al., 2019. Low crops; occasional obstacles ($z_0=0.1\ m$), high crops; scattered obstacles ($z_0=0.1\ m$) and bushes; numerous obstacles ($z_0=0.5\ m$) were tested in the model.

6.3.2.3 Modelling of flight with lateral velocity in atmospheric boundary conditions

In the model, the multicopter is always flying in the X direction; thus, the lateral velocity applied to the inlet velocity is negative.

The wind can blow from any direction relative to the multicopter. The angle of the wind speed is always relative to the direction of the ground speed vector of the multicopter (clockwise - positive angle). The wind speed (*uw*), lateral velocity (*ux*) and wind direction relative to the multicopter (*wind_dir*) are specified in the *geometry* file (Table 6.8). It is assumed that wind speed is measured at multicopter flight height.

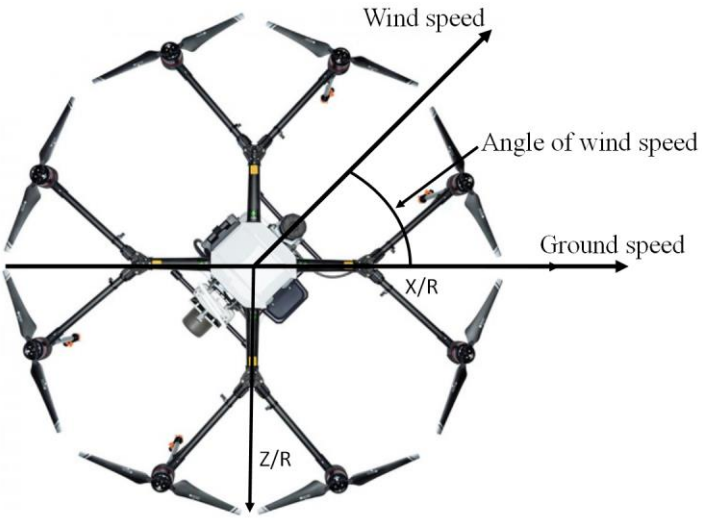

Figure 6.8 The example of the wind speed, ground speed and the angle of the wind speed

In OpenFoam 2012 the atmospheric boundary layer boundary conditions were implemented using the *atmBoundaryLayer* dictionary. The model has been extensively validated in previous studies (Hargreaves et al., 2007, Yang et al., 2017). Other parameters required for the *atmBoundaryLayer* model were specified in *ABLConditions* file.

In the *atmBoundaryLayer* dictionary, the *atmBoundaryLayerInletVelocity* can be applied only perpendicularly to the boundary face. Therefore, the *groovyBC* boundary conditions were used to implement the logarithmic distribution of the wind flow. The wind speed vector was divided by vector components in streamwise (along X axis) and crosswind (along Z axis) directions. This boundary condition was applied to the *SideWall1* and *inlet* face in X and Z directions. In addition, the lateral velocity was applied to the same faces in the X direction (Table 6.9).

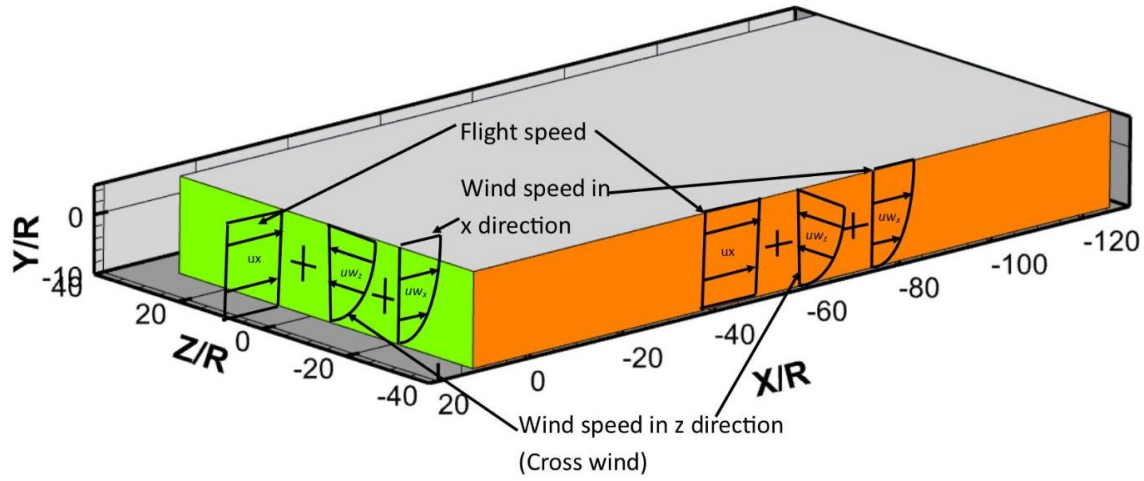

Figure 6.9 Atmospheric boundary conditions in the model

In OpenFoam, the atmospheric boundary layer velocity and lateral velocity code is as follows (Equation 6.19):

$$vector(\ -ux - u_{log} \cdot cos(wind.dir)\ , 0, u_{log} \cdot sin(wind.dir)\ ) \quad \text{(Equation 6.19)}$$

where *ux* is lateral velocity

and u_{log} is wind velocity logarithmic distribution

and *wind.dir* is the wind direction relative to the multicopter.

The boundary conditions applied to the *sideWall1* and *inlet* faces are identical. The *fixedWall* (ground) patch was specified as a moving wall boundary condition with velocity equal to flight speed (*ux*). The zero gradient velocity boundary condition was applied to *sideWall2* and *defaultFaces*.

The TKE was specified as *atmBoundaryLayerInletK* on both *SideWall1* and *Inlet.* The *atmBoundaryLayerInletK* specifies TKE as the function of Y/R coordinate in accordance with Equation 6.17. The *fixedWall* wall was *kqRWallFunction* (Hargreaves et al., 2007).

kqRWallFunction is a simpler representation of the *ZeroGradient* boundary condition (https://www.openfoam.com/documentation/guides/latest/doc/guide-bcs-wall-turbulence-kqRWallFunction.html accessed 29.09.2021).

The specific dissipation rate was specified as *atmBoundaryLayerInletOmega* on both *SideWall1* and *Inlet*. The *atmBoundaryLayerInletOmega* specifies the specific dissipation rate as the function of Y coordinate in accordance with Equation 6.18. The *fixedWall* patch uses the *omegaWallFunction* boundary condition that provides a specific dissipation rate near the wall.

The turbulent viscosity rate (*nut*) was specified for the *fixedWalls* as *atmNutWallFunction*. The zero gradient nut boundary condition was applied to other patches.

6.3.2.4 Plant canopy

The plant was modelled using a porous medium to represent the blocking effect of the plant canopy (Shi et al., 2021, Boulard et al., 2008). The porous medium was modelled by adding the sink term to the Navier-Stokes equation. The source term of the sink consists of two parts: a viscous term and an internal loss term (Equation 6.20).

$$S = -\frac{\mu}{\alpha}U - C_2\frac{\rho}{2}|U|U \qquad \text{(Equation 6.20)}$$

Where μ is air viscosity,

a is permeability,

ρ is air density,

and C_2 is the inertia loss coefficient.

The inertia loss coefficient is the result of multiplication of plant drag coefficient and plant area density (Equation 6.21) (Hong et al., 2018):

$$C_2 = C_d LAD \qquad \text{(Equation 6.21)}$$

Where C_d is plant drag coefficient,

and *LAD* is leaf area density.

The porous medium was implemented using the *fvOption* dictionary that applies the sink term to the selected cells. For tomato plants $a=0.395\ m^2$, $LAD=2.3\ m^{-1}$ and $C_d= 0.32$ (Shi et al., 2021, Boulard et al., 2008). The inertia loss coefficient was $C_2=0.736$. The height of modelled tomato plants was equal to 1.5R (0.4 m) (30-day-old tomato plant), 3R (0.8 m) (60-day-old tomato plant) and 4.5R (1.2m) (90 -day-old tomato plant) (Singh et al., 2015).

For wheat, $LAD=1.5\ m^{-1}$ and $C_d= 0.51$. The inertia loss coefficient is $C_2=0.765$ (Landsberg et al., 1971, Aiken et al., 2003). The inertia loss coefficient of wheat is very similar to the inertial loss coefficient of tomato plants. The viscous term is very small and can be neglected for comparison. Given that the height of the wheat is the same as the height of the tomato plant, the swath patterns are similar for the spraying of wheat and tomato plants.

Maize has a greater leaf area density ($LAD=2.93\ m^{-1}$) than wheat and tomato plants (Landsberg et al.). The drag coefficient of maize ($C_d=0.47$) is similar to wheat (Aiken et al., 2003). The inertia loss coefficient of maize was $C_2=1.337$. Therefore, the multicopter wake decays faster than in tomato plants when spraying in maize, resulting in less spray dispersion.

For grass, $LAD=1.6\ m^{-1}$ and $C_d= 0.34$ (Gillies et al., 2002). The inertia loss coefficient is $C_2=0.544$. These parameters were used in the modelling of spray deposition performed by DJI Agras Mg-1 multicopter.

6.3.3 Solution

The *fvSolution* dictionary defines the computational parameters and convergence criteria for the *SimpleFoam* solver. CFD simulation variables are stored in the cell centre. The variables

must be interpolated from cell centres to face centres to generate the fluxes for the surface integral in the transport equation (Haddadi et al., 2018). A variety of discretisation schemes is available in OpenFOAM (https://www.openfoam.com/documentation/user-guide/6-solving/6.2-numerical-schemes, accessed 30.08.2021). The discretisation schemes used in this study are shown in Table 6.4. They were suggested by a tutorial (http://www.wolfdynamics.com/wiki/tipsandtricks.pdf, accessed 30.08.2021) for mesh non-orthogonality between 40^{o} and 60^{o}. Mesh non-orthogonality is an angle between a face normal vector and a line connecting two cell centres in a mesh (Ishigaki et al., 2017). In all case studies, mesh non-orthogonality did not exceed 50^{o}.

Table 6.4 Discretization scheme used in the fvSchemes dictionary (https://www.openfoam.com/documentation/user-guide/6-solving/6.2-numerical-schemes, accessed 30.08.2021), (Wahono, 2013).

Variable	Discretisation scheme	Numerical behaviour
Gradient schemes		
default grad(U) grad(k) grad(omega)	Gauss linear	Second-order, Gaussian Integration - Using Cell centre values
Divergence schemes		
div(phi, U) div(phi,k) div(phi,omega) div(phi,epsilon)	bounded Gauss linear	Second-order, central differencing for face flux term, unbounded
Laplacian Schemes		
Default	Gauss linear	Linear central differencing, interpolation
Interpolation Schemes		

Default	Linear	Central differencing, unbounded
Surface normal gradient discretisation		
snGrad	limited 1	A blending of corrected and uncorrected schemes

The residual control was used in every model. When the initial residual of the field equation falls below specified values, the solution is terminated. The residual is determined as the difference in the value of a quantity (*p, u, v, w, k* etc.) between iteration t and t+1.

The relaxation factors were equal to 0.95. They control the under-relaxation. This method is used for improving the stability of a computation. Under-relaxation limits the amount of a change of a variable from iteration t to t+1. When the relaxation factor is 0, the solution doesn't change with iteration. When the relaxation factor is 1, the matrix diagonal equality is guaranteed.

6.4 Computational results

6.4.1 Multicopter with APC 1045 rotors

Chapter 4 outlined the PIV experimental data for APC 1045 rotors in lateral flow. The model tested conditions similar to the PIV experiment. In streamwise and spanwise configuration, the model was tested at 2 m/s, 6 m/s and 10 m/s of lateral velocity. The measured rotational speed was equal to 5400 RPM.

6.4.1.1 Geometry and mesh

The domain and mesh required for the analysis were generated using the *blockMesh* dictionary and *geometry* file. The size of the domain was as follows for all computational cases (Table 6.5), (Figure 6.10):

Table 6.5 Size of the domain in the APC 1045 rotor computational analysis

xmax	xmin	ymax	Ymin	zmax	zmin
-100R	10R	5R	-14.17R	-20R	20R

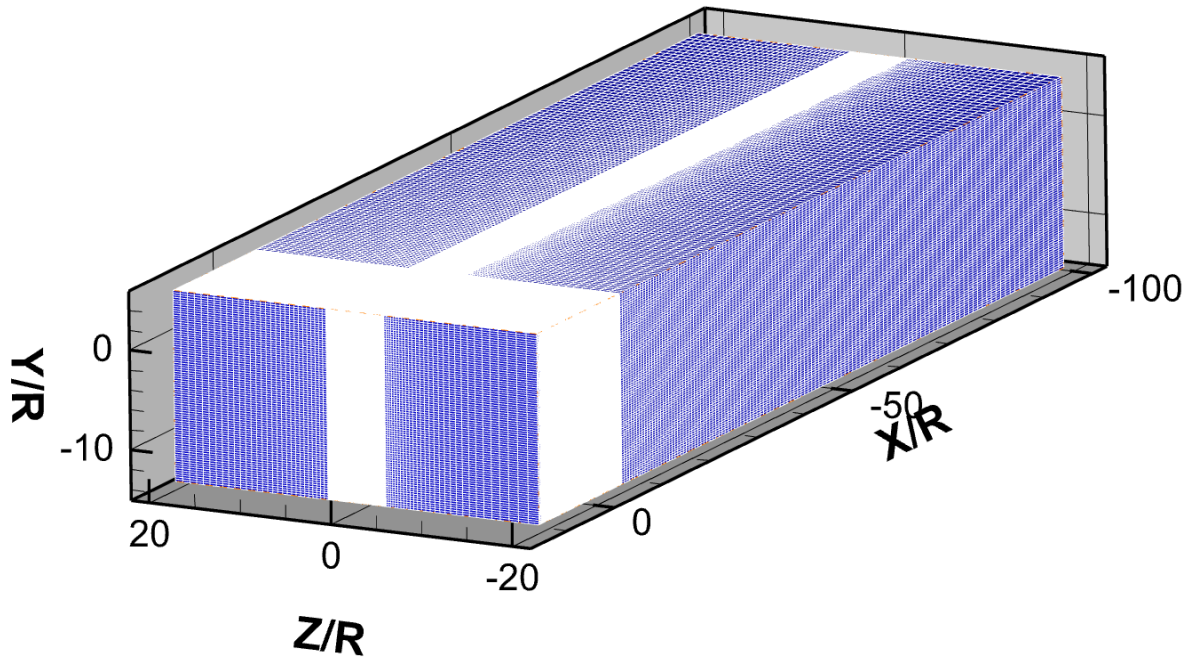

Figure 6.10 Generated mesh for APC 1045 rotors model.

The generated mesh consisted of 5,956,256 hexahedral and 28010 polyhedral elements. The mesh was refined in the zone of rotors and in the zone of rollup vortices. The rotor disk was immersed in the domain at Y/R=0 in streamwise or spanwise configurations (Figure 6.11). A single-rotor disk consists of 571 cells.

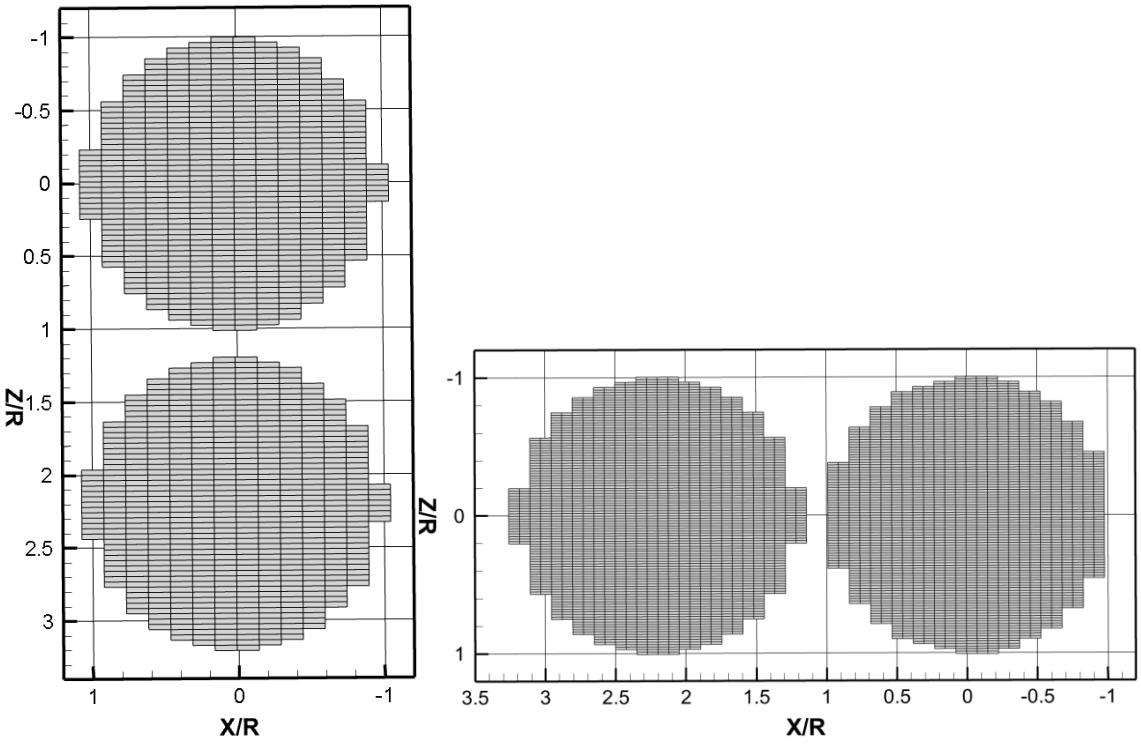

Figure 6.11 Generated rotor disk for spanwise (left) and streamwise (right) configurations

6.4.1.2 Boundary conditions

The model used the velocity flow field from the PIV data for a single APC 1045 rotor (at Y/R=0.1). The downwash velocity was interpolated using cubic polynomial interpolation at Z/R ∈ (0...0.8) (Figure 6.12, Equation 6.22 through Equation 6.24). The swirl velocity was interpolated using a sextic polynomial function at Z/R ∈ (0...0.8). After 0.8R the average downwash and swirl velocities are near to null, but there are velocity fluctuations

corresponding to tip vortices. These velocity fluctuations were taken into account by TKE boundary conditions. The TKE experimental data, retrieved from CTA analysis, was interpolated using a ratio of polynomials (Equation 6.24).

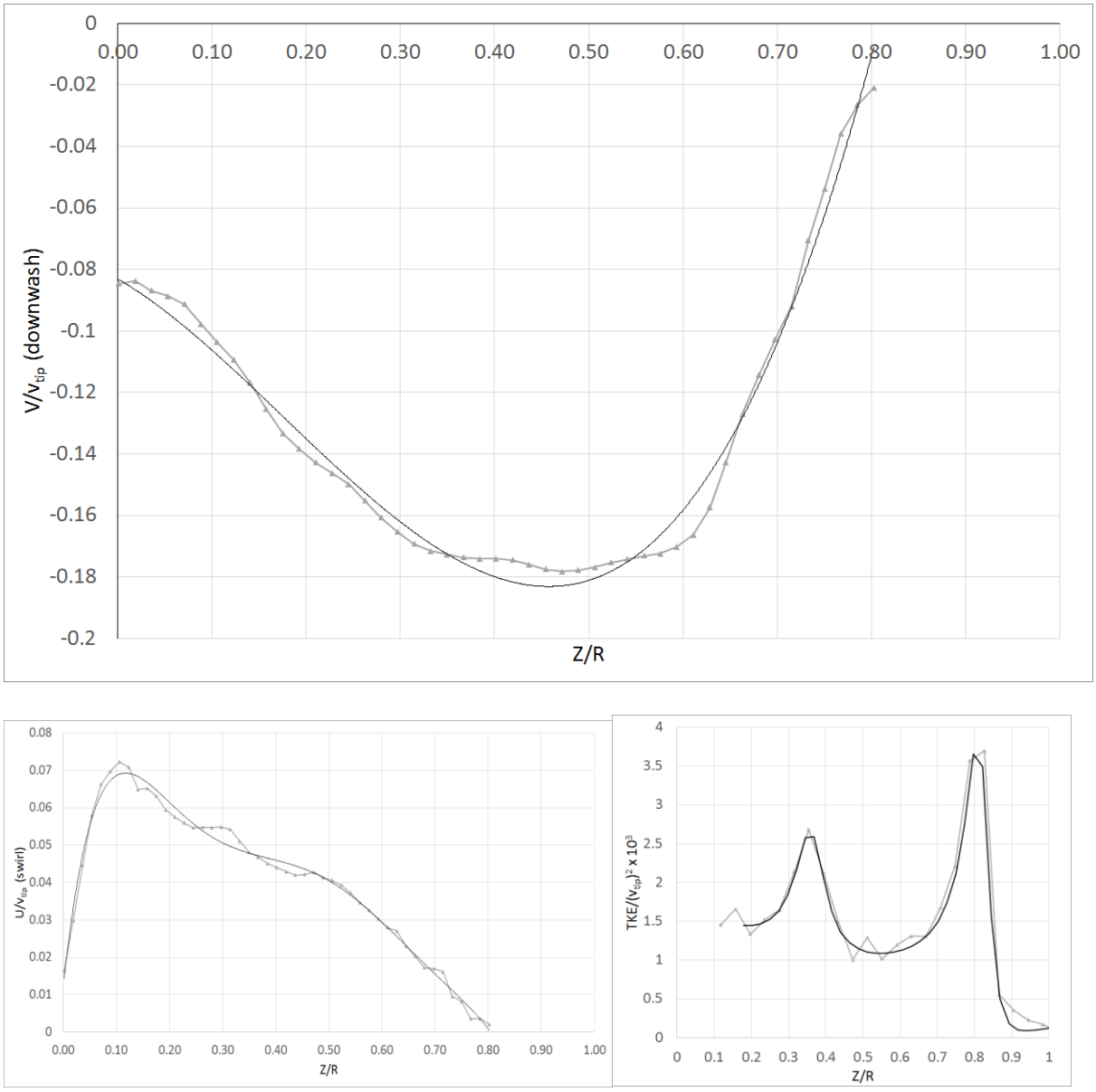

Figure 6.12 Interpolation (black line) of downwash (top), swirl (bottom left) velocity component and TKE (bottom right) measured in a single APC 1045 rotor PIV analysis (grey line with triangular markers)

$$V/v_{tip} = 1.2416(r/Rr)^3 - 0.6571(r/Rr)^2 - 0.1781(r/Rr) - 0.083;\ variation^2 = 0.985$$

(Equation 6.22)

$$U//v_{tip} = -19.126(r/Rr)^6 + 56.098(r/Rr)^5 - 64.399(r/Rr)^4 + 36.271(r/Rr)^3 - 10.319(r/Rr)^2 + 1.2894(r/Rr) + 0.0124;\ variation^2 = 0.9895$$

(Equation 6.23)

$$TKE//v_{tip}^2=(2.961(r/Rr)^4-7.574(r/Rr)^3+6.856(r/Rr)^2-2.58r/Rr+0.3495/(0.1987(r/Rr)^5-0.3891(r/Rr)^4+0.216(r/Rr)^3+0.02593(r/Rr)^2-0.04196r/Rr+0.0073);\ variation^2 = 0.988$$

(Equation 6.24)

The interpolation function was applied to *slave* and *master* boundaries of both rotors simultaneously. In TKE boundary conditions, the peak of the interpolation function in Z/R=0.8 is narrow. The coarse grid does not allow precise modelling of the narrow peak. The mesh independence study verified that the solution is not affected by the mesh size (section 6.4.1.4).

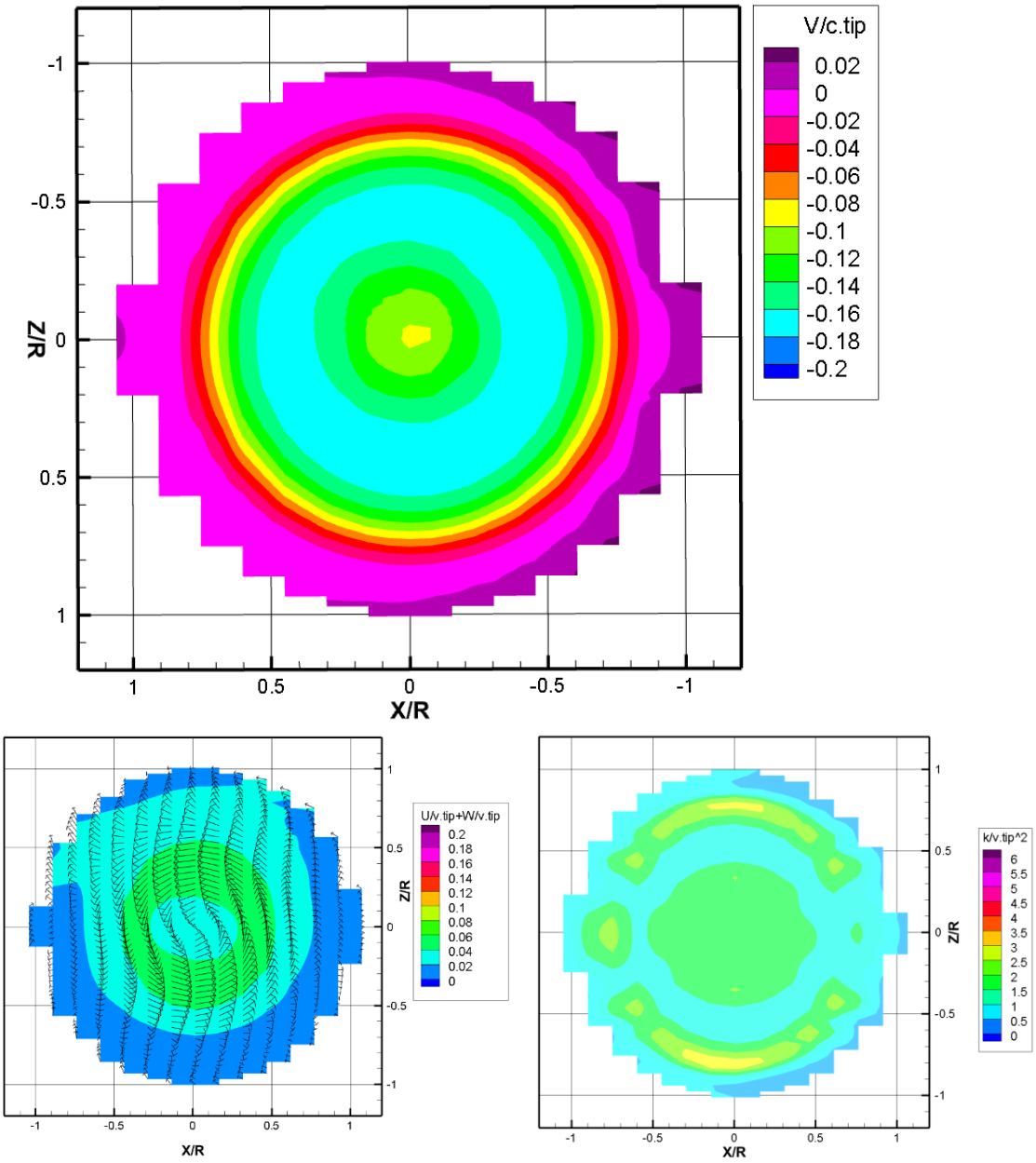

Figure 6.13 Rotor boundary conditions: downwash velocity (top), swirl velocity (bottom left), TKE (bottom right).

Additionally, to mimic the freestream induced flow over the rotor disk, the lateral velocity was added to the X component velocity on the rotor disk.

The summary table of boundary conditions applied in the model can be found in Table 6.6

Table 6.6 Summary of boundary conditions applied in the APC 1045 rotors analysis

	p	U, vector	TKE (k)	omega	nut
inlet	zero gradient	(lateral velocity, 0, 0)	zero gradient	zero gradient	zero gradient
outlet	0	zero gradient	inletOutlet	zero gradient	zero gradient
sideWall1	zero gradient	zero gradient	zero gradient	zero gradient	zero gradient
sideWall2	zero gradient	zero gradient	zero gradient	zero gradient	zero gradient
defaultFaces	zero gradient	zero gradient	zero gradient	zero gradient	zero gradient
fixedWalls	zero gradient	(0, 0, 0)	kqRWallFunction	omegaWallFunction	NutkWallFunction
rotor	zero gradient	groovyBC	groovyBC	zero gradient	zero gradient

6.4.1.3 Results

The results obtained from the computational analysis were compared with the results obtained in PIV experiments.

6.4.1.3.1 Rotors arranged streamwise

Vertical planes (X/R- Y/R) at Z/R=0 (passing through the rotor shaft) through the velocity field show that the leeward wake is shadowed by windward wake and the rotor is tilted by 20º to 25º less than the downwash of the windward rotor (Figure 6.14). The velocity magnitude is normalised by tip velocity in the contour plot. The same effect can be observed in PIV analysis (Chapter 4, Figure 4.28).

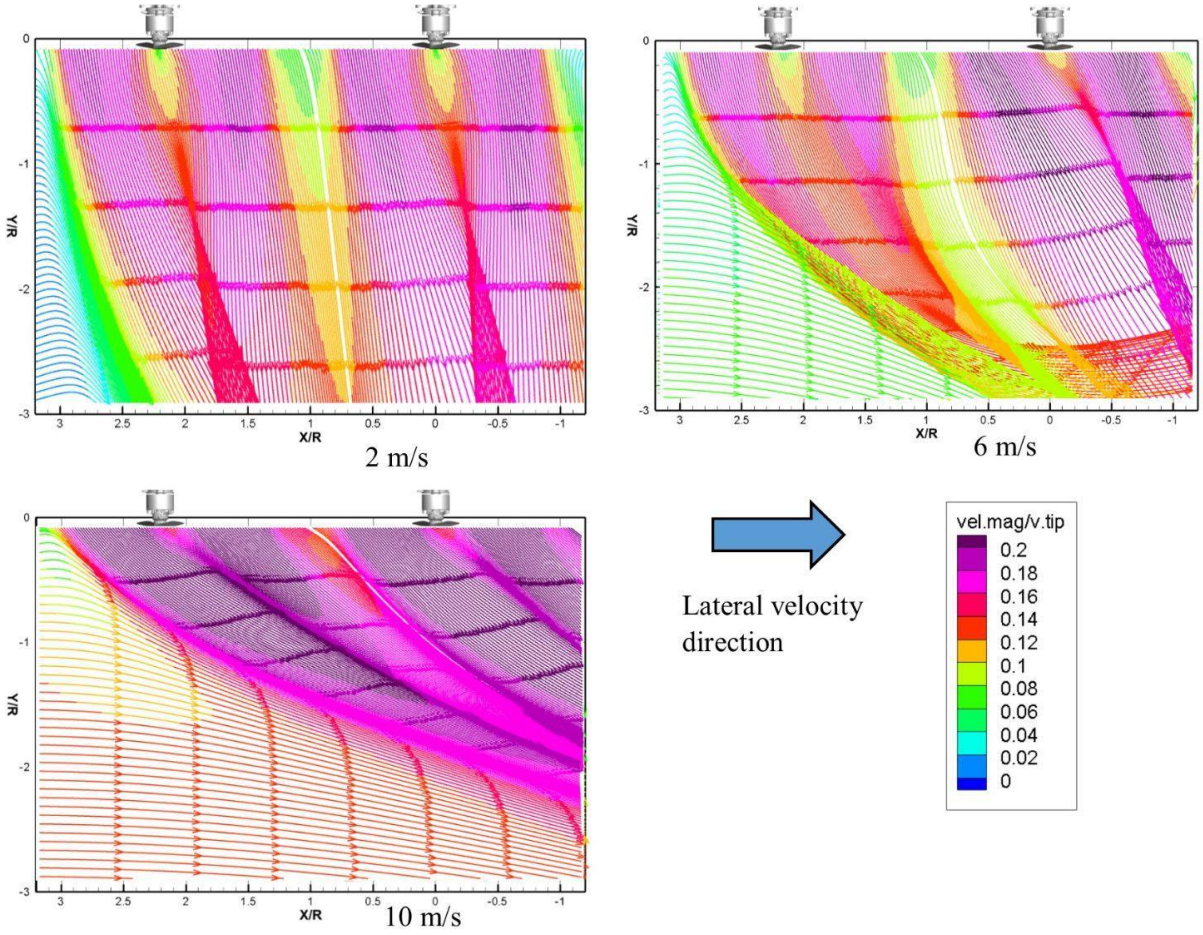

Figure 6.14 Velocity magnitude and streamlines on vertical planes through the axes of the rotors showing the tilt of the downwash of the front and rear rotors at flight speeds of 2 m/s (top left), 6 m/s (top right), 10 m/s (bottom left), and 14 m/s (bottom right). Rotor positions shown with CAD inserts above each plot.

The zone between the rotors remains a low-speed zone because it is shaded by the windward rotor.

The downwash of two rotors positioned streamwise in 6m/s lateral flow (Figure 6.15) is shown in horizontal planes X/R-Z/R through the computational results at Y/R=0.04 (left) and Y/R=1 (right). The velocity magnitude is normalised by tip velocity in the contour plots.

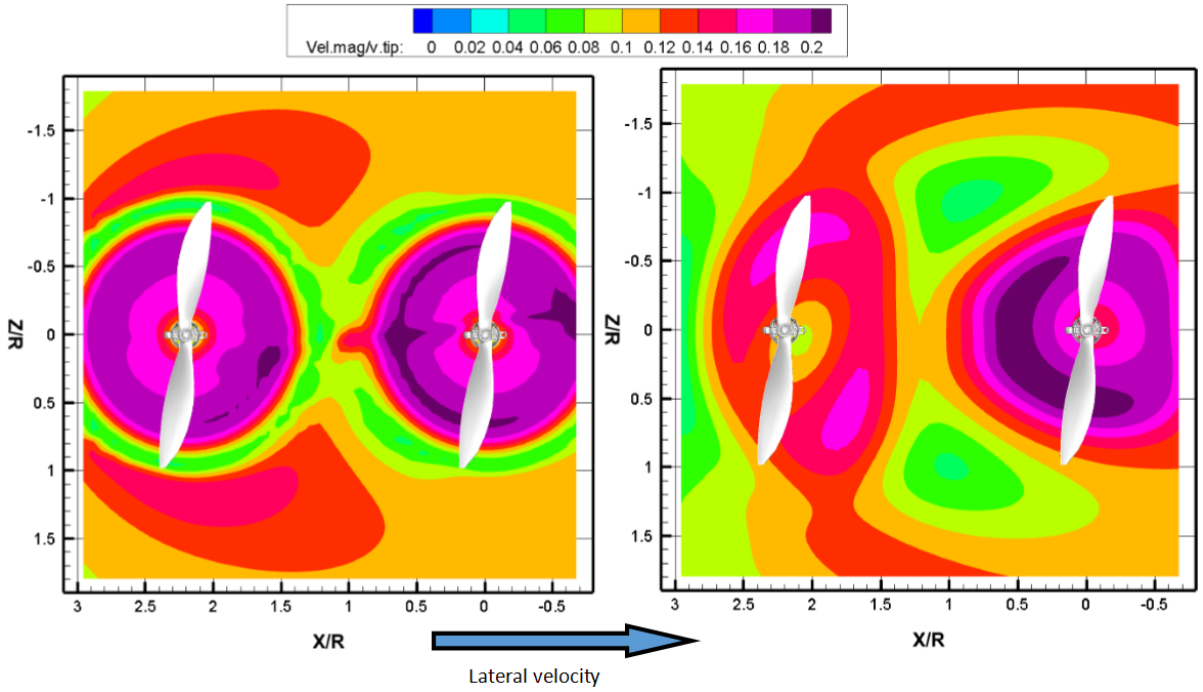

Figure 6.15 Velocity magnitude normalised by rotor tip velocity on horizontal planes below the rotor at a flight speed of 6 m/s: (left) 0.04R below the rotor plane; (right) 1R below the rotor plane.

The downwash of the windward rotor is deformed into a horseshoe shape by the lateral airflow, but the downwash of the lee rotor is nearly circular. In the PIV data, the same influence has been observed (Chapter 4, Figure 4.30). This observation started at a lateral velocity of 6 m/s.

The rollup vortex is an area of upward-flowing air generated by the rotor tip interacting with a lateral velocity. This effect was observed in PIV analysis and is present in CFD modelling (Figure 6.16).

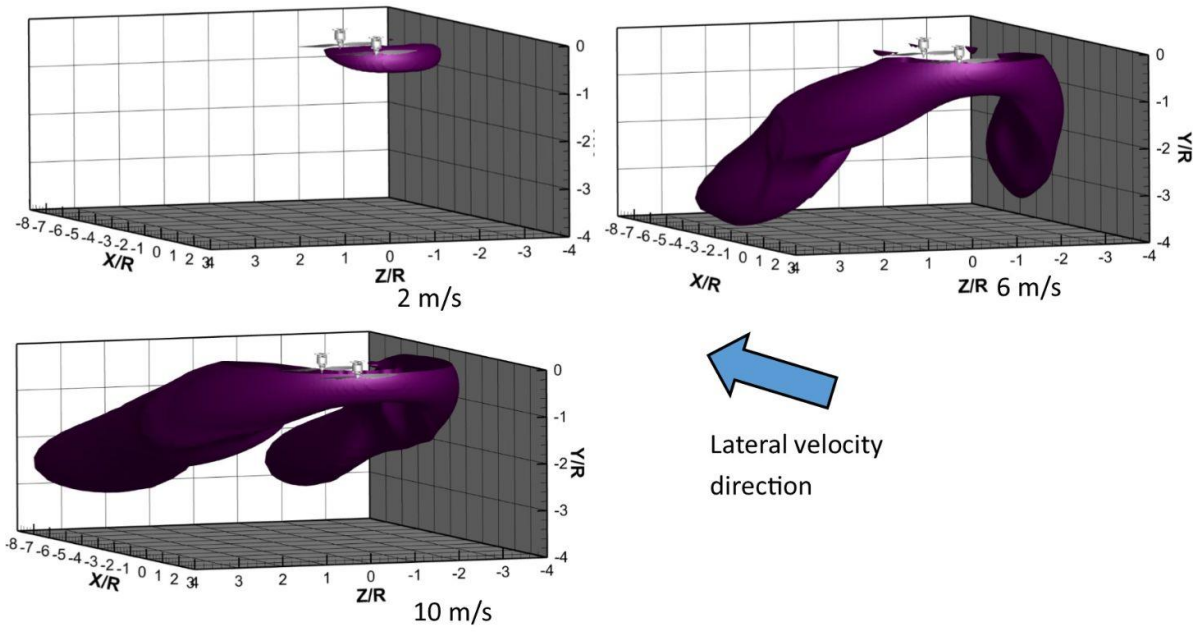

Figure 6.16 Isosurface of vertically upward air velocity V/v.tip=+0.024 at a flight speed of 2 m/s (top, left); 6m/s (top right) 10 m/s (bottom left).

As the flight speed increases, this region of upward velocity becomes smaller in the vertical direction (-Y/R) and expands in the upwind and downwind directions (+X/R,-X/R). The windward rotor has previously been seen to shield the flow over the leeward rotor. Because the leeward rotor experiences less lateral velocity, the vortex of interaction on the leeward rotor is not visible at 2m/s and 6m/s lateral velocity. However, the vortex of interaction exists at 10m/s lateral flow on both rotors.

A direct comparison was performed between modelled and experimental PIV data velocity components. The cell data was sampled at a vertical distance (Y/R) from the rotor disk equal to -1 along the stream direction (X/R).

For the comparison, the velocity was collected from PIV and model data at a vertical distance of Y/R=-1 away from the rotor disc (Figure 6.17 through Figure 6.19). The one standard

deviation. shown on the PIV graph was obtained from a sequence of images obtained in a relative experiment (Chapter 2, Chapter 3).

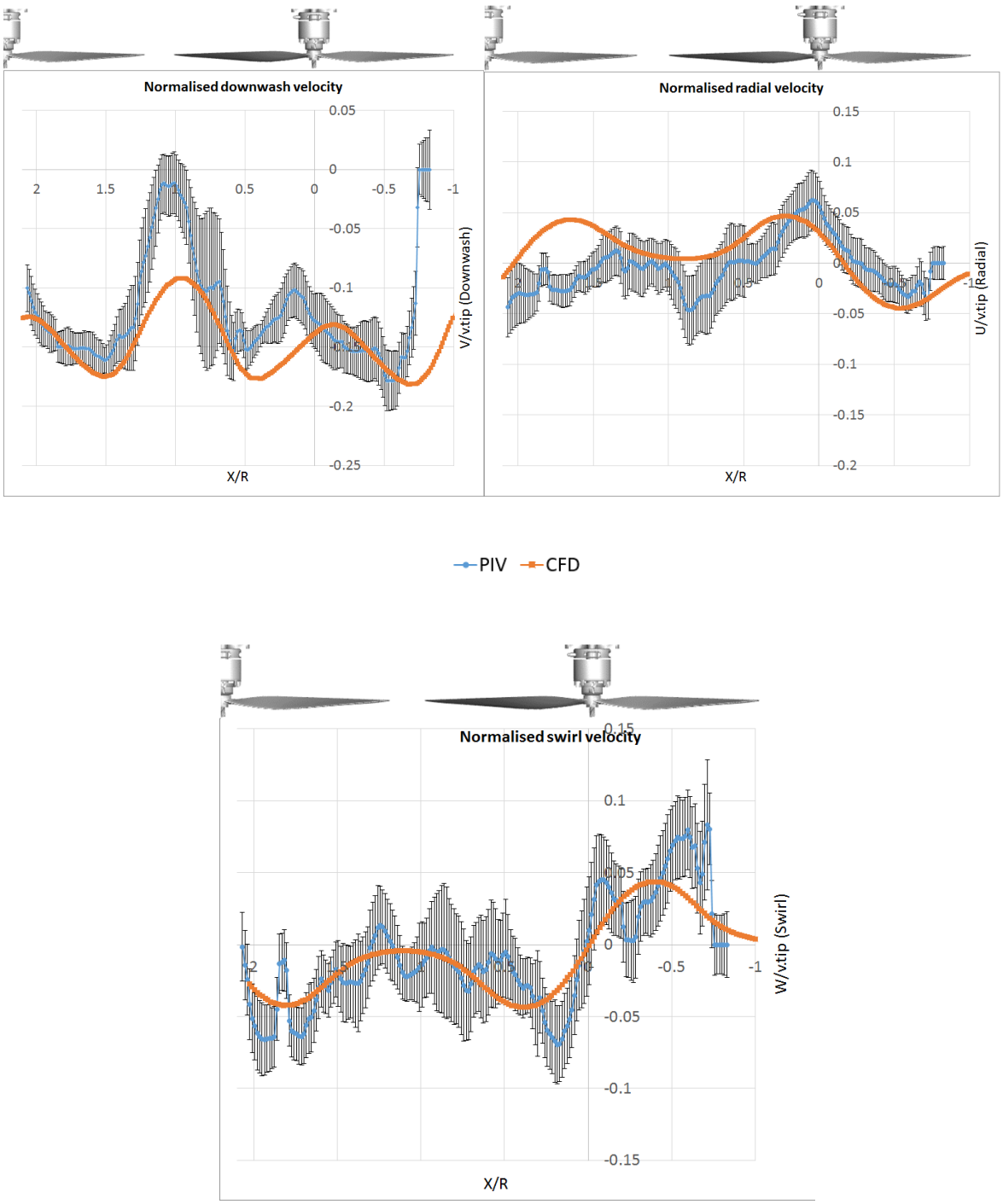

Figure 6.17 Comparison of PIV (blue circles) and CFD (orange squares) downwash (top), radial (bottom left) and swirl (bottom right) velocity components in the 2m/s streamwise configuration when Y/R=-1, Z/R =0

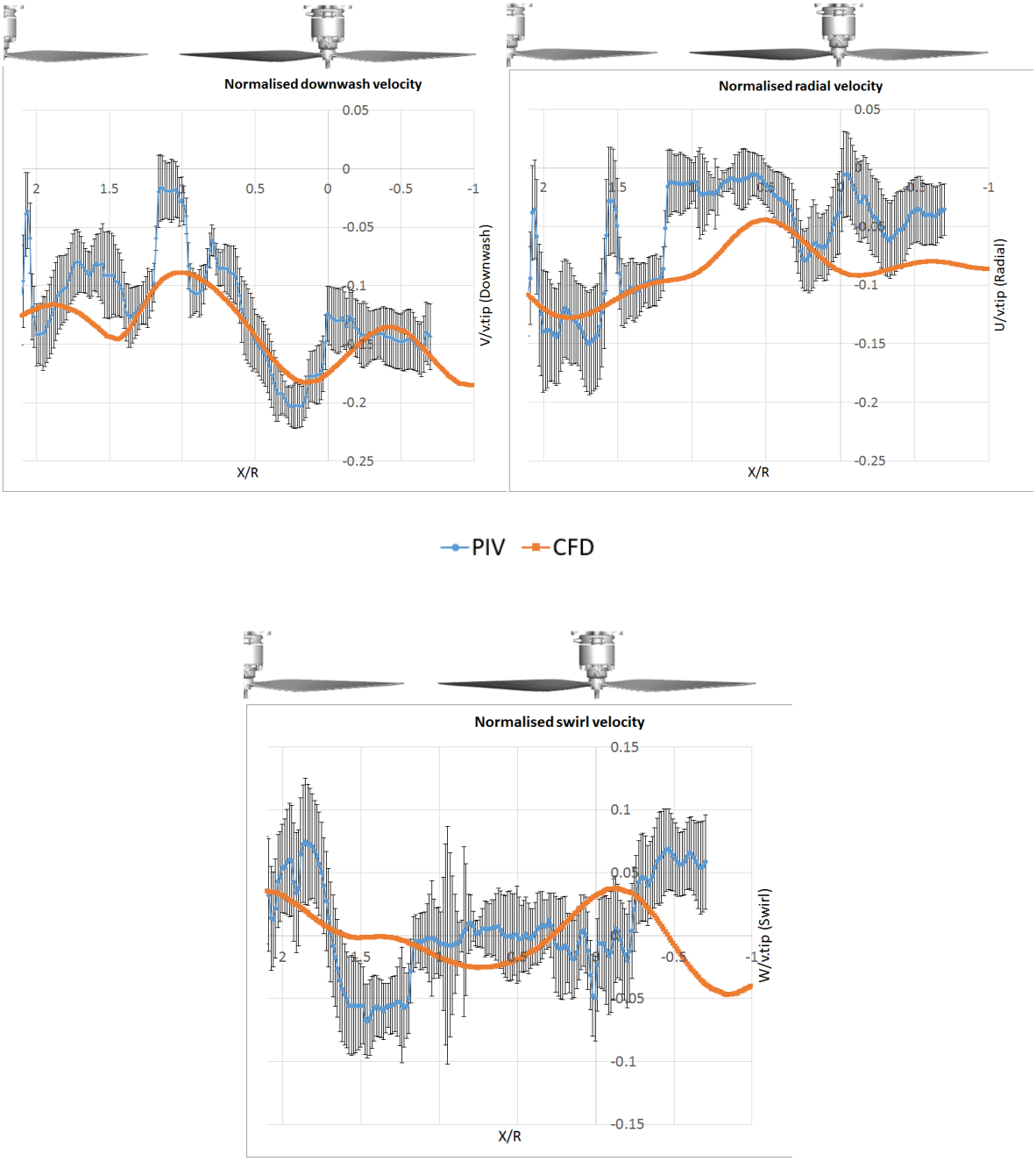

Figure 6.18 Comparison of PIV (blue circles) and CFD (orange squares) downwash (top), radial (bottom left) and swirl (bottom right) velocity components in the 6m/s streamwise configuration when Y/R=-1, Z/R =0

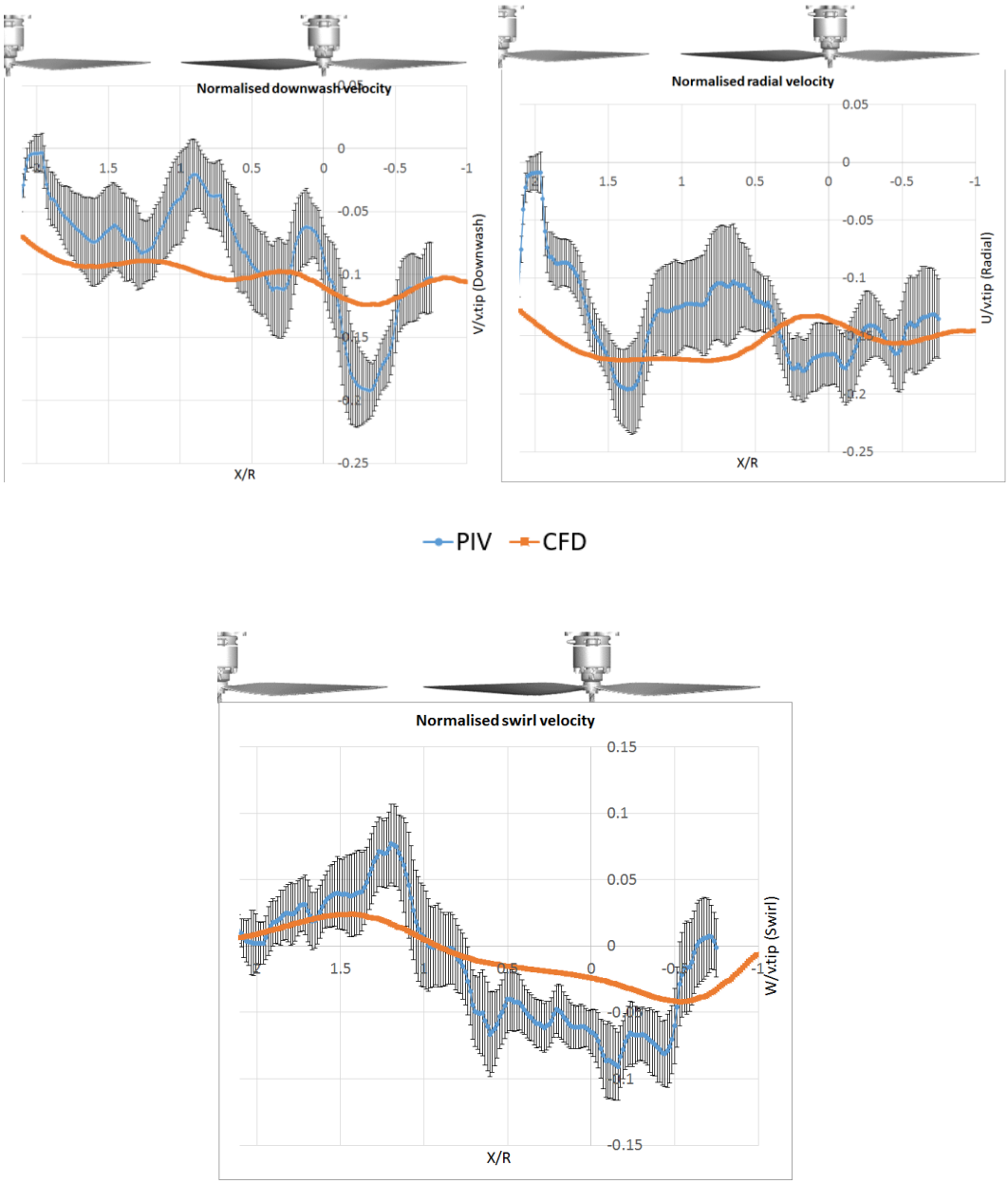

Figure 6.19 Comparison of PIV (blue circles) and CFD (orange squares) downwash (top), radial (bottom left) and swirl (bottom right) velocity components in the 10m/s streamwise configuration when Y/R=-1, Z/R =0

At lateral velocities of 2 m/s and 6 m/s, the downwash, swirl, and radial velocity components of the model are mostly within one S.D. of PIV data. At 10 m/s lateral velocity, the downwash velocity components of the CFD and PIV data do not match. The major discrepancy is in zones with near-zero velocity (between rotors and under the centre of the rotor). In PIV data, the

downwash and swirl components decrease to near-zero values. In CFD data, the downwash and swirl velocity components are lower than the main downwash but do not decrease to zero. This can be explained by numerical dissipation introduced by the CFD code. A similar discrepancy was previously reported at lower mesh resolutions by Cadieux et al., (2017). Another explanation of the velocity vector field difference in the zone between rotors is the influence of rotor tip vortices. The generated vortices interact strongly (Chapter 4). This may generate the upward velocity region between rotors. In addition, rotor tip vortices generate a radial velocity component on the rotor disk. In CFD, the tip vortex was mimicked by TKE. This method does not prescribe the propagation of the vortex with the downward propagation of the wake. Therefore, there was less interaction between wakes in the zone between rotors. The radial velocity component was not introduced to the model, which may explain the difference between radial velocity components in CFD and PIV experiments. Boundary conditions are another source of uncertainty. The rotor boundary conditions used for CFD analysis were obtained without lateral velocity present in the flow. In PIV experiments, lateral velocity was generated by a wind tunnel, which can introduce a source of turbulence near the mouth of the wind tunnel. The rotor was placed after a wind tunnel diverging section, 200 mm approximately below the edge of the jet.

6.4.1.3.2 Rotors arranged spanwise

At a flight speed of 2m/s, the zone of upward velocity generated by the tip vortex is generated, increasing in volume as the flight speed increases. A similar effect was observed in PIV (Chapter 4, Figure 4.35). It is demonstrated by the iso-surface of vertically upward air velocity V/v.tip=+0.024 (Figure 6.20).

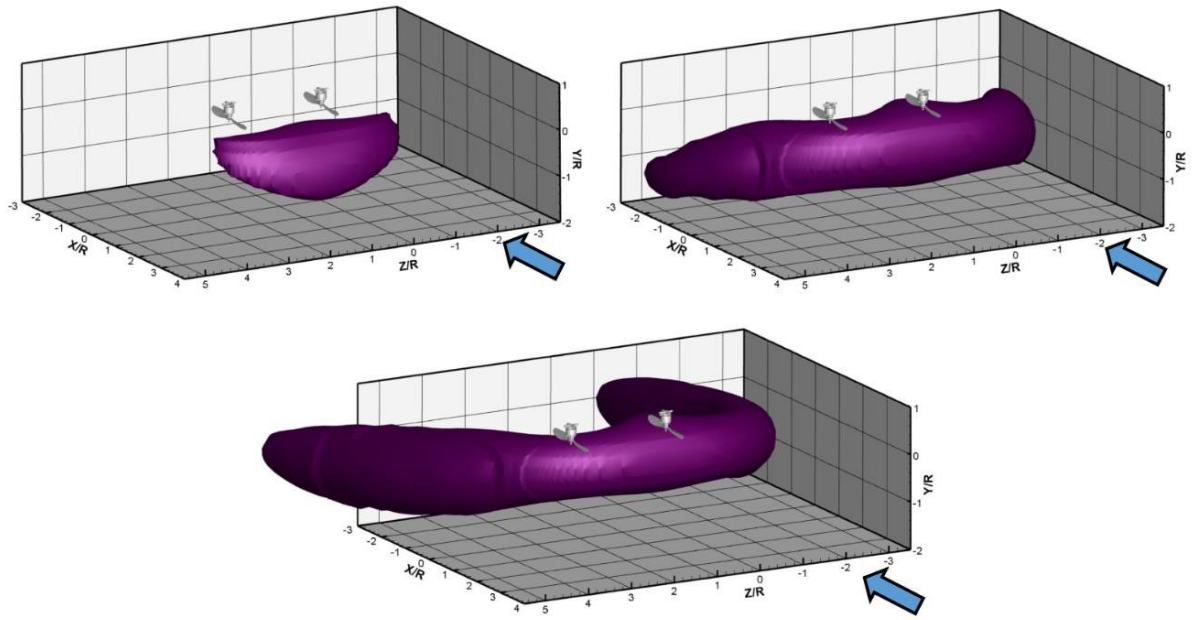

Figure 6.20 Iso-surface of vertically upward air velocity V/v.tip=+0.024; flight speed 2m/s (top left), 6m/s (top right), 10m/s (bottom).

PIV and model data were used to sample velocity at a vertical distance of Y/R=-1 away from the rotor disc for comparison. The 1 S.D. depicted on the PIV (Figure 6.21 and Figure 6.22) graph was obtained from a sequence of images obtained in an experiment (Chapter 2, Chapter 4).

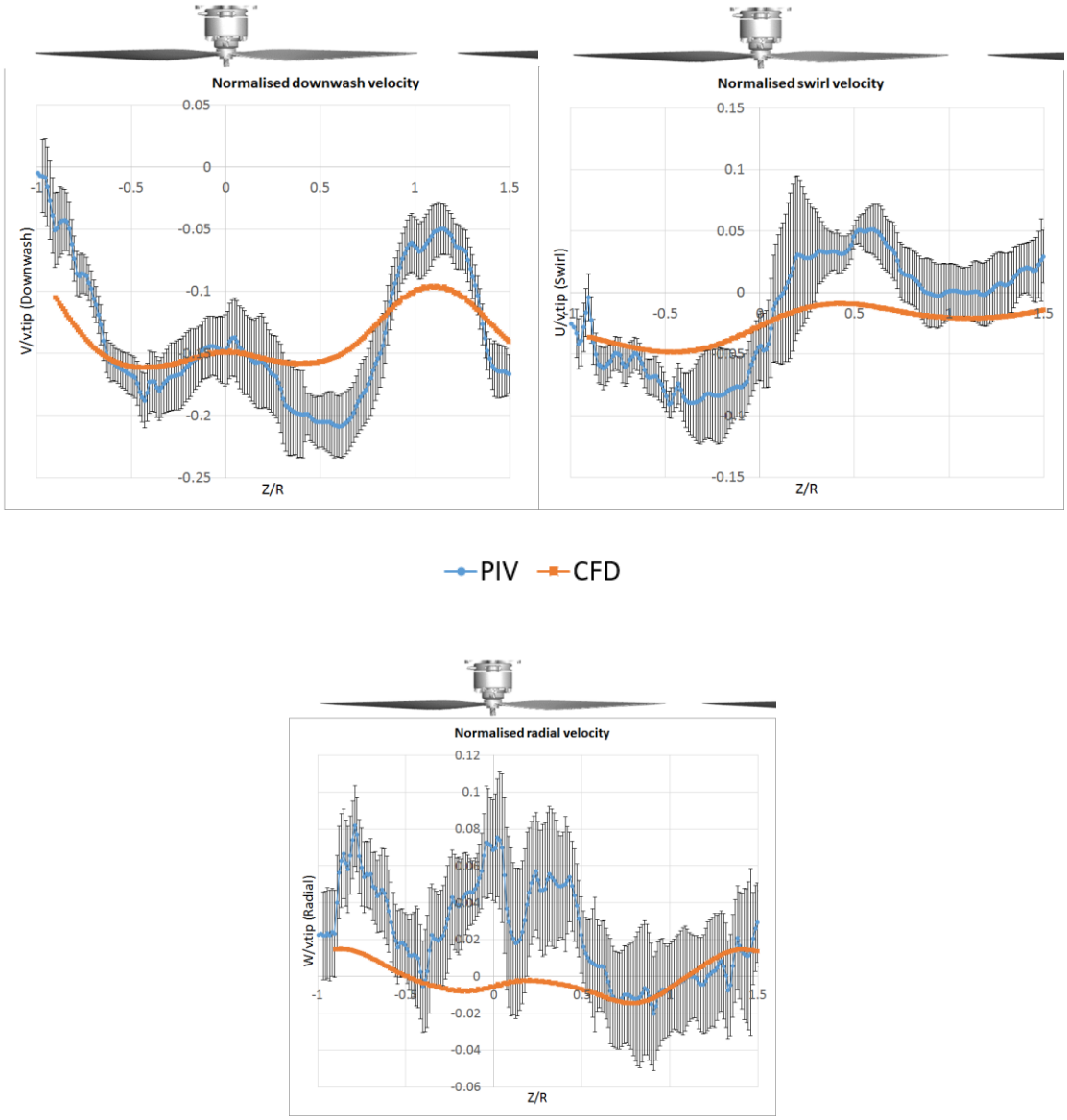

Figure 6.21 Comparison of PIV (blue circles) and CFD (orange squares) downwash (top), radial (bottom left) and swirl (bottom right) velocity components in the 2m/s spanwise configuration when Y/R=-0.5, X/R =0

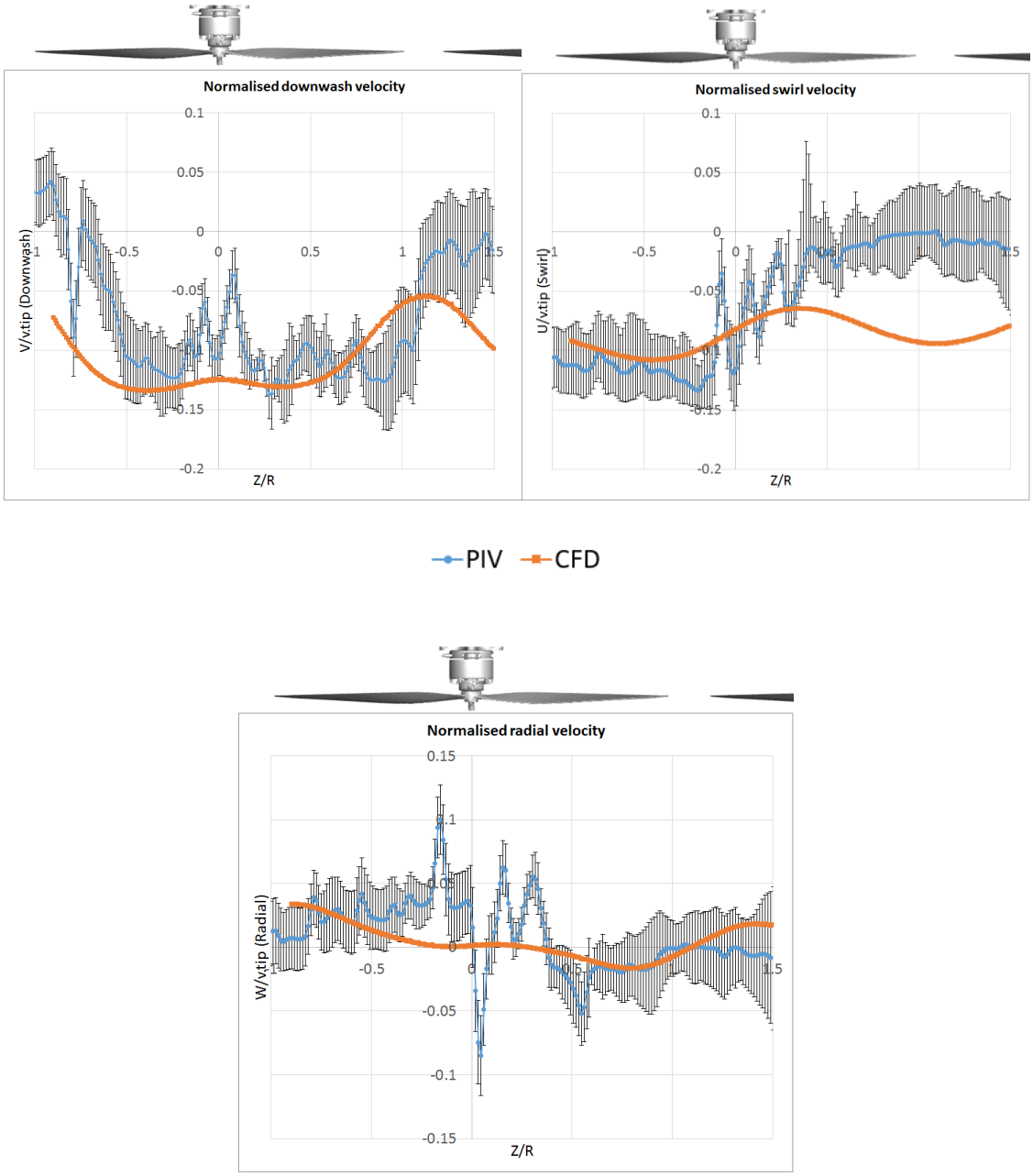

Figure 6.22 Comparison of PIV (blue circles) and CFD (orange squares) downwash (top), radial (bottom left) and swirl (bottom right) velocity components in the 6m/s spanwise configuration when Y/R=-0.5, X/R =0

In 2 m/s lateral velocity flight, the downwash, swirl and radial velocity components are mostly within 1 S.D. At a lateral velocity of 6 m/s, the wakes merge. This rotor interaction effect is thought to exist due to the low-pressure zone between rotors. This effect is generated by interacting vortices not prescribed in the model. The downwash in PIV data is shifted towards

another rotor (+Z), which is not observed in CFD analysis. The over-dissipative CFD was found in the present mesh in zones of near-zero velocity (under the centre of the rotor and between rotors). The mesh independence study (Discussed in section 6.4.1.4) demonstrated the zones of over-dissipative CFD.

6.4.1.4 Mesh independence study

A mesh independence study is required to test whether the obtained wake velocity field does not depend on the mesh size. In streamwise and spanwise configurations, the following mesh parameters were tested (Table 6.7):

Table 6.7 Mesh size parameters used for the mesh independence study of APC 1045 rotors in streamwise and spanwise configurations.

	Coarse mesh	Regular mesh	Fine mesh
Number of cells	5’956’256	10’386’342	18’076’608
Number of cells in one rotor disk	571	1090	1528

The velocity for different mesh sizes was sampled at Y/R=-1 (Figure 6.23) for rotors in streamwise configuration.

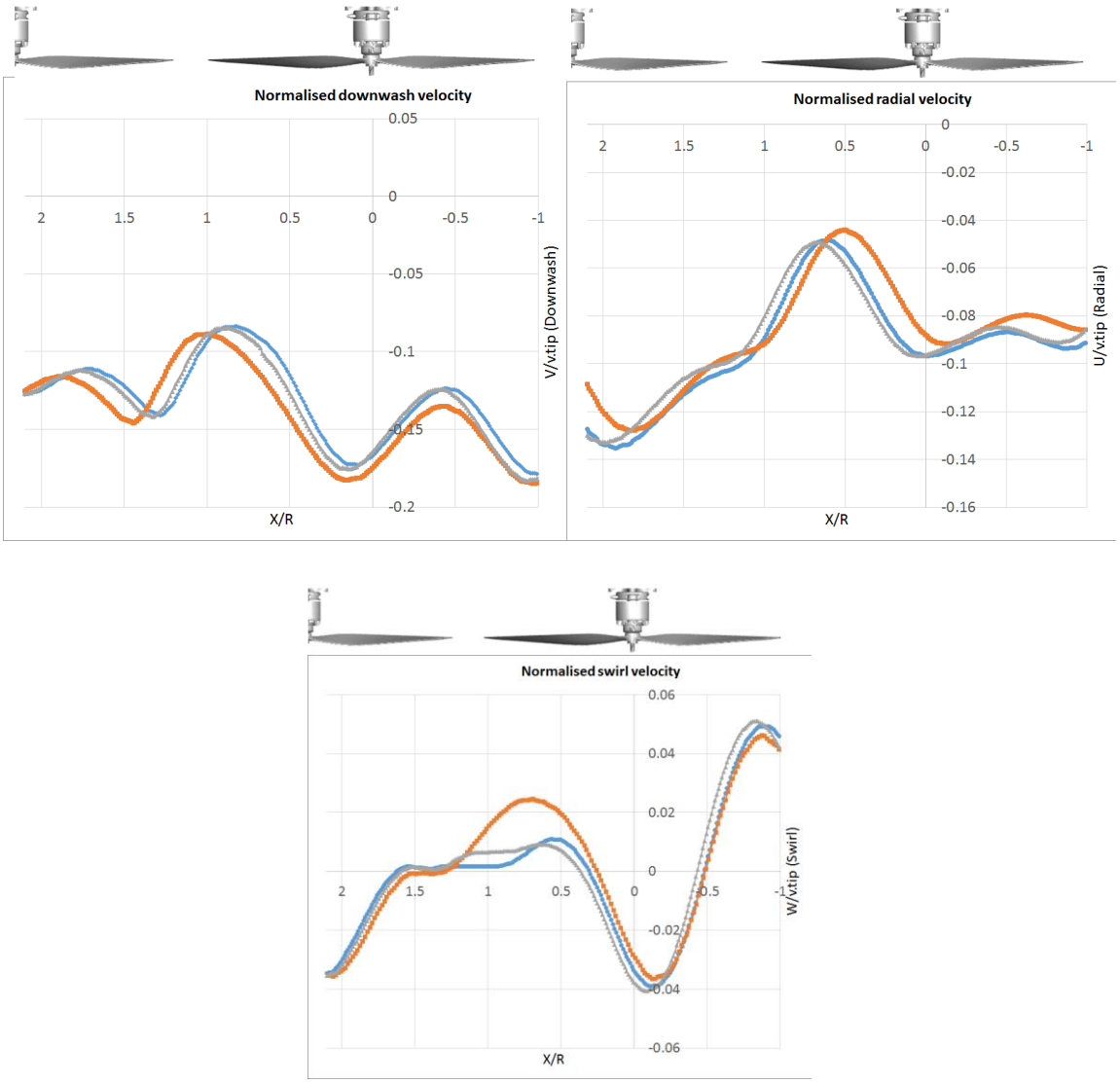

Figure 6.23 CFD computational results with coarse mesh (orange squares), regular mesh (grey circles) and fine mesh (blue squares). Downwash (top left), radial (top right), and swirl (bottom) normalised velocity components in the 6 m/s streamwise configuration when Y/R=-1, Z/R =0.

The normalised downwash and radial velocity components are similar. The downwash and radial velocity components in the lateral (X/R) direction are dependent on grid size. The offset in X/R (lateral direction) may be explained by different grid sizes. The swirl velocity component is dependent on mesh size in the zone between rotors. This may be explained by a numerical dissipation in the result with coarse mesh.

The velocity for different mesh sizes was sampled at Y/R=0.5 (Figure 6.24) for rotors in spanwise configuration.

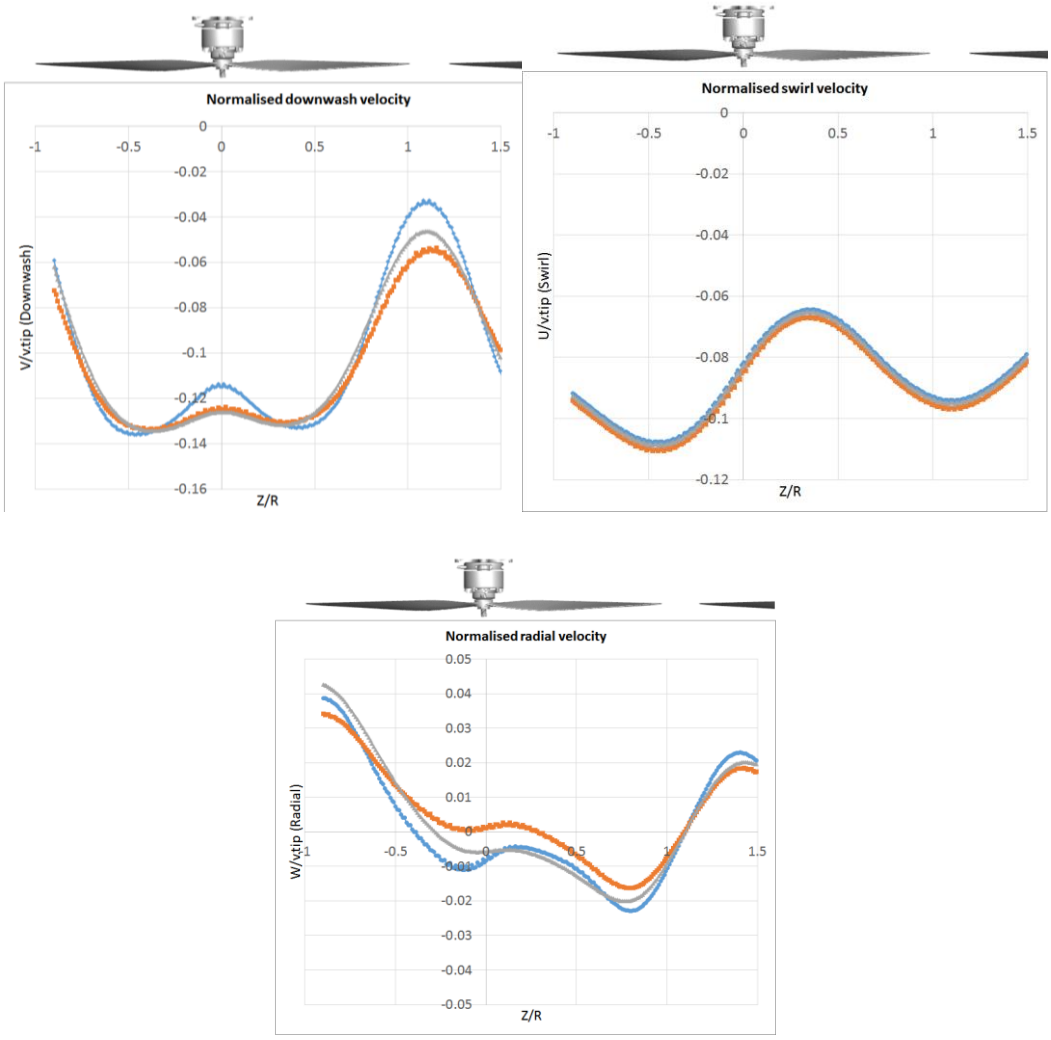

Figure 6.24 CFD computational results with coarse mesh (orange squares) and fine mesh (blue squares). Downwash (top left), radial (top right) and swirl (bottom) normalised velocity components in the 6 m/s spanwise configuration when Y/R=-0.5, Z/R =0.

In the spanwise configuration, the solution is dependent on mesh size in zones where the specified boundary conditions are zero or near zero (between rotors and under the centre of the rotor). In addition, in the sampled plane, the radial velocity was not described in any boundary

condition. Therefore, the radial velocity component depends on mesh size. However, this component is very small (0.04v_{tip} maximum) compared to the downwash velocity component.

6.4.2 Multicopter with DJI E7000 rotors

6.4.2.1 Geometry

The domain and mesh necessary for the analysis were generated using the *blockMesh* dictionary and *geometry* file. The domain size was as follows (Table 6.8, Figure 6.25):

Table 6.8 Domain size in the DJI E7000 rotors computational analysis

xmax	xmin	ymax	ymin	zmax	zmin
-10R	4.76R	5R	-7.14R	-10R	10R

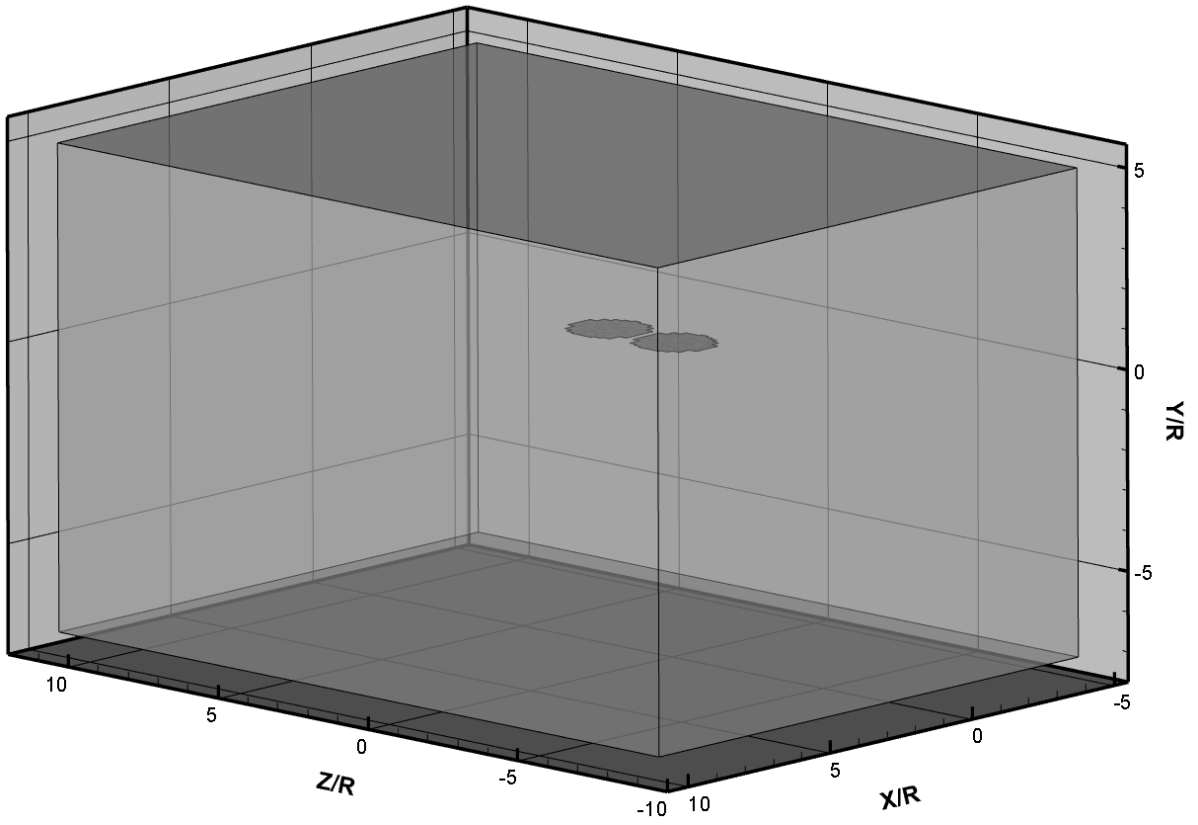

Figure 6.25 Generated domain for DJE E7000 rotors model.

There were 7’696’290 hexahedral and 5742 polyhedral elements in the produced mesh. The mesh was refined in the rotor zone. The rotor disc was immersed in the domain at Y/R=0. There are 278 cells in a single rotor disc.

6.4.2.2 Boundary conditions

The model used the velocity flow field from PIV data for a single DJI E 7000 rotor (at Y/R=0.1). The downwash and swirl velocities were interpolated using quadrinomial interpolation at $Z/R \in (0...0.85)$. (Figure 6.26, Equation 6.25 through Equation 6.27). The TKE experimental data, retrieved from CTA analysis, was interpolated by rational function with polynomial function in denominator.

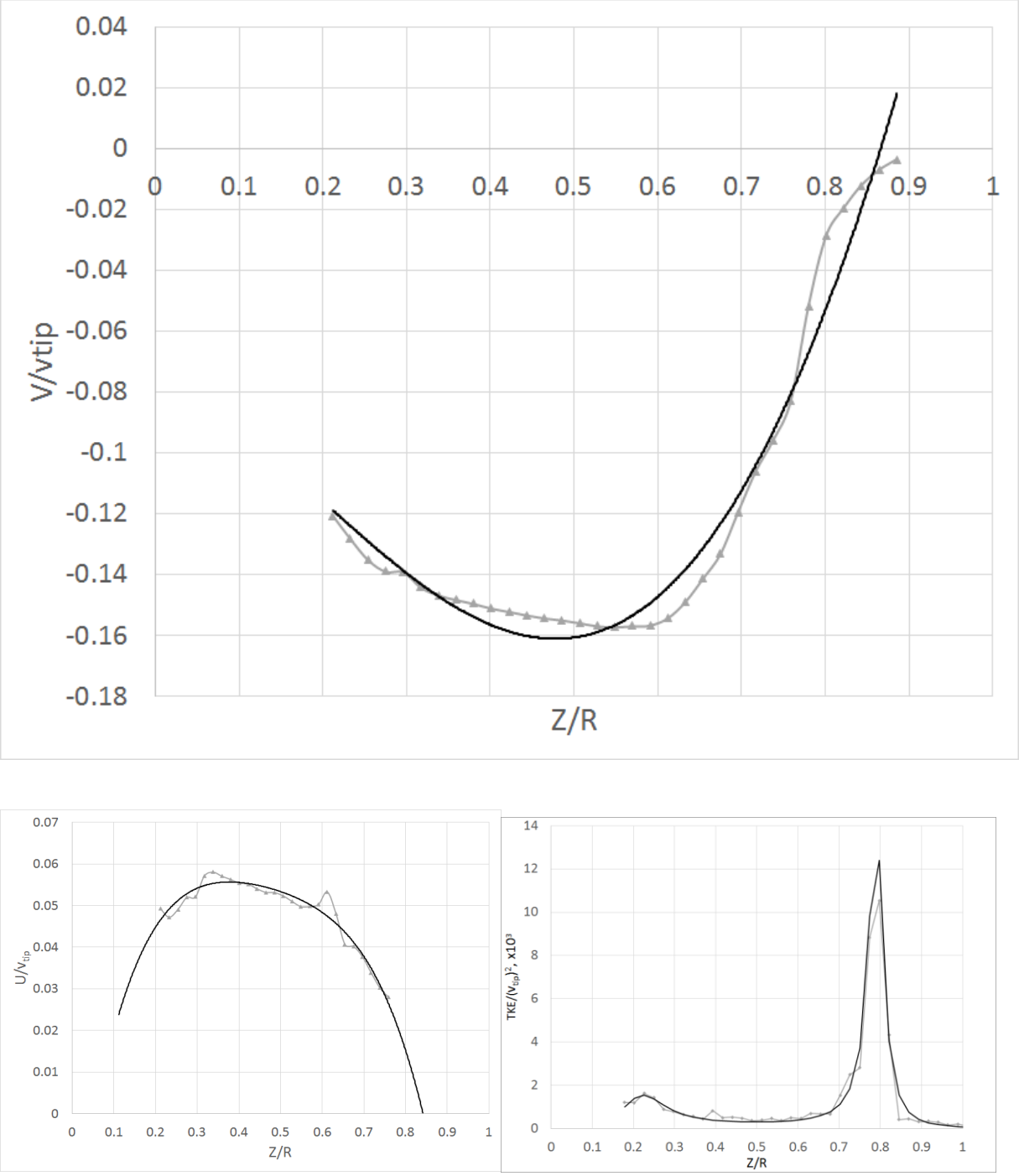

Figure 6.26 The interpolation (black line) of downwash (top) and swirl (bottom left) velocity components and turbulence kinetic energy (bottom right) measured in a single DJI E7000 rotor PIV analysis (grey line with triangular markers)

$$V/v_{tip} = -0.4504(r/Rr)^4 + 1.6327(r/Rr)^3 - 0.8873(r/Rr)^2 - 0.0735(r/Rr) - 0.0781;\ R^2 = 0.97$$

(Equation 6.25)

$$U/v_{tip} = -1.4843(r/Rr)^4 + 2.8016(r/Rr)^3 - 2.1013(r/Rr)^2 + 0.7079(r/Rr) - 0.0327;\ R^2 = 0.94$$

(Equation 6.26)

$$TKE/v_{tip}^2 = 0.01275/(0.1987(r/Rr)^4 - 0.4028(r/Rr)^3 + 0.272(r/Rr)^2 - 0.0705(r/Rr) + 0.0062);\ R^2 = 0.94$$

(Equation 6.27)

The interpolation function was applied to *slave* and *master* boundaries of both rotors simultaneously.

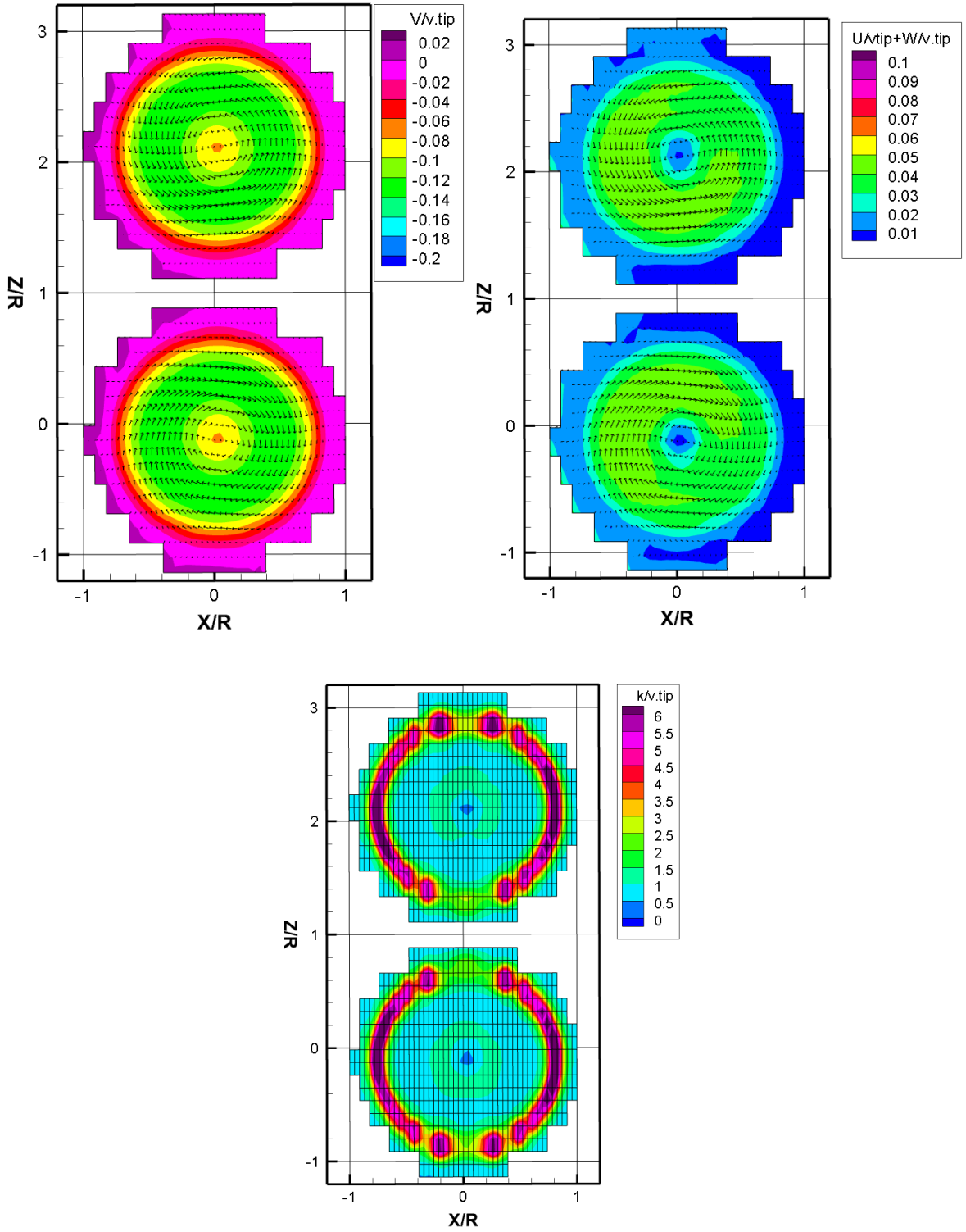

Figure 6.27 DJI E7000 rotor boundary conditions: downwash velocity (top), swirl velocity (top right), TKE (bottom right).

Table 6.9 Summary of boundary conditions applied in the DJI E7000 rotors analysis

	p	U	TKE (k)	omega	nut
inlet	zero gradient	zero gradient	zero gradient	zero gradient	zero gradient
outlet	zero gradient	zero gradient	inletOutlet	zero gradient	zero gradient
sideWall1	zero gradient	zero gradient	zero gradient	zero gradient	zero gradient
sideWall2	zero gradient	zero gradient	zero gradient	zero gradient	zero gradient
defaultFaces	0	zero gradient	zero gradient	zero gradient	zero gradient
fixedWalls	zero gradient	(0, 0, 0)	kqRWallFunction	omegaWallFunction	NutkWallFunction
rotor	zero gradient	groovyBC	groovyBC	zero gradient	zero gradient

6.4.2.3 Result and comparison to experimental data

Figure 6.28 shows the wake of the DJI E7000 rotor affected by an adjacent counter-rotating wake. The streamlines on a plane (Y/R-Z/R) passing through the shafts of both rotors (X/R=0) are coloured by velocity magnitude normalised by rotor tip velocity.

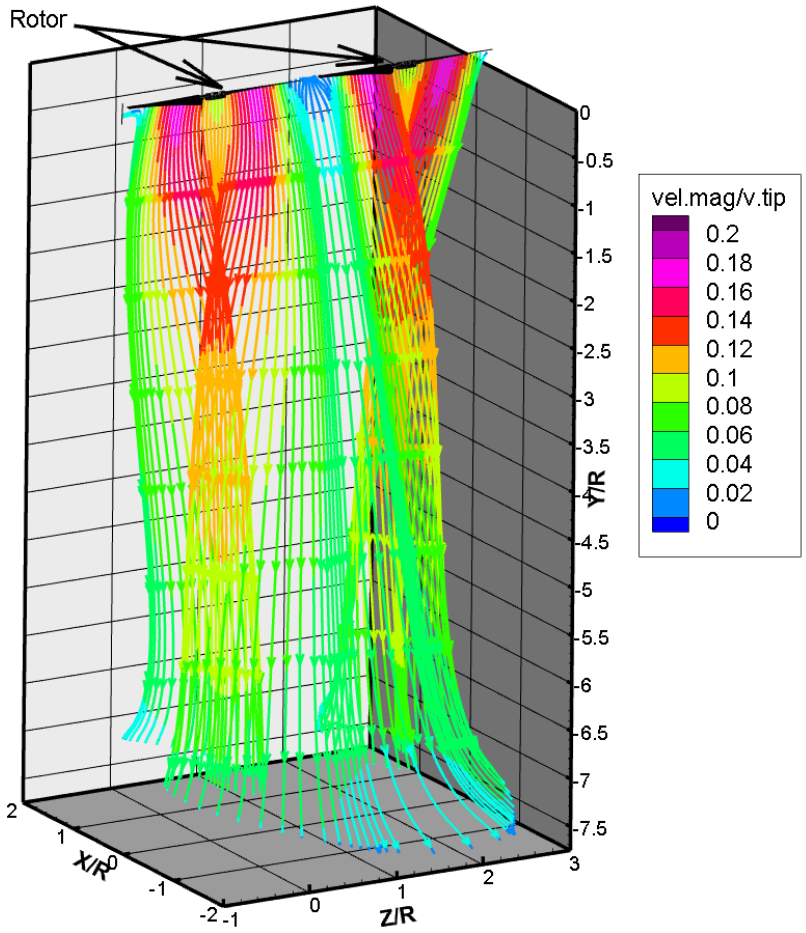

Figure 6.28 Velocity magnitude and streamlines on vertical planes through the axes of the rotors

The high-speed (red-purple) regions are the downwash of the two rotors. The tilt of the downwash is less significant in the model than in the PIV data (Chapter 4, Figure 4.18). A strong swirl is observed in the plot. Influenced by the ground effect, at Y/R=-6…-6.5 streamlines bend towards the direction of rotation of the rotors.

For the comparison between PIV and model data, velocity was sampled at vertical distance Y/R=-0.5 away from the rotor disk. The 1 S.D. shown on the PIV graph was obtained from classic PIV analysis (Figure 6.29) (Chapter 2).

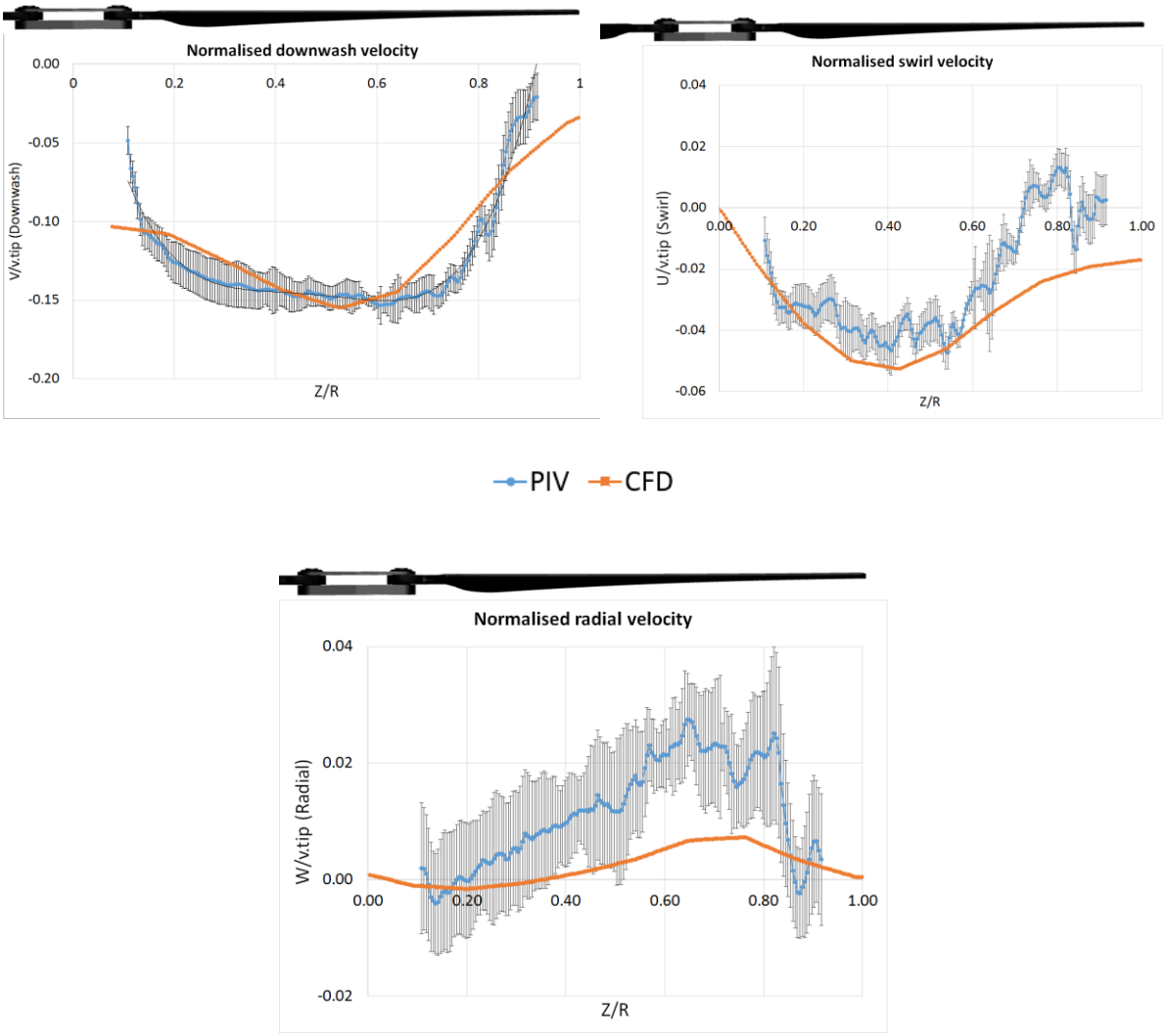

Figure 6.29 Comparison of PIV (blue circles) and CFD (orange squares) downwash (top), swirl (bottom left) and radial (bottom right) velocity components of two adjacent co-planar counter-rotating DJI E7000 rotors when Y/R=-0.5, X/R=0

The downwash of two DJI rotors is within one standard deviation at X/R 0...0.6R. After 0.6R the interaction effect dominates in the flow and the model does not reflect this well. The swirl velocity component is stronger in the model, which may be explained by the influence of the adjacent rotor. The radial velocity component was not introduced to the model, but positive radial velocity is observed. This component corresponds to the tilt of the wake.

The major influence on the velocity flow field in the zone of interaction is the interaction of tip vortices. It was supposed that tip vortices generated the region of low pressure between rotors. Because of this low-pressure region, wakes were tilted towards each other. Tip vortices were modelled as sources of TKE, though their real effect also includes a radial flow which was not modelled. Therefore, the merge of the wakes is less significant in the model than in the PIV experiment. Tip vortices generate the upward velocity region between adjacent counter-rotating rotors (Chapter 4). The upward velocity region is not observed in the model because tip vortices were not modelled.

6.4.2.4 Mesh independence study

Two different meshes were tested to prove that the velocity vector field modelled for two DJI E7000 rotors does not depend on mesh size (Table 6.10). The velocity for different mesh sizes was sampled at Y/R=-0.5 (Figure 6.30)

Table 6.10 Mesh size parameters used for the mesh independence study of DJI E7000 rotors.

	Coarse mesh	Fine mesh
Number of cells	7’696’290	18’976’074
Number of cells in one rotor disk	278	834

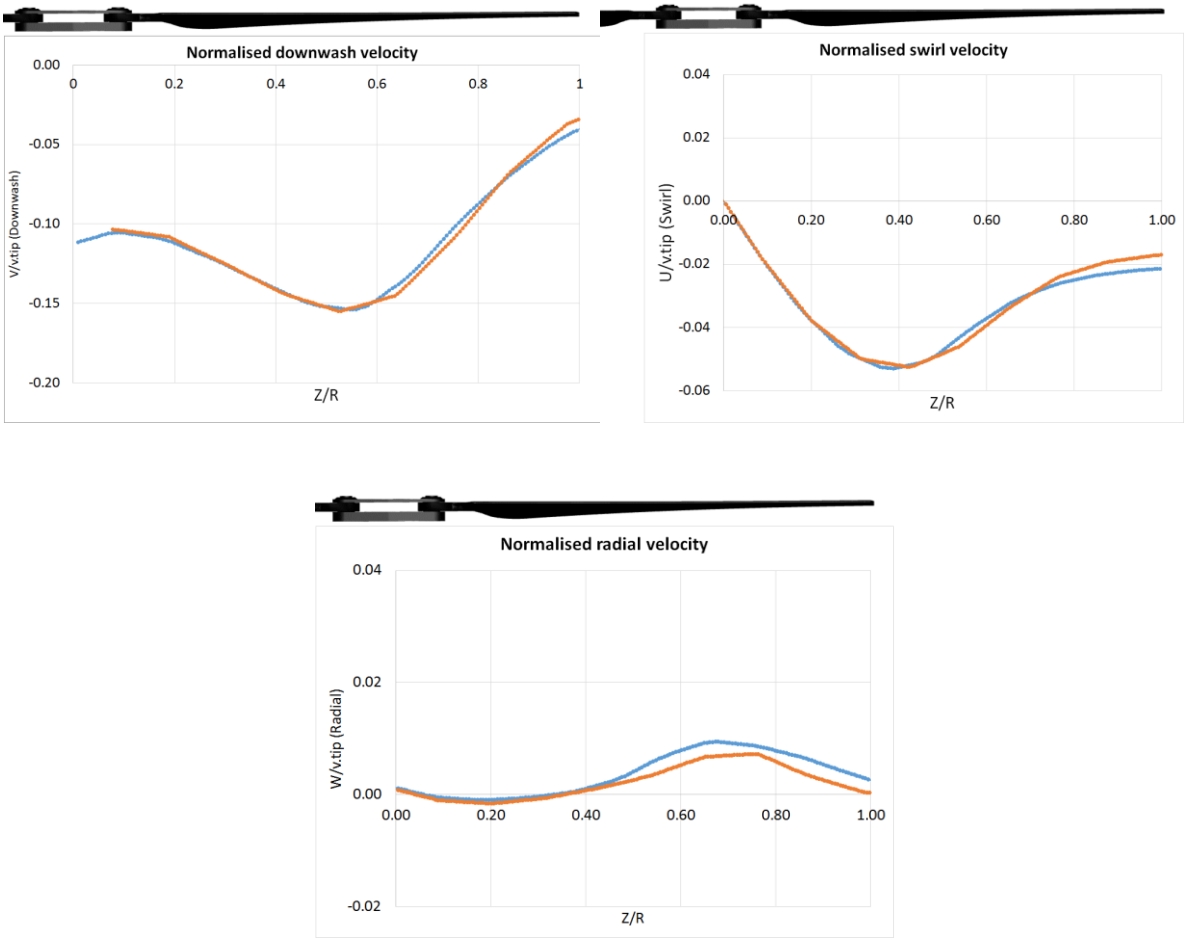

Figure 6.30 CFD computational results with coarse mesh (orange squares) and fine mesh (blue squares). Downwash (top left), radial (top right), and swirl (bottom) normalised velocity components in the 6 m/s spanwise configuration when Y/R=-0.5, Z/R =0.

The mesh independence study showed that the wake velocity field is mesh-size-independent as both coarse and fine mesh returned a similar result.

6.4.3 DJI Agras MG-1 multicopter

The DJI Agras MG-1 multicopter has been used by several scholars (Richardson et al. 2019, Martin et al., 2019). This is the legacy version of DJI Agras multicopters that utilised a DJI E2000 rotor system. These rotors were not experimentally evaluated in this research but it is assumed that they have a similar wake structure to a DJI E7000 propulsion system.

The experimental swath pattern analysis was provided by Dr Brian Richardson for comparison with the model. Flights 4, 9 and 29 were chosen for comparison with the model and for model optimisation (Table 6.11)

Table 6.11 DJI Agras MG1 flight parameters used in swath pattern experimental investigation

Flight	Droplet size	Spray used (kg)	Spray duration (s)	Output (L/min)	Ground speed (m/s)	Flight height (m)	Wind Speed (m/s)	Wind_dir(°)	Temp (°C)	RH (%)
4	Small	0.614	15.97	2.307	2.850	2.8	1.07	223.5	13.8	62.95
9	Small	0.690	18.20	2.275	2.900	2.7	2.19	261.2	14.5	63.14
29	Small	N/a	N/a	N/a	4.88	3.3	0.04	N/A	23.9	49.89

Flight 4 (F4) was chosen because the wind speed was ⅓ of the ground speed. In Flight 9 (F9) the wind speed was ¾ of the flight speed. The reason for selecting these flights was a wide range of wind to ground speed ratios. In flight 29 (F29) the wind speed was near zero. The reason for selecting this flight conditions is high ground speed.

The sensitivity of the swath pattern to the mesh size and residual error was studied.

Chapter 7 evaluated the influence of multicopter variables on the swath pattern. The rotational speed of rotors was not recorded in the experiments; thus, the highest, lowest, and average rotational speeds were tested in the model (Table 6.12).

The stabilisation and control of multicopter is performed by variation of tilt, roll and yaw angles. These angles were not recorded by the flight controller in the Richardson et al., (2019) experiments. The sensitivity of the swath to change in roll, pitch and yaw angles by +-5^{o} was

tested in the model for flight 4, flight 9 and flight 29 conditions. According to Brosy et al., (2017) the multicopter tilts by 5^{o} approximately when experiencing 4.8 m/s lateral velocity.

Table 6.12 Modelled flight parameter in the analysis of DJI Agras MG-1 multicopter

Flight	Rotational speed of all rotors, RPM			Height above the ground, m		
F4	2475	2750	3020	2.5	2.8	3.1
F9	2475	2750	3020	2.5	2.7	3.1
F29	2475	2750	3020	3	3.3	3.6

6.4.3.1 Geometry

In the model, the Agras MG-1 multicopter was defined by three variables: *R=0.2665* (radius of rotor), *Rm=0.8* (radius of multicopter), and *dr=0.045* (distance between rotor arcs). Each rotor has its number (Figure 6.31). The rotor was presented as velocity boundary conditions submerged into the domain.

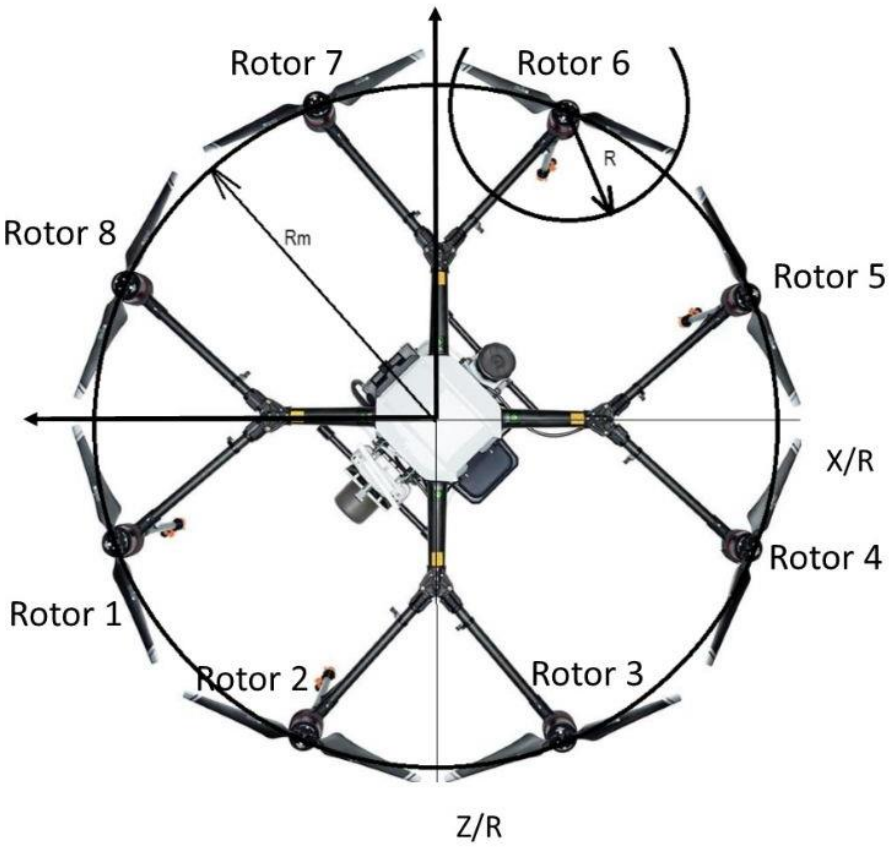

Figure 6.31 DJI Agras MG-1 multicopter parameters *Rm, R* and *nor* and coordinate

The origin is in the geometrical centre of the multicopter. Figure 6.32 shows the disks representing the rotor boundary conditions code that defines the position of each rotor:

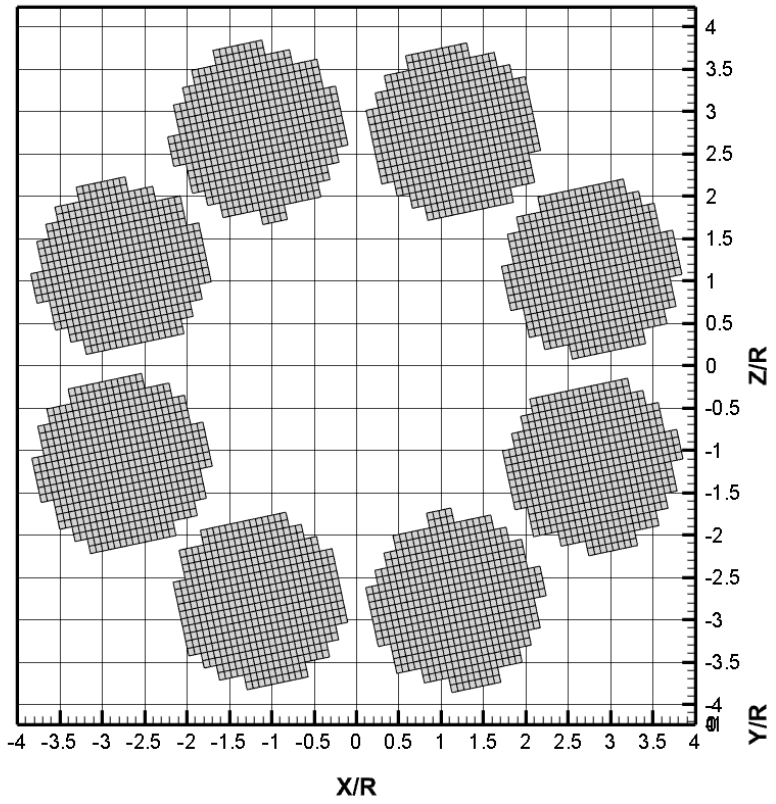

Figure 6.32 Generated rotor disk for DJI Agras MG-1 multicopter

In flight 9 (F9) the influence of the body of a multicopter on the swath pattern was studied. The body is represented as wall boundary conditions inside the domain (Figure 6.33)

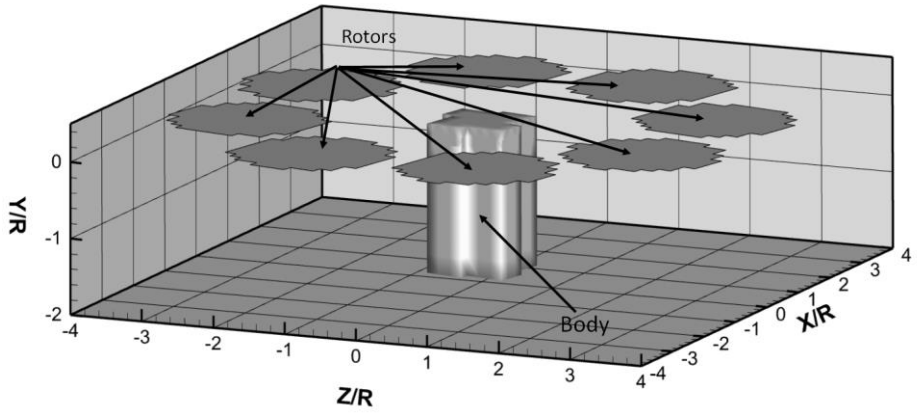

Figure 6.33 Model of DJI Agras MG-1 multicopter with a body

For all flight conditions tested, the normalised domain extent was defined as in Table 6.13 and Figure 6.34:

Table 6.13 Domain size in the DJI Agras MG-1 rotors computational analysis

xmax	xmin	ymax	Ymin	zmax	zmin
-130R	8R	5R	Flight variable	-35R	35R

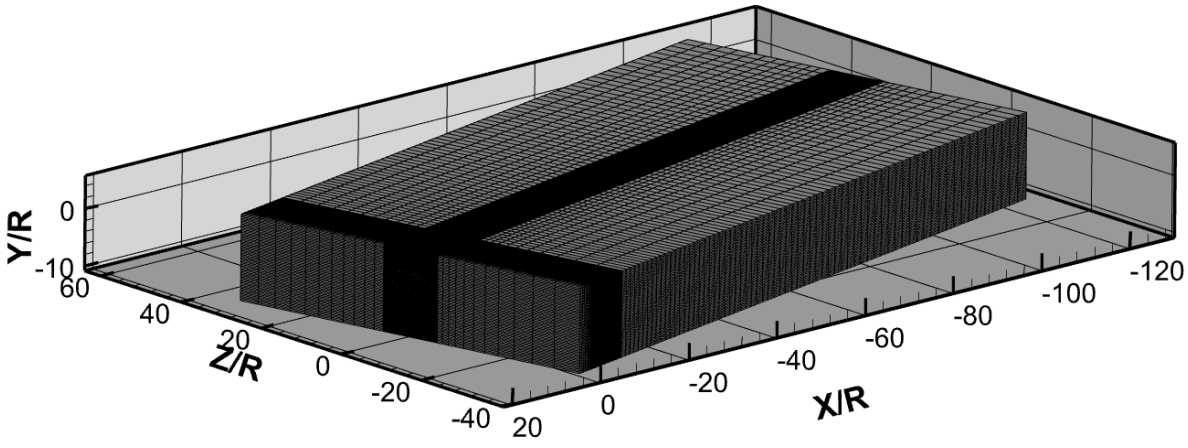

Figure 6.34 Meshed domain of DJI Agras MG-1 model.

To have the streamlines on the multicopter level parallel to the domain edge, the entire domain was rotated around the Y/R axis. The angle of rotation was equal to 9 degrees for F4 and 12 degrees for F9. In F29 the wind speed was near zero; therefore, the domain was not rotated.

6.4.3.2 Boundary conditions

6.4.3.2.1 Rotor boundary conditions

The model used the velocity flow field from PIV data for a single DJI E 7000 rotor (at Y/R=-0.1). The downwash and swirl velocities were interpolated using 4th order polynomial interpolation at $Z/R \in (0...0.85)$. (Figure 6.26, Equation 6.25 through Equation 6.27). The TKE experimental data, retrieved from CTA analysis, was interpolated by rational function with polynomial function in denominator. To mimic the freestream flow over the rotor disk, the vector sum of wind velocity and lateral velocity was computed, and the result projected along the X and Z axes. This velocity was added to the rotor boundary conditions.

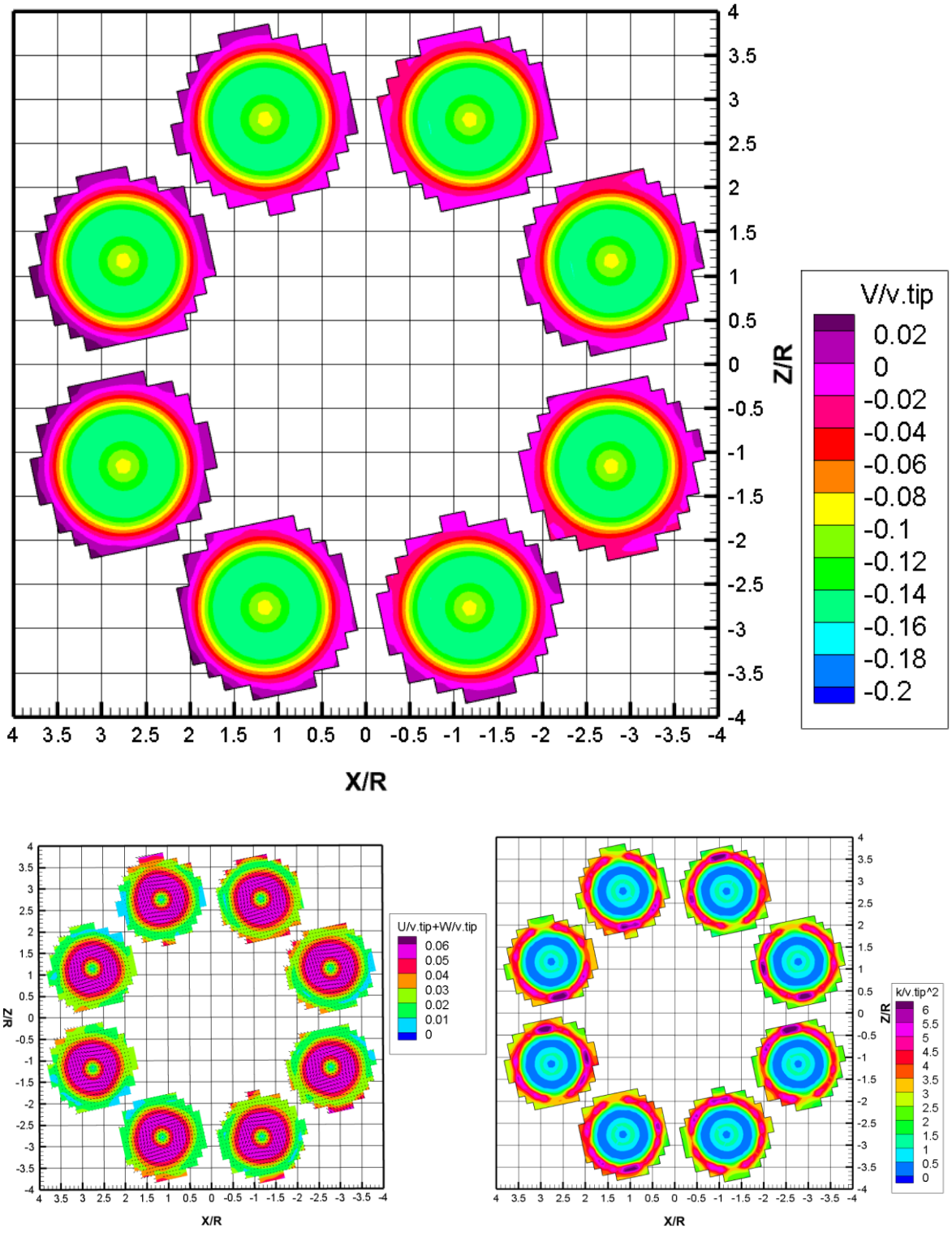

Figure 6.35 DJI Agras MG-1 rotors boundary conditions: downwash velocity (top), swirl velocity (top right), TKE (bottom right).

Table 6.14 Summary of boundary conditions applied in the DJI Agras MG-1 rotors analysis

	p	U	TKE (k)	omega	nut
inlet	zero gradient	(lateral velocity, 0, cross wind speed)	atmBoundaryLayerInletK	atmBoundaryLayerInletOmega	atmBoundaryLayerInletNut
outlet	0	zero gradient	inletOutlet	zero gradient	zero gradient
sideWall1	zero gradient	(lateral velocity, 0, cross wind speed)	atmBoundaryLayerInletK	atmBoundaryLayerInletOmega	atmBoundaryLayerInletNut
sideWall2	zero gradient	zero gradient	zero gradient	zero gradient	zero gradient
defaultFaces	zero gradient	zero gradient	zero gradient	zero gradient	zero gradient
fixedWalls	zero gradient	(lateral velocity, 0, cross wind speed)	kqRWallFunction	omegaWallFunction	NutkWallFunction
rotors	zero gradient	groovyBC	groovyBC	zero gradient	zero gradient

6.4.3.2.2 Atmospheric boundary conditions

Wind speed and direction depend on the flight. The crosswind speed, W from the Table 6.15 was applied to the *sideWall1* boundary. The U (True airspeed) velocity was applied to the *inlet* boundary.

Table 6.15 Flight and wind velocity reported in the experimental analysis of swath pattern

Flight	Wind speed (uw, m/s)	Wind direction (Magnetic compass)	Wind direction (Relative to multicopter)	Wind speed component along the flight trajectory, m/s	Crosswind, W, m/s (Crosswind)	U, lateral (Ground speed), m/s	U (True airspeed), m/s
4	1.07	223.47	43.47	0.777	0.736	2.850	3.627
9	2.19	261.23	81.23	0.334	2.164	2.900	3.234
29	0.04	N/A	N/A	N/A	N/A	4.88	4.88

6.4.3.3 Results

Strong rollup vortices were observed in the PIV analysis. These vortices are the result of the interaction between rotor wake and lateral velocity. In Chapter 4 it was shown that a portion of the spray follows the rollup vortices. Spray carried by the vortices will travel laterally much further than spray in the main downwash.

Rollup vortices are also observed in the CFD model. In Figure 6.36 through Figure 6.38, the rollup vortices are shown by the streamlines coloured by velocity magnitude.

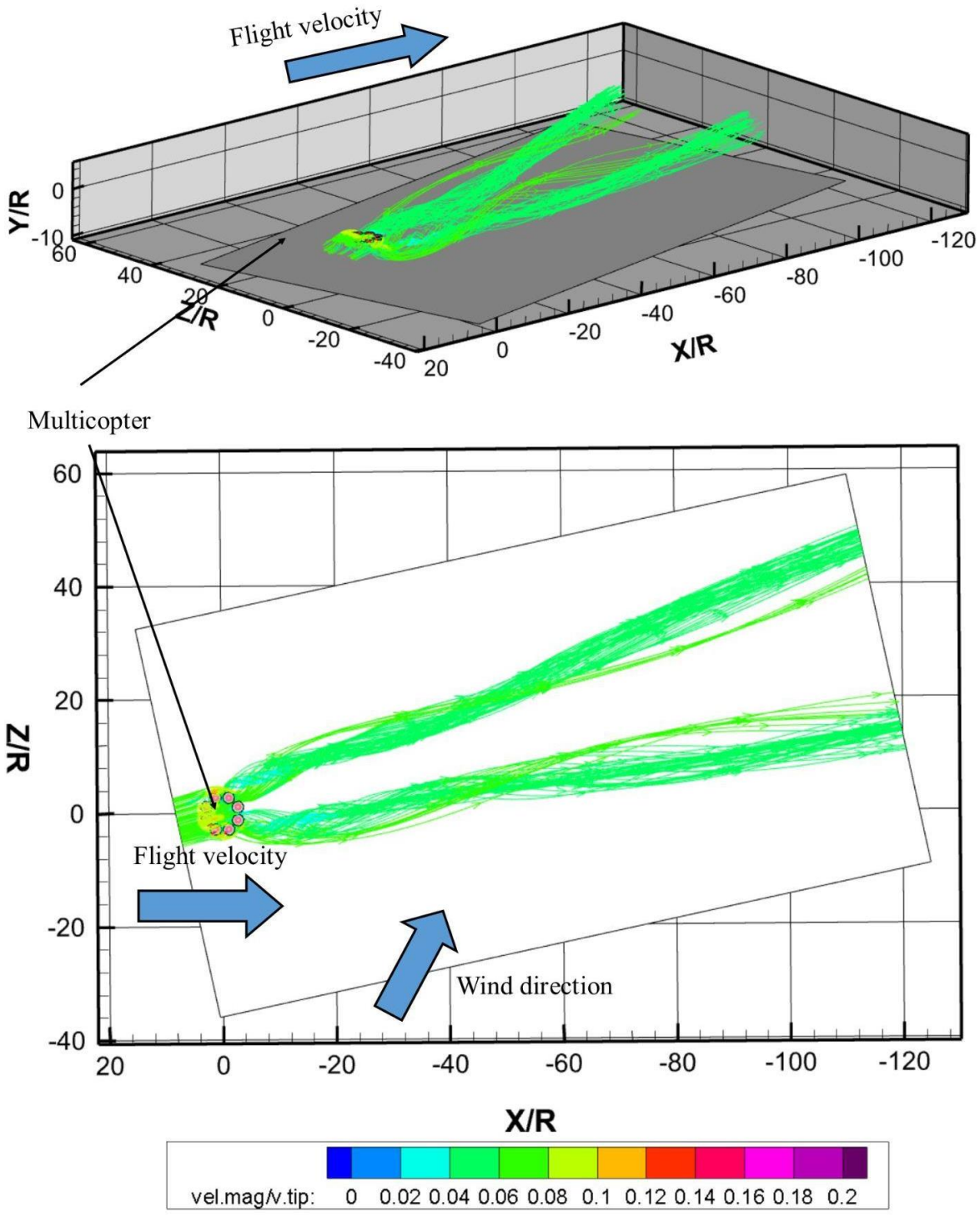

Figure 6.36 The DJI Agras MG-1 multicopter in flight 4 conditions with rollup vortices shown by streamlines coloured by velocity magnitude

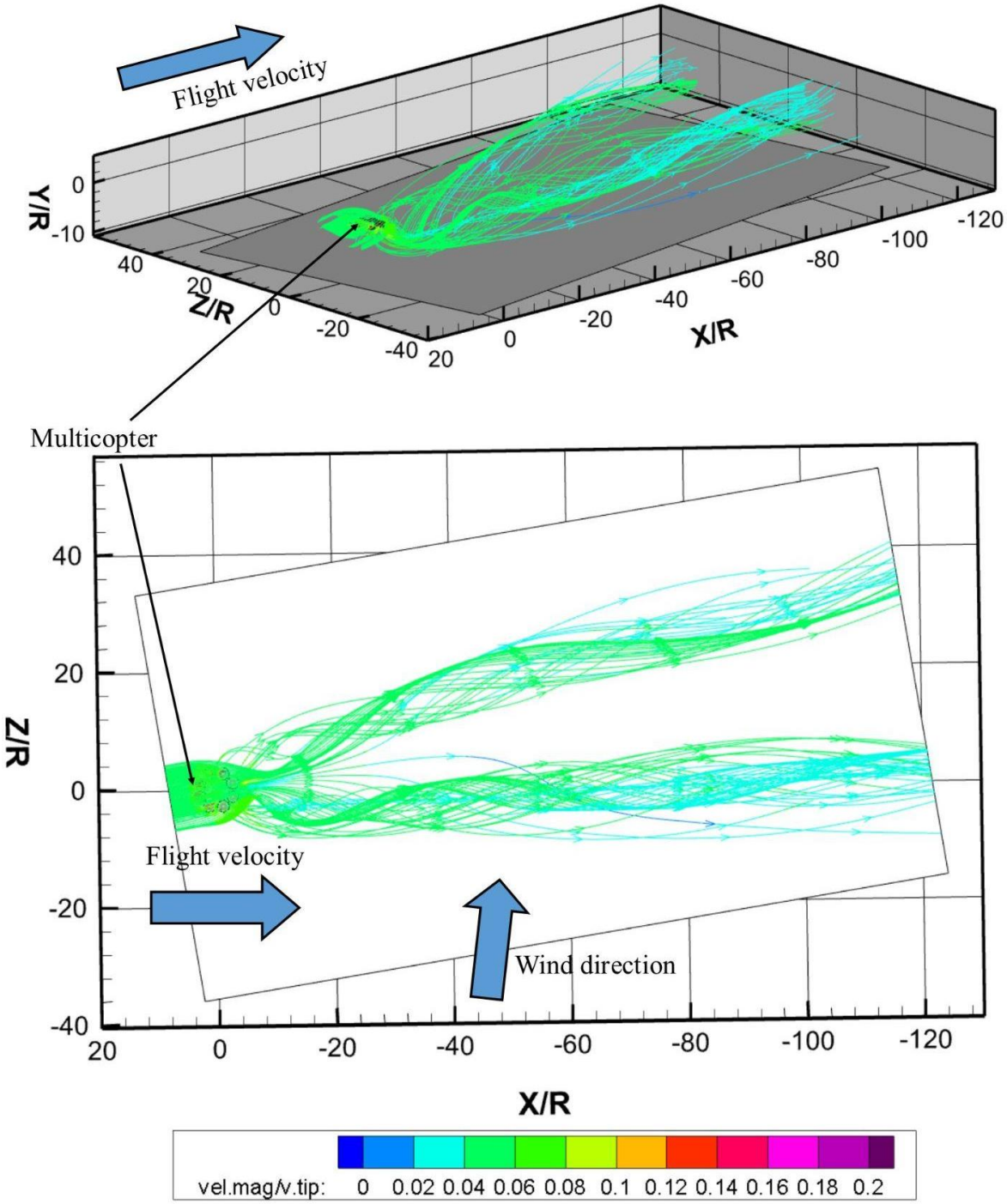

Figure 6.37 The DJI Agras MG-1 multicopter in flight 9 conditions with rollup vortices shown by streamlines coloured by velocity magnitude

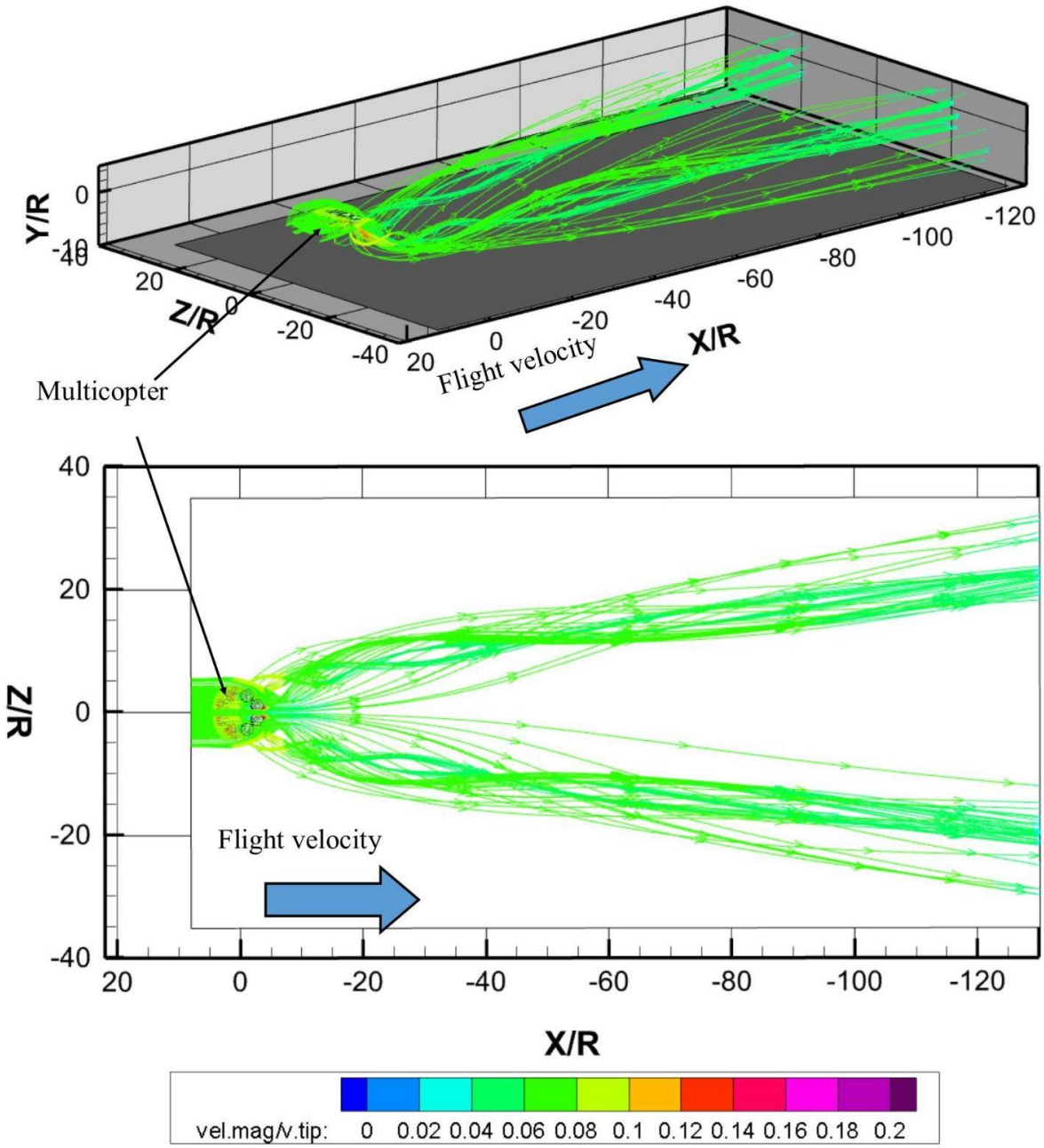

Figure 6.38 The DJI Agras MG-1 multicopter in flight 29 conditions with rollup vortices shown by streamlines coloured by velocity magnitude

It can be observed that only two rollup vortices are generated in the multicopter. They are attached to the free ends of the rotors exposed to lateral velocity. The distance between two vortices in the +-Z direction increases with distance from the multicopter.

The velocity flow field obtained in this study was used for spray pattern prediction. The spray pattern was compared to Richardson et al., 2019 experimental result (Chapter 5). The mesh independence study can be found in Chapter 6. The presence of the canopy was modelled in conditions taken from the Flight 9 experiment. The influence of the plant canopy on spray deposition can be found in Chapter 6.

6.5 Conclusion of chapter

In nonzero lateral velocity, the model showed effects similar to those observed in PIV. In the streamwise configuration, the leeward rotor is shadowed by the windward rotor. As a result, the wake streamlines of the windward rotor are more tilted than those of the leeward rotor. The zone of upward velocity generation is observed on the windward part of the windward rotor. This zone corresponds to the rollup tip vortex and expands in a streamwise direction. The upward velocity zone on the leeward rotor is observed at 10 m/s lateral velocity. The generation of the upward velocity region is also observed in the streamwise configuration. It is attached to the windward part of both rotors and propagates laterally in the streamwise direction.

At lateral velocities of 2 m/s and 6 m/s, the downwash, swirl, and radial velocity components of the model are mostly within one standard deviation of PIV data. At 10 m/s lateral velocity, the downwash velocity components of the CFD and PIV data do not match. The major discrepancy is in zones with near-zero velocity (between rotors and under the centre of the rotor). In PIV data, the downwash and swirl components decrease to near-zero values. In CFD data, the downwash and swirl velocity components are lower than the main downwash but do not decrease to zero. This can be explained by numerical dissipation introduced by the CFD code. Another explanation of the velocity vector field difference in the zone between rotors is

the influence of rotor tip vortices. The generated vortices interact strongly and can generate the radial velocity component on the rotor disk. The method of vortex prescription in CFD does not include the propagation of the vortex with the downward motion of the wake. Therefore, there was less interaction between wakes in the zone between rotors. The rotor boundary conditions used for CFD analysis were obtained without lateral velocity present in the flow. In PIV experiments, lateral velocity was generated by a wind tunnel, which can introduce a source of turbulence near the mouth of the wind tunnel.

Using the example of Agras MG-1 multicopter, it was shown that the model can compute the flow field with wind boundary conditions. Rollup vortices were generated in the model.

The pressure (p), turbulence kinetic energy (TKE), turbulence kinetic energy dissipation rate (ω), and velocity (U) values computed by the model can be used for spray pattern prediction. This will be demonstrated in Chapter 7.

7. Spray distribution analysis in OpenFOAM

In Chapter 6 a method for fast computational analysis of a multicopter wake was presented. This chapter presents the analysis of the spray pattern inside the flow field obtained from CFD analysis. The results were tested against the experimental data. The spray experimental data was obtained under DJI E7000 rotor flow field in hovering and DJI Agras Mg-1 (Richardson et al., 2019) multicopter in flight with lateral velocity.

7.1 Governing equations

7.1.1 Particle motion equation

The Lagrangian approach described in Chapter 5 (Equations 5.1 through 5.9) is used to evaluate the spray trajectories inside the field obtained from CFD computational analysis.

Coupling between the air flow field and the particles may be modelled in different ways:

- One-way coupling when the motion of the particles does not influence air behaviour
- Two-way coupling where the motion the particles influences air behaviour
- Four-way coupling, where particle collisions are considered.

Particle mass loading (Equation 7.1) was calculated to select the right method:

$$\beta = \frac{\text{particulate mass per unit volume of flow}}{\text{fluid mass per unit volume of flow}} \quad \text{(Equation 7.1)}$$

If particle mass loading is more than 0.2 two-way coupling is expected in the system. For particle mass loading exceeding 0.6, the collision effect must be considered (Brown et al., 2002).

For example, in spray modelling with DJI rotors, the particle mass loading doesn't exceed 9.01×10^{-4} (mass of particles is 0.09933 kg in the entire domain, the mass of air is 108.36 kg in the domain). In the spray modelling with DJI Agras Mg-1 multicopter, the particle mass loading doesn't exceed 1.26×10^{-5} (mass of particles is 0.03844 kg in the entire domain, the mass of air is 3043.18 kg in the domain). Therefore, the one-way coupling model was chosen for the analysis.

7.1.2 Particulate dispersion

Tracking particle flow through a turbulent environment requires knowledge of the instantaneous velocity. Unfortunately, the Reynolds averaged Navier-Stokes model does not provide instantaneous velocity. Therefore, the instantaneous velocity must be calculated using either stochastic or deterministic methods. There are two stochastic particulate dispersion models available in OpenFOAM: *StochasticDispersionRANS* and *GradientDispersionRANS.*

In OpenFOAM the discrete random walk (DRW) model is applied. The fluctuation component of velocity (Equation 7.2) is prescribed by a Gaussian distribution function (Greifzu et al., 2015).

$$u_{turb} = \zeta \underline{d} \sigma \qquad \text{(Equation 7.2)}$$

Where ζ is the vector formed by a normally distributed random number;

The standard deviation is determined with (Equation 7.3):

$$\sigma = \sqrt{\frac{2k}{3}} \quad \text{(Equation 7.3)}$$

$\underline{\boldsymbol{d}}$ is the vector that characterises the spatial randomness of fluctuating velocity (Greifzu et al., 2015).

The major difference between the StochasticDispersionRANS and GradientDispersionRANS models is in the vector ($\underline{\boldsymbol{d}}$). The Stochastic Dispersion model uses a random direction and is calculated in spherical coordinates (Equation 7.4):

$$\begin{gathered} \theta = 2\pi \cdot rnd; \\ u = 2rnd - 1; \\ a = \sqrt{1 - u^2}; \\ \underline{d} = (a \cdot \cos(\theta),\ a \cdot \sin(\theta),\ u). \end{gathered} \quad \text{(Equation 7.4)}$$

Where *rnd* is a random number from 0 to 1.

In the Gradient Dispersion model, the vector d is calculated as a ratio of the gradient and magnitude gradient of the turbulence kinetic energy (TKE) (Equation 7.5):

$$\underline{d} = -grad(k)/mag(grad(k)) \quad \text{(Equation 7.5)}$$

Where *k* is the turbulence kinetic energy.

Both models were tested in the present work.

7.1.3 Evaporation model

Chapter 4 evaluated near-field droplet behaviour. As the tracking time was less than 0.1 seconds, it was assumed that spray evaporation could be neglected. Increasing the computational domain size and time, over which droplets are tracked, requires evaporation to be evaluated.

During evaporation, particle mass decreases. In the same flow conditions, particles with a smaller mass would have a smaller Stokes number.

Several authors have evaluated the simple model of evaporation of agricultural spray, fitted to experimental data (Trayford and Welch, 1977; Bilanin et al., 1989). In this mode, change in mass during evaporation is described by the following equation (Equation 7.6):

$$\frac{d_m}{d_t} = 2\pi dD(\rho_{ff} - \rho_{nf}) \quad \text{(Equation 7.6)}$$

Where:

ρ_{ff} is the density of water vapour in the far-field (Equation 7.7):

$$\rho_{ff} = \frac{RH}{100} \frac{p_s}{R_w T_{air}} \quad \text{(Equation 7.7)}$$

ρ_{nf} is the density of water vapour at the surface of the droplet (Equation 7.8):

$$\rho_{nf} = \varphi X_{water} \frac{p_s}{R_w (T_{drop})} \quad \text{(Equation 7.8)}$$

m is the mass of the droplet,

d is the particle diameter,

D is the diffusion coefficient of water in the air,

RH is the relative humidity,

$p_s\ (T_{drop})$ is the saturation vapour pressure of water at the temperature of the air,

R_w is the specific gas constant of water,

T_{air} is the temperature of the air,

γ is the activity coefficient (assumed 1),

X_{water} is the mass fraction of water in the droplet,

p_s *(T_drop)* is the saturation vapour pressure of water at the temperature of the droplet,

and T_{drop} is the temperature of the droplet.

The calculation of particle diameter in discrete form from Equation 7.9:

$$d_{i+1} = \sqrt[3]{(d_i)^3 + \frac{2Dd_i(\rho_{ff} - \rho_{nf})dt}{\frac{1}{6}\rho}} \quad \text{(Equation 7.9)}$$

Where *dt* is the time step.

A similar method was used in the AGDISP model (Bilanin et al., 1989) and by Rowiński (2019). This is an idealised model for a single droplet when humidity conditions change from saturated near the droplet surface to ambient far from the droplet surface. In aerial spraying, the evaporated mass changes the local humidity in the droplet cloud. Each individual droplet in the cloud undergoes evaporation at various rates. In fact, the evaporation of all of the droplets (including droplets on the edge) is delayed by the presence of locally higher humidity due to the spray cloud (Teske et al., 2011). To estimate the evaporation rate, the two-way coupled approach must be introduced to the model. However, this adds to the complexity of the computational model and increases computational time. Teske et al. (2011) offered an empirical correction for humidity to account for droplet evaporation in the cloud (Equation 7.10):

$$\text{Effective RH} = 54.2 + 0.458 \times \text{RH} \quad \text{(Equation 7.10)}$$

where the relative humidity *RH* is a percentage. The *Effective RH* was used instead of *RH* as in Equation 7.7.

As mentioned by Teske et al., (2011), the Effective RH correction was validated by comparison to field experimental results of Bird et al., (2009) with the following range of variables (Table 7.1):

Table 7.1 Field trial conditions (Adapted from Bird et al., 2009)

Parameter	Minimum	Maximum
Wind speed (m/s) at 2-m height	1.3	7.7
Relative humidity (%)	9	93
Temperature (^{o}C)	0	35
Drop size (VMD) (microns)	160	811

The experiments conducted by Richardson et al. (2019) were within the range of field trial conditions tested by Teske et al. (2011).

7.2 Implementation of particle tracking in OpenFOAM

7.2.1 Introduction

There are several possibilities for Lagrangian tracking in OpenFOAM. The *lagrangian/intermediate* library includes the following classes:

• CollidingParcel

• ReactingParcel

• ReactingMultiphaseParcel

• ThermoParcel

• KinematicParcel

Particle mass loading is less than 0.2 for all computational cases in the multicopter spraying. Therefore, a one-way coupling Lagrangian tracking algorithm can be used for spray

computation. The particles are not reacting or changing phase. Therefore, the uncoupled *KinematicParcel* class can be used in the analysis.

Instead of tracking individually, the *KinematicParcel* class uses the parcel approach. A parcel is a set of particles with the same properties. This allows the use of less computational power for tracking.

The *kinematicCloudProperties* dictionary specified constant spray properties, particle forces and injection type. In the constant properties, density was set at 1000 kg/m^3 and remained unchanged in computational analysis. The specified particle forces were gravity force (*gravity*) and sphere drag (*sphereDrag*). The injection type was described separately for each nozzle.

7.2.2 Nozzle modeling parameters

Most of the nozzles used to spray from multicopters are cone types (solid cone or hollow cone). Nozzle parameters were described in Chapter 4. The *kinematicCloudProperties* OpenFoam dictionary (a set of submodels, algorithms or equations) used the ConeInjection model to describe the nozzle parameters. The parameters and description are given in the table below (Table 7.2):

Table 7.2 Parameters of the *coneInjection* nozzle model in the *kinematicCloudProperties* dictionary

massTotal	The total mass of spray from a single nozzle within the duration of spray
injectionMethod	Method of spray injection, e.g point, disk
flowType	Specifies the parameters of outlet velocity description: e.g., constant velocity, pressure-driven velocity, flow rate and discharge
duration	Duration of spray in seconds

parcelPerSecond	Number of parcels per second
position	Position of spray in a global coordinate system
direction	The direction of spray is a global coordinate system
OuterDiameter	The outer diameter of the nozzle orifice
innerDiameter	The inner diameter of the nozzle orifice
Cd	Nozzle discharge coefficient
thetaInner	Inner half cone angle (Chapter 4, Figure 2)
thetaOuter	Outer half cone angle (Chapter 4, Figure 2)

The outlet velocity of the nozzle is determined by Equation 7.11

$$u = \frac{\dot{m}}{C_d \rho A} \qquad \text{(Equation 7.11)}$$

Where the mass flow rate ($\dot{m}$) is determined by the division of *MassTotal* by the *duration,*

and area (*A*) is the area of the nozzle aperture.

The number of parcels per second determines how many particles are in a single parcel. To decrease the computational cost, the number of parcels can be decreased.

For most nozzles, the log-normal distribution is a reasonable approximation for the true droplet size distribution. In OpenFOAM the log-normal particle size variation was described with a Rosin-Ramler distribution (Yoon et al., 2004) (Equation 7.13):

$$Fd(x) = \frac{1 - e^{-\left(\left(\frac{x}{d}\right)^n + \left(\frac{d_0}{d}\right)^n\right)}}{1 - e^{-\left(\left(\frac{d_1}{d}\right)^n + \left(\frac{d_0}{d}\right)^n\right)}} \qquad \text{(Equation 7.12)}$$

Where *Fd(x)* is the cumulative distribution function of particle diameter,

d is mean particle diameter,

d_0 is minimum particle diameter,

d_1 is maximum particle diameter,

and n is a spread parameter (Yoon et al., 2004).

7.2.3 Implementation of the evaporation model in the OpenFOAM

The evaporation model is not directly available in the *KinematicParcel* class. Thus, the evaporation function was added to the *kinematicParcel* dictionary as the change of particle diameter with time using Equation 7.9. The evaporation was modeled in OpenFoam in Flight 4 boundary conditions with 4 nozzles installed under the multicopter. The CFD model is described in Chapter 6 and in this chapter. Evaporation was tested at a relative humidity of 30% and a temperature of 25℃. The initial particle diameter was 100 microns. Figure 7.1 shows the evaporation process calculated using Equation 7.6 through Equation 7.10.

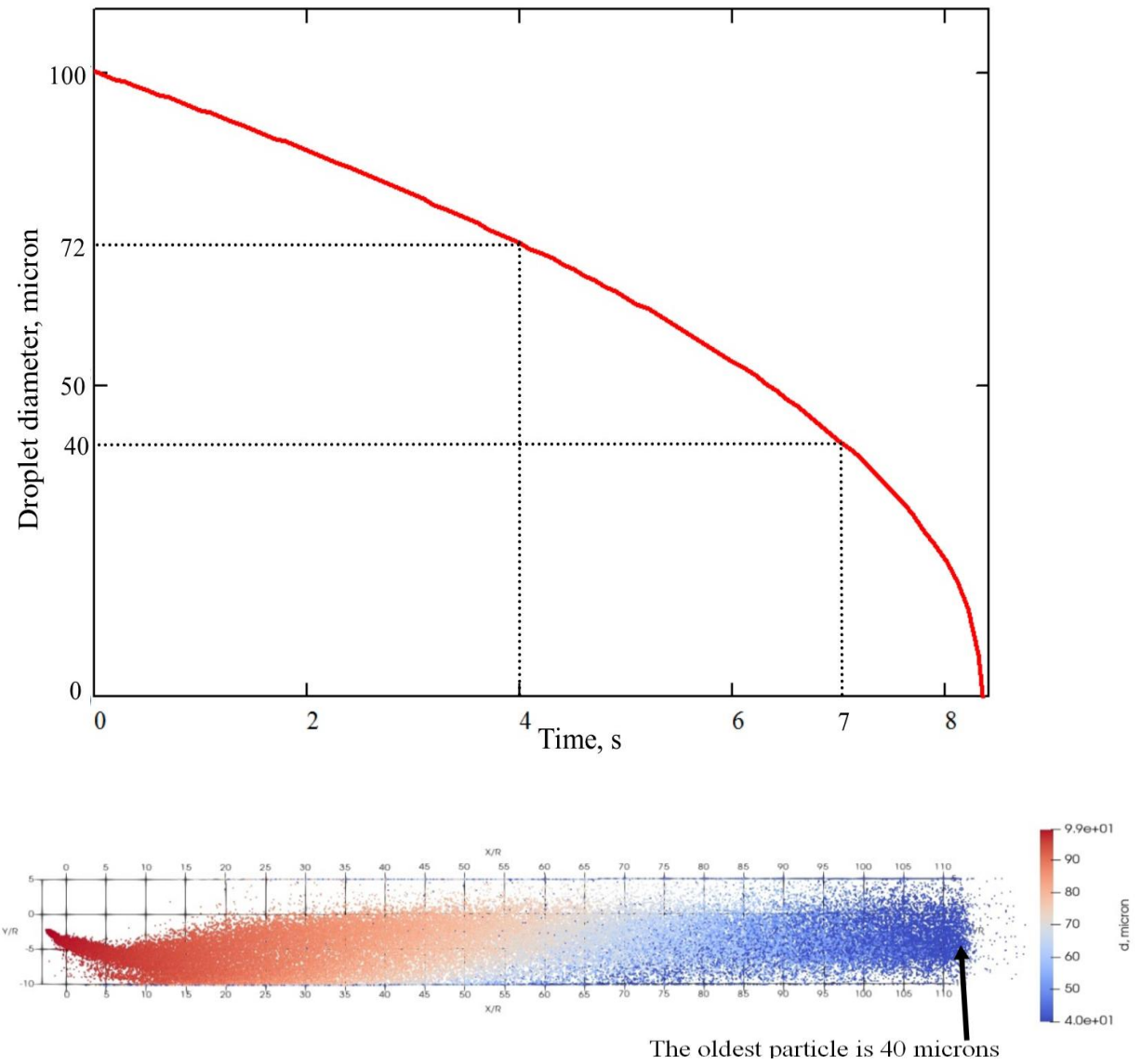

Figure 7.1 Evaporation of 100-micron particles over time: graph of evaporation (top), evaporation of monodisperse particles in multicopter flow field at t=7s, X/R-Y/R plane (bottom).

The particle diameter is 72 microns at 4 seconds and 40 microns at 7 seconds in Figure 7.1.

After 8.2 seconds the particle completely evaporates.

7.2.4 Swath pattern analysis in the model

The swath pattern on the ground is the distribution of the spray material along the spanwise (Z) coordinate of the craft. To obtain the swath pattern two variables are required: spray mass distribution along the side coordinate (Z/R) and the sprayed area.

To calculate the spray mass distribution on the ground, the Z side of the ground plane (*fixedWalls* in the model) was divided into equal strips (Figure 7.2, left). The mass of particles deposited on each strip was collected. For each time step, a file was written containing the strip coordinates and total mass on the strip.

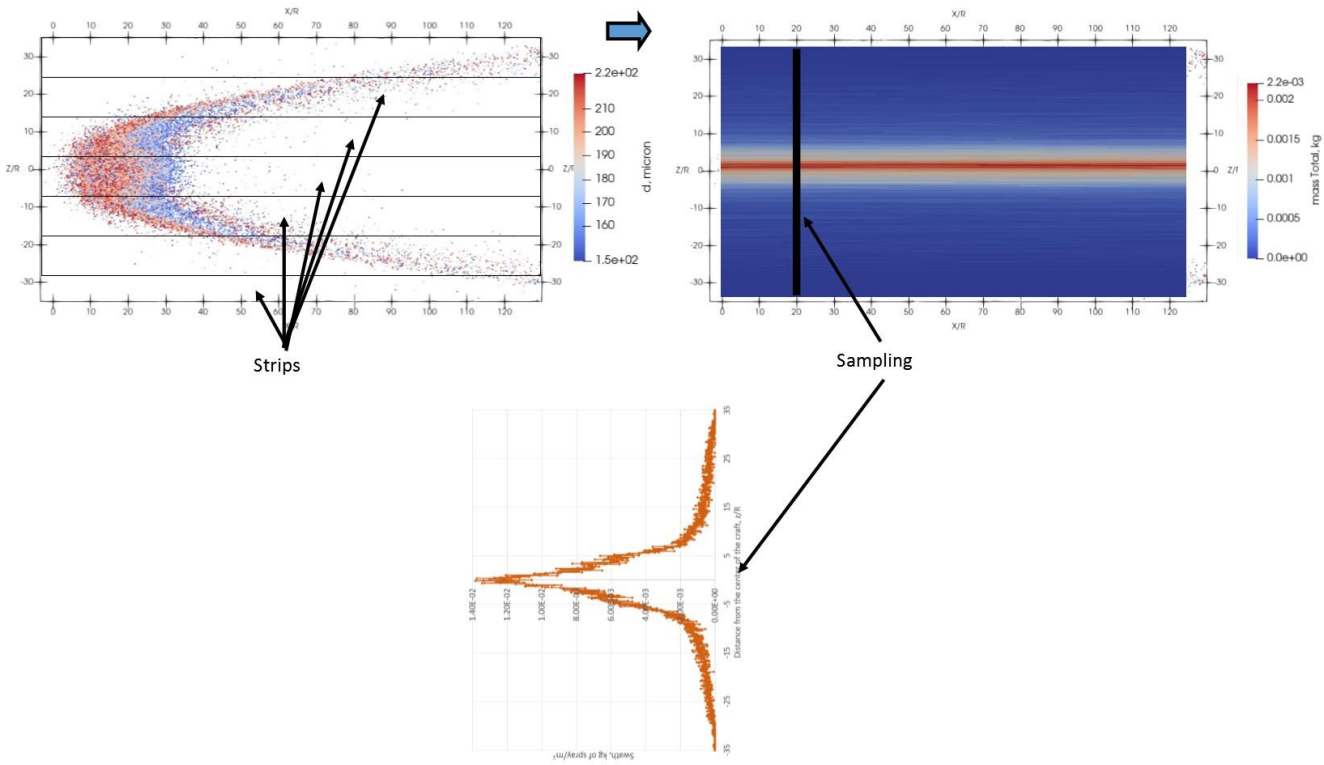

Figure 7.2 Total mass collection procedure of the strips

To calculate the area, the strip width (△(Z/R)) was multiplied by the distance of the multicopter flight. The start time of the flight is when the first spray touched any strip of the ground plane.

The end time is when all spray material was on the ground. The speed was assumed to be constant through each flight.

An important characteristic of the quality of the swath pattern is the spray deposit variation, described with the coefficient of variation (CV, %, Equation 7.13), (Richardson et al., 1993, 2004):

$$CV(\%) = \text{standard deviation of deposition} \times \frac{100}{\text{mean deposition}} \quad \text{(Equation 7.13)}$$

The maximum level of deposit CV is 30% (stated by Parkin et al., (1982); Richardson et al. (2004)). The effective swath is the distance within the swath pattern when the CV of deposition equals the maximum acceptable level of deposit CV.

7.3 Spray deposition analysis and comparison to experiments

7.3.1 DJI E7000

7.3.1.1 Spray deposition experimental measurements

To test spray deposition on the ground, two DJI E7000 rotors were placed 7.14R (3 m) from the ground, with 0.2R (86 mm) tip separation between the tip arcs (Figure 7.3), rotating at 1740 rpm. The rotational speed was measured using the method described in Chapter 3 (error less than 1%). Two nozzle positions were tested: (1) between rotors, 20mm below the rotor plane (Figure 7.3, top right) and (2) 0.6R from the centre of the rotor, 20mm below the rotor plane (Figure 7.3, bottom right). In the experiment, the nozzle was precisely placed in the desired position. The linear error of the nozzle position was +-0.5 mm, the angular error is +-0.5

degrees. The nozzle was a Teejet TXA 800050VK spraying water at 3 bars (ASABE S572.1 'Very Fine' category).

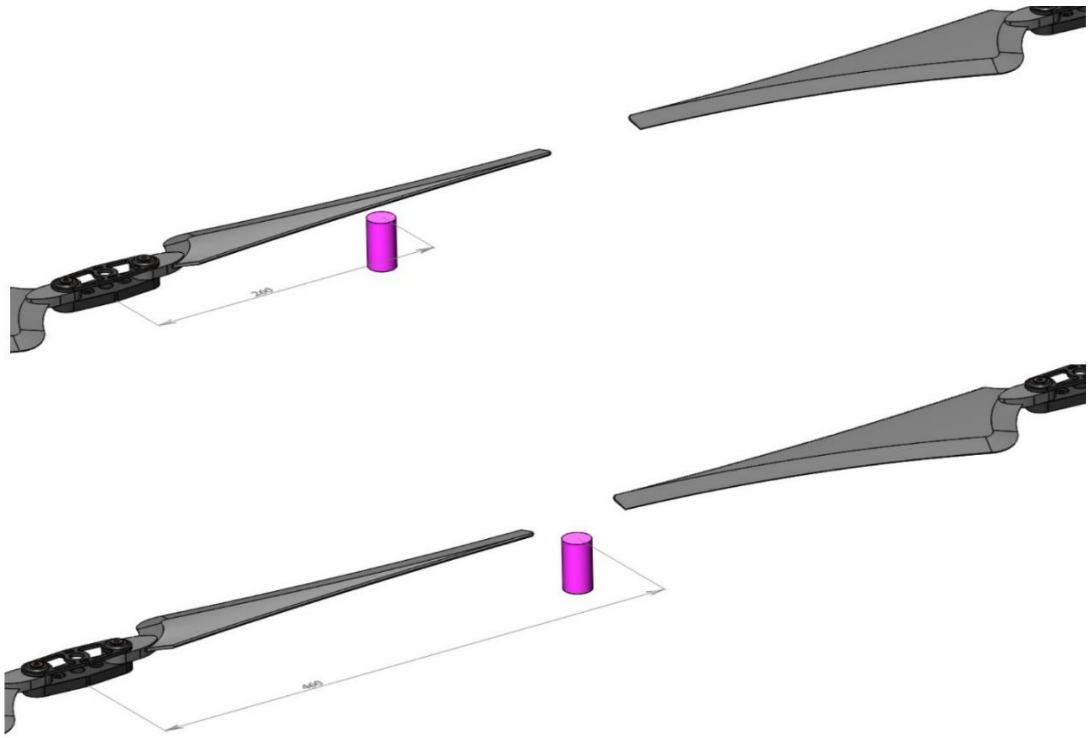

Figure 7.3 The CAD model of the experimental setup for testing spray deposition pattern. DJI E7000 system. Two counter-rotating co-planar rotors with spraying nozzle (purple cylinder in the CAD model) installed under the greatest downwash (top) and between rotors (bottom).

Styrofoam sheets were laid on the ground and water with blue dye was sprayed for 60 seconds. An image of the Styrofoam was processed using ImageJ. The image was binarized and divided into interrogation windows 15x15 pixels in size. The number of white pixels in each window was calculated. The result is shown in Figure 7.4 where the colour contours represent the coverage of the Styrofoam: 100% (red) is fully covered by a liquid, 0% (white) has no liquid detected. The coordinate system originates in the centre of the nozzle. The grey dot marks a position vertically underneath the nozzle. The linear artefact is due to the join between two sheets of Styrofoam. Here, a 2.4 mm step in surface level affects the near-surface flow.

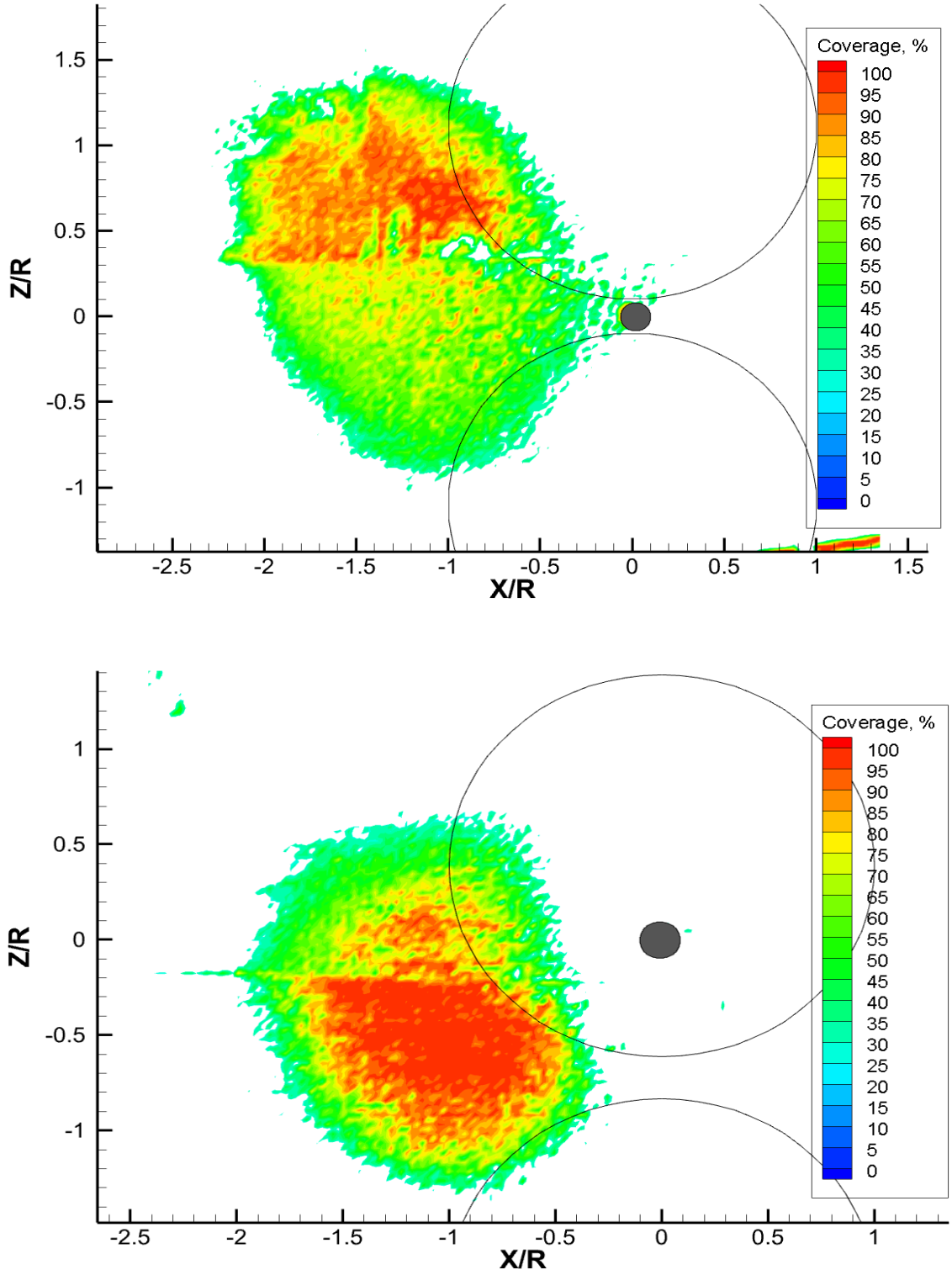

Figure 7.4 Spray deposition pattern on the ground (zero horizontal velocity). Top: nozzle between rotors; bottom: nozzle placed underneath the fastest downwash.

In both cases, the centre of mass of the deposited spray footprint was shifted relative to the nozzle. Spray released from a nozzle in the region of fastest downwash (0.6R) is more concentrated, i.e., has a smaller footprint, than spray released between the rotor discs. The area with 30% or greater coverage was 0.67 m^2 when the nozzle was placed under the greatest downwash and 0.90 m^2 when the nozzle was placed between rotor disks. With the nozzle between the rotors, some water was found on the walls (3.57 R or 1.5 m away), suggesting that the rotors are in ground effect with the downwash spreading radially where it meets the floor. The lateral motion of the spray is less severe with the nozzle located in the region of greatest downwash.

7.3.1.2 Spray deposition modelling

The modelling of the spraying multicopter was performed using the following spray parameters in the *kinematicCloudProperties* dictionary (Table 7.3):

Table 7.3 Parameters of the *coneInjection* nozzle model in the *kinematicCloudProperties* dictionary

massTotal	0.033 kg/per nozzle
injectionMethod	disk
flowType	flow rate and discharge
duration	3 seconds
parcelPerSecond	10000 per nozzle
position	*(0, 0, 0)* (origin in centre of nozzle)
direction	(0, -1, 0)
outerDiameter	0.71 mm
innerDiameter	0 mm
Cd	0.9
thetaInner	40°
thetaOuter	0°

The reported ground deposition in the model was mass per unit area. To compare the modelled and experimental results, mass per unit area was converted to coverage. Assuming that the surface of the ground is dry and smooth, the maximum spreading diameter was (Equation 7.14) (Scheller et al., 1995):

$$d_{\text{impact}} = d_d\left(Re_i\sqrt{We_i}\right)^{0.166} \qquad \text{(Equation 7.14)}$$

Where d_d is volume mean diameter (VMD) used in the model,

$Re = \frac{\rho_{droplet} V_{droplet} d_{droplet}}{\mu_{droplet}}$ is an impact Reynolds number,

$We_i = \frac{\rho_d V_d^2 d_d}{\sigma_d}$ is an impact Weber number,

$V_{droplet}$ is droplet velocity

ρ is a droplet density,

μ is a droplet viscosity,

σ is a droplet surface tension.

The average impact velocity reported by the model was 5.2 m/s. The average impact particle diameter (VMD=87 microns) was 225 microns. 25 particles on average would be required to fully cover 1 mm^2 of the ground. The total weight of 25 particles was $8.62x10^{-9}$ kg. This total weight was used to normalise the model output and obtain the coverage.

Figure 7.5 presents the coverage on the ground plane obtained from the model (left) and coverage obtained from the experiment (right).

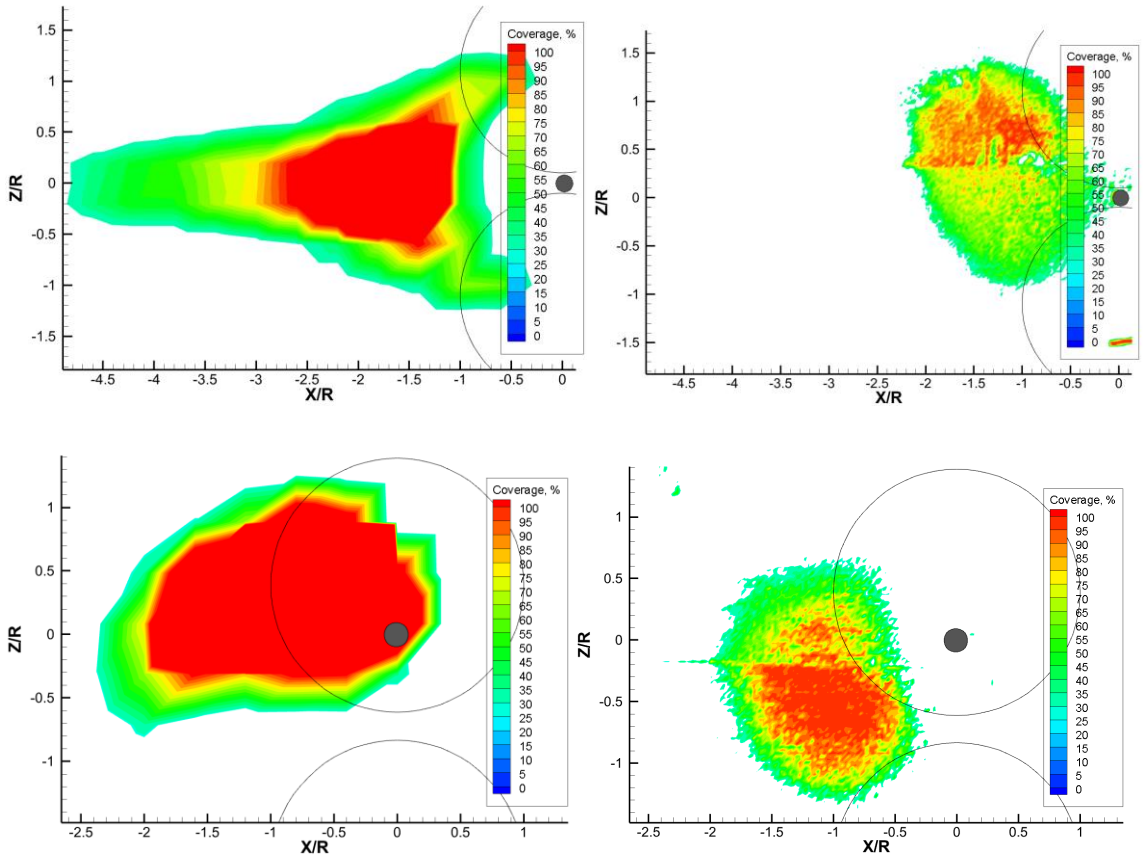

Figure 7.5 Spray deposition pattern on the ground. Top left: model, nozzle between rotors; top right: experiment, nozzle between rotors. Bottom left: model, nozzle placed in the region of greatest downwash the fastest downwash; bottom right: experiment, nozzle placed in the region of greatest downwash.

As in the experimental analysis, the centre of mass of the deposited spray footprint is shifted relative to the nozzle. Spray released from a nozzle in the region of fastest downwash (0.6R) is more concentrated, i.e., has a smaller footprint and larger mass deposition in the centre of the spray than spray released between the rotor discs.

Two parameters were used to compare modelled and experimental ground deposition: the position of the centre of gravity of the footprint and the total area of the footprint.

With the nozzle between rotors, the lateral offset of the centre of mass of the footprint in the Z direction was -1.28R (0.546 m) in the experiment and -1.9R (0.79 m) in the model. In the model, the footprint is symmetrical around the X/R axis. The footprint is not symmetrical in experimental analysis, with a positive shift to Z/R=0.21.

Modelling and experimental analysis of the spray footprint differ when the nozzle is in the zone of greatest downwash. In the X direction, the lateral offset of the centre of mass of the footprint is -1.11R (-0.47 m) in the experiment and -0.79R (0.33 m) in the model. In the Z direction, the lateral offset of the centre of mass of the footprint is -0.36R (-0.15 m) in the experiment and 0.24R (-0.1 m) in the model.

There is a noticeable shift between footprints. The possible sources of this shift are a difference in rotational speed between experiment and model, the method of modelling of tip vortices, a phase difference between the rotors, the proximity of walls and ceiling, variation in the geometrical position of the nozzle, or the presence of particles that are not within the assumed droplet size distribution of the nozzle.

The possible sources of the variance between model and experiment were tested in the model: rotation speed of both rotors (tested at 1560 RPM, 1740 RPM, and 1910 RPM), nozzle angular

position variation (tested +(clockwise) -(negative) 10^{o} tilt angles around the X and Z axes, Figure 7.6). The ceiling and the nearest wall were represented in the model.

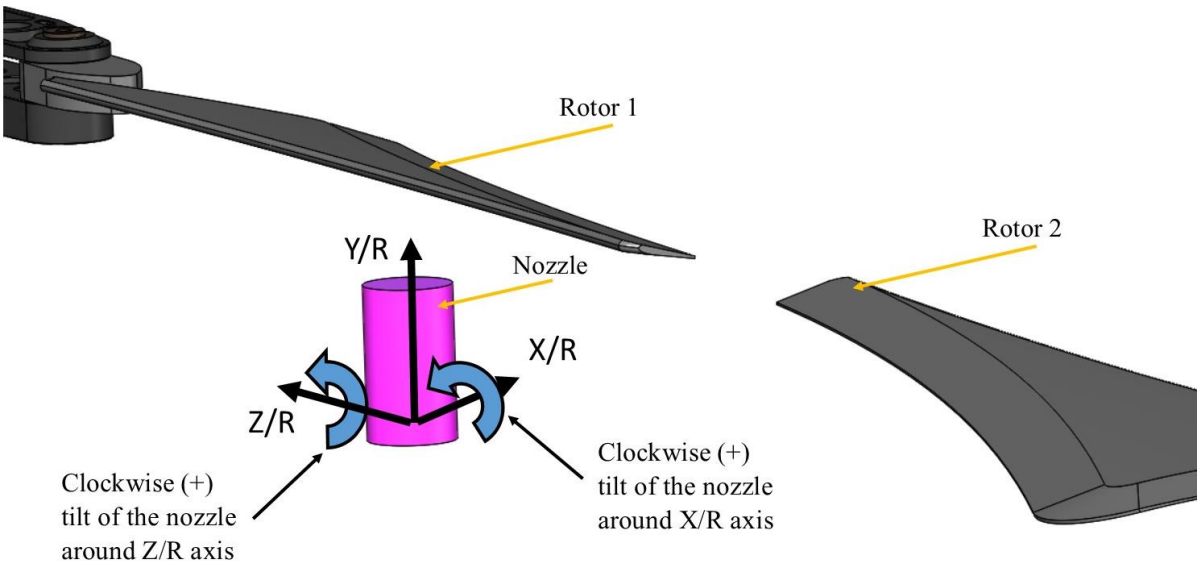

Figure 7.6 Nozzle angular position variation schematic

Figure 7.7 shows the contour plot of the ground footprint with different parameters tested in the model when the nozzle is placed between rotors. Table 7.4 shows the total area of the footprint, and X/R and Z/R positions of the footprint's centre of mass when the nozzle is placed between rotors.

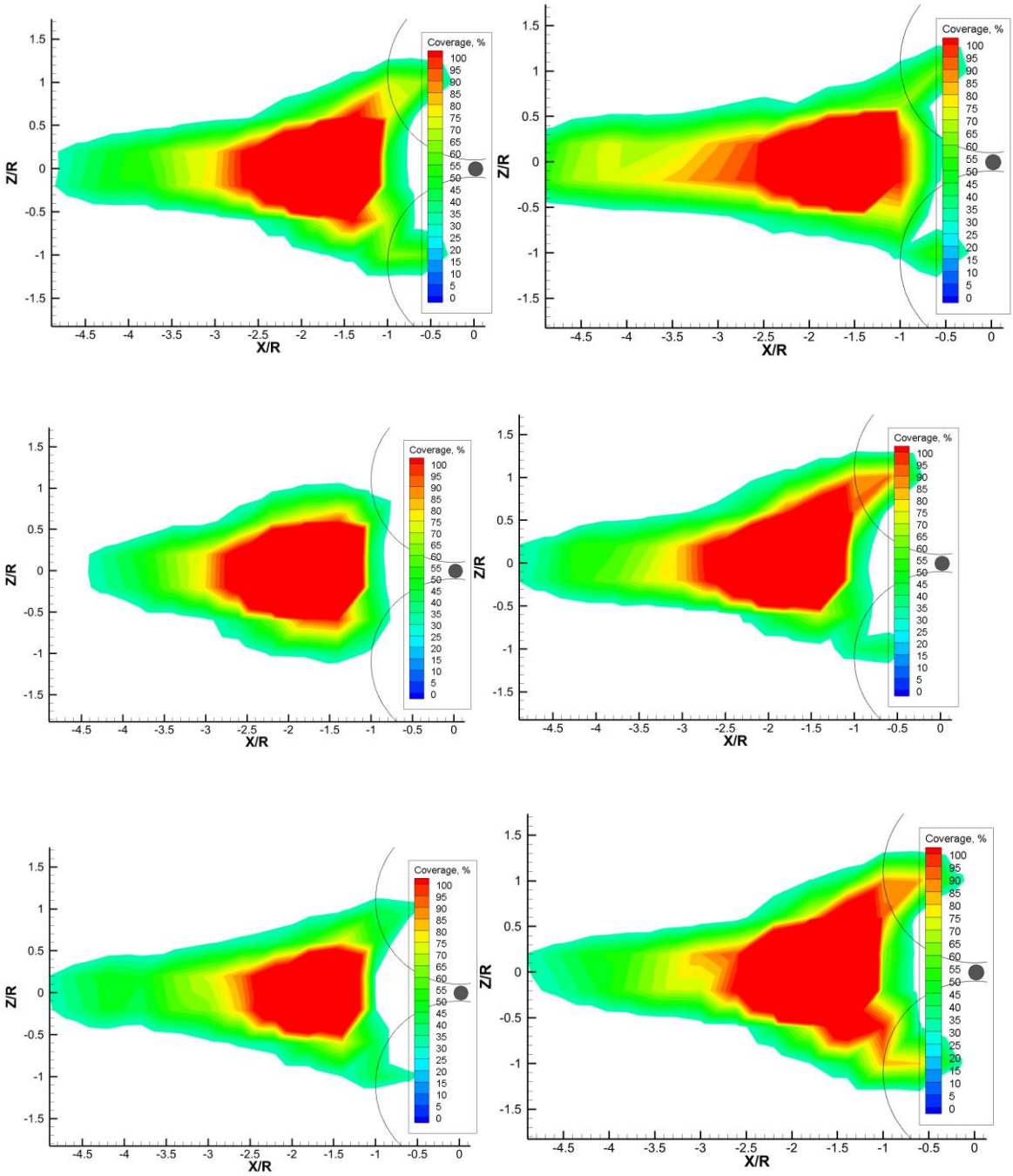

Figure 7.7 Spray deposition pattern on the ground when the nozzle is placed between rotors at rotational speeds of: a) 1740 rpm, nozzle not tilted; b) 1560 rpm, nozzle not tilted; c) 1970 rpm, nozzle not tilted; d) 1740 rpm, nozzle tilt is 10° counterclockwise around X axis; e) 1740 rpm, nozzle tilt is 10° clockwise around Z axis; f) 1740 rpm, nozzle tilt is 10° counterclockwise around Z axis.

Table 7.4 Total area of footprint, X/R and Z/R positions of footprint centre of mass when nozzle is placed between rotors.

	Normalised area of 30% coverage	X/R position of centre of gravity	Z/R position of centre of gravity
Experiment	3.08	-1.28	0.21
Model, 1740 RPM (Base case)	2.96	-1.9	0
Model, 1560 RPM	4.08	-2.29	0
Model, 1910 RPM	2.94	-1.89	0
Model, 1740 RPM Nozzle counterclockwise tilt around X axis -10º	3.12	-1.95	0.12
Model, 1740 RPM Nozzle clockwise tilt around Z axis 10º	2.72	-2.13	0
Model, 1740 RPM Nozzle counterclockwise tilt around Z axis 10º	3.44	-1.8	0

Figure 7.8 shows the contour plot of the ground footprint with different parameters tested in the model when the nozzle was placed under the greatest downwash. Table 7.5 shows the total area of the footprint and X/R and Z/R positions of the footprint's centre of mass when the nozzle was placed under the greatest downwash.

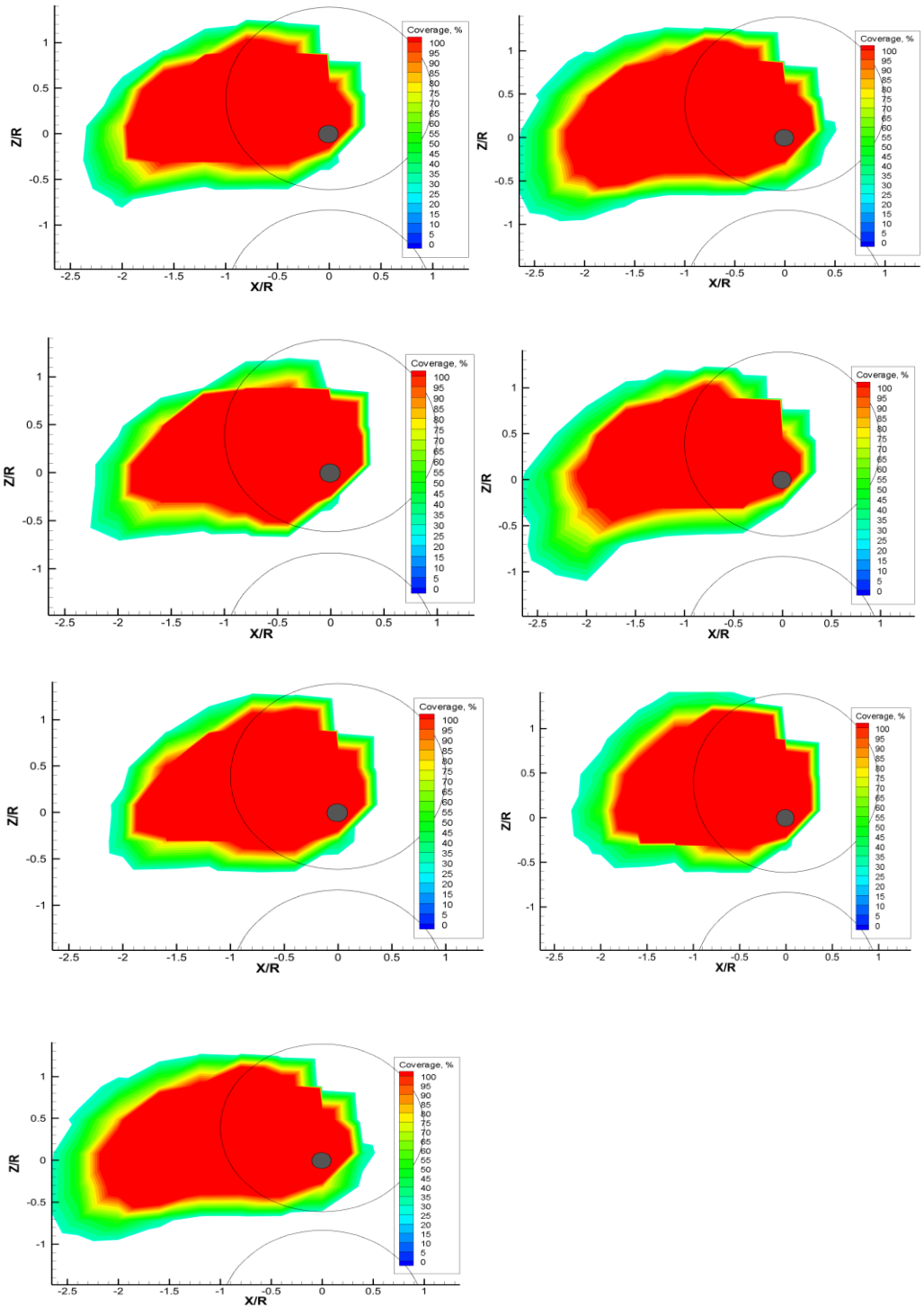

Figure 7.8 Spray deposition pattern on the ground when the nozzle is placed under the greatest downwash at rotational speeds of: a) 1740 rpm, nozzle not tilted; b) 1560 rpm, , nozzle not tilted; c) 1970 rpm, , nozzle not tilted; d) 1740 rpm, nozzle tilt is 10º clockwise around X axis; e) 1740 rpm, nozzle tilt is 10º counterclockwise around X axis; f) 1740 rpm, nozzle tilt is 10º clockwise around Z axis; g) 1740 rpm, nozzle tilt is 10º counterclockwise around Z axis.

Table 7.5 Total area of footprint, X/R and Z/R positions of footprint centre of mass when the nozzle is placed under the greatest downwash.

	Normalised area of 30% coverage	X/R position of centre of gravity	Z/R position of centre of gravity
Experiment	2.19	-1.11	-0.36
Model, 1740 RPM (Base case)	2.24	-0.79	0.24
Model, 1560 RPM	3.12	-0.9	0.23
Model, 1910 RPM	1.76	-0.67	0.17
Model, 1740 RPM Nozzle tilt clockwise around X axis 10º	2.56	-0.85	0.23
Model, 1740 RPM Nozzle tilt counterclockwise around X axis 10º	1.92	-0.75	0.22
Model, 1740 RPM Nozzle tilt clockwise around Z axis 10º	2.56	-0.74	0.28
Model, 1740 RPM Nozzle tilt counterclockwise around Z axis -10º	3.12	-0.89	0.23

All the tested parameters influence spray distribution on the ground. Increasing rotor rotational speed decreases the spray footprint and lateral drift for both nozzle positions. The tilt of the nozzle affects the area of the footprint and the lateral drift of the spray.

7.3.2 DJI Agras MG-1 multicopter

In the experimental analysis, four TJ60 11002 nozzles (TeeJet Technologies, Spraying Systems Co., Wheaton, IL, USA) were used. They operated at 2 bar pressure. The droplet size falls within ASABE 572.1 “fine” category. The nozzles were positioned under the 4 rotors and were

flown with the nozzles either in a windward or leeward position (Richardson et al., 2019) (Figure 7.9).

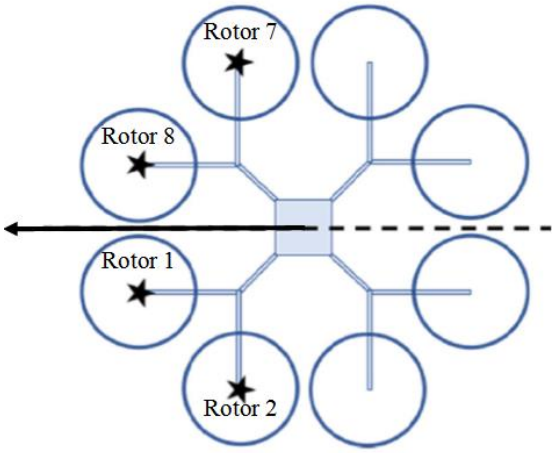

Figure 7.9 The AGRAS MG-1 with its rotors (circles) and nozzle placements (stars) (adapter from Richardson et al., 2019).

The spray distribution on the ground was captured on steel plates sitting 25 mm away from the ground. A fluorescent tracer was added to the sprayed water in a proportion of 100 mL/L. After spraying, the plates were allowed to dry and fluorescence was measured using the standard technique (Narin et al., 2015).

The spraying multicopter was modelled with the following parameters of spray for all flights (Table 7.6):

Table 7.6 Parameters of the *coneInjection* nozzle model in the *kinematicCloudProperties* dictionary

massTotal	0.00961 kg/per nozzle
injectionMethod	disk
flowType	Flow rate and discharge
duration	1 second, (9 second checked)
parcelPerSecond	10000 per nozzle
position	*(xr1, -0.02, zr1)* Under rotor 1 *(xr2, -0.02, zr2)* Under rotor 2 *(xr7, -0.02, zr7)* Under rotor 7 *(xr8, -0.02, zr8)* Under rotor 8
direction	(0, -1, 0)
OuterDiameter	1.6 mm
innerDiameter	0 mm
Cd	0.9
thetaInner	55°
thetaOuter	0°

In the model, the spray deposition was sampled at 25 mm distance from the ground for consistency with the experiment. The evaporation of the spray was included in the model.

7.3.2.1 Flight 4 (F4)

Flight 4 (F4) had a reported height above ground of 2.8 metres, a flight speed of 2.85 m/s, and a cross wind speed of 0.736 m/s (Chapter 6, Table 6.11). The model accounted for the evaporation of the droplets (Equations 7.6-7.9). Relative humidity (RH) was reported at 63% and temperature was reported at 14℃.

Figure 7.10 shows the view in the direction of flight (X/R) of spray released under the multicopter at 1 s (top), 2 s (middle) and 3 s (bottom). Parcels are coloured according to particle diameter in the parcel.

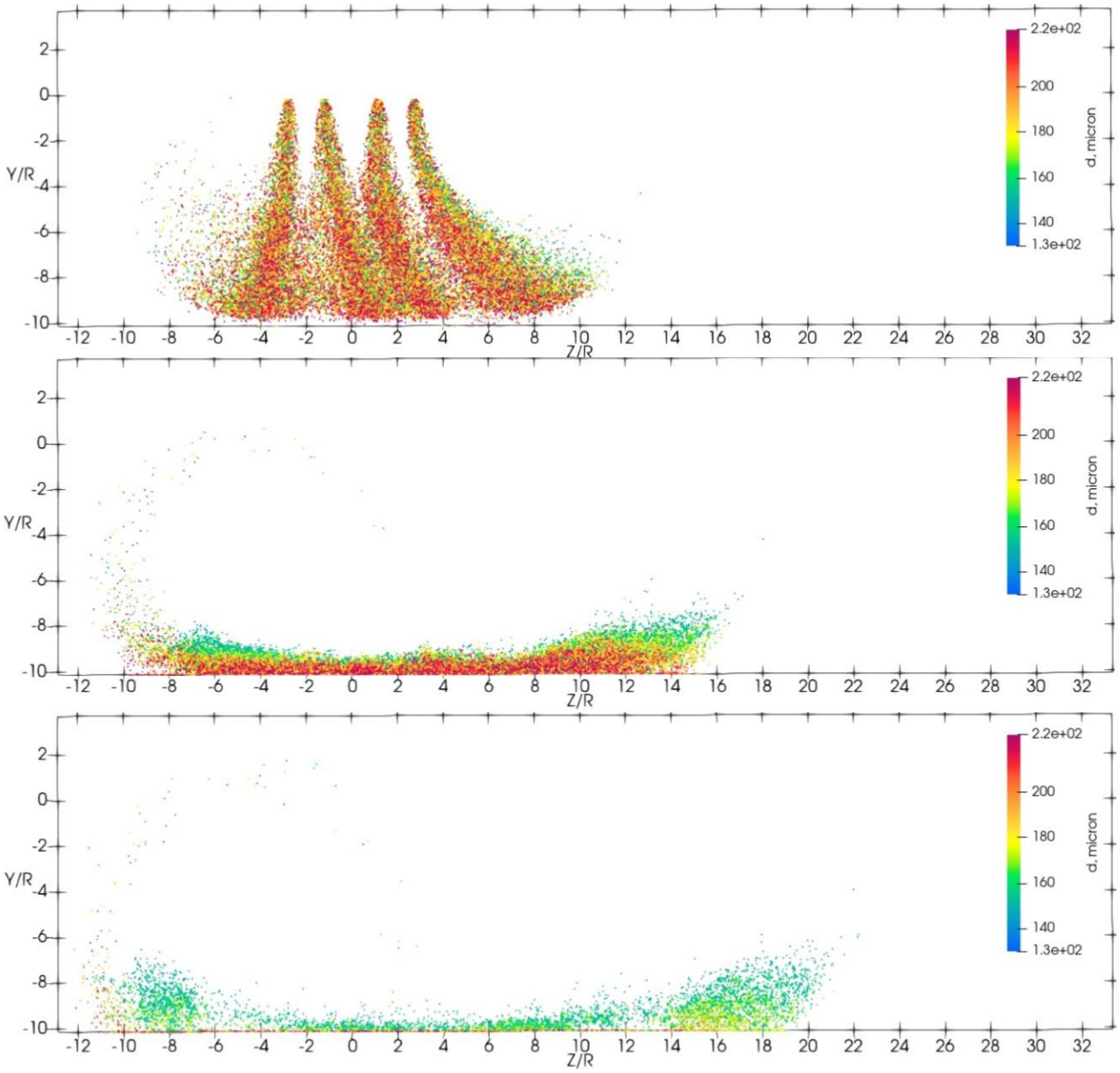

Figure 7.10 View in the direction of flight (X/R) of spray released in flight 4 under the multicopter at 1 s (top), 2 s (middle) and 3 s (bottom). Parcels are coloured according to particle diameter in microns.

Figure 7.10 shows that the spray is influenced by the main downwash and rollup vortices. The spray drifts in the direction of the wind (+Z).

The view from above on the ground plane shows the strong influence of rollup vortices on spray deposition (Figure 7.11). Smaller particles, trapped in the rollup vortex, drift further away in a downwind direction. The furthest particle drift was reported at X/R =-90 (-23.9 m) Z/R=30 (8 m).

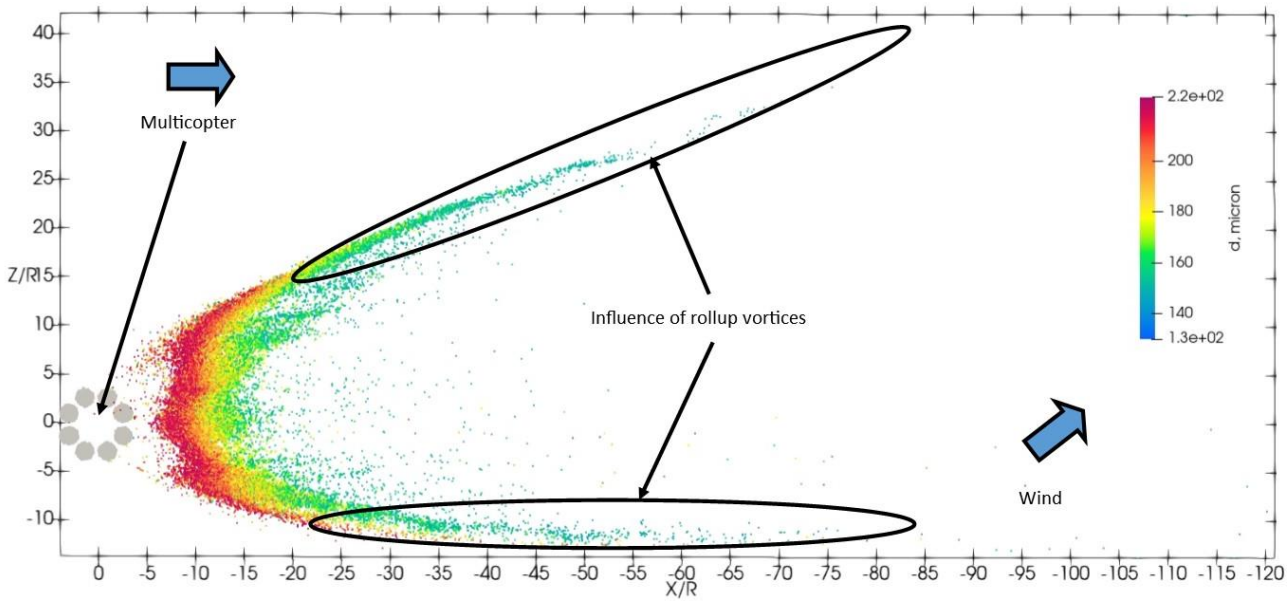

Figure 7.11 View from above of spray released in flight 4 under the multicopter at 10 s. Parcels are coloured according to particle diameter in microns. The arrows show the wind and flight velocity directions. The multicopter is at X/R=0, Z/R=0.

Larger particles deposit on the ground earlier than smaller particles. Some of the smaller particles (180 microns and smaller) are lifted up by the rollup vortices and are traversed far away from the release point.

The reported flight height was 2.8 m (10.5 R). To test the influence of a possible height uncertainty on the swath, the spraying multicopter was modelled with flight heights of 2.5 m (9.38R) and 3.1 m (11.63R) (Figure 7.12).

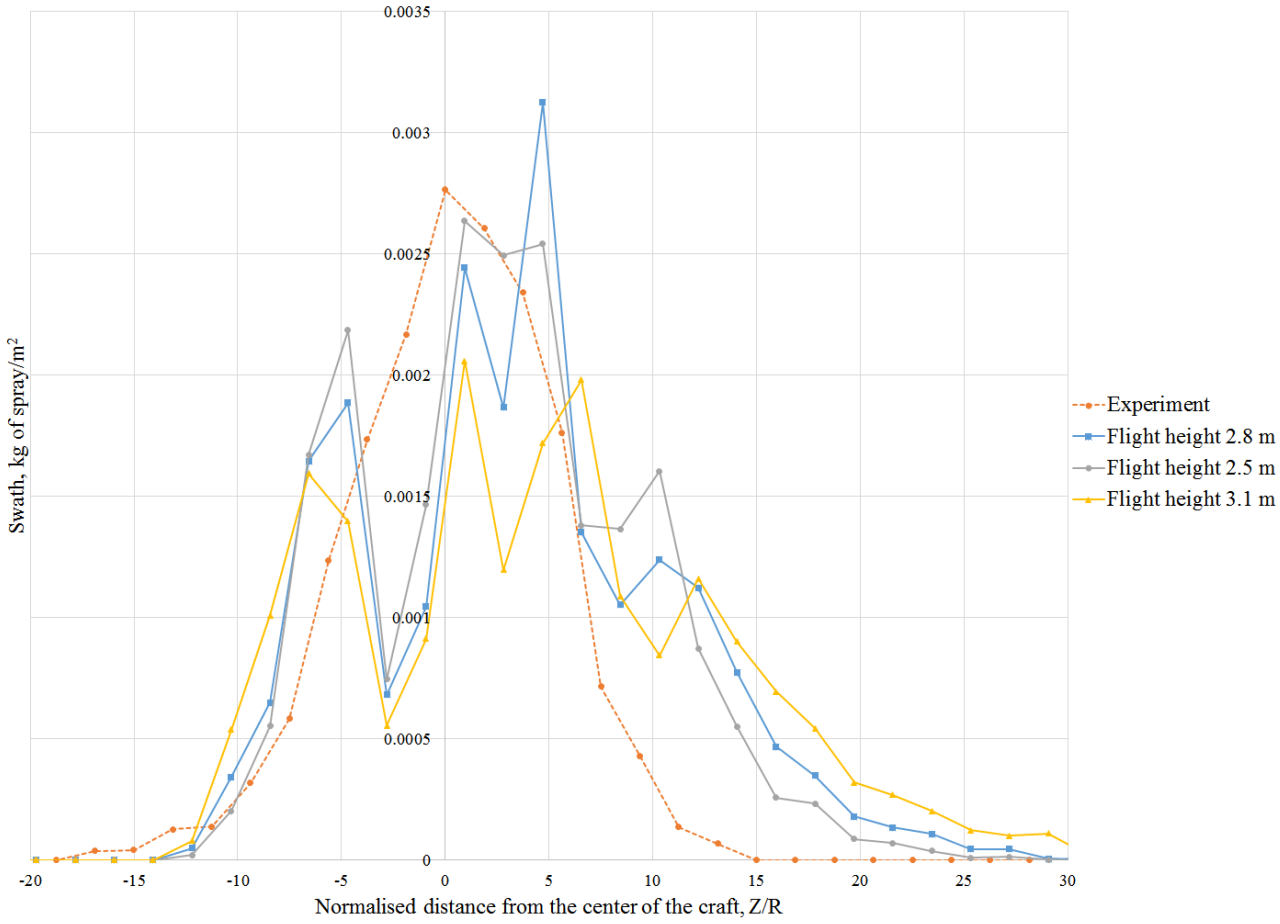

Figure 7.12 Modelled swath pattern of spray (kg/m^2) deposited on the ground in Flight 4 conditions at release heights of 2.8 m (blue line with rectangular dots), 2.5 m (grey line with rhomboid dots) and 3.1 m (yellow line with triangular dots).

Height does not significantly influence the spatial extent of spray deposition (Figure 7.12). However, the amount of deposition in the extreme points of the graphs decreases with increase of the flight height. This may be explained by droplet evaporation as a result of particles traveling a longer distance to the ground.

The rotational speed of rotors depends on the weight of a multicopter. Gross weights were not reported for each multicopter flight. Therefore, different rotor rotational speeds were modelled. The main modelled rotational speed was 2750 RPM. In addition, speeds of 3020 RPM (+10%) and 2750 RPM (-10 %) were modelled (Figure 7.12)

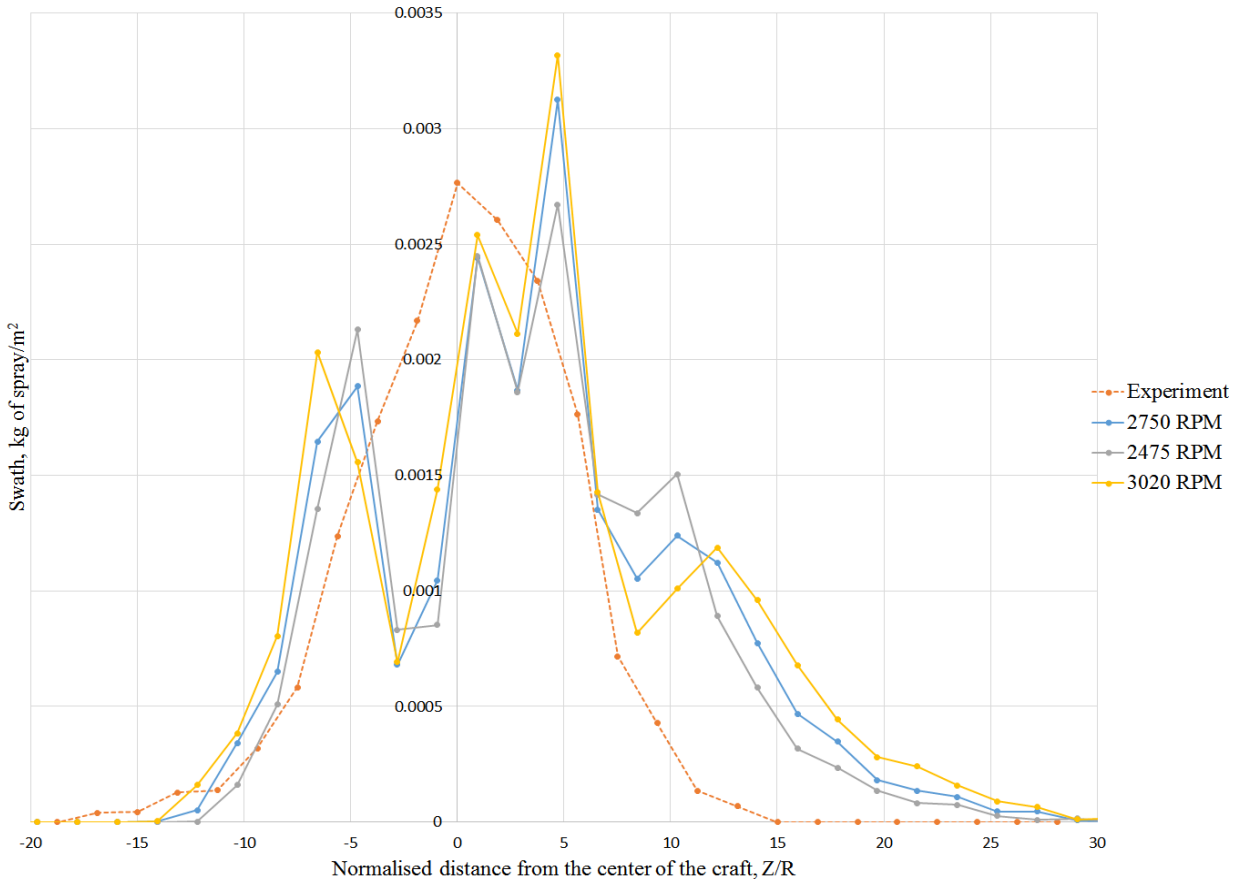

Figure 7.13 Modelled swath pattern of spray (kg/m2) deposited on the ground in Flight 4 conditions when the rotational speed of all rotors is 2750 RPM (blue line with circular dots), 2475 RPM (grey line with rhomboid dots) and 3020 RPM (yellow line with triangular dots).

The swath pattern depends on the rotational speed of rotors. The maximum width of swath increases with increase of rotational speed. The local peak on the leeward side of the swath, formed by the rollup vortex, is drifting away from the multicopter (+Z) with an increase of rotational speed. The weight of the multicopter decreases with spray liquid consumption. Therefore, the swath pattern will change over the course of the flight.

The yaw angle was not reported during the spraying experiment. It was assumed that the yaw angle was changing during the flight from -5^{o} to +5^{o} around the Y axis (Figure 7.14).

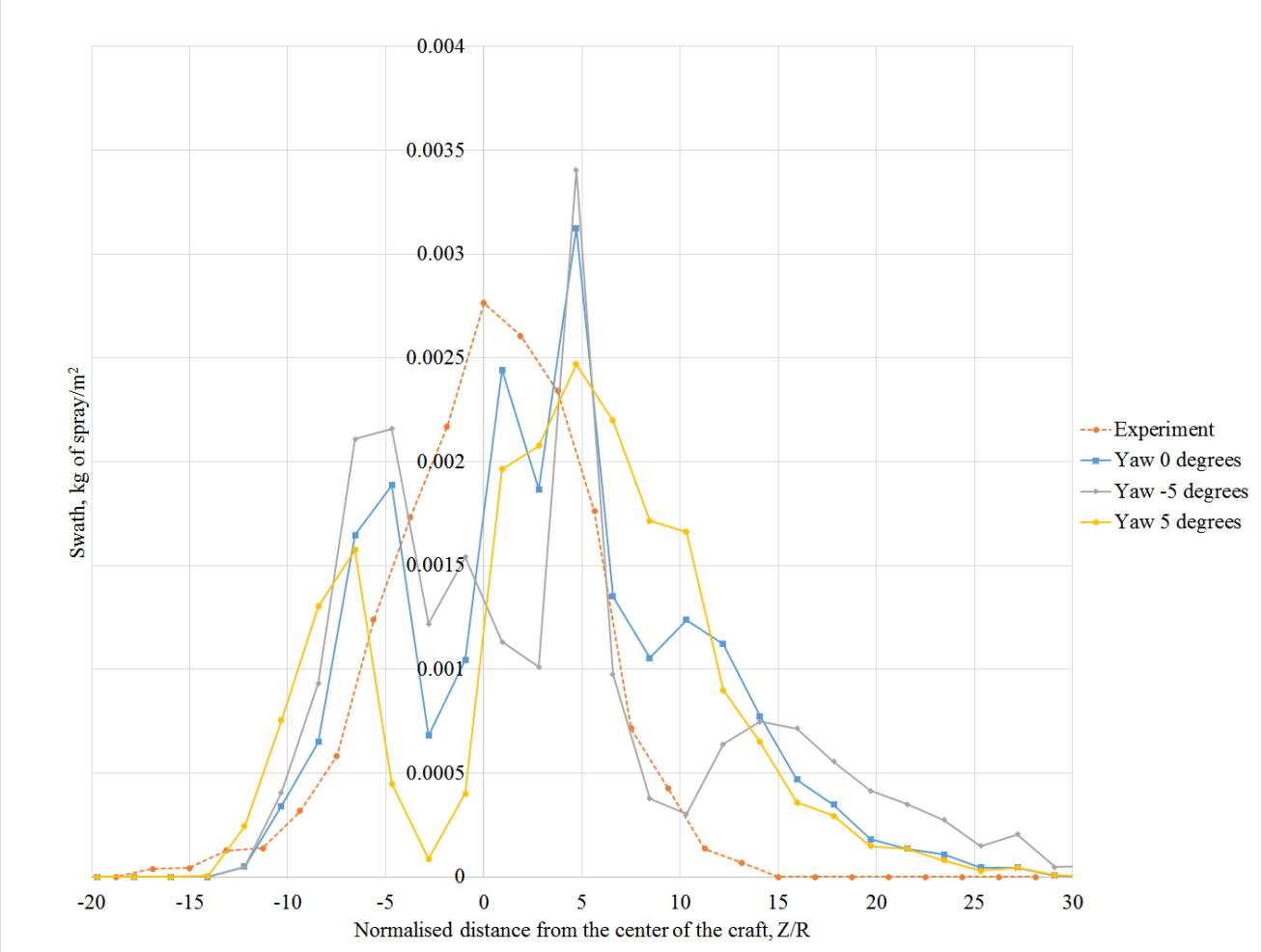

Figure 7.14 Modelled swath pattern of spray (kg/m^2) deposited on the ground in Flight 4 conditions when the yaw angle of the multicopter is 0º (blue line with rectangular dots), -5º (grey line with rhomboid dots) and +5º (yellow line with circular dots).

The swath pattern depends on the yaw angle of the multicopter. When yawing, the nozzles are not symmetrical around the direction of flight. With negative yaw, the total swath is wider than with a neutral or positive yaw angle.

The roll angle was not reported in the experiment. The roll angle was assumed to be -5º to +5º around the X axis (clockwise-positive) (Figure 7.15).

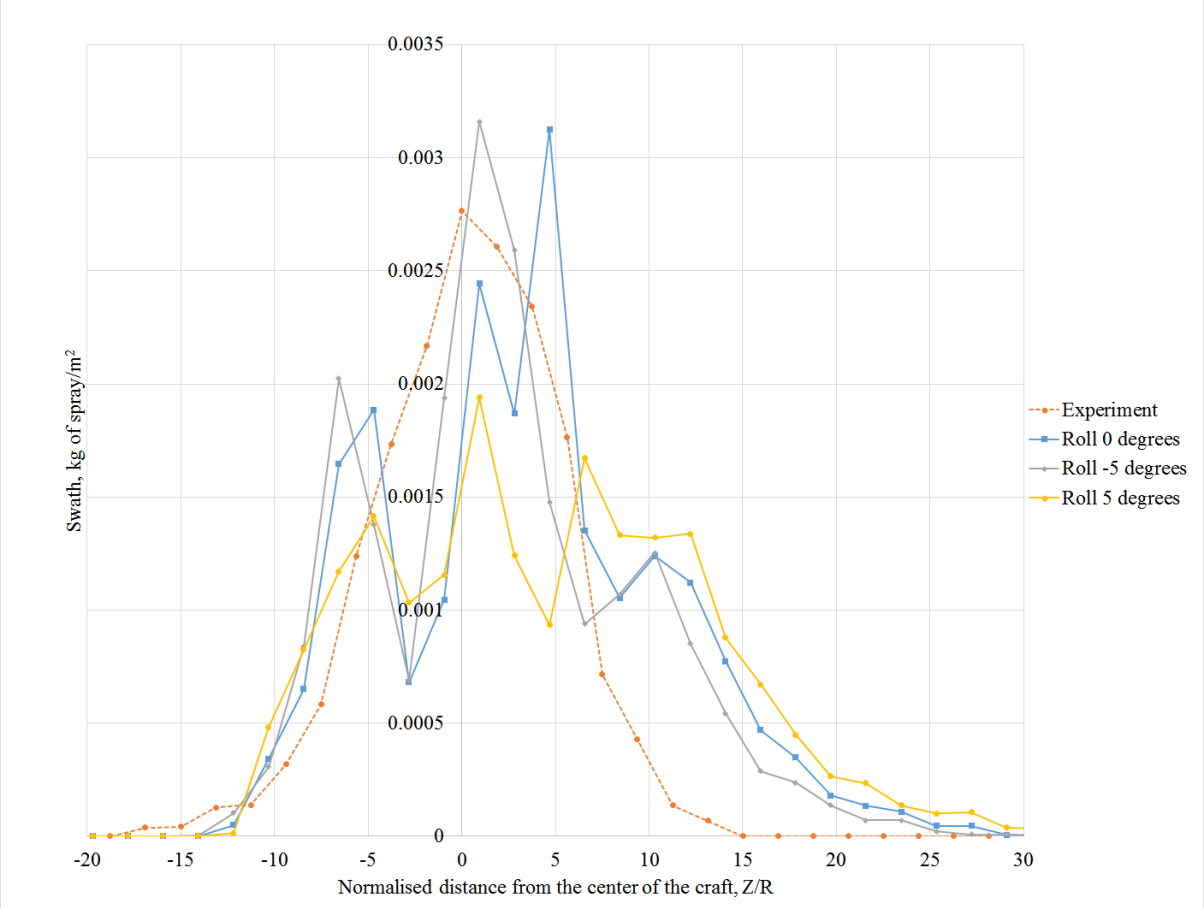

Figure 7.15 Modelled swath pattern of spray (kg/m^2) deposited on the ground in Flight 4 conditions when the roll angle of multicopter is 0º (blue line with rectangular dots), -5º (grey line with rhomboid dots) and +5º (yellow line with triangular dots).

The changing roll angle does not significantly influence the spatial extent of spray deposition. However, the amount of deposition decreases with increasing roll angle.

The roughness of terrain wasn't reported in Richardson et al., 2019 experiments. Therefore, the roughness of terrain= 0.1 m, 0.25 m, and 0.5 was tested (refer to section 6.3.2.2, table 6.3). When the roughness of terrain was 0.5 (bushes, numerous obstacles), the modelled swath was closest to the experimental swath (Figure 7.16).

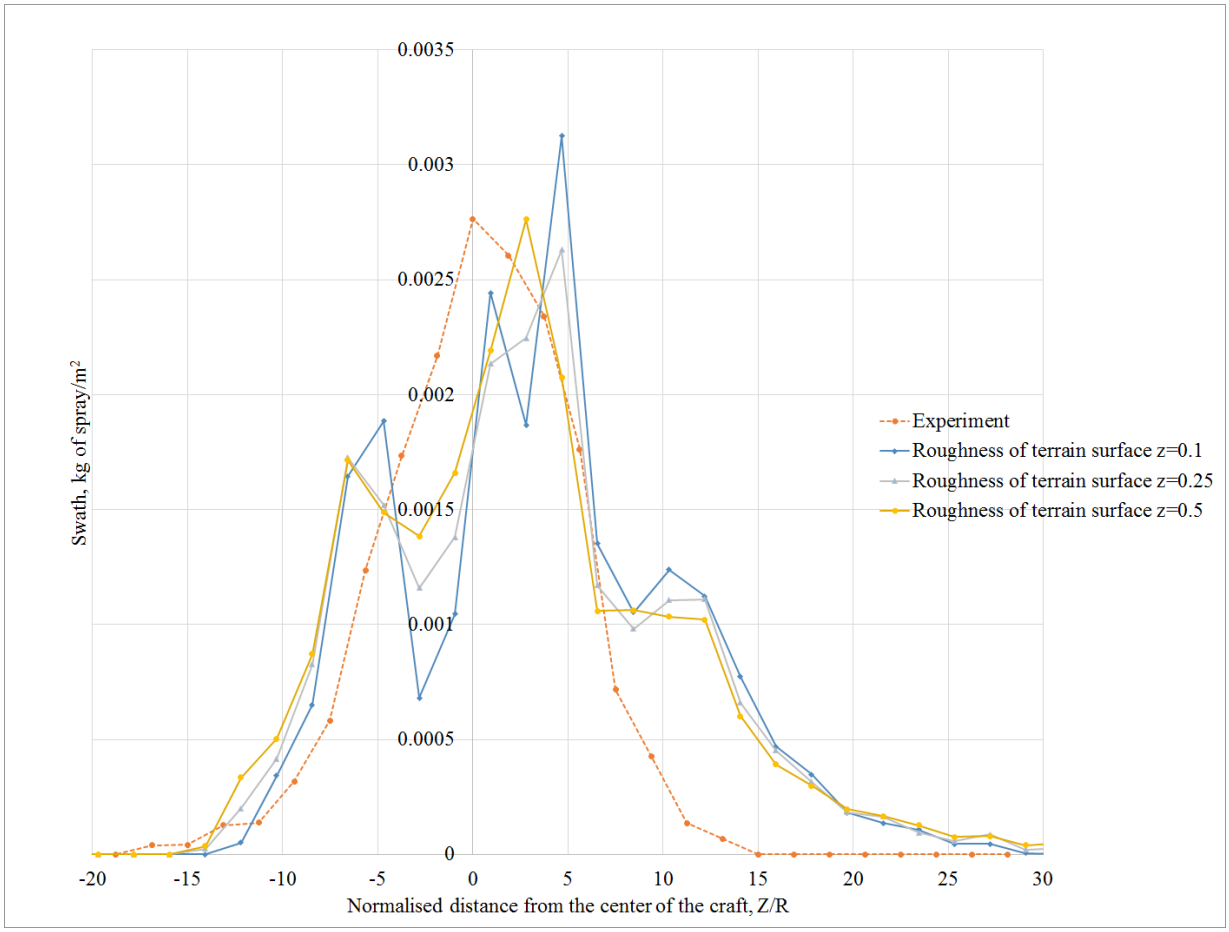

Figure 7.16 Modelled swath pattern of spray (kg/m^2) deposited on the ground in Flight 4 conditions when the roughness of the terrain was 0.1 m (blue line with rhomboid dots), the roughness of the terrain was 0.25 m (grey line with triangular dots), and the roughness of the terrain was 0.5 m (yellow line with circular dots).

The mean spray deposition is shown on Figure 7.17. The error bars on the swath pattern represent one standard deviation of ground deposition of all variables tested in the model. The modelled mean spray deposition has its peak at Z/R=4.8 (1.279 m) and a local extreme minimum between peaks at Z/R=-2.5 (-0.667 m). This local extreme minimum was not observed in the experiment.

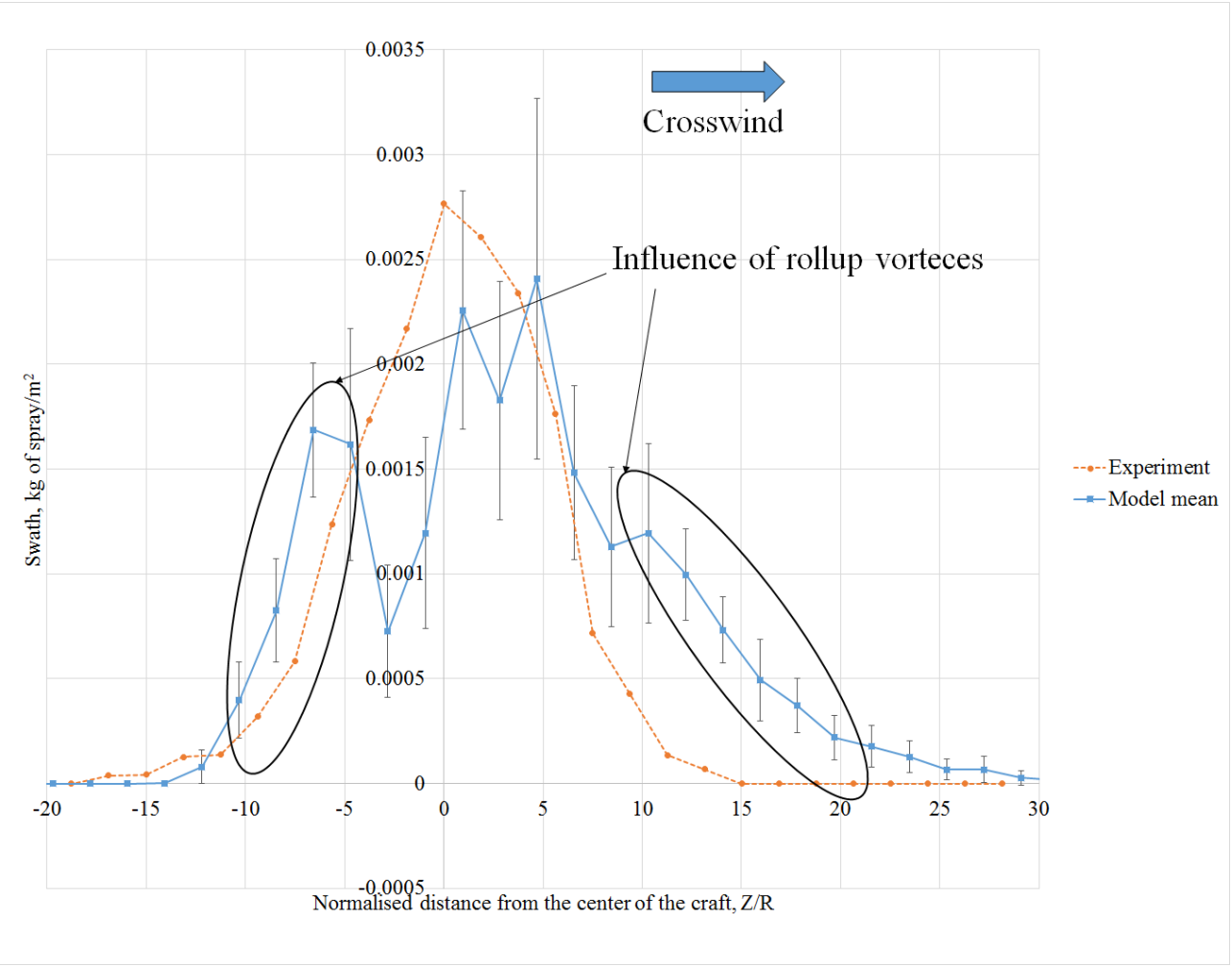

Figure 7.17 The swath pattern of spray (kg/m^2) deposited on the ground in Flight 4 conditions. The orange line with circular dots is the swath obtained in the experiment. The blue line with square dots is the swath obtained in the model. The arrow shows the direction of the crosswind. The black ellipses show the part of the swath influenced by the rollup vortices.

The modelled swath was closest to the experimentally obtained swath when the surface roughness was equal to 0.5 m (bushes, suburb) and the rotational speed of all rotors was equal to 2475 rpm. In an experiment by Richardson et al. (2019), the trial was undertaken on the recently mown grass. The grass reduces the distance travelled by the rollup vortex (Chapter 1, Section 1.3.2), thereby reducing the drift of the spray (Figure 7.18). A 0.75R (0.2m) tall plant

canopy (grass) was implemented in the model as a porous medium (section 6.3.2.4). For grass, $LAD=1.6\ m^{-1}$ and $C_d= 0.34$ (Gillies et al., 2002). The inertia loss coefficient was $C_2=0.544$.

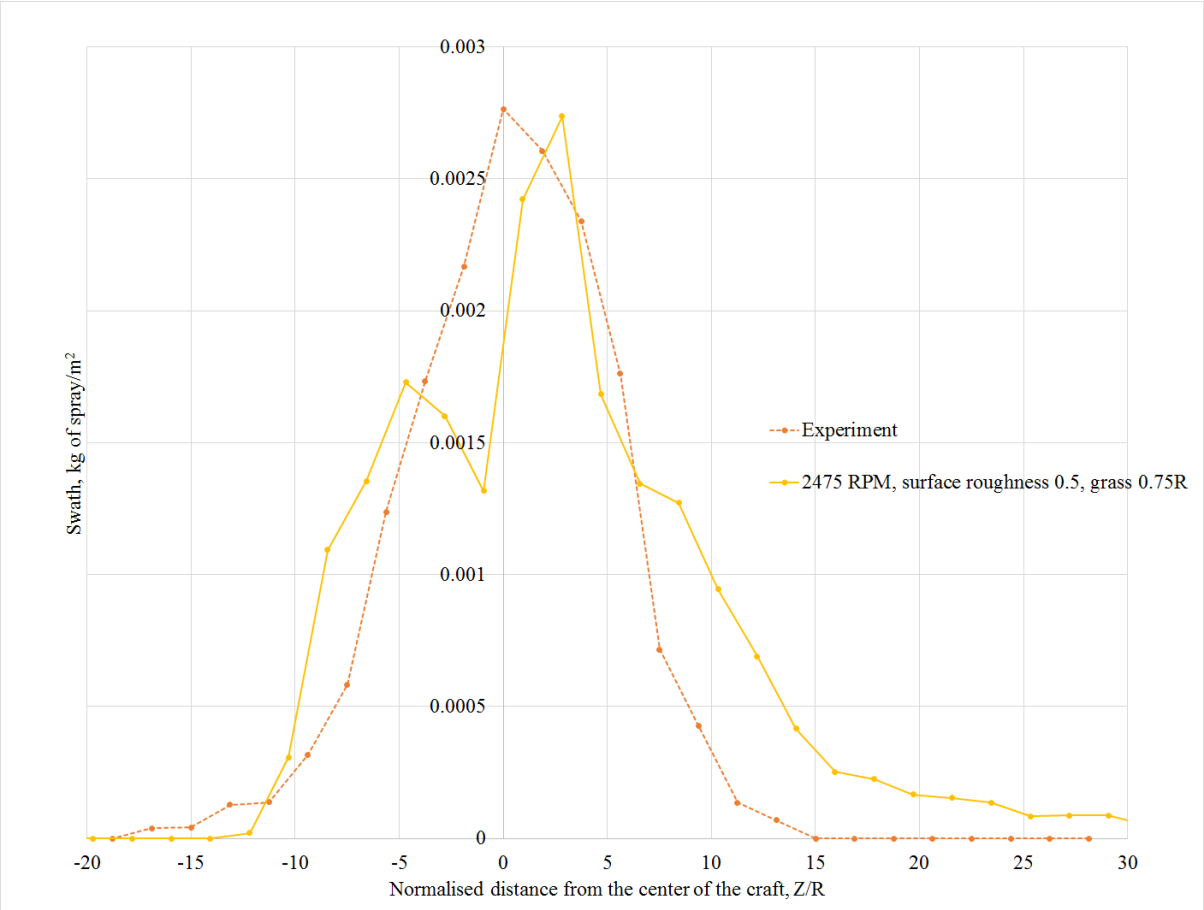

Figure 7.18 Modelled swath pattern of spray (kg/m^2) deposited on the ground in Flight 4 conditions when the roughness of the terrain was 0.5 m, rotational speed of all rotors was 2475 rpm and the plant canopy was 0.75R tall (yellow line with circular dots).

7.3.2.2 Flight 9 (F9)

In Flight 9, the recorded height above the ground was 2.7 m, flight speed was 2.9 m/s, and recorded crosswind speed was 2.164 m/s (Chapter 6, Table 6.11). The evaporation of the droplets was included in the model. Relative humidity (RH) was reported at 63% and temperature was reported at 14°C.

Figure 7.19 shows the view in the direction of flight (X) of the spray released under a multicopter at 1 s (top), 2 s (middle) and 3 s (bottom). Parcels are coloured according to particle diameter.

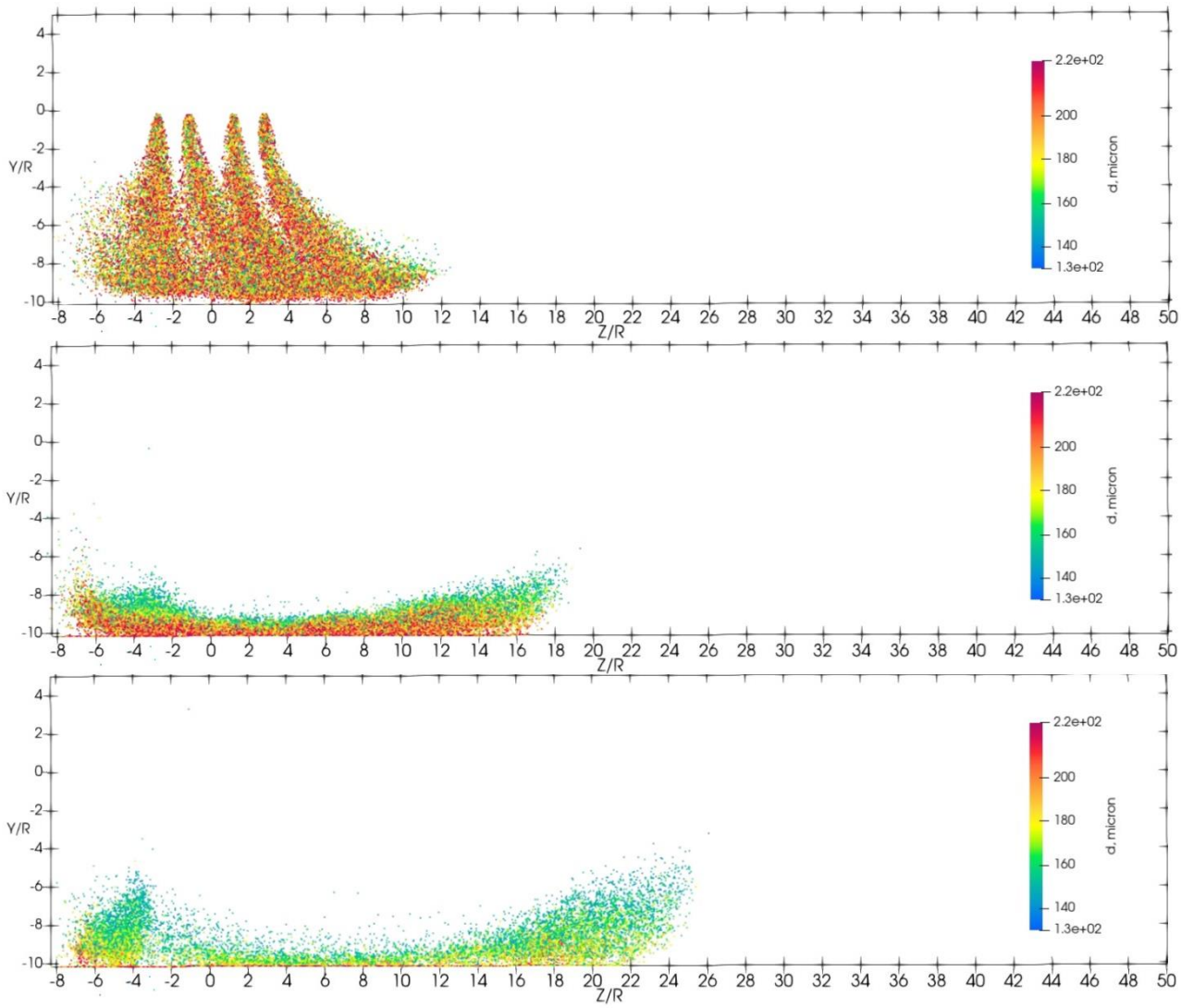

Figure 7.19 View in the direction of flight (X/R) of the spray released in Flight 9 under the multicopter at 1 s (top), 2 s (middle) and 3 s (bottom). Parcels are coloured according to particle diameter in microns.

Similarly to Flight 4 in Figure 7.20, the spray is influenced by the main downwash and rollup vortices.

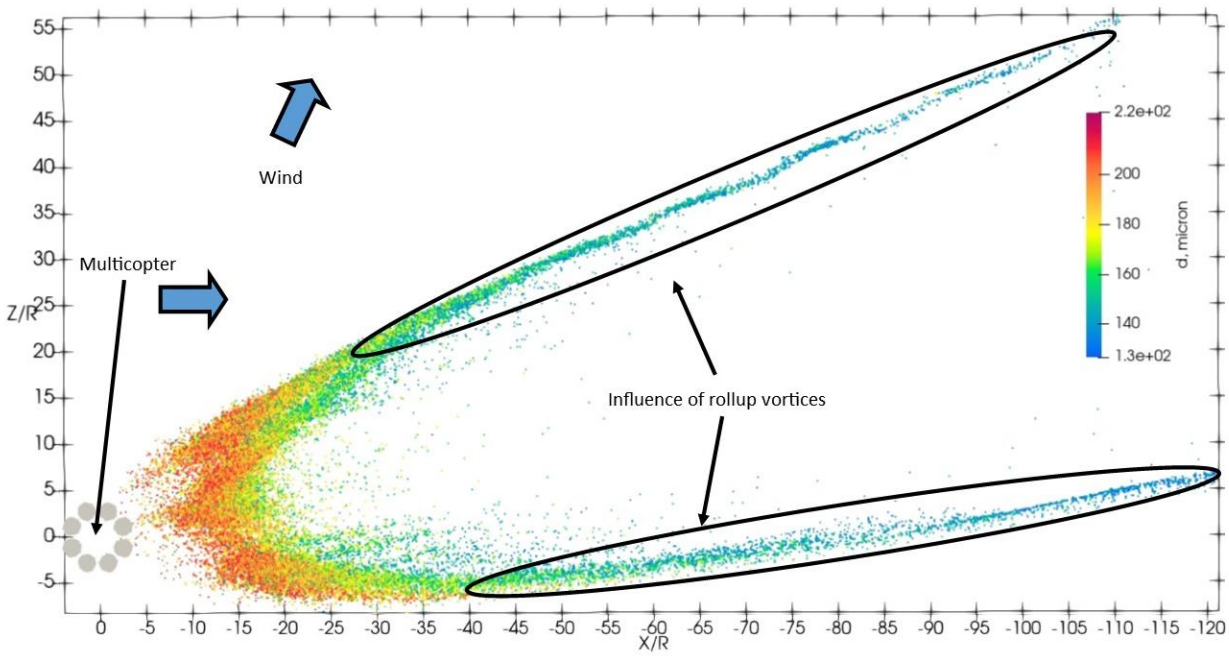

Figure 7.20 View from above of the spray released in Flight 9 under the multicopter at 10 s. Parcels are coloured according to particle diameter in microns. The arrows show wind and flight velocity directions. The multicopter is at X/R=0, Z/R=0.

Larger particles deposit on the ground earlier than smaller particles. Smaller particles are lifted by the rollup vortices and are traversed far away from the initial release point.

The reported flight height was 2.7 m (10.13 R). To test possible height uncertainty the spraying multicopter was modelled at flight heights of 2.5 m (9.38R) and 3.1 m (11.63R). The height does not significantly influence the width of the swath (Figure 7.21).

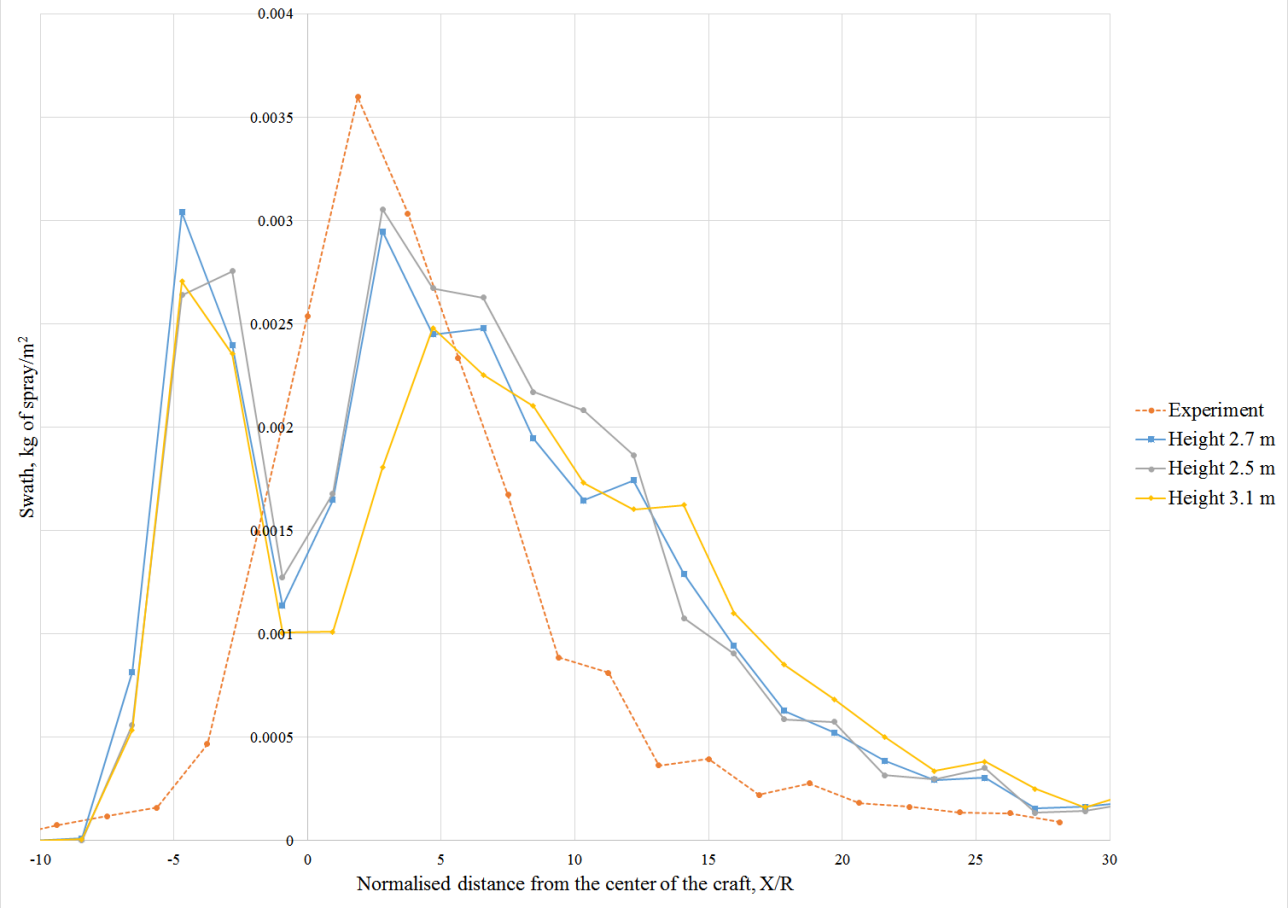

Figure 7.21 Modelled swath pattern of spray (kg/m^2) deposited on the ground in Flight 9 conditions at release heights of 2.7 m (blue line with rectangular dots), 2.5 m (grey line with circular dots) and 3.1 m (yellow line with rhomboid dots).

Rotational speeds similar to Flight 4 were modelled for Flight 9 (Figure 7.22).

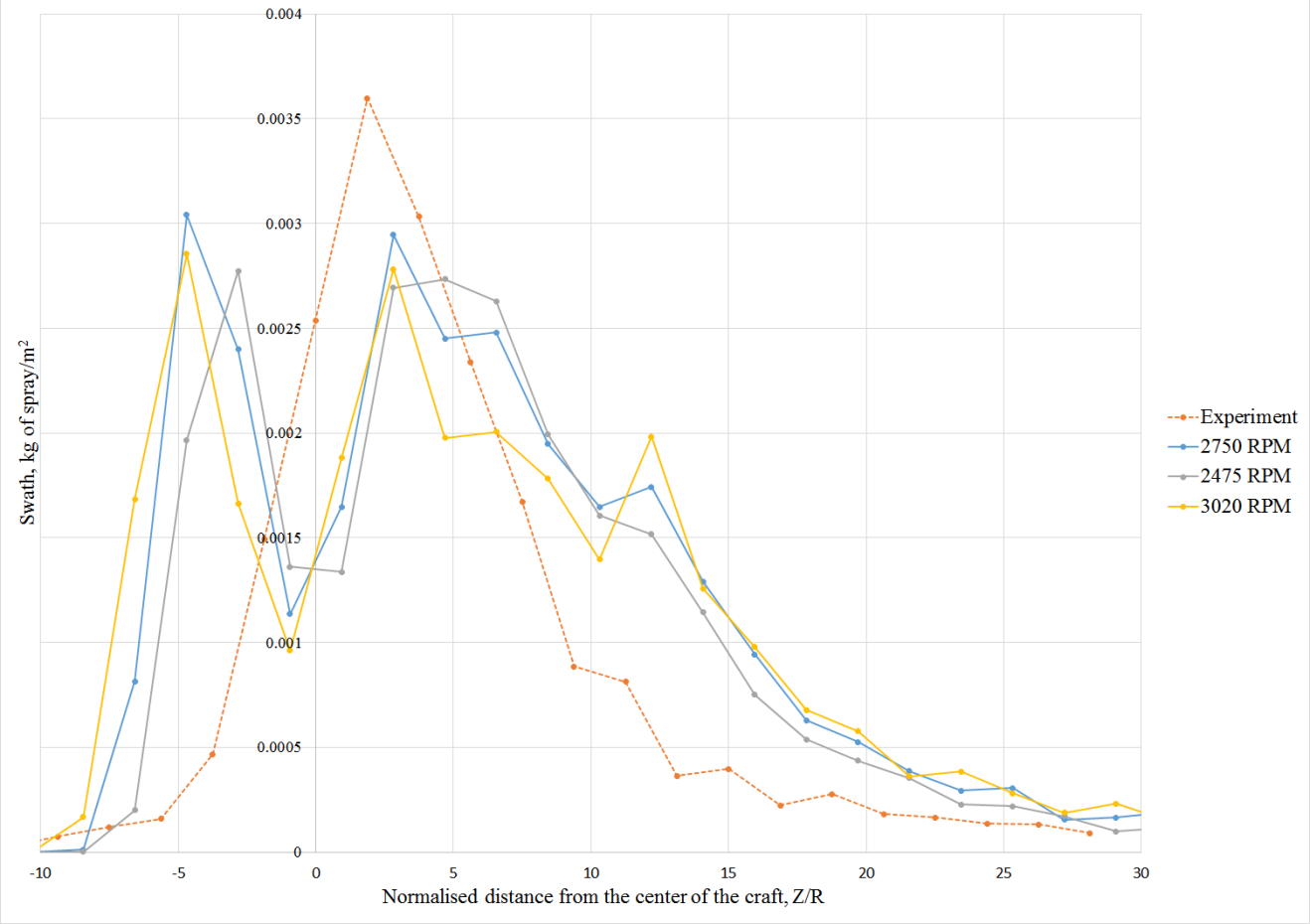

Figure 7.22 Modelled swath pattern of spray (kg/m^2) deposited on the ground in Flight 9 conditions when the rotational speed of all rotors is 2750 RPM (blue line with circular dots), 2475 RPM (grey line with rhomboid dots) and 3020 RPM (yellow line with triangular dots).

The swath pattern depends on the rotational speed of the multicopter. The swath is wider on the windward side (-Z/R axis) than on the leeward side of the crosswind (+Z/R axis). An additional local peak can be observed at 3020 RPM at Z/R=12.5 (3.33 m) due to the influence of the rollup vortex that is stronger at higher rotational speeds of rotors.

The yaw angle was not reported during the spraying experiment. It was assumed the yaw angle was changing during the flight from -5^o to +5^o (clockwise-positive) around the vertical (Y) axis (Figure 7.23).

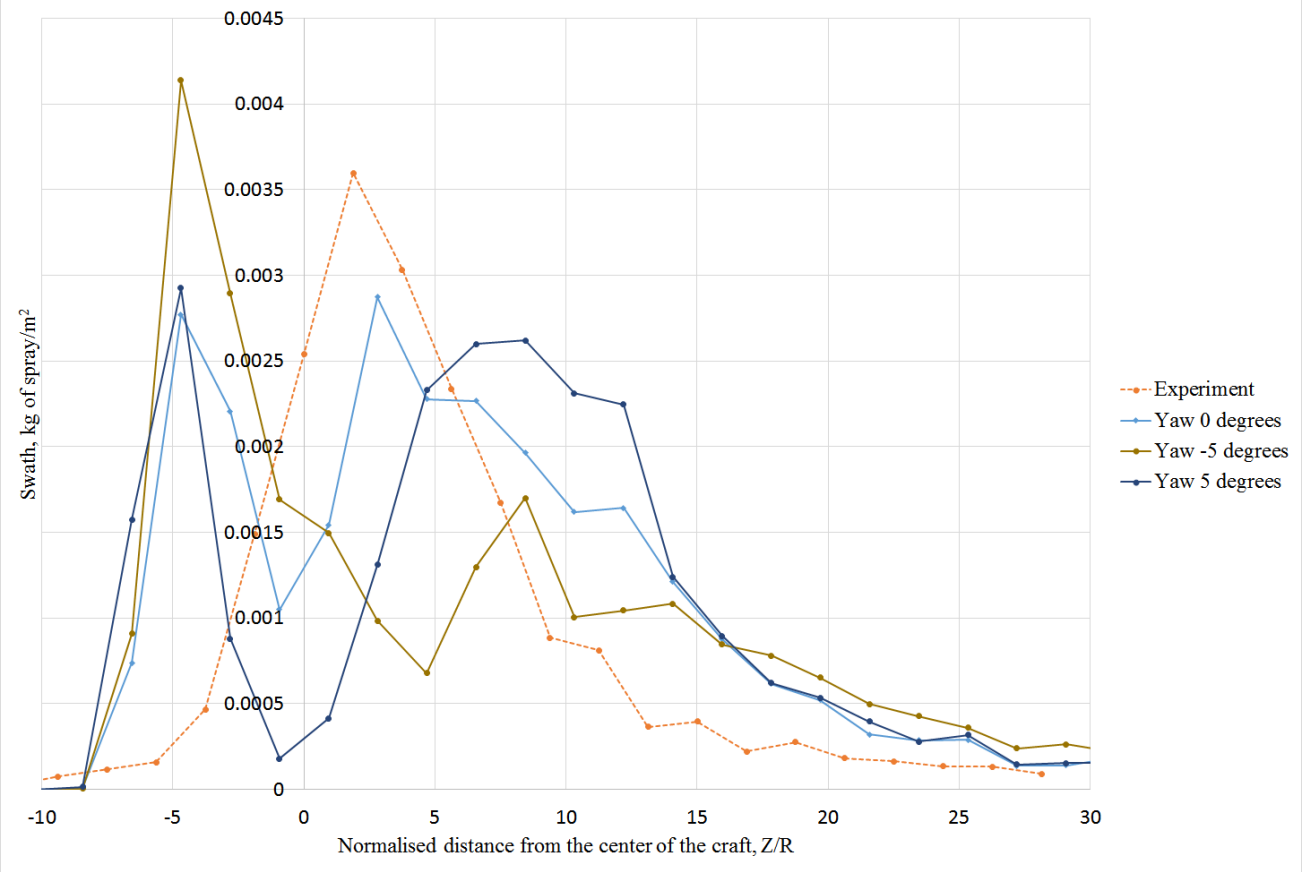

Figure 7.23 Modelled swath pattern of spray (kg/m^2) deposited on the ground in Flight 9 conditions when the yaw angle of the multicopter is 0º (blue line with rhomboid dots), -5º (brown line with circular dots) and +5º (dark blue line with circular dots).

The change of the yaw angle significantly alters the swath. When yawing, the nozzles are not symmetrical around the direction of flight. As a result, there is a large accumulation of spray mass on one of the sides of the multicopter. When yaw is -5^o the peak of the swath is at -5R (-1.33 m). When yaw angle was +5^o, peaks were observed at -5R (-1.33 m) and 7R (1.87 m) (Figure 7.24).

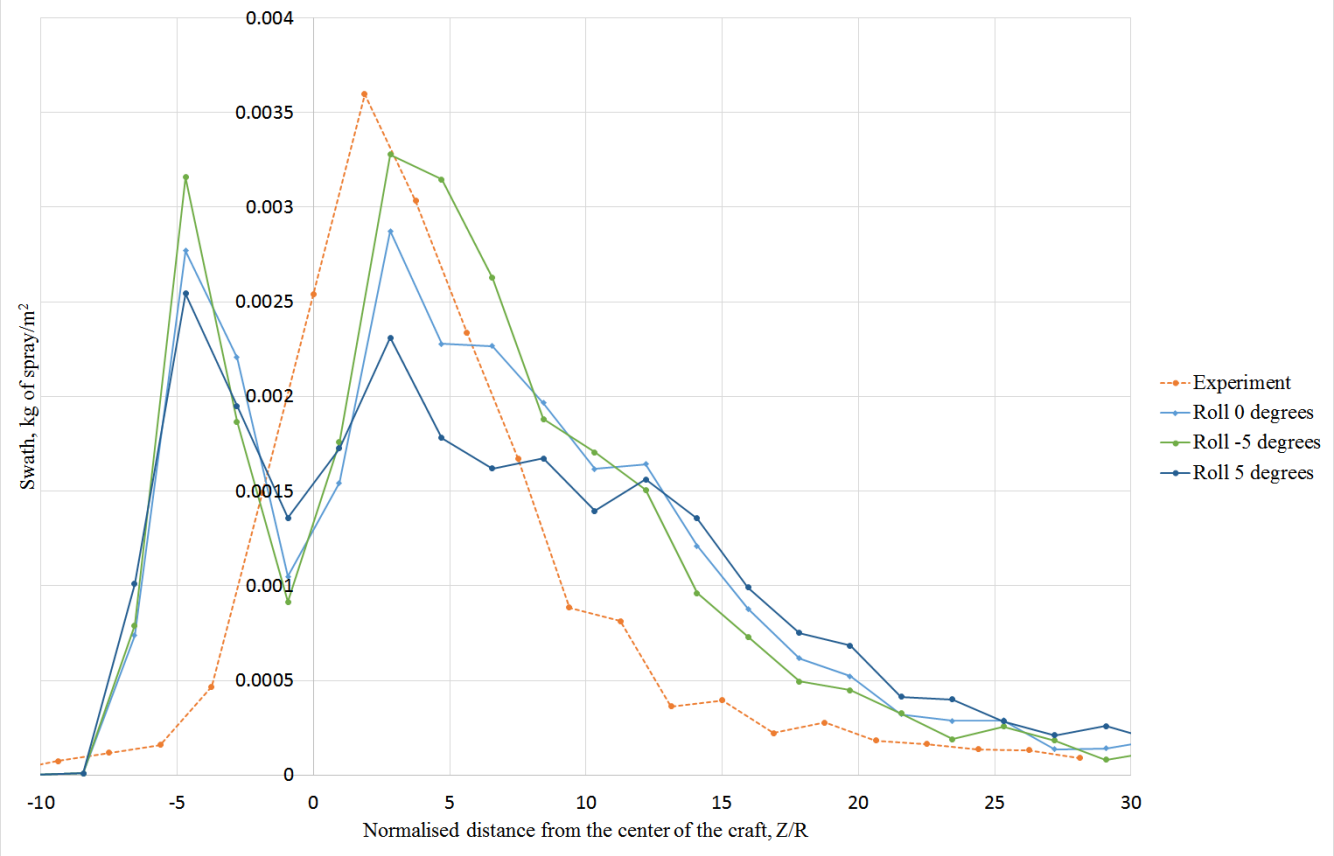

Figure 7.24 Modelled swath pattern of spray (kg/m^2) deposited on the ground in Flight 9 conditions when the roll angle of the multicopter is 0º (blue line with rhomboid dots), -5º (green line with circular dots) and +5º (dark blue line with circular dots).

Changes in roll angle do not significantly affect the width of spray deposition. The amount of deposition at the leeward part of the swath (+Z/R) decreases with increasing roll angle.

The tilt angle was assumed to be +5^o. The change of the tilt angle does not noticeably change the swath pattern (Figure 7.25).

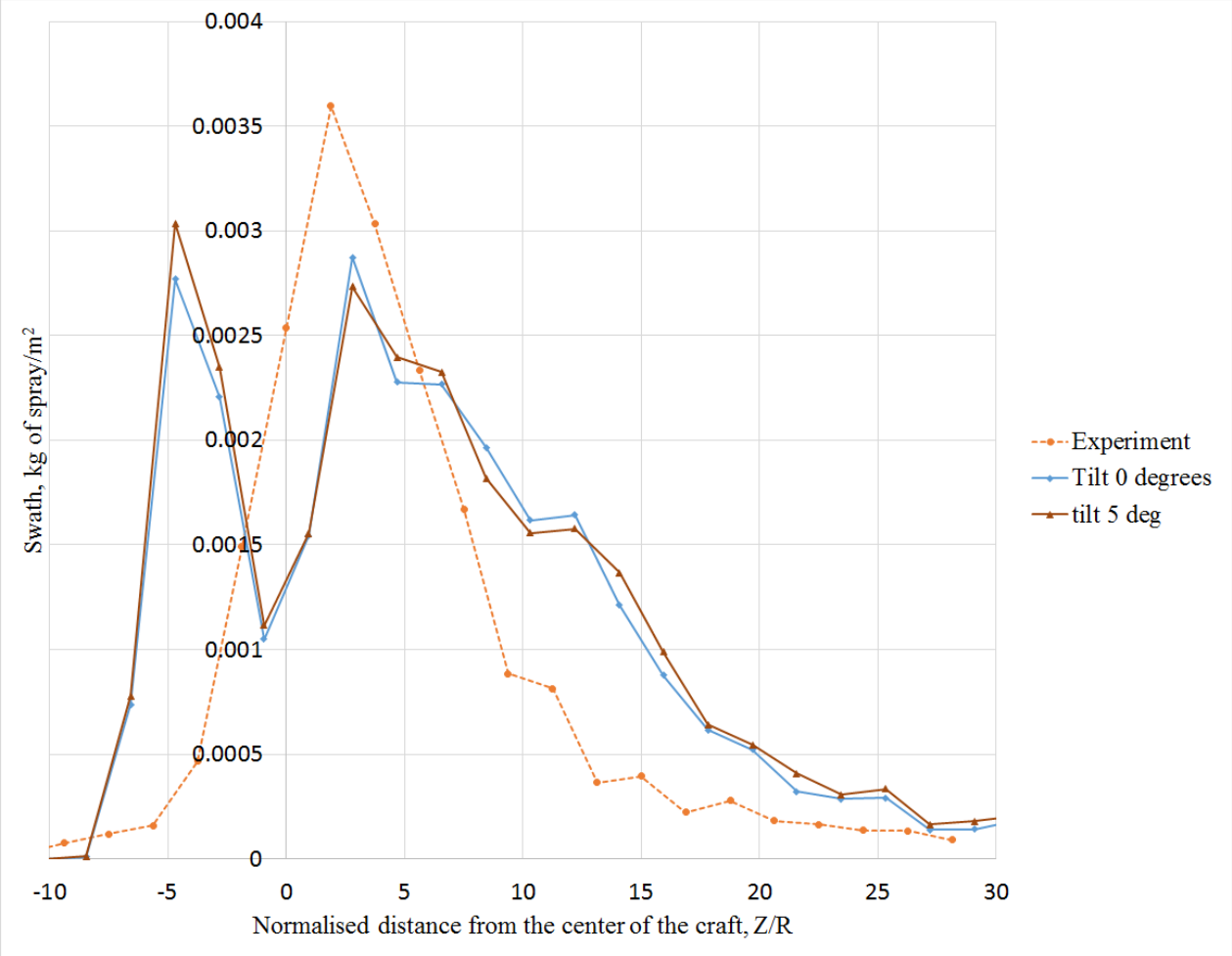

Figure 7.25 Modelled swath pattern of spray (kg/m^2) deposited on the ground in Flight 9 conditions when the tilt angle of the multicopter is 0^o (blue line with rhomboid dots), and +5^o (brown line with triangular dots).

Similarly to flight 4, the roughness of terrain= 0.1 m, 0.25 m, and 0.5 was tested (refer to section 6.3.2.2, table 6.3). When the roughness of terrain was 0.5 (i.e., bushes, numerous obstacles), the modelled swath was closest to the experimental swath (Figure 7.26).

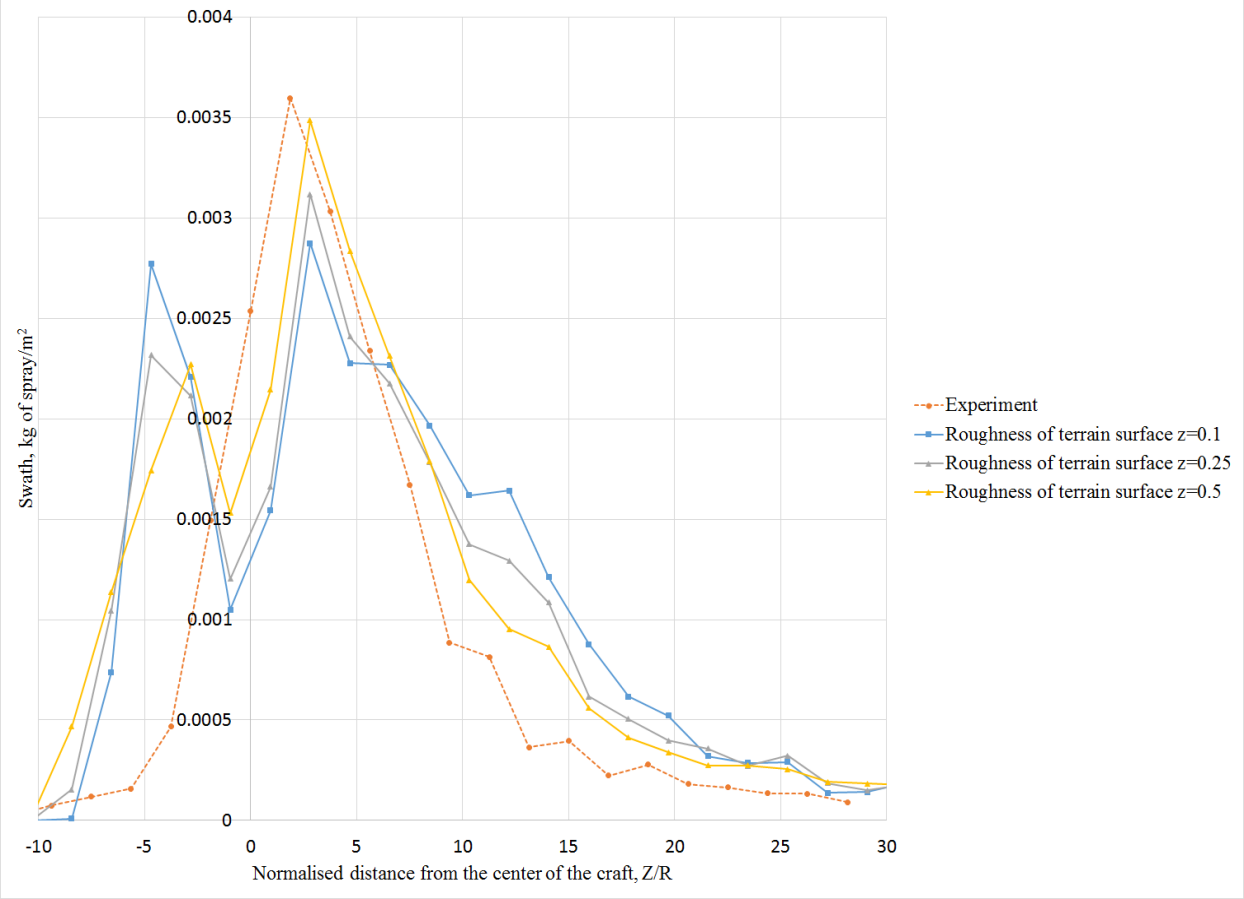

Figure 7.26 Modelled swath pattern of spray (kg/m^2) deposited on the ground in Flight 9 conditions when the roughness of the terrain was 0.1 m (blue line with rectangular dots), the roughness of the terrain was 0.25 m (grey line with triangular dots), and the roughness of the terrain was 0.5 m (yellow line with triangular dots).

The mean swath pattern of all variables tested is shown in Figure 7.27. The error bars on the swath pattern represents one standard deviation of ground deposition of all variables tested in the model. The horizontal error bars on the swath obtained experimentally represent the normalised drift (±0.94 R (0.25 m)) of the multicopter observed by Richardson et al. (2019).

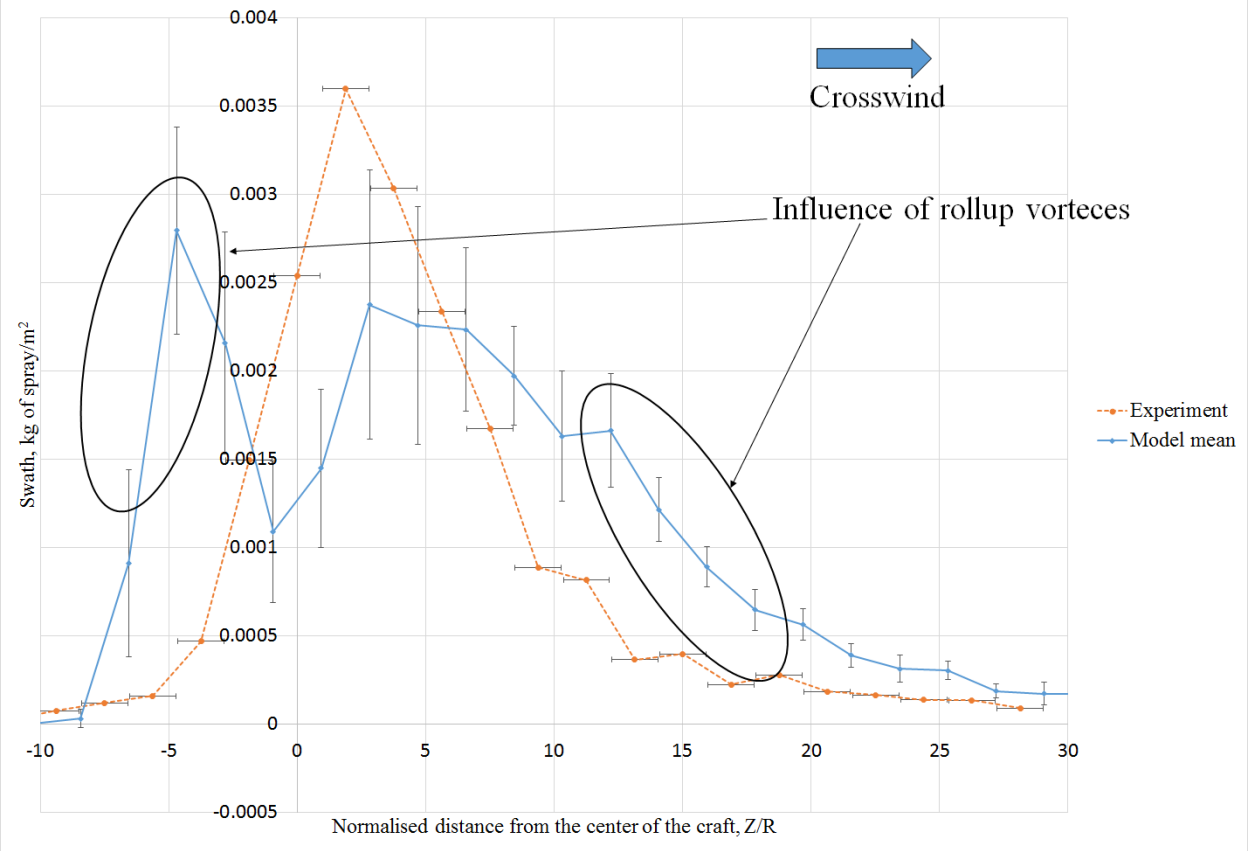

Figure 7.27 Swath pattern of spray (kg/m2) deposited on the ground in Flight 9 conditions. The orange dotted line with circular dots is the swath obtained in the experiment. The blue line with rhomboid dots is the swath obtained in the model. The arrow shows the direction of the crosswind. The black ellipses show the part of the swath influenced by the rollup vortices.

The modelled spray deposition has two peaks at Z/R=-4.8 (-1.279 m) and Z/R=2.5 (Z=0.667 m) and an extreme local minimum between them at Z/R=-0.5 (-0.1332 m). The experimental swath pattern has its local peak at Z/R=0.4 (Z=107m); the local extreme minimum was not observed in the experiment.

The modelled swath was closest to the experimentally obtained swath when the surface roughness was equal to 0.5 (bushes, suburb) and the rotational speed of all rotors was equal to 2475 rpm. Similarly to flight 4, 0.75R tall plant canopy was added to the model (Figure 7.28)

(section 6.3.2.4). For grass, $LAD=1.6\ m^{-1}$ and $C_d= 0.34$ (Gillies et al., 2002). The inertia loss coefficient was $C_2=0.544$.

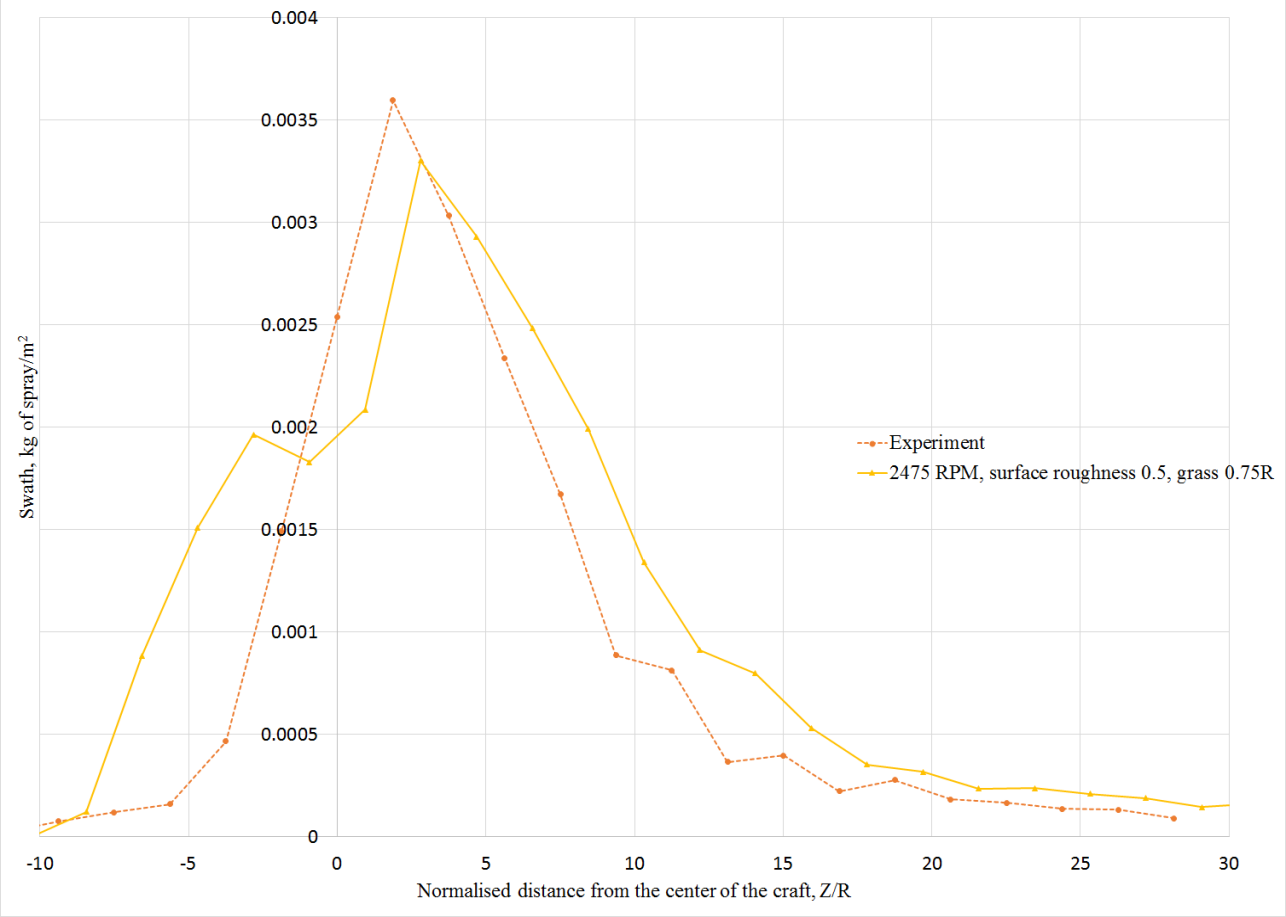

Figure 7.28 Modelled swath pattern of spray (kg/m^2) deposited on the ground in Flight 9 conditions when the roughness of the terrain was 0.5 m, rotational speed of all rotors was 2475 rpm and the plant canopy was 0.75R tall (yellow line with circular dots).

The Agras Mg-1 has a body consisting of a tank for liquid and battery holders. Since modelling the tank is computationally expensive, the influence of the body (Chapter 6, Figure 6.33) on the swath pattern was evaluated for Flight 9 conditions.

As shown in Figure 7.29, the body does not significantly change the swath pattern. No difference in the swath pattern was observed in the windward part of the crosswind, where the

rollup vortex is shaded by the tank. There is a slight change in the swath peaks at Z1/R=0.5 and Z/R=12. This does not affect the swath width.

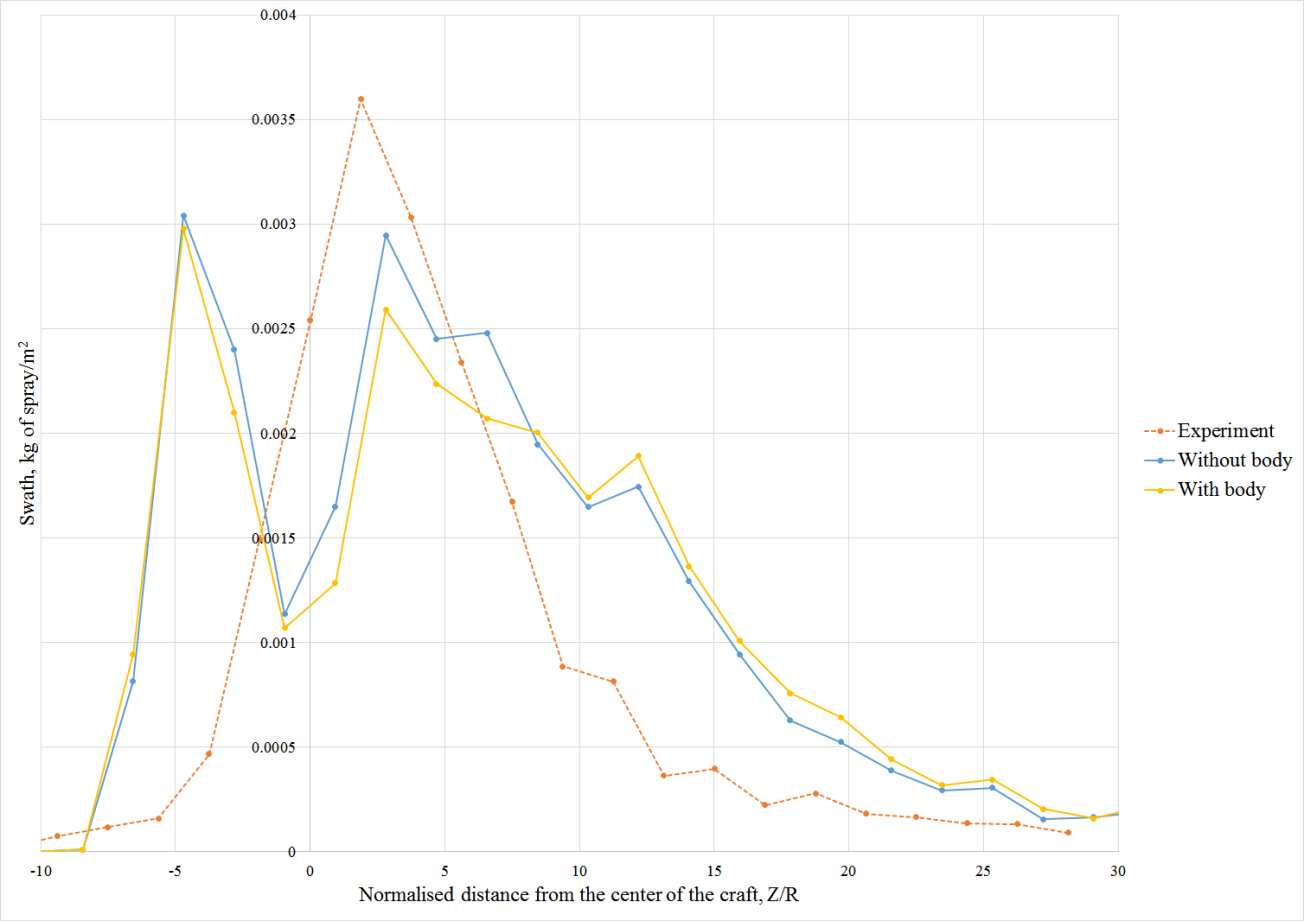

Figure 7.29 Modelled swath pattern of spray (kg/m^2) deposited on the ground in Flight 9 conditions when the body is not included in the model (blue line with circular dots), and when the body is included (yellow line with circular dots).

It is assumed that the difference is more significant with greater lateral speeds because of the shaded zone behind the body. The body was not considered in the analysis of other flight cases.

7.3.2.3 Flight 29 (F29)

In Flight 29, the wind speed was reported at 0.04 m/s. Flight speed was significantly higher in Flight 29 compared to Flights 4 and 9. The model considered the evaporation of the droplets. Relative humidity (RH) was reported at 49% and temperature at 23.9℃.

Figure 7.30 shows the view in the direction of flight (X/R) of the spray released under the multicopter at 1 s (top), 2 s (middle) and 3 s (bottom). Parcels are coloured according to particle diameter.

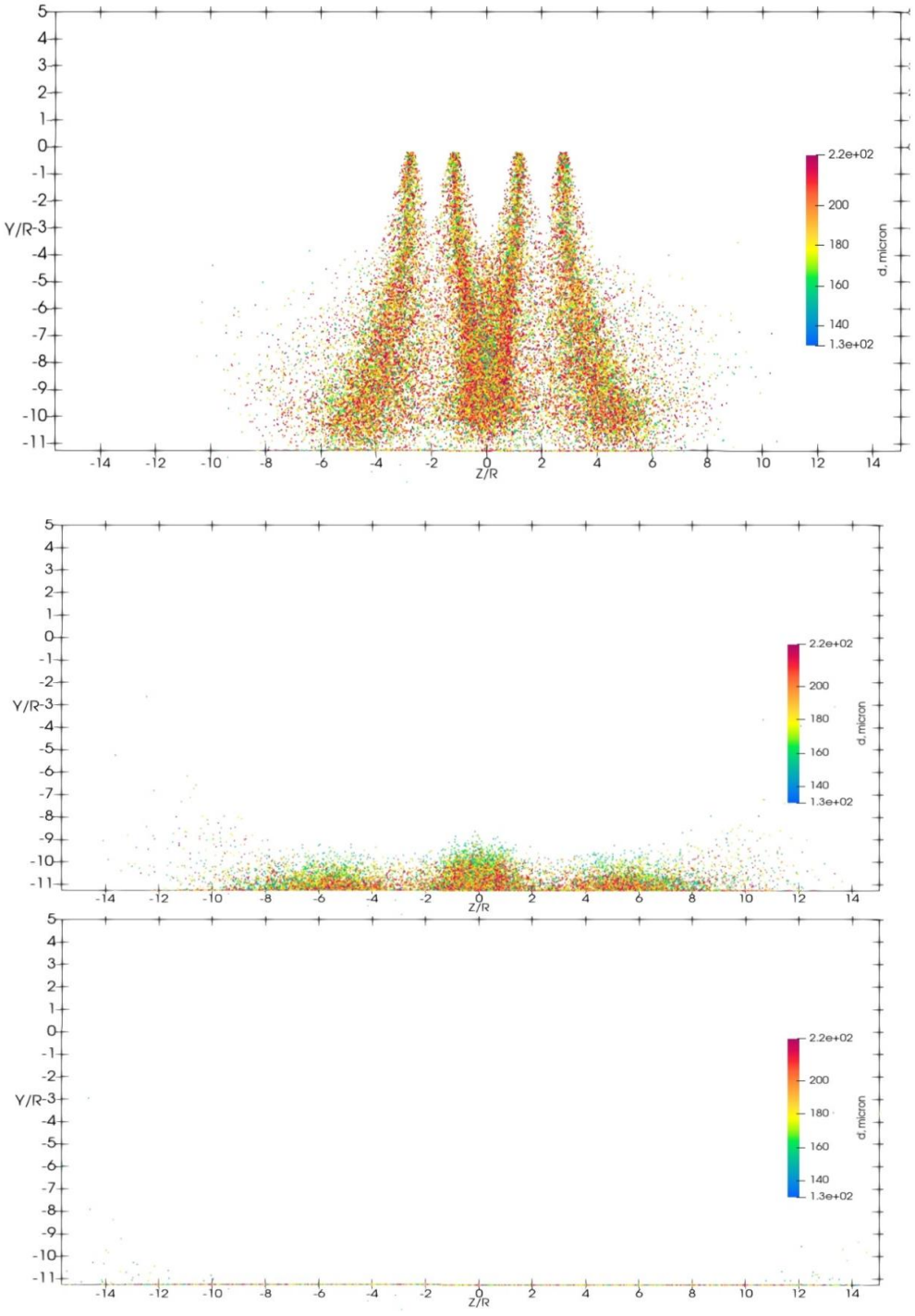

Figure 7.30 View in the direction of flight (X/R) of spray released in Flight 29 under the multicopter at 1 s (top), 2 s (middle) and 3 s (bottom). Parcels are coloured according to particle diameter in microns.

Figure 7.30 shows that the spray is influenced by the main downwash and rollup vortices.

The rollup vortices have a strong impact on spray deposition and can be seen on the ground plane. (Figure 7.31). Smaller particles caught in the rollup vortex move downwind, further away. The most significant particle drift was recorded at X/R =-53 (14.12 m) Z/R=+-15 (4 m).

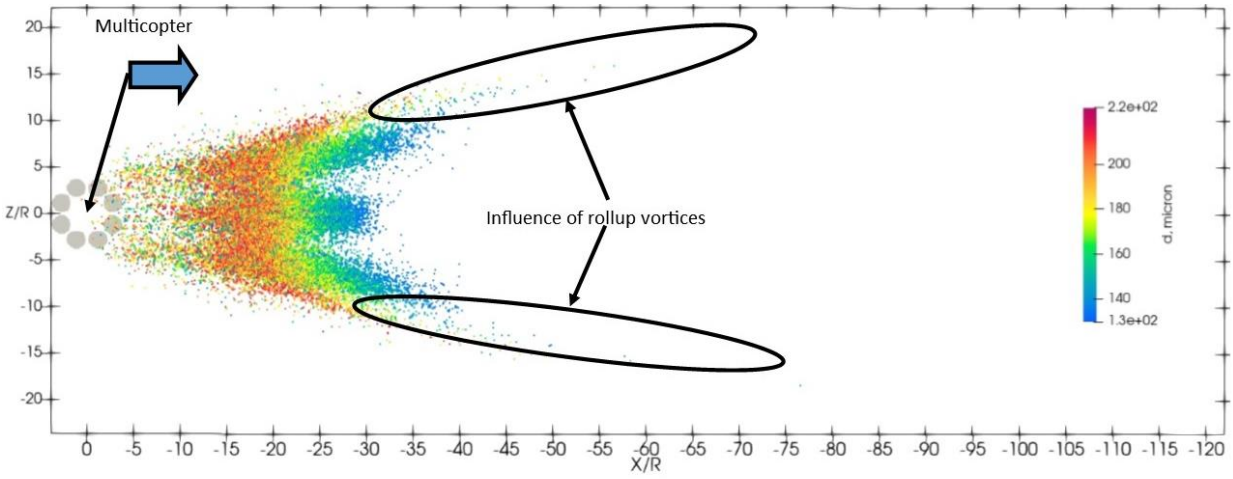

Figure 7.31 View from above of spray released in Flight 29 under the multicopter at 10 s. Parcels are coloured according to particle diameter in microns. The arrows show wind and flight velocity directions. The multicopter is at X/R=0, Z/R=0.

The reported flight height was 3 m (11.25R). To test possible height uncertainty, the spraying multicopter was modelled at flight heights of 2.7 m (10.13R) and 3.3 m (12.38R).

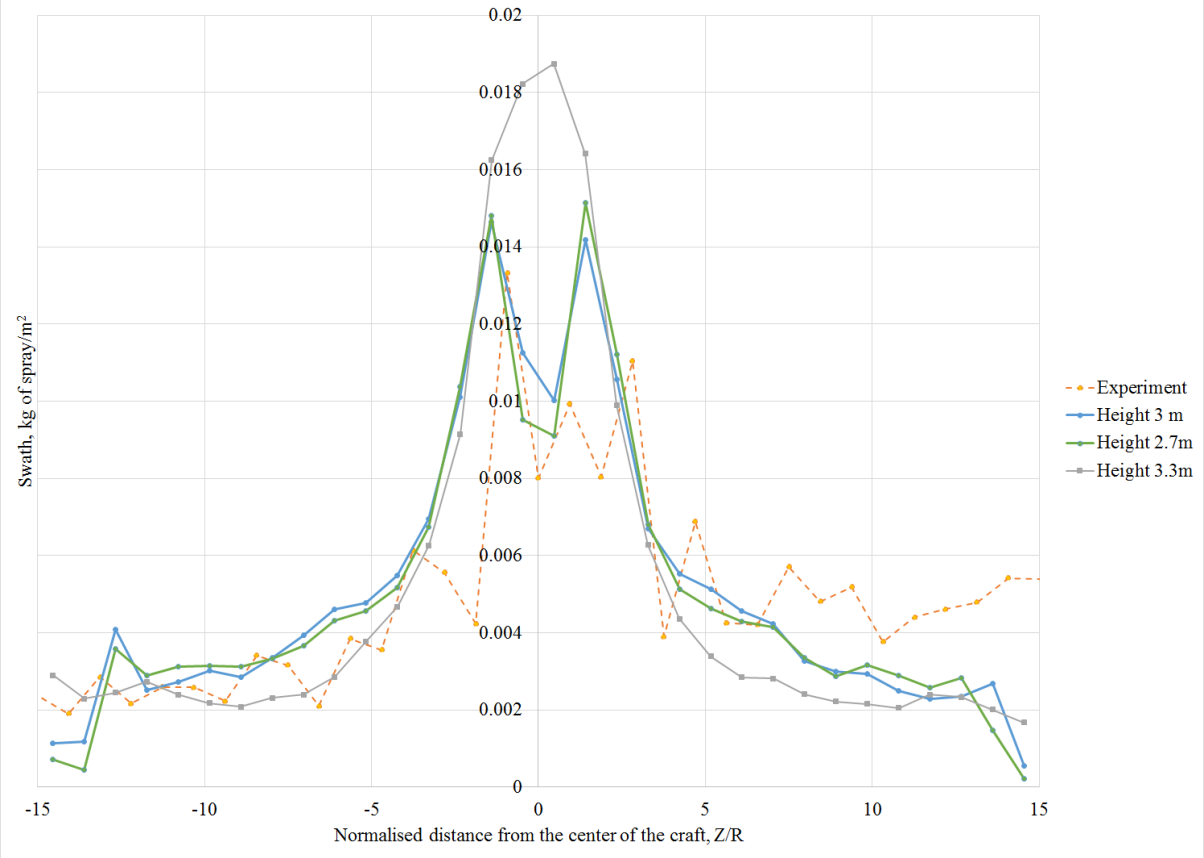

Figure 7.32 Modelled swath pattern of spray (kg/m^2) deposited on the ground in Flight 29 conditions when released at heights of 3 m (blue line with rhomboid dots), 2.7 m (green line with circular dots) and 3.3 m (grey line with rectangular dots).

Similarly to Flights 4 and 9, the width of the swath is unaffected by the height of the multicopter flight (Figure 7.32Figure 7.32). However, in the centre of a multicopter (Z/R=0) the amount of deposited spray increases with height.

Figure 7.33 shows the swath pattern when the rotational speed of all rotors is 2750 RPM, 2475 RPM and 3020 RPM.

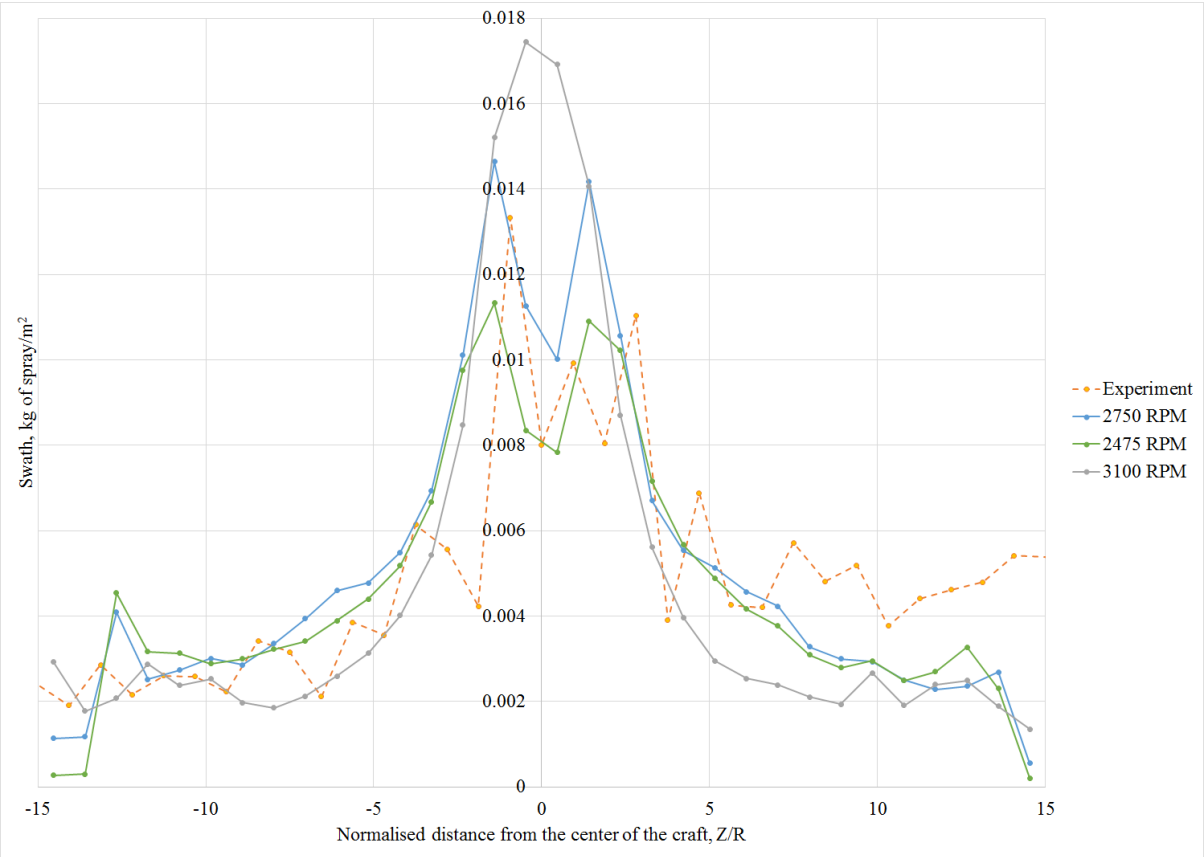

Figure 7.33 Modelled swath pattern of spray (kg/m^2) deposited on the ground in Flight 29 conditions when the rotational speed of all rotors is 2750 RPM (blue line with circular dots), 2475 RPM (grey line with circular dots) and 3020 RPM (green line with circular dots).

Swath width does not significantly change with changing rotational speed of the multicopter rotors. Deposition of spray on the ground does change. In the centre of a multicopter (Z/R=0) the amount of deposited spray increases with increase of the rotational speed of all rotors.

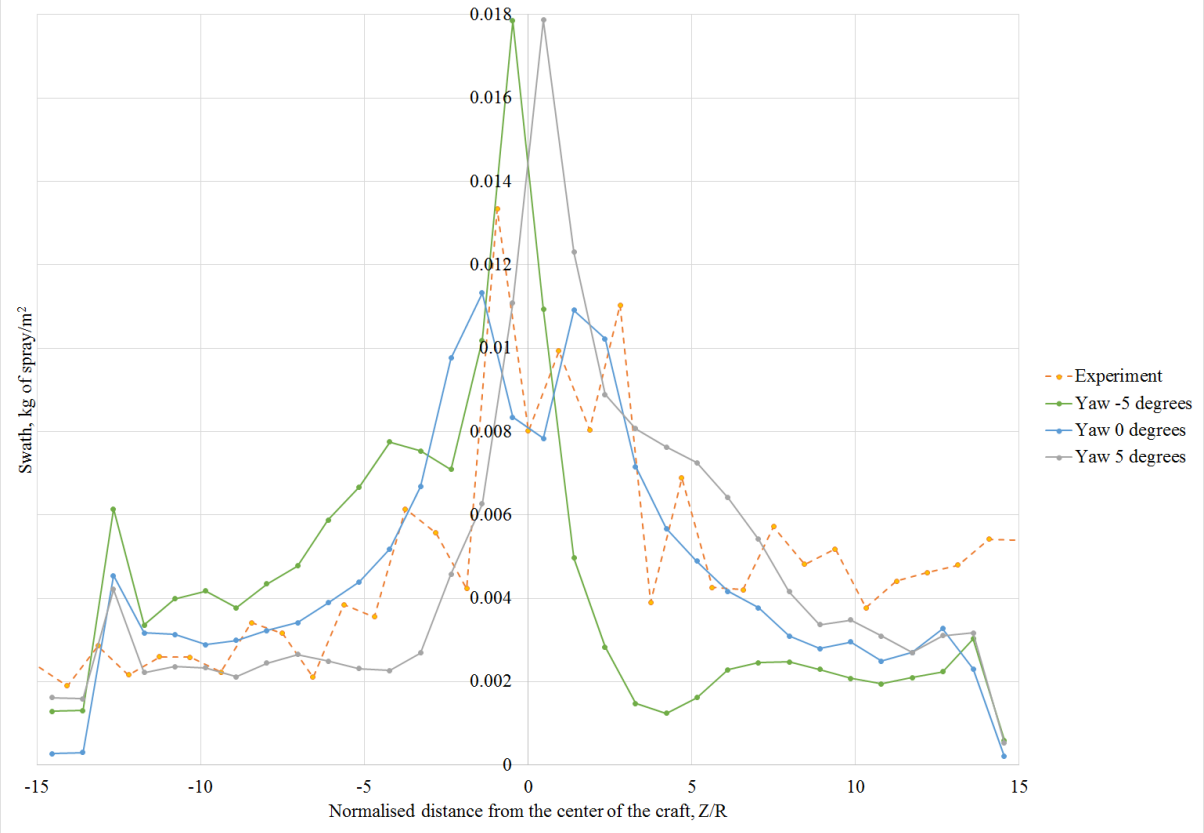

Figure 7.34 Modelled swath pattern of spray (kg/m^2) deposited on the ground in Flight 29 conditions when the yaw angle of the multicopter is 0º (blue line with circular dots), -5º (green line with circular dots) and +5º (grey line with circular dots).

The change of the yaw angle significantly alters the swath. When the yaw angle is nonzero, the nozzles are not symmetrical around the direction of flight. As a result, there is a large accumulation of spray mass on one of the sides of the multicopter. When yaw is -5º the peak of the swath shifts to -0.7R (-0.67 m). When yaw angle is +5º, the peak shifts to 0.7R (0.67 m).

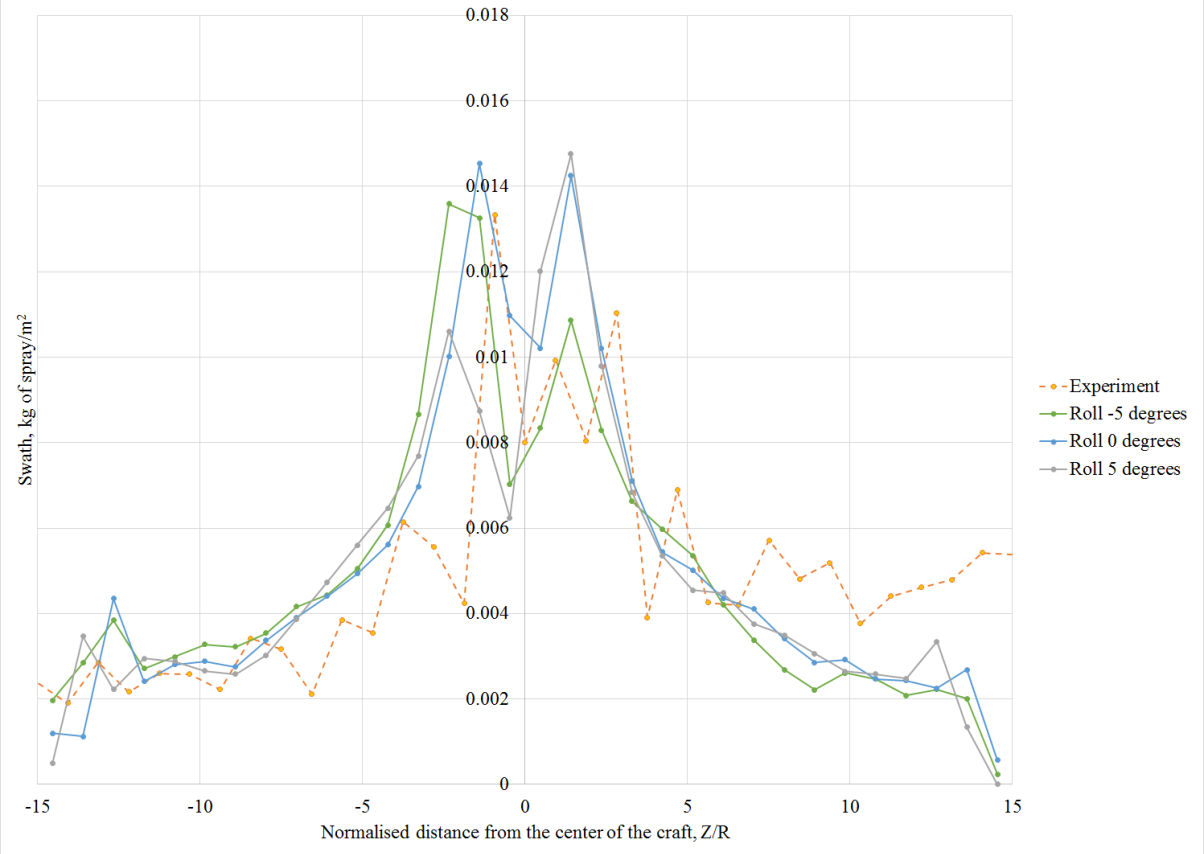

Figure 7.35 Modelled swath pattern of spray (kg/m^2) deposited on the ground in Flight 29 conditions when the roll angle of the multicopter is 0º (blue line with circular dots), -5º (green line with circular dots) and +5º (dark blue line with circular dots).

The swath becomes non-symmetrical with changing roll angle, with more spray deposited under the higher side of the multicopter.

The mean modelled spray deposition (Figure 7.36) is highest at Z/R=-2R…2R. These central peaks is the contribution of two nozzles located under the front rotor (rotor 1 and rotor 8). The same peaks were observed experimentally. There are less contributions of rollup vortices compared to Flight 4 and Flight 9.

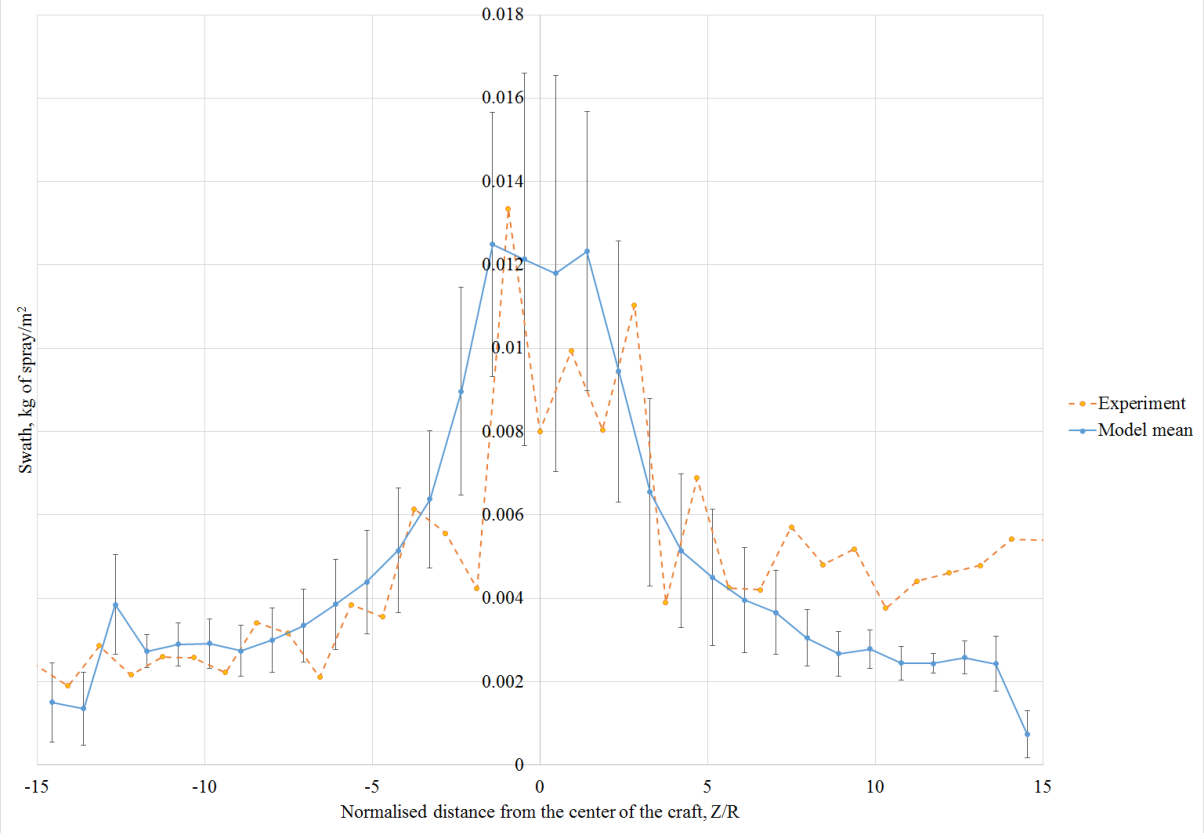

Figure 7.36 Swath pattern of spray (kg/m^2) deposited on the ground in Flight 29 conditions. The orange line with circular dots is the swath obtained in the experiment. The blue line with circular dots is the swath obtained in the model. The black ellipses show the part of the swath influenced by the rollup vortices.

The modelled swath was closest to the experimentally obtained swath when the surface roughness was equal to 0.5 (bushes, suburb) and the rotational speed of all rotors was equal to 2475 rpm. Similarly to flight 4, 0.75R tall plant canopy was added to the model (Figure 7.28) (section 6.3.2.4). For grass, $LAD=1.6\ m^{-1}$ and $C_d= 0.34$ (Gillies et al., 2002). The inertia loss coefficient was $C_2=0.544$.

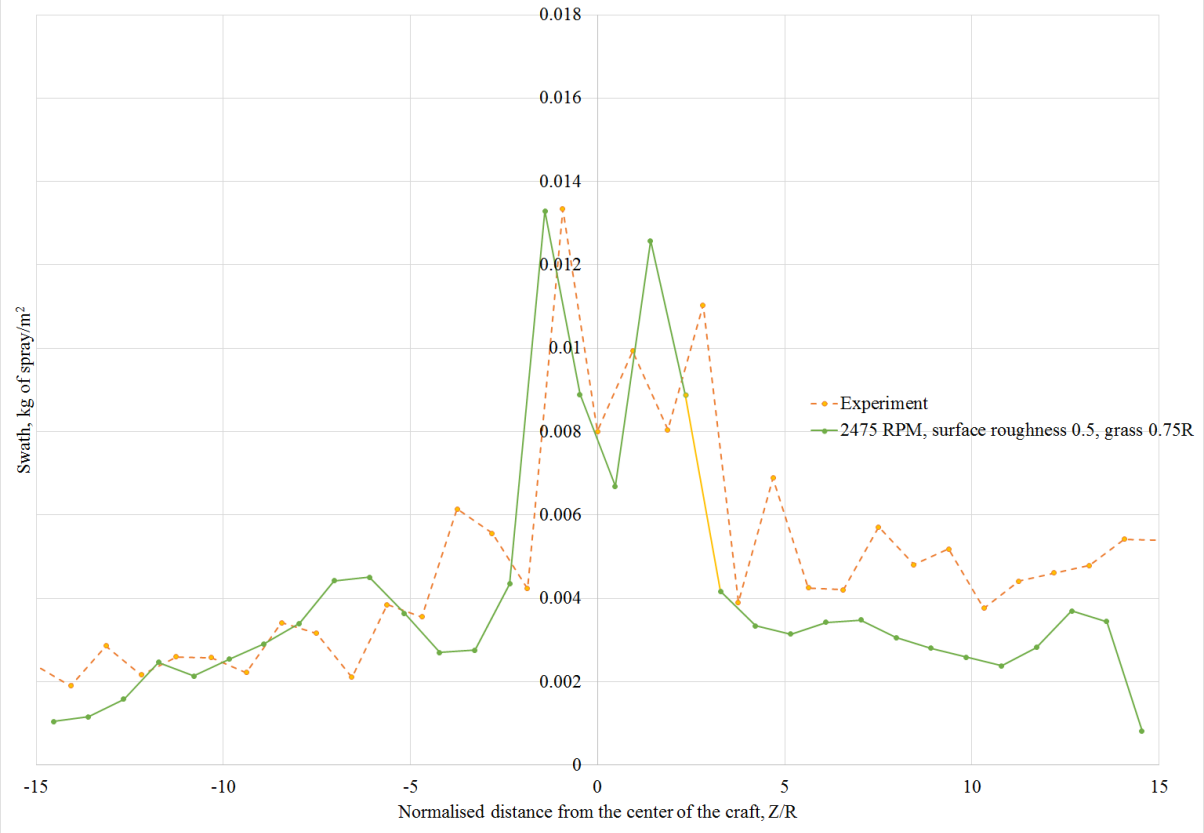

Figure 7.37 Modelled swath pattern of spray (kg/m2) deposited on the ground in Flight 29 conditions when the roughness of the terrain was 0.5 m, rotational speed of all rotors was 2475 rpm and the plant canopy was 0.75R tall (yellow line with circular dots).

7.3.2.4 Swath separation analysis for all flights modelled

The 30% CV (Equation 7.13) of swath pattern was analysed for every flight and every condition tested. Figure 7.38 shows the experimental and modelled effective swath (30%) for all modelled flight parameters and one standard deviation of the effective swath.

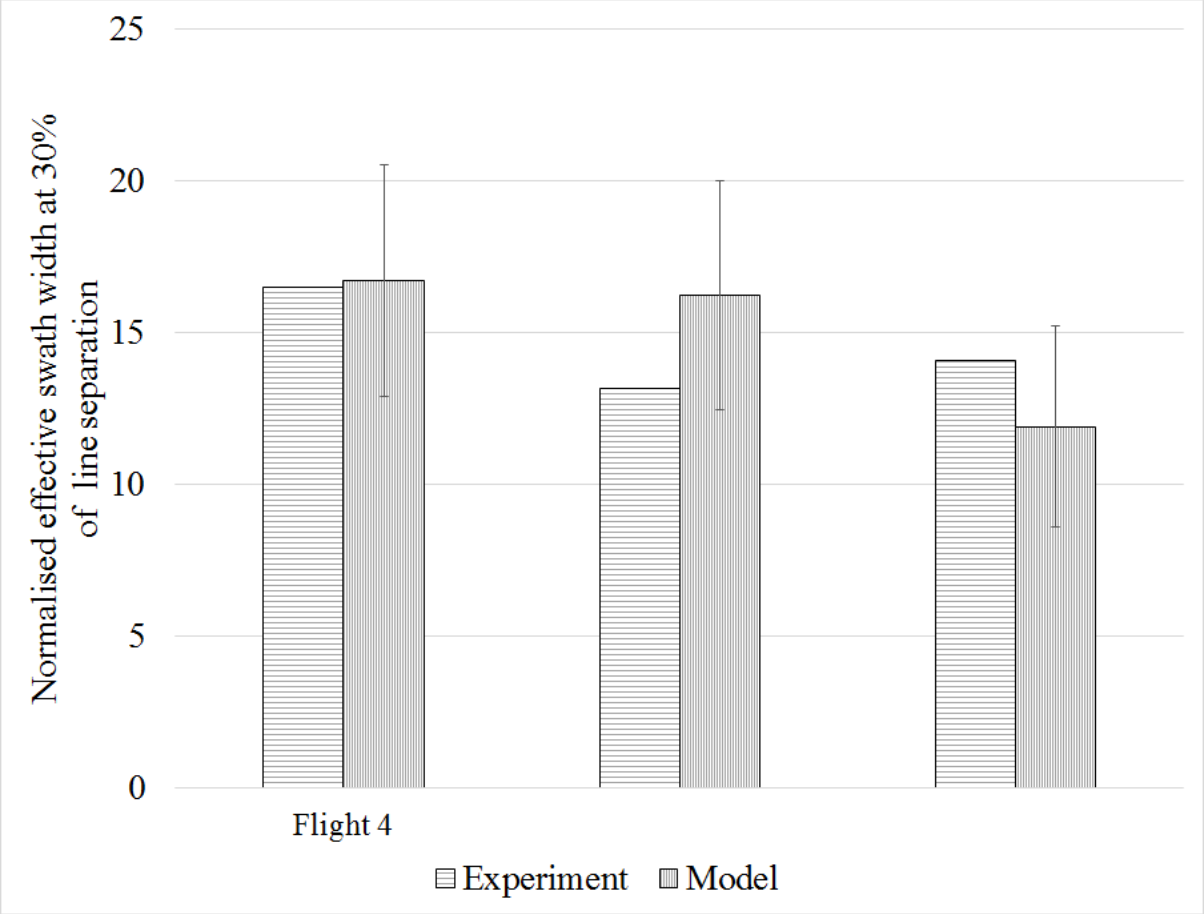

Figure 7.38 Effective swath for Flights 4 (left), 9 (middle) and 29 (right), calculated for experimental (horizontal hatch) and modelled (vertical hatch) swath patterns.

In all flights the effective swaths are within one standard deviation.

7.3.2.5 Flight in the presence of plant canopy

The influence of the plant canopy on spray dispersion was tested in the conditions of flight 9. Three different plant heights normalised by rotor radius (Hp) were tested: Hp= 1.5R (0.4 m) (Figure 7.32 top), 3R (0.8 m) (Figure 7.32 middle) and 4.5R (1.2m) (Figure 7.32 bottom). Figure 7.39 shows parcels on the ground when all the released spray was deposited (t=10 s). The parcels are coloured by parcel diameter in microns.

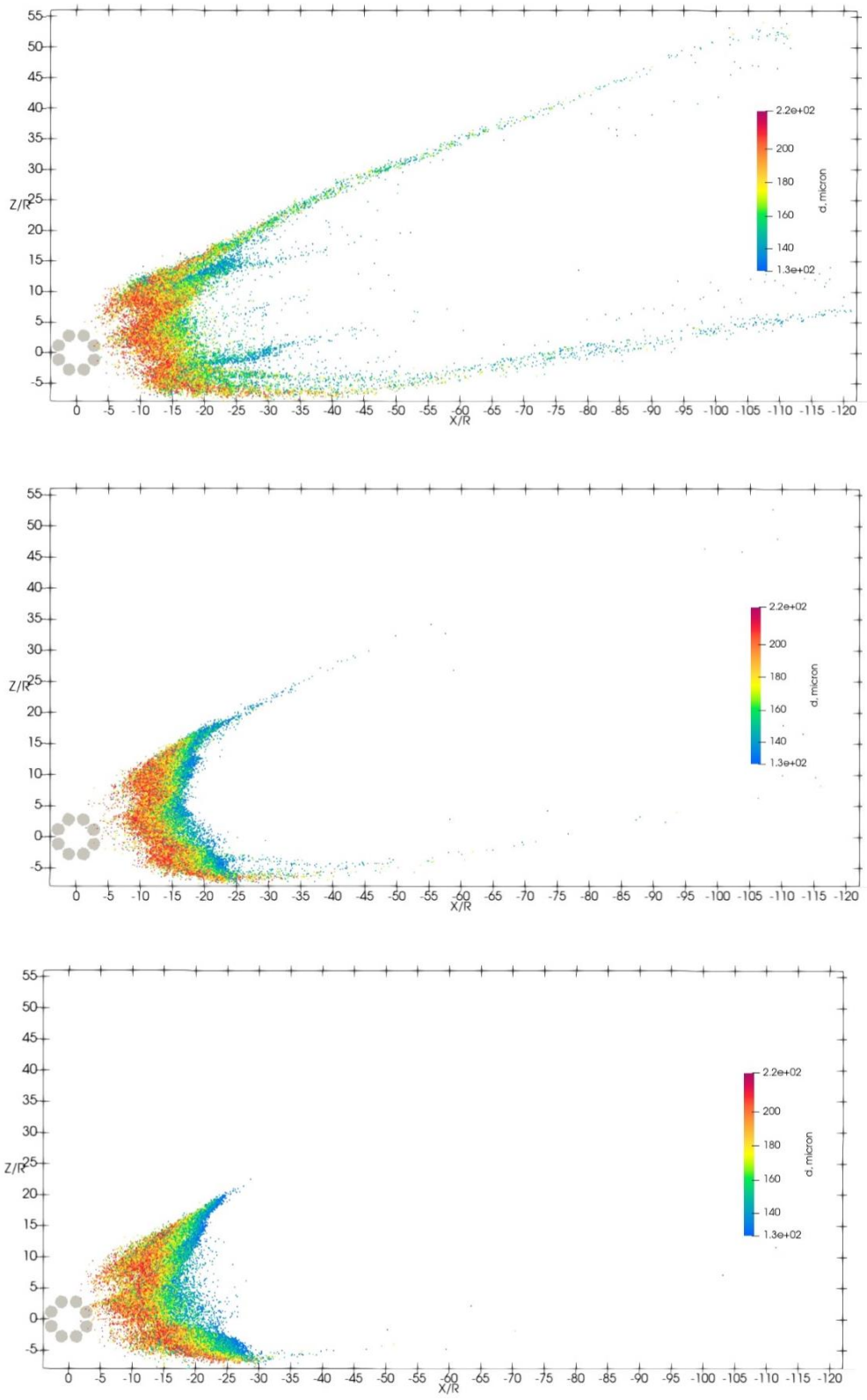

Figure 7.39 View from above of spray released in Flight 9 under the multicopter at 10 s, when Hp=1.5R (top), Hp=3R (middle) and Hp=4.5R (bottom). Parcels are coloured according to particle diameter in microns. The multicopter is at X/R=0, Z/R=0.

The drift of spray decreases with increasing plant height. The plant canopy interacts with rollup vortices and does not allow them to penetrate in the streamwise direction. Figure 7.40 shows the front view of the spraying multicopter when t=3 s. The spray, carried by the rollup vortices, remains in the air (at t=3s) when the plant canopy height is 1.5R (0.4 m) (Figure 7.40, top). When the plant height is 4.5R (1.2m) most droplets are on the ground (Figure 7.40, bottom).

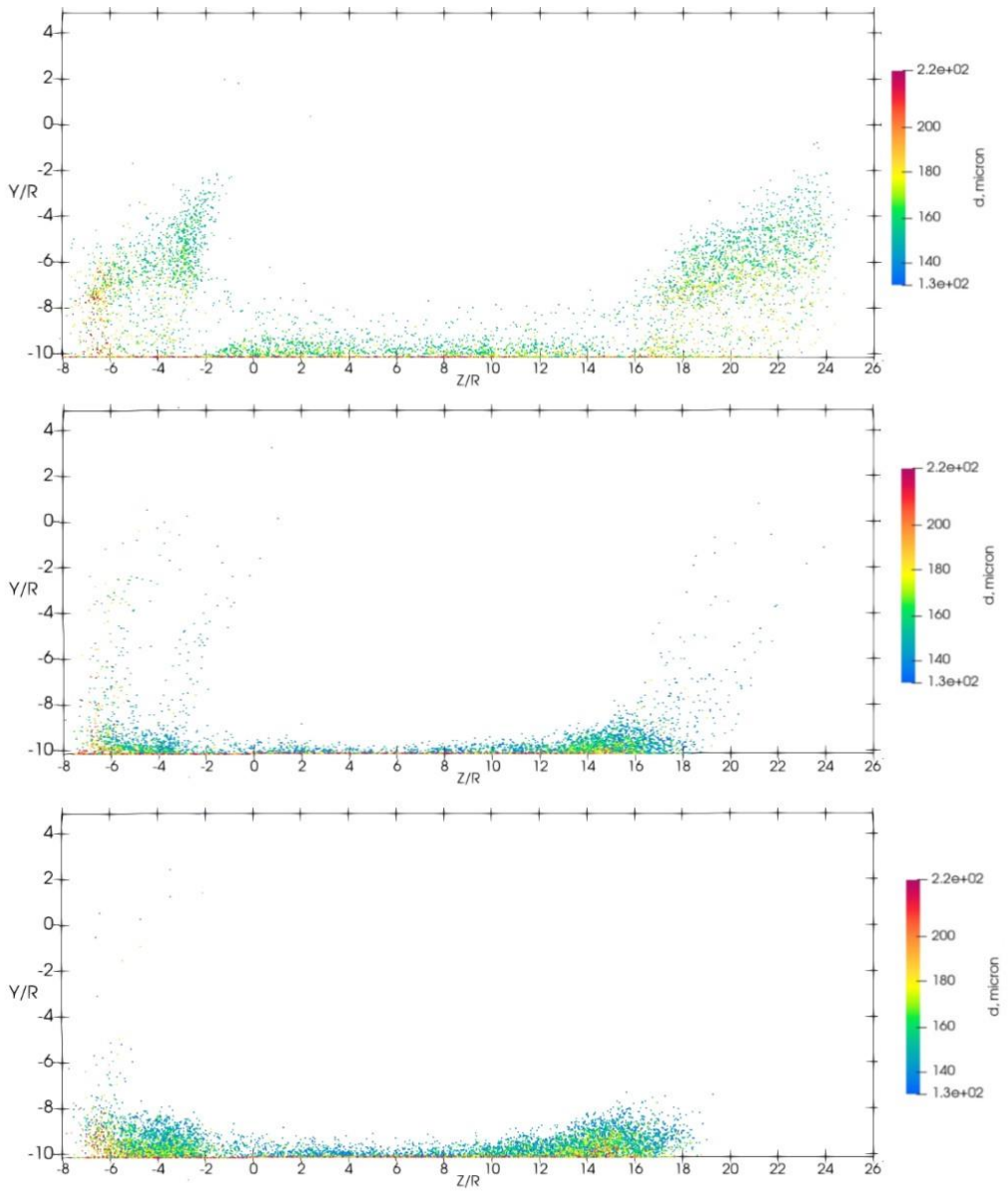

Figure 7.40 View in the direction of flight (X/R) of spray released in Flight 9 under the multicopter at t=3 s, when Hp=1.5R (top), Hp=3R (middle) and Hp=4.5R (bottom). Parcels are coloured according to particle diameter in microns.

The presence of plants affects the swath pattern. All of the plant heights tested affect the drift of the spray by interacting with rollup vortices. Figure 7.41 shows the swath pattern on the ground when plant height is H_p=1.5R (0.4 m), 3R (0.8 m) and 4.5R (1.2m).

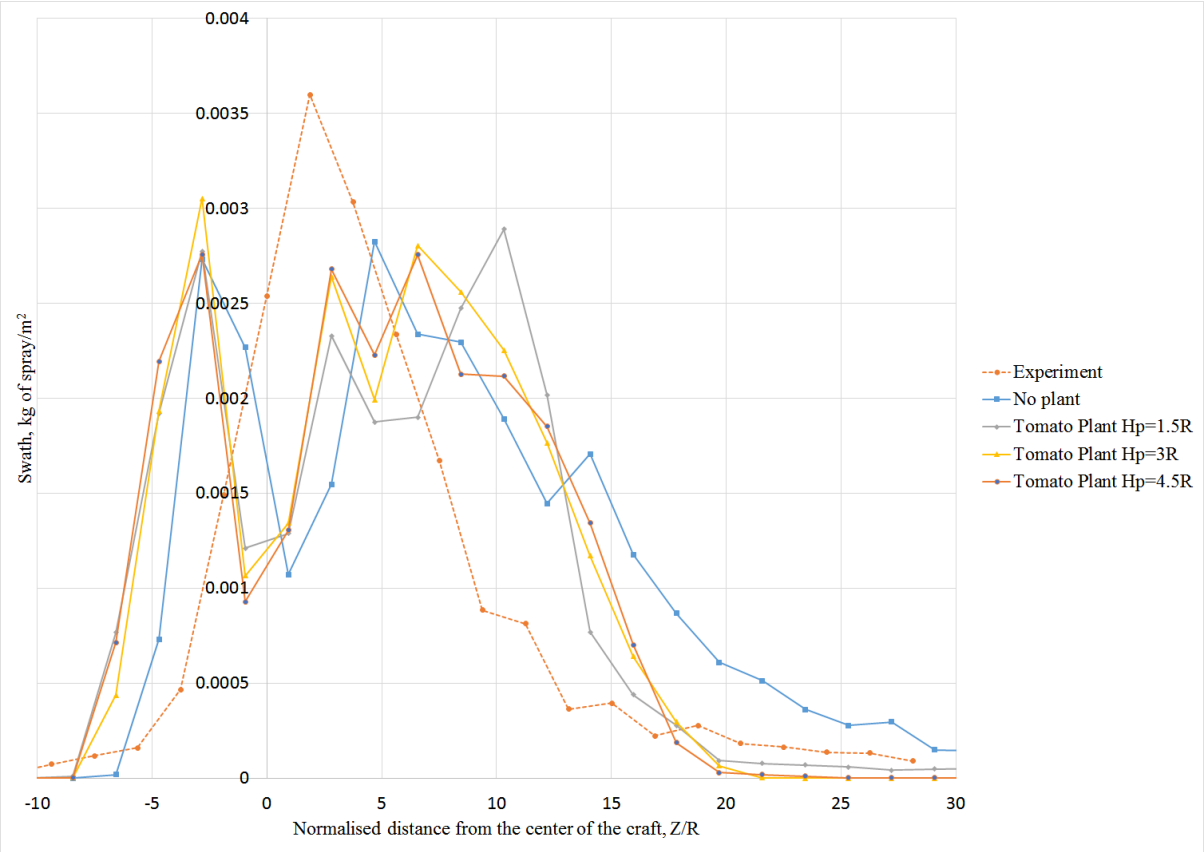

Figure 7.41 Modelled swath pattern of spray (kg/m^2) deposited on the ground in Flight 9 conditions when no plants present (blue line), and at plant heights Hp=1.5R (grey line), Hp=3R (yellow line) and Hp=4.5R (orange line).

At the windward part of the swath, the spray drifts 2.5R (0.67 m) further than in the model with plants. On the leeward part of the swath pattern the difference in the maximum drift is more than 10R (2.66 m).

The model predicts the spray dispersion on the ground or on some distance away from the ground. However, no function in the model predicts the coverage of the spray on the foliage.

The wake may move the leaves around. The upper leaves may intercept droplets and shield the lower leaves.

7.4 Model sensitivity analysis

The sensitivity study was performed to prove that the ground deposition swath pattern is not dependent on residual error, number of cells in the mesh, or integration time step of the Lagrangian particle tracker.

7.4.1 Flight 4 (F4)

Increasing the number of cells in the wake analysis did not show a significant influence on the swath pattern in Flight 4 (Figure 7.42).

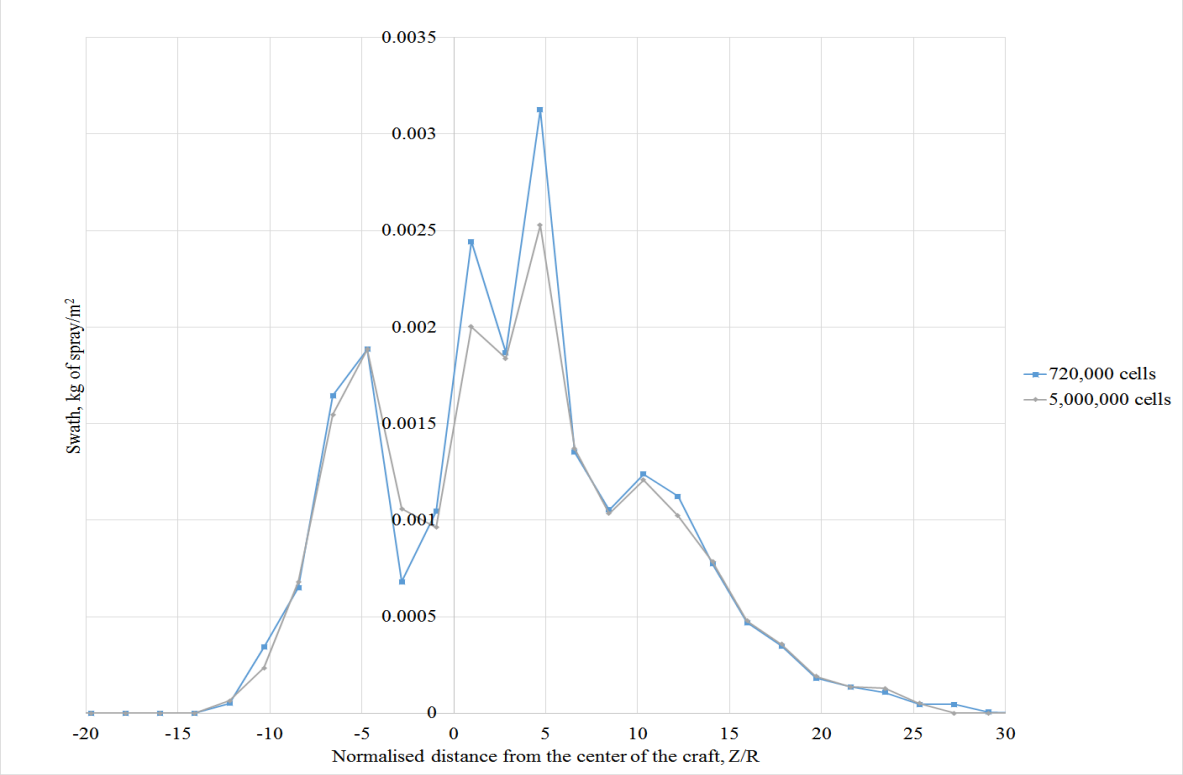

Figure 7.42 Modelled swath pattern of spray (kg/m^2) deposited on the ground in Flight 4 conditions when the number of cells is 2 million elements (blue line with rectangular dots) and 4 million elements (grey line with rhomboid dots).

To decrease computational time, it was decided to check if increasing of the residual error termination control (refer to section 6.3.3) changes the swath pattern. By default, the velocity *(U)* residual error of the simpleFoam solver equalled $1x10^{-4}$. The residual error of pressure *(p), TKE (k)* and *omega* equals $1x10^{-3}$. The computational analysis with 2 million cells on the 8-core Intel® Core™ i7-6700 CPU @ 3.40GHz computer with 32Gb RAM took 3.5 hours to converge. Stopping convergence when residuals are an order of magnitude higher decreased the computational time to 12 minutes.

Figure 7.43 presents the swath pattern for default residual errors (blue line with dots) and swath pattern with residual error increased by an order of magnitude (grey line with squares). The swath patterns are identical; as a result, greater residual error is a reasonable solution.

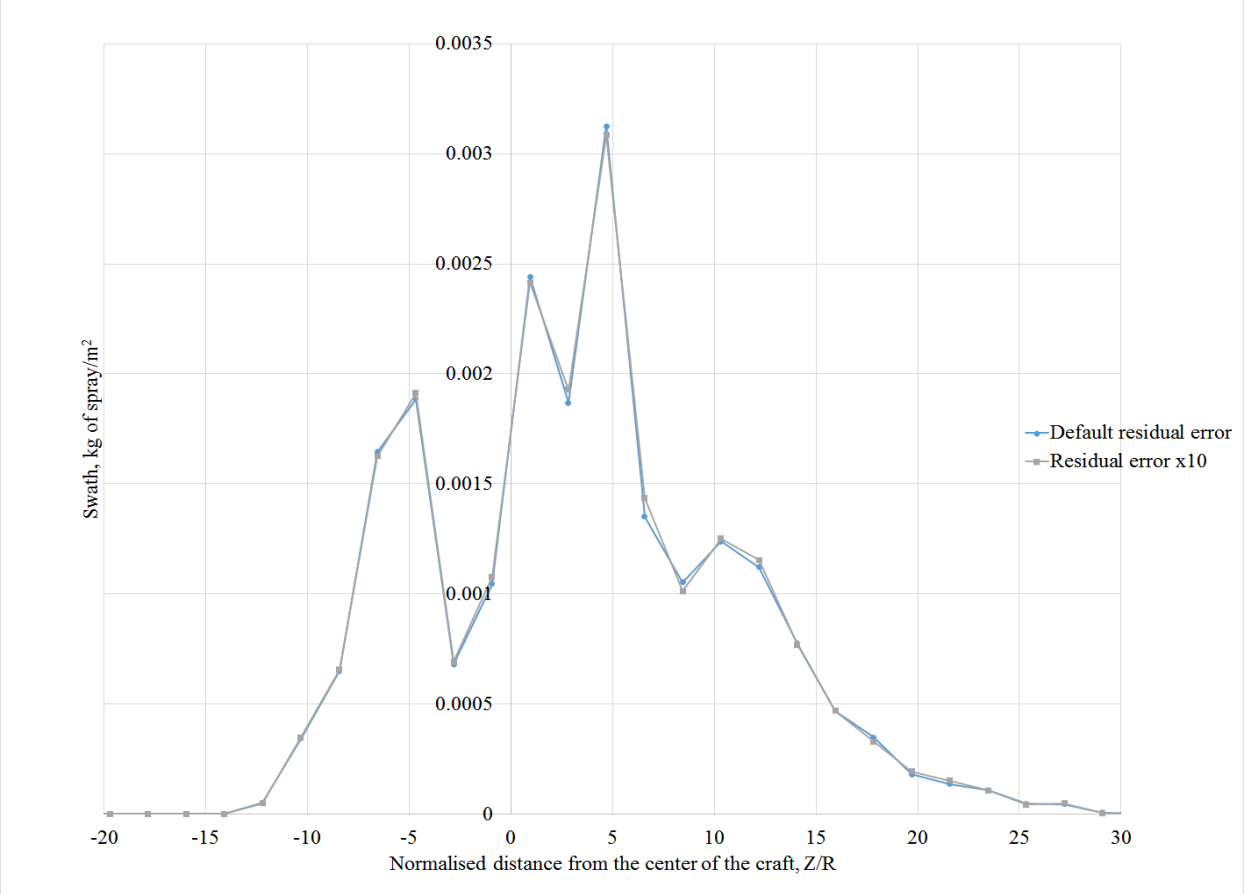

Figure 7.43 Modelled swath pattern of spray (kg/m^2) deposited on the ground in Flight 4 conditions when residual error has the default values (blue line with circular dots) and when residual error is one order of magnitude greater than the default (grey line with rectangular dots).

7.4.2 Flight 9 (F9)

Increasing the number of cells in the wake analysis did not show an influence on the swath pattern in Flight 9 (Figure 7.44).

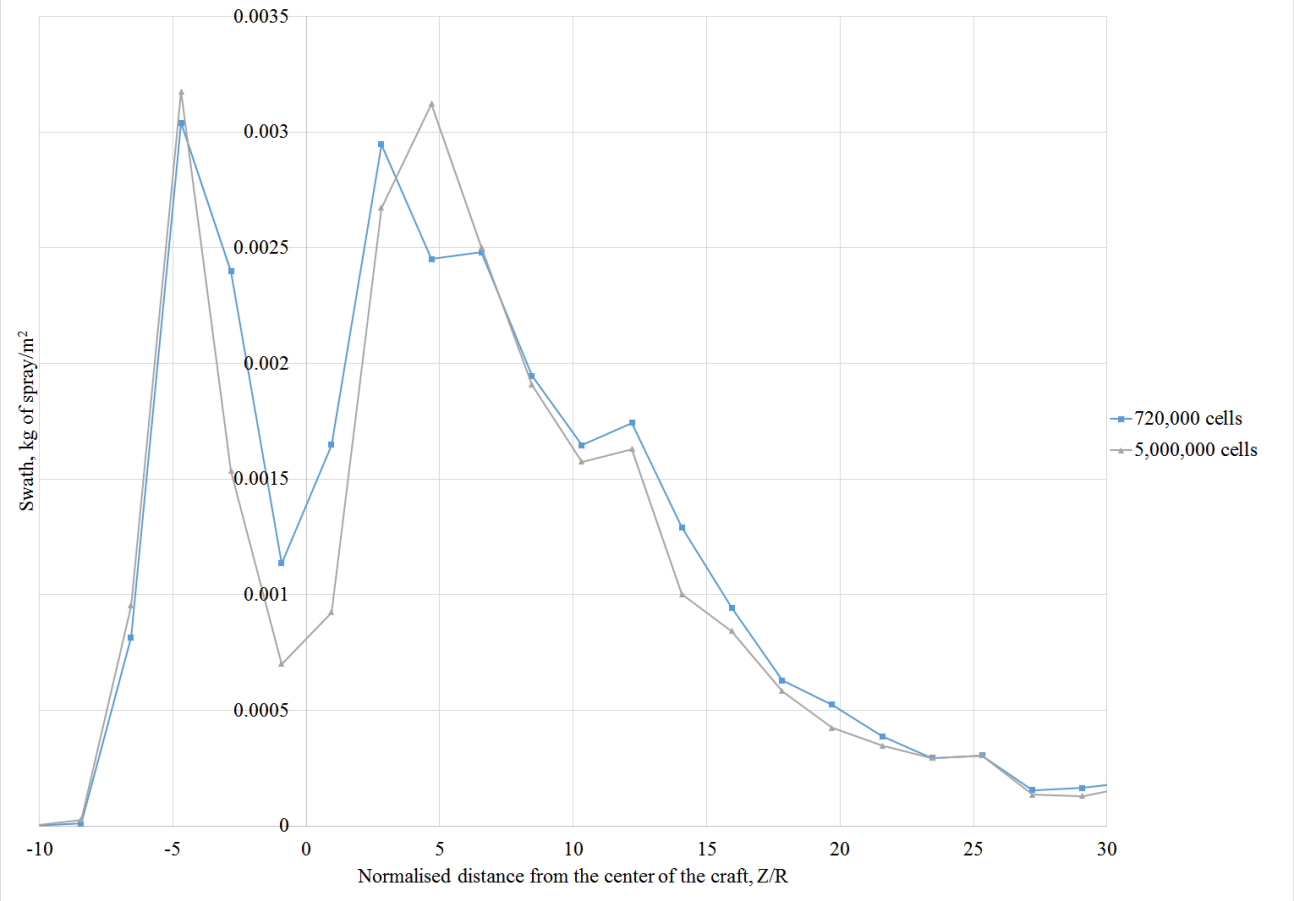

Figure 7.44 Modelled swath pattern of spray (kg/m^2) deposited on the ground in Flight 9 conditions when the number of cells is 2 million elements (blue line with rectangular dots) and 4 million elements (grey line with triangular dots).

Figure 7.45 presents the swath pattern for default residual errors (blue line with dots), and with residual error increased by an order of magnitude (grey line with triangle). The swath patterns are identical; therefore, it is possible to use increased residual error. Increasing residual error by one more order of magnitude changes the swath pattern.

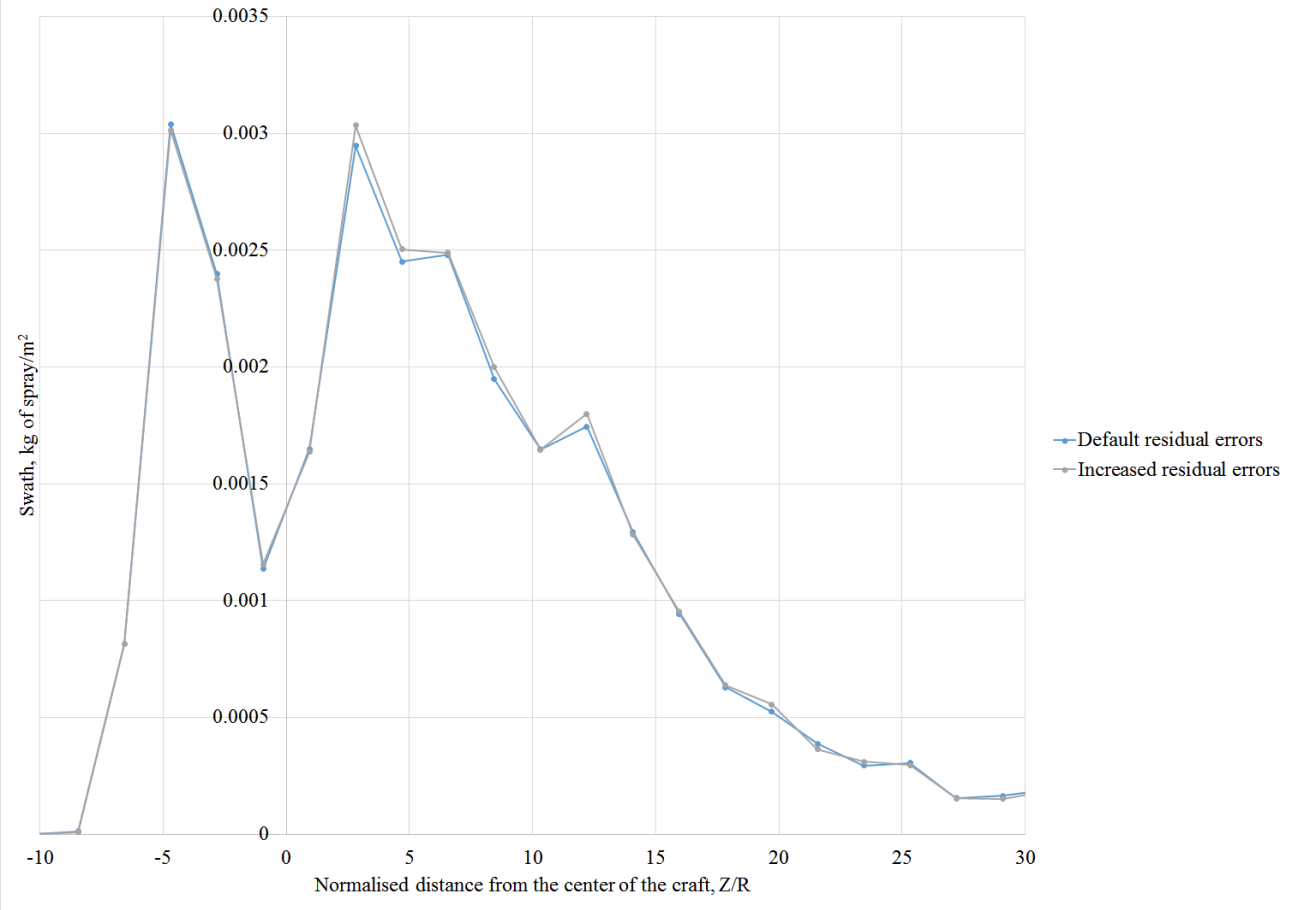

Figure 7.45 Modelled swath pattern of spray (kg/m^2) deposited on the ground in Flight 9 conditions when residual error has the default values (blue line with circular dots) and when residual error is one order of magnitude greater than the default (grey line with circular dots).

Three integrational time steps in the Lagrangian particle tracking were tested in the model. Decreasing the time step from 0.1 s to 0.01 s changes the swath pattern on the leeward side of the swath pattern. Decreasing the time step from 0.01 s to 0.001 s doesn't change the swath pattern. Therefore, it was decided to use 0.01 s (Figure 7.46). The computational time of spray deposition in Flight 9 increased from 3.5 minutes to 5 minutes. Only one core of the processor was used for the particle tracking. If it is necessary to decrease the computational time further, it is possible to use several cores.

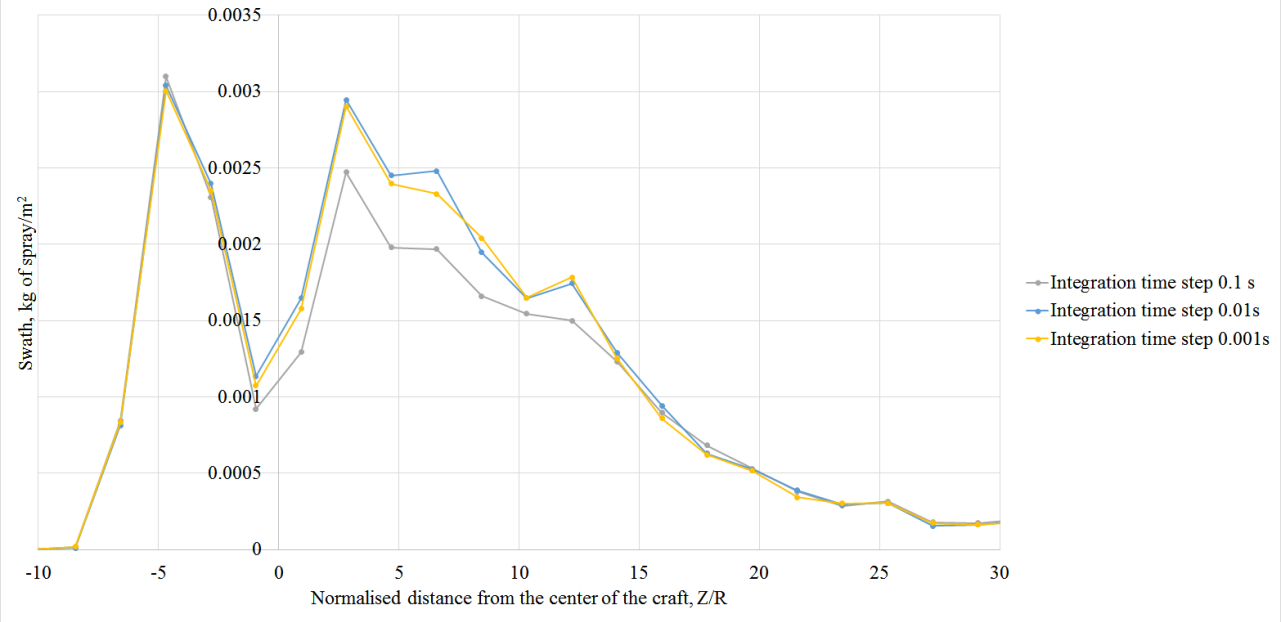

Figure 7.46 Modelled swath pattern of spray (kg/m^2) deposited on the ground in Flight 9 conditions when the integrational time step in the Lagrangian particle tracking algorithm is 0.01 s (blue line with circular dots) and 0.1 s (grey line with circular dots), 0.01 s (blue line with circular dots) and 0.001 s (yellow line with circular dots).

In the Lagrangian particle tracking algorithm, it is possible to use two dispersion models: gradient dispersion and stochastic dispersion. These models were tested in Flight 9 (Figure 7.47).

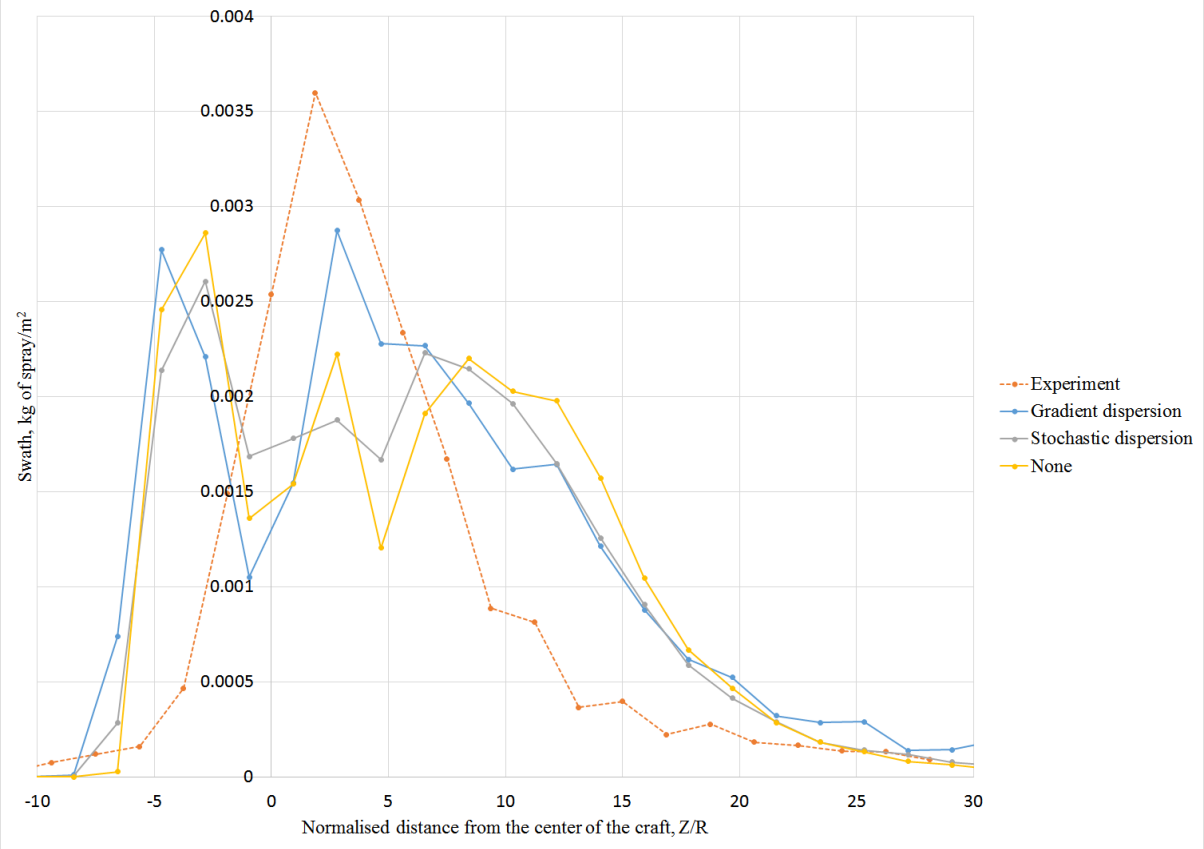

Figure 7.47 Modelled swath pattern of spray (kg/m^2) deposited on the ground in Flight 9 conditions when the gradient dispersion model was used in the Lagrangian tracking model (blue line with circular dots), when the stochastic dispersion model was used in the Lagrangian tracking model (grey line with circular dots), and when no dispersion was used in the Lagrangian tracking model (yellow line with circular dots).

The dispersion model influences spray deposition on the ground. It was decided to use the gradient dispersion model as it takes into account the gradient of TKE and closest to the experiment.

7.4.3 Flight 29 (F29)

For Flight 29, only the influence of residual error was checked. Figure 7.45 shows the swath pattern for default residual errors (blue line), and with residual error increased by an order of

magnitude (grey line). The swath patterns are identical; therefore, it is possible to use increased residual error.

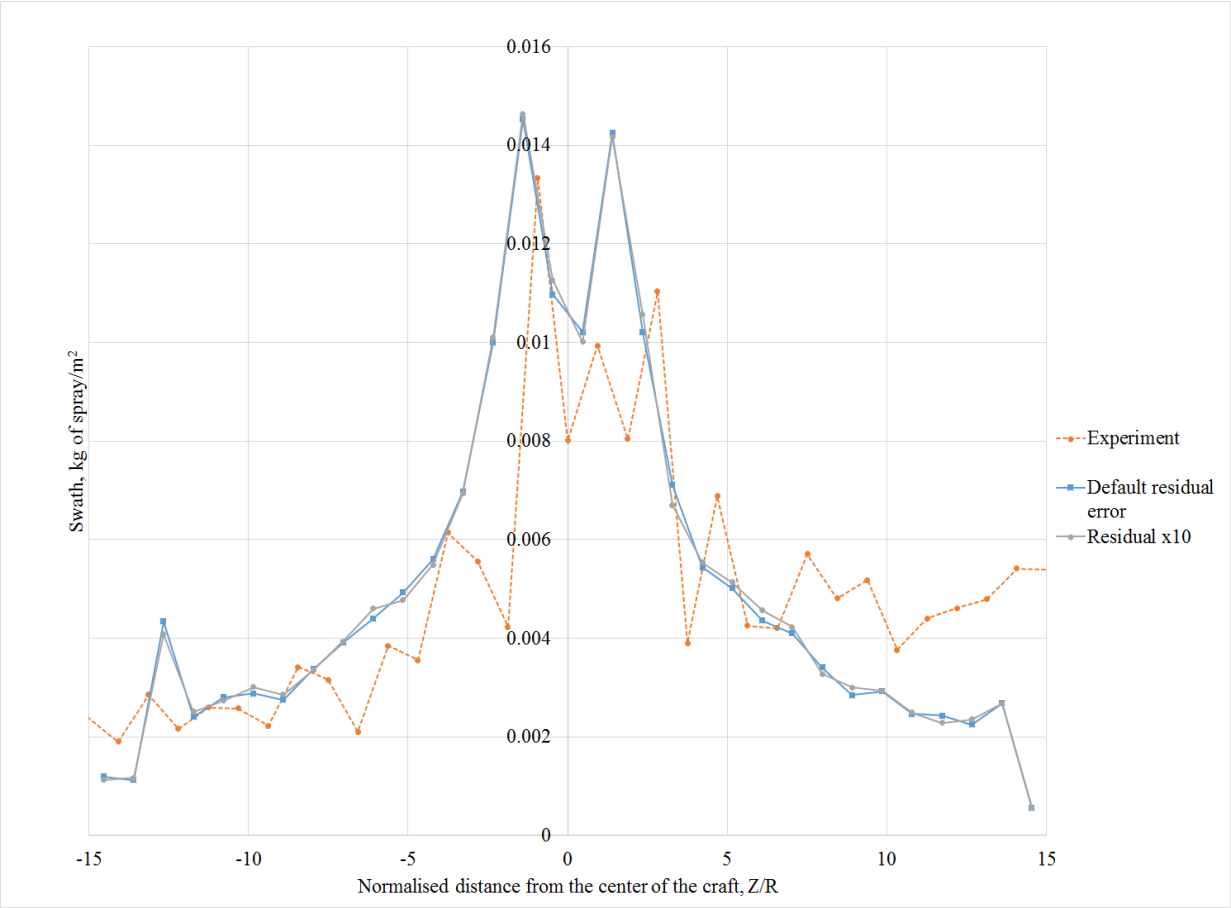

Figure 7.48 Modelled swath pattern of spray (kg/m^2) deposited on the ground in Flight 29 conditions when residual error has the default values (blue line with rectangular dots) and when residual error is one order of magnitude greater than the default (grey line with rhomboid dots).

7.5 Discussion

The model analysed spray dispersion on the ground in hover flight and in flight with lateral velocity.

7.5.1 Hover flight (no lateral velocity)

Two counter rotating DJI E7000 rotors were used without lateral velocity to test the spray footprint on the ground. Two spray nozzle positions were tested: between rotors, 20mm below the rotor plane (Figure 7.3, top right) and 0.6R from the centre of the rotor, 20mm below the rotor plane (Figure 7.3, bottom right). The spatial extent of deposited spray was measured in experiments. The model replicated the conditions of the experiment and reported the deposition of the spray on the ground.

The difference between modelled and experimental spray deposition can be explained by the following assumptions of the model:

1) The model uses a rotor flow field fitted to an isolated rotor, i.e., it is modelling two isolated rotors which happen to be close to each other and are not interacting. Therefore, wake interaction of two isolated rotors was less severe in the model, with the tilt of the wakes towards each other being less pronounced than in the experiment. Chapter 6 described that two isolated rotors and the method of prescription of tip vortices can be reasonably used to model two genuinely interacting rotors.
2) The model describes the rotor tip vortex by prescribing the turbulence kinetic energy (TKE) (Chapter 6). The tip vortex in the model does not propagate with the downwash, does not have a helical structure, and doesn't generate the periodical radial velocity component, observed in PIV experiment (Chapter 3).

The accuracy of velocity flow fields is enough for a system that predicts multicopter flow fields as a part of pre-flight or post-flight deposition analysis (Chapter 6). Operationally, the crosswind speed and desired craft speed and spray height is sufficient to determine the spray pattern and/or determine the optimal coverage and optimal flight path (given that parameters of multicopter are known).

When the nozzle was placed between rotors, the footprint is shifted towards the positive Z-axis in the experiment. There is no drift in the Z direction in the model because of non-interacting rotor wakes in the model. The greatest effect on the spray deposition drift towards the Z axis was the tilt of the nozzle around the X-axis. Another noticeable effect in the model, when nozzle was placed between rotors, was a large footprint elongation in the negative X direction. This starts at approximately -3R (-1.26m) and travels up to -5R (2.1 m). Coverage in the zone of a large drift is 30-50%, mostly composed of small particles. It is assumed that the large lateral drift was not observed in the experiment because the majority of small particles went into the region of upward velocity and contaminated the rotors or drifted away from the main deposition one. As mentioned in Chapter 6, the upward velocity region was not observed in the model with no lateral velocity.

7.5.2 Lateral velocity

Flight 4, flight 9 and flight 29 conditions supported those found in the experiment. The spatial extent of the swath and deposition on the swath was similar. The effective swath width is within one standard deviation of the model in all modelled flights. The standard deviation of effective swath width is 23% in the model in all modelled flights. The model showed the swath depends on the yaw and roll angles of the multicopter, the rotational speed of the rotors and the roughness of the terrain. In addition, the lateral drift of small particles, carried by rollup vortices, was observed in the model. Richardson et al. (2019) did not observe this drift because the rollup vortices were suppressed by the presence of grass.

A common effect observed in the model was the presence of local minima on the swath pattern diagram (-2.5R in Flight 4, -0.5R in Flight 9). Such an effect was not observed in the experimental analysis. The explanation for the local minimum in the model is the separation due to the rollup vortices. The rollup vortices carry the spray streamwise. However, there is

sideways drift in the spray carried by the rollup vortices. The sideways motion generates a separation of the spray carried by the main downwash(es) and the spray carried by the rollup vortices. The same effect was observed by Wen et al. (2019). In their experiment, the spray pattern released from the multicopter (4 x 383 mm radius rotors) was tested in a wind tunnel with 1-7 m/s lateral velocity in a stable laboratory environment. Swath analysis of the spray, performed by Wen et al. (2019), showed the local minimum in spray deposition under the centre of the multicopter. In this research, it was shown (Figure 7.16 Figure 7.26) that the local minima in the swath are less severe with higher roughness of the terrain surface. Therefore, to obtain a precise swath, it is recommended to consider the terrain roughness and a presence of a plant canopy.

7.6 Conclusion

This chapter has presented an application of Lagrangian particle tracking to model spray deposition. Spray released in the multicopter wake velocity field can be tracked using *kinematicParcel* class in OpenFOAM. The evaporation model was developed and implemented into the *kinematicParcel* class in OpenFOAM. The deposition of the spray can be calculated and translated into a swath pattern. The model was validated against several flight conditions: hovering flight and flight with different lateral velocities.

In hovering flight, the spray footprint of two nozzle positions was modelled and compared to experimental analysis. The nozzle positions were between rotors and under the rotor. Both in the model and in the experiment, spray from the nozzle placed between rotors was more dispersed than the spray from the nozzle placed under the greatest downwash of the rotor. When the nozzle was placed between rotors, the centre of mass of the footprint traversed -1.3R

in the experiment and -1.5R in the model in the X direction. The spray footprint was symmetrical around the X/R axis in the model. In the experimental analysis, the spray drifted towards positive Z.

The drift of spray, released under the greatest downwash, in the Z direction was -1R (-0.42 m) in the experiment and -0.5R (-0.21 m) in the model. The drift of the centre of mass of the spray footprint in the X direction was -0.4R (-0.168 m) in experiments and 0.3R (0.126 m) in the model. This difference may be explained by the method of modelling of rotor tip vortices.

In flight with lateral velocity, several flight conditions were tested. In Flight 4 (true air speed 3.627 m/s, ground speed 2.85 m/s, crosswind speed 0.736 m/s) and in Flight 9 (true air speed 3.234 m/s, ground speed 2.9 m/s, crosswind speed 2.164 m/s) the spatial extent of the swath pattern is similar in the model and experiment. The effective swath width is within one standard deviation in the model and the experiment. The one standard deviation of the effective swath width was equal to 23 %. The swath was heavily dependent on the roll and yaw angles. Therefore, the maximum roll and yaw angles must be obtained from the flight controller of the multicopter for the precise swath analysis. The average rotation speed and height expected in the flight can be chosen for the successful prediction of the effective swath. The swath closest to the experiment was obtained when the terrain roughness was equal to 0.5 m that corresponds to the terrain with bushes, obstacles. A possible source of disagreement between swath in the model and the experiment is the presence of a plant canopy (grass) in the experiment. The plant canopy interacts with rollup vortices and does not allow them to penetrate in the streamwise direction. The influence of the canopy was modelled using the porous medium. Figure 7.37 shows that the drift of spray is less severe in the presence of a plant canopy.

The model can be used to evaluate the swath pattern on the ground for the multicopter.

8. Conclusions and future work

8.1 Conclusions

The research objective was to study multicopter wake and its influence on liquid spraying performance. The ultimate goal was to introduce a universal model for spray deposition on the ground for different multicopters and different flight and environmental conditions and to check if a model could be solved quickly enough for real-time control in changing wind conditions. The problem was divided into two parts: a study of multicopter wake during flight and a study of spray behaviour under the influence of multicopter wake.

Chapter 1 reviewed the literature, surveying the main theories of isolated wake evaluation and numerical techniques for the computational analysis of multicopter wake. The literature shows that the wake of adjacent rotors depends on the distance between rotors, with interaction effects observed between two coplanar counter-rotating rotors. Rollup vortex generation has been observed in flight with lateral velocity. Rollup vortices can be predicted using rotor disk simplification in computational fluid dynamics.

Flow in the far field is affected by the flying multicopter, ground, atmospheric wind and plant canopy. The ground effect on the flying multicopter is stronger than on single rotor craft. Multicopter wake is affected by plant canopy and varies with plant phenotype.

Spray deposition can be evaluated either numerically or experimentally. The literature shows how spray deposition on plants depends on the flight parameters of multicopter (height, speed) and plant parameters (phenotype, wettability, roughness).

For the multicopter wake analysis, stereo particle image velocimetry (SPIV) was chosen as the primary experimental technique. The particles were produced either by Laskin nozzles or a smoke machine. In every experiment, velocity was measured in one or more planes. When the number of planes was more than one, the data between planes was interpolated using weighted inverse-distance interpolation. The uncertainty of experimental analysis was calculated using the peak signal-to-noise ratio method, which assumes that error in pixel displacement follows a Gaussian distribution. The secondary velocity measurement tool was constant temperature anemometry (CTA) using a three-axial probe. CTA experimental analysis was used to verify the SPIV velocity flow field. Additionally, turbulent kinetic energy was obtained from CTA analysis.

CTA and SPIV were used to analyse isolated rotor wakes for the APC 1047 (127 mm radius, 119.3 mm pitch), APC 1045 (127 mm radius, 114.3 mm pitch), APC 1040 (127 mm radius, 101.6 mm pitch) and DJI E7000 (420 mm radius, 230 mm pitch). The wake vector field, normalised by rotor tip velocity, remained similar with changing rotational speed.

It was shown that multicopters can be divided into several parts, with two rotors in each part. Therefore, the experimental setup could be simplified by using two rotors instead of four. The magnitude similarity index was found to be near one (one corresponds to the best fit) when comparing velocity fields of two adjacent counter-rotating rotors in the presence of other rotors and when tested isolated. The exception was the zone of influence of adjacent rotors.

Two APC 1045 counter-rotating coplanar rotors were used for the analysis of multicopter rotors in hover flight. Rotor arc spacings of 02R, 0.36R and 0.55R were chosen for the analysis. SPIV experimental analysis showed the tilt of the rotor wakes towards each other. The tilt angle decreases with tip distance separation. Two counter-rotating coplanar DJI E7000 rotors with

0.2R rotor tip spacing demonstrated similar results. Interaction between the two wakes creates a low-pressure zone between them, causing them to tilt towards each other.

Experimental analysis of two counter-rotating coplanar rotors reported the region of upwash between rotors. The region of upwash was observed at rotor tip spacings of 0.2R, 0.36R, and 0.55R in APC 1045 rotors. The upward velocity region was found outside the rotor disk, 0.6R-1R downstream, depending on tip spacing. The upwash velocity region was observed in DJI E7000 rotors with rotor arcs at 0.2R spacing in every phase lag. With DJI E7000 rotors, maximum upward velocity was observed when neighbouring rotors are 45° apart and neither rotor's tip is at its closest approach to the neighbouring rotor's arc. Upward velocity magnitude peaks when one of the rotor tips is at its closest approach to the neighbouring rotor's arc. Upward velocity magnitude is weakly dependent or independent of rotational speed over the range of 1740-2150 rpm.

The wakes of adjacent coplanar counter-rotating rotors in a multicopter interact strongly when lateral velocity is present in the flow. In streamwise configuration, the wake of the windward rotor tilts 20-25^{o} degrees more than the leeward rotor. This was observed at lateral velocities of 6 m/s, 10 m/s and 14 m/s. Increasing tip spacing to 2R at a lateral velocity of 6 m/s did not influence the tilt angles of interacting wakes. The shading of the leeward wake by the windward wake is the cause of different tilt angles between two wakes in streamwise configuration. Another contributing factor to the tilt of rotor wakes is the zone of low pressure between rotors that was described for hovering rotors.

There are regions of upwash in the wake in the presence of lateral velocity. In streamwise configuration, this region was attached to the windward side of the windward rotor disk. The upward velocity region (as part of rollup vortices) extends downstream with lateral velocity. In spanwise configuration, the zone of upward velocity is attached to the windward side of both

rotors. It extends downstream with lateral velocity near the free side of the rotor disk. However, in the presence of another counter-rotating rotor, the zone of upward velocity does not have the downstream lateral component when lateral velocity is between 2-6 m/s. In the 10 m/s lateral velocity experiment, the upward velocity region in the zone of two-rotor interaction increases downstream in the direction of lateral velocity.

The data field obtained from SPIV analysis was used to track spray deposition near the rotor under the influence of rotor wake. Based on the results, it is recommended to avoid placing the nozzle immediately under the arc swept by the rotor tip (0.8R-1R), especially in the zone between rotors. This will result in some spray being drawn upwards, decreasing spraying efficiency and potentially entering the electrical components of the multicopter. By choosing the correct nozzle location, smaller particles can be delivered to the target without the drift caused by lateral velocity (wind, forward or side motion of the craft). The recommended nozzle position is the zone of strongest downwash. This location depends on the type of rotor, but generally is between 0.5-0.7 times the rotor radius.

Based on the experimental results, a simplified model was developed for the analysis of spray patterns under influence of multicopter wake. The model was written in the OpenFoam environment and does not depend on any commercial software.

The size of the domain was chosen to have the spray from the multicopter deposited on the ground within the domain. The mesh was optimised to have the fastest convergence. The model used k-omega SST RANS turbulence. Rotor disk simplification was used as a boundary condition inside the domain. The velocity field boundary condition was obtained from SPIV data. The turbulence kinetic energy obtained in the CTA experiment was used in the rotor boundary condition. Natural wind with a logarithmic variation of wind speed with height was

incorporated into the model. Wind in the model can come from any direction relative to the multicopter.

Two APC 1045 rotors were modelled flying at 2 m/s, 6 m/s, 10 m/s in streamwise and spanwise configurations. The velocity magnitude is within one standard deviation under rotors at 2 m/s and 6 m/s. Differences between the model and SPIV results increase with increasing lateral velocity. In the model, strong interaction was observed between leeward and windward rotors in streamwise configuration. Similarly to the SPIV experiment, the leeward rotor was shaded by the windward rotor in the model. Therefore, the wake inclination angle of the leeward rotor was smaller than in the windward rotor. The effects of upward velocity were observed in the model. The location of the upward velocity region was similar in the model and experiment in both spanwise and streamwise configurations.

Two DJI E7000 coplanar counter rotating rotors were modelled in hovering flight. The obtained velocity field under the rotor was within one standard deviation of SPIV experimental results. However, between rotors the obtained velocity field was not within one standard deviation and an upward velocity region was not discovered. This confirms that the source of upward velocity region generation is interacting vortices, as these were not introduced into the model.

A DJI Agras MG-1 multicopter was modelled to allow comparison of swath patterns in the model and in the experiment. Wake modelling showed two roll-up vortices present in the multicopter, extending in a streamwise direction. The spanwise distance between vortices increases with distance from the multicopter.

Pressure, turbulence kinetic energy, turbulence dissipation rate and velocity model outputs were used for spray pattern prediction. Spray released in the multicopter wake velocity field was tracked in OpenFoam using Lagrangian particle tracking. An evaporation model was

implemented into a particle tracking algorithm. The deposition of spray on the surface was transformed into a swath pattern.

In hovering flight, the spray footprints of two nozzle positions were modelled and compared to experimental results. The comparison showed that the model can be used to estimate spray footprints. The differences between the model and the experiment may be explained by the influence of nearby walls and the roughness of the Styrofoam surface in experiments.

The swath pattern in the wake of a DJI Agras MG-1 multicopter in different flights (true airspeed 3.627 m/s, ground speed 2.85 m/s, and crosswind speed 0.736 m/s, true airspeed 3.234 m/s, ground speed 2.9 m/s, and crosswind speed 2.164 m/s, at true air speed 4.88 m/s, ground speed 4.88 m/s, and crosswind speed 0.04 m/s), is comparable in the model and experiment. The experimentally obtained and modelled effective swath width (30% line separation) is within one standard deviation of the model.

In all flight trials, the modelled swath was closest to the experimentally obtained swath when the surface roughness was equal to 0.5 (bushes, suburb) and the rotational speed of all rotors was equal to 2475 rpm with 0.75R (0.2m) tall plant canopy (grass) represented in the model as a porous medium layer.

The model can be used to evaluate the swath pattern on the ground for the multicopter. The model showed acceptable efficiency for hovering flight and flight velocities up to 5 m/s when flight parameters can be approximately estimated. The model can be used for higher lateral velocities if the actual flight parameters (rotational speed of a rotor, tilt, yaw of a multicopter) are measured and incorporated to the model. The computational time depends on the model. The minimum computational time was equal to 12 minutes per analysis. Such computational time was achieved in the analysis of spray deposited by DJI Agras Mg-1 multicopter (all flights) when the velocity *(U)* residual error was $1x10^{-3}$, residual error of pressure *(p), TKE (k)*

and *omega* was equal $1x10^{-3}$. The computational analysis was performed on the desktop with the 8-core Intel® Core™ i7-6700 CPU @ 3.40GHz computer and 32Gb RAM

8.2 Future work

The experimental analysis was conducted with rotors that are coplanar and not ducted as this is the most common multicopter layout. Future experimental work can be addressed to the study of multicopters with coaxial and ducted rotor layouts. If the wake behaviour of coaxial or ducted rotors is known, it can be introduced to the model. The current experimental study was based on DJI family rotors and APC family rotors. It has shown that the flow patterns of different rotor families are similar. When a new rotor is introduced, the downwash of the isolated rotor must be experimentally quantified for a precise result.

The model for quantifying swath patterns in the multicopter flow field can predict swath patterns with reasonable accuracy. The computational time required for the analysis is around 12 minutes. For successful application of the model, computational time can be decreased. The domain shape is a parallelepiped: computational time can be decreased by using an optimised domain shape (e.g., several bonded parallelepipeds). The minimum required number of cells was chosen in the model. The mesh could be very coarse in the region where no wake was present. Therefore, the adaptive mesh generation can be used to optimise the mesh size where required. Additionally, the computational time can be decreased by using the prescribed velocity field, prescribed turbulence kinetic energy, and turbulence kinetic energy dissipation rate. To achieve this, machine learning algorithms can be introduced to the model. Decreasing the computational time opens perspectives for real-time swath analysis.

In the spray analysis, an evaporation model was introduced. When evaporation occurs, the local change in humidity is modelled by an empirical function. A first-principles approach would increase the precision of the model by accounting for the phase change of the sprayed liquid, as the evaporated spray would influence local humidity.

For acceptance in general practice, the model must be verified by testing in different flight and environmental conditions. Swath pattern analysis at different flight heights, multicopter speeds and crosswind speeds must be tested and compared to the model. Multicopters can be tested in different terrains (hills, slopes, etc.) and in city environments (walls, buildings, etc.). Additionally, the model can be compiled with a user-friendly interface that will reduce the time needed for computational preparation.

References

Adrian, Ronald J. “Particle-Imaging Techniques for Experimental Fluid Mechanics.” *Annual Review of Fluid Mechanics*, vol. 23, no. 1, 1991, pp. 261–304., doi:10.1146/annurev.fl.23.010191.001401.

Aiken, R. M., et al. “Scaling Effects of Standing Crop Residues on the Wind Profile.” *Agronomy Journal*, vol. 95, no. 4, 2003, pp. 1041–1046., doi:10.2134/agronj2003.1041.

Aleksandrov, Dmitri, and Igor Penkov. “Optimization of Lift Force of Mini Quadrotor Helicopter by Changing of Gap Size between Rotors.” *Solid State Phenomena*, vol. 198, 2013, pp. 226–231., doi:10.4028/www.scientific.net/ssp.198.226.

Andersson, Bengt. *Computational Fluid Dynamics for Engineers*. Cambridge University Press, 2020.

Barton, I. E. “Comparison of SIMPLE- and PISO-Type Algorithms for Transient Flows.” *International Journal for Numerical Methods in Fluids*, vol. 26, no. 4, 1998, pp. 459–483., doi:10.1002/(sici)1097-0363(19980228)26:4<459::aid-fld645>3.0.co;2-u.

Bauknecht, André, et al. “Airborne Visualization of Helicopter Blade Tip Vortices.” *Journal of Visualization*, vol. 20, no. 1, 2016, pp. 139–150., doi:10.1007/s12650-016-0389-z.

Bhattacharya, Sayantan, et al. “Stereo-Particle Image Velocimetry Uncertainty Quantification.” *Measurement Science and Technology*, vol. 28, no. 1, 2016, p. 015301., doi:10.1088/1361-6501/28/1/015301.

Bianchini, Alessandro, et al. “Potential of the Virtual Blade Model in the Analysis of Wind Turbine Wakes Using Wind Tunnel Blind Tests.” *Energy Procedia*, vol. 126, 2017, pp. 573–580., doi:10.1016/j.egypro.2017.08.212.

Bilanin, Alan J., et al. “AGDISP: The Aircraft Spray Dispersion Model, Code Development and Experimental Validation.” *Transactions of the ASAE*, vol. 32, no. 1, 1989, pp. 0327–0334., doi:10.13031/2013.31005.

Birch, D., et al. “Rollup and Near-Field Behavior of a Tip Vortex.” *Journal of Aircraft*, vol. 40, no. 3, 2003, pp. 603–607., doi:10.2514/2.3137.

Bogos, Stefan, et al. “Turbulence Models in CFD Simulation of Low-Reynolds Number Airfoils Flow.” 2015, doi:10.1063/1.4912704.

Boulard, T., et al. “Airflow And Microclimate Patterns In A One-Hectare Canary Type Greenhouse: An Experimental And Cfd Assisted Study.” *Acta Horticulturae*, no. 801, 2008, pp. 837–846., doi:10.17660/actahortic.2008.801.98.

Brosy, Caroline, et al. “Simultaneous Multicopter-Based Air Sampling and Sensing of Meteorological Variables.” *Atmospheric Measurement Techniques*, vol. 10, no. 8, 2017, pp. 2773–2784., doi:10.5194/amt-10-2773-2017.

Brown, G.j. “Erosion Prediction in Slurry Pipeline Tee-Junctions.” *Applied Mathematical Modelling*, vol. 26, no. 2, 2002, pp. 155–170., doi:10.1016/s0307-904x(01)00053-1.

Bruun, H H. “Hot-Wire Anemometry: Principles and Signal Analysis.” *Measurement Science and Technology*, vol. 7, no. 10, 1996, doi:10.1088/0957-0233/7/10/024.

Cadieux, Francois, et al. “Effects of Numerical Dissipation on the Interpretation of Simulation Results in Computational Fluid Dynamics.” *Computers & Fluids*, vol. 154, 2017, pp. 256–272., doi:10.1016/j.compfluid.2017.06.009.

Charonko, John J, and Pavlos P Vlachos. “Estimation of Uncertainty Bounds for Individual Particle Image Velocimetry Measurements from Cross-Correlation Peak Ratio.” *Measurement*

Science and Technology, vol. 24, no. 6, 2013, p. 065301., doi:10.1088/0957-0233/24/6/065301.

Chatellier, Ludovic, and John Fitzpatrick. "Spatio-Temporal Correlation Analysis of Turbulent Flows Using Global and Single-Point Measurements." *Experiments in Fluids*, vol. 38, no. 5, 2005, pp. 563–575., doi:10.1007/s00348-004-0910-3.

Cheeseman, I.c., and J.d.l. Gregory. "The Effect Of The Ground On The Performance Of A Helicopter." *Performance*, 1959, doi:10.1016/b978-1-4831-9729-6.50023-1.

Chen, Yu, et al. "Spray Deposition inside Tree Canopies from a Newly Developed Variable-Rate Air-Assisted Sprayer." *Transactions of the ASABE*, 2013, pp. 1263–1272., doi:10.13031/trans.56.9839.

Clift, Roland, et al. *Bubbles, Drops, and Particles*. Dover, 2006.

Coradini, Murilo Franco, and Robson Leal Da Silva. "Hot-Wire Anemometers: Design And Engineering Applications." *17th Brazilian Congress of Thermal Sciences and Engineering*, 2018, doi:10.26678/abcm.encit2018.cit18-0240.

Daponte, Pasquale, et al. "A Review on the Use of Drones for Precision Agriculture." *IOP Conference Series: Earth and Environmental Science*, vol. 275, 2019, p. 012022., doi:10.1088/1755-1315/275/1/012022.

Dorr, Gary J., et al. "Towards a Model of Spray–Canopy Interactions: Interception, Shatter, Bounce and Retention of Droplets on Horizontal Leaves." *Ecological Modelling*, vol. 290, 2014, pp. 94–101., doi:10.1016/j.ecolmodel.2013.11.002.

Fengbo, Yang, et al. "Numerical Simulation and Experimental Verification on Downwash Air Flow of Six-Rotor Agricultural Unmanned Aerial Vehicle in Hover." *International Journal of*

Agricultural and Biological Engineering, vol. 10, no. 4, 2017, pp. 41–53., doi:10.25165/j.ijabe.20171004.3077.

Gill, Rajan, and Raffaello D'andrea. "Propeller Thrust and Drag in Forward Flight." *2017 IEEE Conference on Control Technology and Applications (CCTA)*, 2017, doi:10.1109/ccta.2017.8062443.

Gillies, J. A., et al. "Drag Coefficient and Plant Form Response to Wind Speed in Three Plant Species: Burning Bush (Euonymus Alatus), Colorado Blue Spruce (Picea Pungens Glauca.), and Fountain Grass (Pennisetum Setaceum)." *Journal of Geophysical Research: Atmospheres*, vol. 107, no. D24, 2002, doi:10.1029/2001jd001259.

Guo, Baoyu, et al. "Simulation of the Agglomeration in a Spray Using Lagrangian Particle Tracking." *Applied Mathematical Modelling*, vol. 28, no. 3, 2004, pp. 273–290., doi:10.1016/s0307-904x(03)00133-1.

"Discharge Coefficients of Flat Fan Nozzles." *2016 ASABE International Meeting*, 2016, doi:10.13031/aim.20162460834.

Grace, Jennifer C, et al. "Evaluation of the AGDISP Canopy Model." *2011 Louisville, Kentucky, August 7 - August 10, 2011*, 2011, doi:10.13031/2013.37341.

Gray, Robin B. "An Aerodynamic Analysis Of A Singlebladed Rotor In Hovering And Low-Speed Forward Flight As Determined From Smoke Studies Of The Vorticity Distribution In The Wake." 1956, doi:10.21236/ad0122600.

Greifzu, Franziska, et al. "Assessment of Particle-Tracking Models for Dispersed Particle-Laden Flows Implemented in OpenFOAM and ANSYS FLUENT." *Engineering Applications of Computational Fluid Mechanics*, vol. 10, no. 1, 2015, pp. 30–43., doi:10.1080/19942060.2015.1104266.

Griffiths, Daniel A., et al. “Predictions of Rotor Performance in Ground Effect Using a Free-Vortex Wake Model.” *Journal of the American Helicopter Society*, vol. 50, no. 4, 2005, pp. 302–314., doi:10.4050/1.3092867.

Guo, Shuang, et al. “Optimization of the Factors Affecting Droplet Deposition in Rice Fields by Rotary Unmanned Aerial Vehicles (UAVs).” *Precision Agriculture*, 2021, doi:10.1007/s11119-021-09818-7.

Haddadi, Bahram, et al. “Membrane Modeling Using CFD: Combined Evaluation of Mass Transfer and Geometrical Influences in 1D and 3D.” *Journal of Membrane Science*, vol. 563, 2018, pp. 199–209., doi:10.1016/j.memsci.2018.05.040.

Hargreaves, D.m., and N.g. Wright. “On the Use of the k– Model in Commercial CFD Software to Model the Neutral Atmospheric Boundary Layer.” *Journal of Wind Engineering and Industrial Aerodynamics*, vol. 95, no. 5, 2007, pp. 355–369., doi:10.1016/j.jweia.2006.08.002.

Hart, John. “Comparison of Turbulence Modeling Approaches to the Simulation of a Dimpled Sphere.” *Procedia Engineering*, vol. 147, 2016, pp. 68–73., doi:10.1016/j.proeng.2016.06.191.

Hong, Se-Woon, et al. “CFD Simulation of Airflow inside Tree Canopies Discharged from Air-Assisted Sprayers.” *Computers and Electronics in Agriculture*, vol. 149, 2018, pp. 121–132., doi:10.1016/j.compag.2017.07.011.

Hong, Se-Woon, et al. “Fluid Dynamic Approaches for Prediction of Spray Drift from Ground Pesticide Applications: A Review.” *Agronomy*, vol. 11, no. 6, 2021, p. 1182., doi:10.3390/agronomy11061182.

Hu, B., et al. “Large Eddy Simulation of a Turbulent Non-Reacting Spray Jet.” *Volume 2: Emissions Control Systems; Instrumentation, Controls, and Hybrids; Numerical Simulation; Engine Design and Mechanical Development*, 2015, doi:10.1115/icef2015-1033.

Hulst, H. C. Van De, and V. Twersky. “Light Scattering by Small Particles.” *Physics Today*, vol. 10, no. 12, 1957, pp. 28–30., doi:10.1063/1.3060205.

Hulst, H. C. van de. *Light Scattering: by Small Particles*. Dover, 1981.

Ishigaki, Masahiro, et al. “Influence of Mesh Non-Orthogonality on Numerical Simulation of Buoyant Jet Flows.” *Nuclear Engineering and Design*, vol. 314, 2017, pp. 326–337., doi:10.1016/j.nucengdes.2017.02.010

Johnson, Wayne. *Rotorcraft Aeromechanics*. Cambridge University Press, 2013.

Joulain, Antoine, et al. “Numerical Investigation of the Vortex Roll-up from a Helicopter Blade Tip Using a Novel Fixed-Wing Adaptation Method.” *CEAS Aeronautical Journal*, vol. 8, no. 2, 2017, pp. 245–260., doi:10.1007/s13272-016-0234-z.

Insight 4G™ global image, acquisition, analysis, & display users guide. (2015) (P/N 600511). Shoreview, MI: *TSI Incorporated*.

Jørgensen, F. E. How to measure turbulence with hot-wire anemometers - a practical guide. Dantec Dynamics A/S Tonsbakken, 2005.

Kabaliuk, N., et al. “Blood Drop Size in Passive Dripping from Weapons.” *Forensic Science International*, vol. 228, no. 1-3, 2013, pp. 75–82., doi:10.1016/j.forsciint.2013.02.023.

Kähler, C. J., et al. “Generation and Control of Tracer Particles for Optical Flow Investigations in Air.” *Particle Image Velocimetry: Recent Improvements*, 2004, pp. 417–426., doi:10.1007/978-3-642-18795-7_30.

Landgrebe, Anton J. “An Analytical and Experimental Investigation of Helicopter Rotor Hover Performance and Wake Geometry Characteristics.” 1971, doi:10.21236/ad0728835.

Landsberg, J. J., and G. B. James. “Wind Profiles in Plant Canopies: Studies on an Analytical Model.” *The Journal of Applied Ecology*, vol. 8, no. 3, 1971, p. 729., doi:10.2307/2402680.

Marshall, Jeffrey S., and Shuiqing Q. Li. *Adhesive Particle Flow: a Discrete-Element Approach*. Cambridge University Press, 2014.

Martin, Daniel E., et al. “Effect of Application Height and Ground Speed on Spray Pattern and Droplet Spectra from Remotely Piloted Aerial Application Systems.” *Drones*, vol. 3, no. 4, 2019, p. 83., doi:10.3390/drones3040083.

Massinon, Mathieu, et al. “Spray Droplet Impaction Outcomes for Different Plant Species and Spray Formulations.” *Crop Protection*, vol. 99, 2017, pp. 65–75., doi:10.1016/j.cropro.2017.05.003.

Meana-Fernández, Andrés, et al. “Turbulence-Model Comparison for Aerodynamic-Performance Prediction of a Typical Vertical-Axis Wind-Turbine Airfoil.” *Energies*, vol. 12, no. 3, 2019, p. 488., doi:10.3390/en12030488.

Menter, F. R. “Two-Equation Eddy-Viscosity Turbulence Models for Engineering Applications.” *AIAA Journal*, vol. 32, no. 8, 1994, pp. 1598–1605., doi:10.2514/3.12149.

Misiorowski, Matthew, et al. “Computational Study on Rotor Interactional Effects for a Quadcopter in Edgewise Flight.” *AIAA Journal*, vol. 57, no. 12, 2019, pp. 5309–5319., doi:10.2514/1.j058369.

Muiruri, Patrick Irungu, et al. “A Comparative Study of RANS-Based Turbulence Models for an Upscale Wind Turbine Blade.” *SN Applied Sciences*, vol. 1, no. 3, 2019, doi:10.1007/s42452-019-0254-5.

Nairn, J.j., and W.a. Forster. “Photostability of Pyranine and Suitability as a Spray Drift Tracer.” *New Zealand Plant Protection*, vol. 68, 2015, pp. 32–37., doi:10.30843/nzpp.2015.68.5795.

Parkin, C.s., and J.c. Wyatt. “The Determination of Flight-Lane Separations for the Aerial Application of Herbicides.” *Crop Protection*, vol. 1, no. 3, 1982, pp. 309–321., doi:10.1016/0261-2194(82)90006-0.

Prasad, A. K. “Stereoscopic Particle Image Velocimetry.” *Experiments in Fluids*, vol. 29, no. 2, 2000, pp. 103–116., doi:10.1007/s003480000143.

Raffel, Markus, et al. *Particle Image Velocimetry: a Practical Guide*. Springer-Verlag Berlin Heidelberg, 2007.

Rahman, Mohammad Fatin Fatihur, et al. “A Comparative Study on Application of Unmanned Aerial Vehicle Systems in Agriculture.” *Agriculture*, vol. 11, no. 1, 2021, p. 22., doi:10.3390/agriculture11010022.

Richardson, B., et al. “Quantification of Herbicide Spray Deposit Variation Following Aerial Application in Forestry Operations.” *Proceedings of the New Zealand Plant Protection Conference*, vol. 46, 1993, pp. 319–324., doi:10.30843/nzpp.1993.46.11148.

Richardson, B., et al. “Defining Acceptable Levels Of Herbicide Deposit Variation From Aerial Spraying.” *Applied Engineering in Agriculture*, vol. 20, no. 3, 2004, pp. 259–267., doi:10.13031/2013.16059.

Richardson, B., et al. “Swath Pattern Analysis from a Multi-Rotor Unmanned Aerial Vehicle Configured for Pesticide Application.” *Pest Management Science*, vol. 76, no. 4, 2019, pp. 1282–1290., doi:10.1002/ps.5638.

Rowiński, Robert S. “Mathematical Models and Computer Simulations of Aerial Spraying and Droplets Distribution in a Target Site.” *Transactions on Aerospace Research*, vol. 2019, no. 3, 2019, pp. 24–42., doi:10.2478/tar-2019-0015.

Sanchez-Cuevas, Pedro, et al. “Characterization of the Aerodynamic Ground Effect and Its Influence in Multirotor Control.” *International Journal of Aerospace Engineering*, vol. 2017, 2017, pp. 1–17., doi:10.1155/2017/1823056.

Scharnowski, Sven, and Christian J. Kähler. “Particle Image Velocimetry - Classical Operating Rules from Today’s Perspective.” *Optics and Lasers in Engineering*, vol. 135, 2020, p. 106185., doi:10.1016/j.optlaseng.2020.106185.

Scheller, Brian L., and Douglas W. Bousfield. “Newtonian Drop Impact with a Solid Surface.” *AIChE Journal*, vol. 41, no. 6, 1995, pp. 1357–1367., doi:10.1002/aic.690410602.

Schou, Wayne C, et al. “Building Canopy Retention into AGDISP: Preliminary Models and Results.” *2011 Louisville, Kentucky, August 7 - August 10, 2011*, 2011, doi:10.13031/2013.37286.

Sharf, I., et al. “Ground Effect Experiments and Model Validation with Draganflyer X8 Rotorcraft.” *2014 International Conference on Unmanned Aircraft Systems (ICUAS)*, 2014, doi:10.1109/icuas.2014.6842370.

Shi, Qiang, et al. “The Airflow Field Characteristics of UAV Flight in a Greenhouse.” *Agriculture*, vol. 11, no. 7, 2021, p. 634., doi:10.3390/agriculture11070634.

Shukla, Dhwanil, et al. “Aerodynamic Interactions Study on Low-Re Coaxial and Quad-Rotor Configurations.” *Volume 7: Fluids Engineering*, 2017, doi:10.1115/imece2017-71005.

Singh, Jitendra, et al. “Growth, Quality and Pest Infestation in Tomato under Protected Cultivation in Semi-Arid Region of Punjab.” *Indian Journal of Horticulture*, vol. 72, no. 4, 2015, p. 518., doi:10.5958/0974-0112.2015.00095.x.

Stajuda, Mateusz, et al. “Modified Virtual Blade Method for Propeller Modelling.” *Mechanics and Mechanical Engineering*, vol. 22, no. 2, 2018, pp. 603–618., doi:10.2478/mme-2018-0048.

Tanabe, Yasutada, et al. “Quadrotor Drone Hovering in Ground Effect.” *Journal of Robotics and Mechatronics*, vol. 33, no. 2, 2021, pp. 339–347., doi:10.20965/jrm.2021.p0339.

Tecplot 2013 User’s Manual. (2013) (Release 1/.). Bellevue, WA: Tecplot, inc. www.tecplot.com/documentation/

Teske, Milton E., et al. “AgDrift®: A Model for Estimating near-Field Spray Drift from Aerial Applications.” *Environmental Toxicology and Chemistry*, vol. 21, no. 3, 2002, pp. 659–671., doi:10.1002/etc.5620210327.

Teske, M. E., et al. “Modification of Droplet Evaporation in the Simulation of Fine Droplet Motion Using AGDISP.” *Transactions of the ASABE*, vol. 54, no. 2, 2011, pp. 417–421., doi:10.13031/2013.36444.

Teske, Milton E., et al. “Prediction of Aerial Spray Release from UAVs.” *Transactions of the ASABE*, vol. 61, no. 3, 2018, pp. 909–918., doi:10.13031/trans.12701.

Trayford, R.s., and L.w. Welch. “Aerial Spraying: A Simulation of Factors Influencing the Distribution and Recovery of Liquid Droplets.” *Journal of Agricultural Engineering Research*, vol. 22, no. 2, 1977, pp. 183–196., doi:10.1016/0021-8634(77)90062-2.

Versteeg, H. K., and W. Malalasekera. *An Introduction to Computational Fluid Dynamics: the Finite Volume Method*. Pearson Education, 2011.

Vogeltanz, Tomas. “Comparison of Open-Source CFD Software for Aerodynamic Analysis of Mini-UAV.” *2015 IEEE/AIAA 34th Digital Avionics Systems Conference (DASC)*, 2015, doi:10.1109/dasc.2015.7311438.

Vu, Ngoc Anh, et al. “Electric Propulsion System Sizing Methodology for an Agriculture Multicopter.” *Aerospace Science and Technology*, vol. 90, 2019, pp. 314–326., doi:10.1016/j.ast.2019.04.044.

Wahono, S.. “Development of Virtual Blade Model for Modelling Helicopter Rotor Downwash in OpenFOAM.”, *Defence science and technology organisation Fishermans Bend (Australia), aerospace division*, (2013), doi=10.1.1.951.836

Wen, Sheng, et al. “Numerical Analysis and Validation of Spray Distributions Disturbed by Quad-Rotor Drone Wake at Different Flight Speeds.” *Computers and Electronics in Agriculture*, vol. 166, 2019, p. 105036., doi:10.1016/j.compag.2019.105036.

Widnall, Sheila E., and Thomas L. Wolf. “Effect of Tip Vortex Structure on Helicopter Noise Due to Blade-Vortex Interaction.” *Journal of Aircraft*, vol. 17, no. 10, 1980, pp. 705–711., doi:10.2514/3.44681.

World meteorological organization, Guide to Meteorological Instruments and Methods of Observation No. 8, 2008

Yang, Yi, et al. “Consistent Inflow Boundary Conditions for Modelling the Neutral Equilibrium Atmospheric Boundary Layer for the SST k-ω Model.” *Wind and Structures*, vol. 24, no. 5, 2017, pp. 465–480., doi:10.12989/was.2017.24.5.465.

Yang, Yi, et al. “New Inflow Boundary Conditions for Modelling the Neutral Equilibrium Atmospheric Boundary Layer in Computational Wind Engineering.” *Journal of Wind*

Engineering and Industrial Aerodynamics, vol. 97, no. 2, 2009, pp. 88–95., doi:10.1016/j.jweia.2008.12.001.

Yeong, Siew Ping, and Sharul Sham Dol. "Aerodynamic Optimization of Micro Aerial Vehicle." *Journal of Applied Fluid Mechanics*, vol. 9, no. 7, 2016, pp. 2111–2121., doi:10.18869/acadpub.jafm.68.236.25522.

Yoon, S.s., et al. "Numerical Modeling and Experimental Measurements of a High Speed Solid-Cone Water Spray for Use in Fire Suppression Applications." *International Journal of Multiphase Flow*, vol. 30, no. 11, 2004, pp. 1369–1388., doi:10.1016/j.ijmultiphaseflow.2004.07.006.

Yoon, Steven, et al. "Computational Analysis of Multi-Rotor Flows." *54th AIAA Aerospace Sciences Meeting*, 2016, doi:10.2514/6.2016-0812.

Zhou, Wenwu, et al. "An Experimental Investigation on Rotor-to-Rotor Interactions of Small UAV Propellers." *35th AIAA Applied Aerodynamics Conference*, 2017, doi:10.2514/6.2017-3744.